# Particle Motion in Colloidal Dispersions: Applications to Microrheology and Nonequilibrium Depletion Interactions.

Thesis by

Aditya S. Khair

In Partial Fulfillment of the Requirements

for the Degree of

Doctor of Philosophy

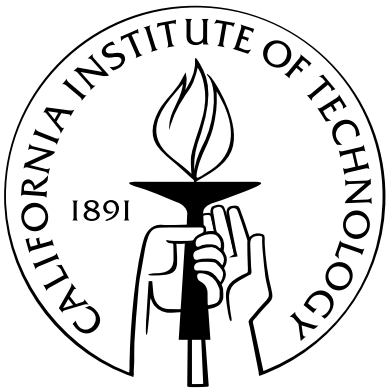


California Institute of Technology

Pasadena, California

2007

(Defended February 6, 2007)

# Acknowledgements

The past four and one-third years I have spent at Caltech have been among the most enjoyable of my life. Many people have contributed to this; unfortunately, I cannot acknowledge each and every person here. I offer my most sincere apologies to those whom I (through ignorance) do not mention below.

Firstly, I wish to thank my thesis adviser, John Brady. John gave me a fantastic research project to work on; allowed me generous vacation time to go back to England; and was always available to talk. As a researcher, John's integrity, curiosity, and rigor serve as the standard that I shall aspire to throughout my professional life.

I would also like to thank the members of my thesis committee — John Seinfeld, Todd Squires, and Zhen-Gang Wang — for their support and interest in my work. In particular, Todd was instrumental in sparking my interest in microrheology and has given me much advice on pursuing a career in academia.

I have been fortunate enough to share the highs and lows of graduate school with some great friends. I thank the members of the Brady research group that I have overlapped with: Josh Black, Ileana Carpen, Alex Leshansky, Ubaldo Cordova, James Swan, Manuj Swaroop, and Andy Downard, for making the sub-basement of Spalding an enjoyable place to work. I also thank Alex Brown, Justin Bois, Rafael Verduzco, Mike Feldman, and Akira Villar for sharing many laughs (and many beers) over the years.

All of the Chemical Engineering staff receive my most sincere thanks. In particular, the graduate-student secretary, Kathy Bubash, and our computer expert, Suresh Guptha, have helped me greatly.

A special thanks goes to Hilda and Sal Martinez, the parents of my fiancée, Vanessa (see below). Hilda and Sal have treated me so kindly and always welcomed me into their home. I will be forever grateful.

I would not have reached this point without the love of my parents. From an early age, they emphasized to me the importance of a good education; furthermore, they provided me every opportunity to get one. Their continued support and encouragement means more to me than they will ever know.

The last, but certainly not the least, acknowledgment goes to the love of my life, Vanessa. She is the one person who can always put on a smile on my face when I am feeling low. I hope that many years from now we can both look back on my time at Caltech with fond memories.

# Abstract

Over the past decade, microrheology has burst onto the scene as a technique to interrogate and manipulate complex fluids and biological materials at the micro- and nano-meter scale. At the heart of microrheology is the use of colloidal 'probe' particles embedded in the material of interest; by tracking the motion of a probe one can ascertain rheological properties of the material. In this study, we propose and investigate a paradigmatic model for microrheology: an externally driven probe traveling through an otherwise quiescent colloidal dispersion. From the probe's motion one can infer a 'microviscosity' of the dispersion via application of Stokes drag law. Depending on the amplitude and time-dependence of the probe's movement, the linear or nonlinear (micro-)rheological response of the dispersion may be inferred: from steady, arbitrary-amplitude motion we compute a nonlinear microviscosity, while small-amplitude oscillatory motion yields a frequency-dependent (complex) microviscosity. These two microviscosities are shown, after appropriate scaling, to be in good agreement with their (macro)-rheological counterparts. Furthermore, we investigate the role played by the probe's shape — sphere, rod, or disc — in microrheological experiments.

Lastly, on a related theme, we consider two spherical probes translating in-line with equal velocities through a colloidal dispersion, as a model for depletion interactions out of equilibrium. The probes disturb the tranquility of the dispersion; in retaliation, the disper-

sion exerts a entropic (depletion) force on each probe, which depends on the velocity of the probes and their separation. When moving 'slowly' we recover the well-known equilibrium depletion attraction between probes. For 'rapid' motion, there is a large accumulation of particles in a thin boundary layer on the upstream side of the leading probe, whereas the trailing probe moves in a tunnel, or wake, of particle-free solvent created by the leading probe. Consequently, the entropic force on the trailing probe vanishes, while the force on the leading probe approaches a limiting value, equal to that for a single translating probe.

# Contents

**Acknowledgements** **iii**

**Abstract** **v**

**1 Introduction** **1**

1.1 Introduction . . . . . 2

1.2 Bibliography . . . . . 10

**2 Single particle motion in colloidal dispersions: a simple model for active and nonlinear microrheology** **13**

2.1 Introduction . . . . . 14

2.2 Nonequilibrium microstructure . . . . . 21

2.3 Average velocity of the probe particle and its interpretation as a microviscosity 26

2.4 Nonequilibrium microstructure and microrheology at small $Pe_b$ . . . . . 32

2.4.1 Perturbation expansion of the structural deformation . . . . . 32

2.4.2 Linear response: The intrinsic microviscosity and its relation to self-diffusivity . . . . . 38

2.4.3 Weakly nonlinear theory . . . . . 44

2.5 Numerical solution of the Smoluchowski equation for arbitrary $Pe_b$ . . . . . 46

2.5.1 Legendre polynomial expansion . . . . . 48

2.5.2 Finite difference methods . . . . . 51

2.6 Results . . . . . 53

2.6.1 No hydrodynamic interactions . . . . . 53

2.6.2 The effect of hydrodynamic interactions . . . . . 57

2.7 Discussion . . . . . 68

2.8 Bibliography . . . . . 75

**Appendices to chapter 2** **78**

2.A The Brownian velocity contribution . . . . . 79

2.B Finite difference method . . . . . 80

2.C Boundary-layer equation . . . . . 83

2.D Boundary-layer analysis of the pair-distribution function at high $Pe_b$ in the absence of hydrodynamic interactions . . . . . 85

2.E Boundary-layer analysis of the pair-distribution function at high $Pe_b$ for $\hat{b} \equiv 1$ 88

**3 "Microviscoelasticity" of colloidal dispersions** **93**

3.1 Introduction . . . . . 94

3.2 Governing equations . . . . . 101

3.2.1 Smoluchowski equation . . . . . 101

3.2.2 Average probe velocity . . . . . 105

3.3 Small-amplitude oscillations . . . . . 105

3.4 Connection between microviscosity and self-diffusivity of the probe particle 110

3.5 Microstructure & microrheology: No hydrodynamic interactions . . . . . 112

3.6 Microstructure & microrheology: Hydrodynamic interactions . . . . . 120

3.7 Scale-up of results to more concentrated dispersions . . . . . 129

3.8 Comparison with experimental data . . . . . 132

3.9 Discussion . . . . . 139

3.10 Bibliography . . . . . 144

**Appendix to chapter 3** **148**

3.A High-frequency asymptotics with hydrodynamic interactions . . . . . 149

**4 Microrheology of colloidal dispersions: shape matters** **153**

4.1 Introduction . . . . . 154

4.2 Nonequilibrium microstructure . . . . . 158

4.2.1 Prolate probe . . . . . 160

4.2.2 Oblate probe . . . . . 162

4.3 Microviscosity . . . . . 163

4.4 Analytical results . . . . . 166

4.4.1 Near equilibrium $Pe \ll 1$ . . . . . 166

4.4.2 Far from equilibrium $Pe \gg 1$ . . . . . 168

4.4.2.1 Oblate probe . . . . . 168

4.4.2.2 Prolate probe . . . . . 171

4.5 Numerical methods . . . . . 176

4.5.1 Legendre polynomial expansion . . . . . 177

4.5.2 Finite differences . . . . . 178

4.6 Results . . . . . 179

4.7 Discussion . . . . . 186

4.8 Bibliography . . . . . 193

**Appendices to chapter 4** **196**

4.A Exact solution of the Smoluchowski equation . . . . . 197

4.B Asymptotic analysis at large $Pe$ . . . . . 199

4.C Prolate probe translating at an angle to its symmetry axis . . . . . 203

**5 On the motion of two particles translating with equal velocities through a colloidal dispersion** **209**

5.1 Introduction . . . . . 210

5.2 Governing equations . . . . . 213

5.2.1 Nonequilibrium microstructure . . . . . 213

5.2.2 Forces on the probes . . . . . 217

5.3 Solution of the Smoluchowski equation . . . . . 219

5.3.1 Non-intersecting excluded volumes: bispherical coordinates . . . . . 220

5.3.2 Intersecting excluded volumes: toroidal coordinates . . . . . 223

5.4 Results . . . . . 226

5.5 Discussion . . . . . 231

5.6 Bibliography . . . . . 237

**6 Conclusions** **239**

6.1 Conclusions & future directions . . . . . 240

6.2 Bibliography . . . . . 247

# List of Figures

2.1 Sketch of the probe and background/bath particle configuration. . . . . 24

2.2 The $O(Pe_b)$ structural deformation function $f_1$ for several values of $\hat{b} = b/a$. 35

2.3 First $O(Pe_b^2)$ structural deformation function $f_2$ for several values of $\hat{b} = b/a$. 36

2.4 Second $O(Pe_b^2)$ structural deformation function $h_2$ for several values of $\hat{b} = b/a$. 37

2.5 The equilibrium microstructure contribution to the intrinsic hydrodynamic microviscosity $\eta_{i,0}^H$ as a function of the excluded radius $\hat{b} = b/a$. . . . . 41

2.6 Intrinsic microviscosity contributions in the limit $Pe_b \to 0$ as a function of $\hat{b} = b/a$. . . . . 43

2.7 The $O(Pe_b^2)$ contribution to the intrinsic hydrodynamic microviscosity $\eta_i^H$ (2.28) as a function of $\hat{b} = b/a$. . . . . 45

2.8 Structural deformation $f(\boldsymbol{s}) = g(\boldsymbol{s}) - 1$ in the symmetry plane of the probe particle as a function of $Pe_b$ for $\hat{b} = 1.00001$. . . . . 47

2.9 Angular dependence of the structural deformation at contact for several $Pe_b$ in the absence of hydrodynamic interactions. . . . . 54

2.10 The pair-distribution function at contact as a function of the polar angle $\theta$ and $Pe_b$ in the absence of hydrodynamic interactions, $\hat{b} \to \infty$. . . . . 56

2.11 The intrinsic microviscosity $\eta_i$ as a function of $Pe_b$ in the absence of hydrodynamic interactions. . . . . 57

2.12 Small $Pe_b$ variation of the intrinsic microviscosity for $\hat{b} = 1.00001$. . . . . 58

2.13 The pair-distribution function at contact as a function of the polar angle $\theta$ and $Pe_b$ in the case of near-full hydrodynamic interactions $\hat{b} = 1.00001$. . . . 59

2.14 Determination of the scaling exponent $\delta$ relating the pair-distribution function at contact to $Pe_b$ for various $\hat{b}$. . . . . 61

2.15 Contributions to the intrinsic microviscosity $\eta_i$ as a function of $Pe_b$ for various $\hat{b}$. 63

2.16 The Brownian intrinsic microviscosity $\eta_i^B$ as a function of $Pe_b$ and $\hat{b}$. . . . . 66

2.17 The intrinsic microviscosity for $\hat{b} = 1.00001$ as a function of $Pe_b$. . . . . 68

2.18 Comparison of the microviscosity and macroviscosity. . . . . 70

3.1 $O(\phi_b)$ coefficient of the low-frequency microviscosity $\eta_0'$ versus $\hat{b} = b/a$. . . . . 109

3.2 Real part of the reduced complex viscosity in the absence of hydrodynamic interactions as a function of dimensionless frequency $\alpha$. . . . . 116

3.3 Imaginary part of the reduced complex viscosity in the absence of hydrodynamic interactions as a function of dimensionless frequency $\alpha$. . . . . 118

3.4 Cox-Merz relationship between the frequency $\omega$ and external force $\boldsymbol{F}^{ext}$ dependence of the relative microviscosity increment, $\Delta\eta_r = \eta_r - 1$. . . . . 119

3.5 Real part of the reduced complex viscosity versus dimensionless frequency $\alpha$ for various $\hat{b} = b/a$. . . . . 121

3.6 Imaginary part of the reduced complex viscosity versus dimensionless frequency $\alpha$ for various $\hat{b} = b/a$. . . . . 122

3.7 Elastic modulus $G'(\alpha)/\phi_b = \alpha\eta''(\alpha)/\phi_b$ versus dimensionless frequency $\alpha$ for various $\hat{b} = b/a$. . . . . 123

3.8 Cox-Merz relationship between the frequency $\omega$ and external force $\boldsymbol{F}^{ext}$ dependence of the relative microviscosity increment, $\Delta_T\eta_r = \eta_r - (1 + \eta_H)$. . . 129

3.9 Comparison of theoretical calculations and experimental data for the real part of the reduced complex viscosity, $(\eta'(\alpha^*)-\eta'_\infty)/(\eta'_0-\eta'_\infty)$, versus dimensionless frequency $\alpha^*(\phi_b) = \omega b^2/2D^s_\infty(\phi_b)$. . . . . 135

3.10 Comparison of theoretical calculations and experimental data for the imaginary part of the reduced complex viscosity, $\eta''(\alpha^*)/(\eta'_0 - \eta'_\infty)$, versus dimensionless frequency $\alpha^*(\phi_b) = \omega b^2/2D^s_\infty(\phi_b)$. . . . . 137

3.11 Real part of the reduced complex viscosity versus dimensionless 'rescaled' frequency $\alpha^* = \omega\tau$. . . . . 138

4.1 Definition sketch for the prolate probe. . . . . 161

4.2 Definition sketch for the oblate probe. . . . . 162

4.3 Plot of the mobility factors $K^{ob}$ and $K^{pr}$ versus probe aspect ratio $\hat{a} = a/b$. . 164

4.4 Microviscosity increments at small $Pe$ as a function of probe's aspect ratio $\hat{a} = a/b$. . . . . 167

4.5 Sketch of the microstructure around a oblate probe at large $Pe$. . . . . 170

4.6 Sketch of the microstructure around an prolate probe at large $Pe$. . . . . 172

4.7 Microviscosity increments at large $Pe$ as a function of probe's aspect ratio $\hat{a} = a/b$. . . . . 174

4.8 Difference in microviscosity increments at small $Pe$ and large $Pe$ as a function of probe aspect ratio $\hat{a} = a/b$. . . . . 175

4.9 Sample finite difference gird for a prolate probe. . . . . 178

4.10 Microstructural deformation, $g-1$, in the symmetry plane of the prolate probe as a function of $Pe$. . . . . 180

4.11 Microstructural deformation, $g-1$, in the symmetry plane of the oblate probe as a function of $Pe$. . . . . 181

4.12 Microviscosity increment for a prolate probe, $\Delta\eta_r^{pr}$, as a function of $Pe = Ub/D$ for different $\hat{a} = a/b$. . . . . 182

4.13 Microviscosity increment for an oblate probe, $\Delta\eta_r^{ob}$, as a function of $Pe = Ub/D$ for different $\hat{a} = a/b$. . . . . 183

4.14 Comparison of microviscosity increments from prolate and oblate probes with the macroviscosity. . . . . 187

4.15 Sketch of a prolate probe translating at angle $\beta$ to its symmetry axis. . . . . 189

5.1 Definition sketch for non-intersecting excluded-volumes, $d > 4$. . . . . 221

5.2 Sample finite difference grid in (transformed) bispherical coordinates. . . . . 222

5.3 Definition sketch for intersecting excluded-volumes, $d < 4$. . . . . 224

5.4 Sample finite difference grid in (transformed) toroidal coordinates. . . . . 225

5.5 Microstructural deformation, $g - 1$, in the symmetry plane of the probes as a function of $Pe$ for $d = 5$. . . . . 226

5.6 Microstructural deformation, $g - 1$, in the symmetry plane of the probes as a function of $Pe$ for $d = 3$. . . . . 228

5.7 Difference in entropic forces, $-(\langle \Delta F_l^z \rangle_2 - \langle \Delta F_t^z \rangle_2)/(\phi kT/a)$, versus $Pe = Ua/D_3$ for various $d$. . . . . 229

5.8 Entropic forces, $\langle \Delta F_i^z \rangle_2/(\phi kT/a)$, versus $d$ for $Pe = 0.0001$. . . . . 230

5.9 Entropic forces, $\langle \Delta F_i^z \rangle_2/(\phi kT/a)$, versus $Pe$ for $d = 3.5$. . . . . 231

5.10 Entropic forces, $\langle \Delta F_i^z \rangle_2/(\phi kT/a)$, versus $d$ for $Pe = 5$. . . . . 232

# List of Tables

2.1 Total $\eta_i$; equilibrium $\eta_{i,0}^H$; compressional ($F_r^{ext} > 0$) $\eta_{i,c}$; and extensional ($F_r^{ext} < 0$) $\eta_{i,e}$ contributions to the intrinsic microviscosity at $Pe_b = 1000$ for full hydrodynamics ($\hat{b} = 1.00001 \approx 1$) and without hydrodynamics ($\hat{b} \to \infty$). 65

3.1 Brief description of the experimental investigations discussed in § 3.8. . . . . 134

# Chapter 1

# Introduction

## 1.1 Introduction

Life isn't simple: for instance, most fluids do not conform to Newton's ideal. Such 'complex fluids', comprising (sub-) micrometer sized particles suspended in a liquid or gas, are ubiquitous: blood, inks, slurries, photonic crystals, aerosols, and bio-materials to name but a few examples. The intricate *microstructure* — the spatio-temporal configuration of the suspended particles — possessed by such materials can lead to fascinating and unexpected macroscopic (collective) phenomena. Moreover, a thorough knowledge of the microstructural response of complex fluids to external body forces and ambient flow fields is of paramount importance, in terms of performance and safety, to the design of industrial, microfluidic, and bio-medical devices.

The study of the flow and mechanical properties of complex fluids is the field of *rheology*. Over the past decade, a number of experimental techniques have burst onto the scene with the ability to infer rheological properties of complex fluids at the micro- (and nano-) meter scale. Collectively, they have come to be known as 'microrheology' (MacKintosh and Schmidt 1999; Waigh 2005). This name was adopted, perhaps, to distinguish these techniques from more traditional (macro-) rheological procedures (e.g. mechanical rheometry), which operate typically on much larger (millimeter or more) length scales. Therein lies the main advantage of micro- over macro-rheology: it requires much smaller amounts of sample. This is a particular advantage for rare, expensive, or biological substances that one simply cannot produce or procure in quantities sufficient for macrorheological testing.

At the heart of microrheology is the use of colloidal 'probe' particles embedded in the material of interest. Through tracking the motion of the probe (via confocal microscopy, e.g.) it is possible to infer rheological properties of the material. In *passive* tracking

experiments the probe moves diffusively due to the random thermal fluctuations of its environment. The mean-squared displacement of the probe is measured, from which the frequency-dependent shear modulus of the material is inferred via a generalized Stokes-Einstein-Sutherland relation (Mason and Weitz 1995). Many diverse systems, such as DNA solutions (Mason et al. 1997), living cells (Caspi et al. 2000; Daniels et al. 2006), and actin networks (Gittes et al. 1997), have been studied using passive microrheology. One should not think, however, that the use of thermally diffusing probes is limited to ascertaining viscoelastic moduli: recent studies have employed them to study protein folding (Tu and Breedveld 2005), 'nanohydrodynamics' at interfaces (Joly et al. 2006); and vortices in non-Newtonian fluids (Atakhorammi et al. 2005).

In passive microrheology one can infer only the near-equilibrium, or linear-response, properties of a material. In contradistinction, *active* microrheology, in which the material is pushed out of equilibrium by driving the probe through it (using, e.g., optical traps or magnetic tweezers), can be used to determine nonlinear viscoelastic properties. Colloidal dispersions (Meyer et al. 2006); suspensions of rod-like particles (Wensink and Löwen 2006); and semiflexible polymer networks (Ter-Oganessian et al. 2005) have recently been investigated using actively driven probes.

As microrheology is a relatively young field, it is only natural that macrorheology is the benchmark to which it is compared. However, is agreement between micro- and macro-rheologically measured properties expected and necessary for microrheology to be considered useful? After all, micro- and macro-rheology probe materials on fundamentally different length scales. Differences in micro and macro measurements are indicative of the physically distinct manner by which the techniques interrogate materials; by investigating and understanding these disparities one can only learn more about a material. Moreover, can

lessons be learned in the micro world that might suggest new experiments to perform at the macroscale? To address these issues, it is important to construct paradigms for microrheological experiments: so that they may be interpreted correctly and compared in a consistent fashion to macrorheological data.

The author's work at Caltech, which is presented in this thesis, has focused on developing theoretical models for active-microrheology experiments, by studying possibly the simplest of scenarios: an externally driven colloidal probe traveling in a monodisperse hard-sphere colloidal dispersion. The hard-sphere dispersion may be regarded as the 'simplest' of complex fluids; indeed, its flow behavior is characterized by only two dimensionless groups: volume fraction and non-dimensional shear-rate (or Péclet number). Nevertheless, it is the perfect starting point for studying active microrheology as its macrorheological properties have been investigated extensively (Russel et al. 1989; Dhont 1996). However, even this simplest of microrheological models contains subtleties: does it matter if one pulls the probe at fixed force or fixed velocity? How does the probe-bath size ratio come into play? What about the probe's shape? What happens if we have multiple (interacting) probes? It is hoped the subsequent chapters of this thesis go at least some way toward answering these questions.

The rest of the thesis is organized as follows. In chapter 2 (published previously, Khair and Brady 2006) we study the motion of a single Brownian probe particle subjected to a constant external force and immersed in a monodisperse suspension of colloidal 'bath' particles. The nonequilibrium configuration of particles induced by the motion of the probe is calculated to first order in the volume fraction of bath particles over the entire range of Péclet number, $Pe$, accounting for hydrodynamic and excluded-volume interactions between the probe and bath particles. Here, $Pe$ is the dimensionless external force on the probe —

a characteristic measure of the degree to which the equilibrium microstructure of the dispersion is distorted. For small $Pe$ the microstructure is primarily dictated by Brownian diffusion and is approximately fore-aft symmetric about the direction of the external force. In the large $Pe$ limit advection is dominant, except in a thin boundary layer in the compressive region of the flow where it is balanced by Brownian diffusion, leading to a highly non-equilibrium microstructure. The computed microstructure is employed to calculate the average translational velocity of the probe, from which a 'microviscosity' of the dispersion can be inferred via application of Stokes drag law. For small departures from equilibrium ($Pe < 1$) the microviscosity 'force-thins' proportional to $Pe^2$ from a Newtonian low-force plateau. For particles with long-range excluded-volume interactions, force-thinning persists until a terminal Newtonian plateau is reached in the limit $Pe \to \infty$. In the case of particles with very short-range excluded-volume interactions, the force-thinning ceases at $Pe \sim O(1)$, at which point the microviscosity attains a minimum value. Beyond $Pe \sim O(1)$ the microstructural boundary layer coincides with the lubrication range of hydrodynamic interactions causing the microviscosity to enter a continuous 'force-thickening' regime. The qualitative picture of the microviscosity variation with $Pe$ is in good agreement with theoretical and computational investigations on the 'macroviscosity' of sheared colloidal dispersions and, after appropriate scaling, we are able to make a direct quantitative comparison.

Depending on the amplitude and time dependence of the probe's movement, the linear or nonlinear rheological response of the dispersion may be inferred: from steady, arbitrary amplitude motion one computes a nonlinear microviscosity (cf. chapter 2) while, as discussed in chapter 3 (published previously, Khair and Brady 2005), small-amplitude oscillatory motion yields a frequency-dependent (complex) microviscosity. Specifically, we consider a probe subjected to a small amplitude oscillatory external force in an otherwise

quiescent colloidal dispersion. The non-equilibrium microstructure of the dispersion is calculated for small departures from equilibrium, i.e. to first order in $Pe$, and to leading order in the bath particle volume fraction. The nonequilibrium microstructure is used to compute the microstructurally-averaged velocity of the probe, from which one may infer a 'complex microviscosity' (or modulus) of the dispersion. The microviscosity is calculated over the entire range of oscillation frequencies, thereby determining the linear viscoelastic response of the dispersion. After appropriate scaling, our results are in qualitative, and near quantitative, agreement with traditional macrorheology studies, suggesting that oscillatory-probe microrheology can be a useful tool to examine the viscoelasticity of colloidal dispersions and perhaps other complex fluids.

In chapter 4 (submitted for publication, Khair and Brady 2007a) we examine a facet of active microrheology that has hitherto been unexplored: namely, what role does the *shape* of the probe play? To address this question, we consider a probe moving at constant velocity through a dispersion of spherical bath particles (of radii $b$). The probe itself is a body of revolution with major and minor semiaxes $a$ and $b$, respectively. The probe's shape is such that when its major(minor) axis is the axis of revolution the excluded-volume, or contact, surface between the probe and a bath particle is a prolate(oblate) spheroid. For a prolate or oblate probe moving along its symmetry axis, we calculate the nonequilibrium microstructure over the entire range of $Pe$, neglecting hydrodynamic interactions. Here, $Pe$ is defined as the non-dimensional velocity of the probe. The microstructure is employed to calculate the average external force on the probe, from which one can again infer a 'microviscosity' of the dispersion via Stokes drag law. The microviscosity is computed as a function of the aspect ratio of the probe, $\hat{a} = a/b$, thereby delineating the role of the probe's shape. For a prolate probe, regardless of the value of $\hat{a}$, the microviscosity

monotonically decreases, or 'velocity-thins', from a Newtonian plateau at small $Pe$ until a second Newtonian plateau is reached as $Pe \to \infty$. After appropriate scaling, we demonstrate this behavior to be in agreement with microrheology studies using spherical probes (Squires and Brady 2005) and macrorheological investigations (Bergenholtz et al. 2002). For an oblate probe, the microviscosity again transitions between two Newtonian plateaus: for $\hat{a} < 3.52$ (to two decimal places) the microviscosity at small $Pe$ is greater than at large $Pe$ (again, velocity-thinning); however, for $\hat{a} > 3.52$ the microviscosity at small $Pe$ is *less* than at large $Pe$, which suggests it 'velocity-thickens' as $Pe$ is increased. This anomalous velocity-thickening — due entirely to the probe shape — highlights the care needed when designing microrheology experiments with non-spherical probes. Lastly, we present a preliminary analysis of a prolate probe moving at an angle $\beta$ to its symmetry axis. In this case, one must apply an external torque to prevent the probe rotating, and we investigate how the torque may be related to the normal stress differences of the dispersion.

In chapter 5 (published previously, Khair and Brady 2007b) we consider the motion of two colloidal particles translating in-line with equal velocities through a colloidal dispersion. Although there is a microrheological application of this problem in generalizing two-point microrheology studies (Crocker et al. 2000) to the active regime, our focus is on the nonequilibrium entropic forces exerted on the probes. In equilibrium, it is well known that entropic forces between colloidal particles are produced by the addition of macromolecular entities (e.g., colloids, rods, polymers) to the suspending fluid. A classic example, first noted by Asakura and Oosawa (1958), is the so-called 'depletion attraction', where two colloidal 'probe' particles in a dilute bath of smaller colloids experience an attractive (depletion) force when the excluded-volume surfaces of the large particles overlap. Away from equilibrium, the depletion interaction between the probes must compete with their driven

motion. The moving probes push the microstructure of the dispersion out of equilibrium; resisting this is the Brownian diffusion of the dispersion 'bath' particles. As a result of the microstructural deformation, the dispersion exerts an entropic, or depletion, force on the probes. The nonequilibrium microstructure and entropic forces are computed to first order in the volume fraction of bath particles, as a function of the probe separation ($\boldsymbol{d}$) and the Péclet number ($Pe$), neglecting hydrodynamic interactions. Here, $Pe$ is the dimensionless velocity of the probes. For $Pe \ll 1$ — the linear-response regime — we recover the (equilibrium) depletion attraction between probes. Away from equilibrium, $Pe > 1$, (and for all $\boldsymbol{d}$) the leading probe acts as a 'bulldozer', accumulating bath particles in a thin boundary layer on its upstream side, while leaving a wake of bath-particle free suspending fluid downstream, in which the trailing probe travels. In this (nonlinear) regime the entropic forces on the probes are both opposite the direction of motion; however, the force on the leading probe is greater (in magnitude) than that on the trailing probe. Far from equilibrium ($Pe \gg 1$) the entropic force on the trailing probe vanishes, whereas the force on the leading probe approaches a limiting value, equal to that for a single probe moving through the dispersion.

Finally, chapter 6 offers some general conclusions and directions for future research.

Before continuing, the author wishes to make two points. First, the chapters that follow were written as individual papers and are thus entirely self contained. The reader may, therefore, read them in whichever order (s)he desires. Nevertheless, note that there is a certain amount of (unavoidable) repetition in the introductory sections of each chapter. Second, for completeness it should be mentioned that the author has also worked on a series of problems concerning the bulk viscosity of suspensions. As these investigations do not fall into the main theme of the author's doctoral research, they are not included in this thesis. However, the interested reader is directed to Khair et al. (2006); Brady et al. (2006);

and Khair (2006) for more details.

## 1.2 Bibliography

S. Asakura and F. Oosawa. On interaction between two bodies immersed in a solution of macromolecules. *J. Chem. Phys.*, 22:1255–1256, 1958.

M. Atakhorammi, G. H. Koenderink, C. F. Schmidt, and F. C. MacKintosh. Short-time inertial response of viscoelastic fluids: observation of vortex propagation. *Phys. Rev. Lett.*, 95:208302, 2005.

J. Bergenholtz, J. F. Brady, and M. Vicic. The non-Newtonian rheology of dilute colloidal suspensions. *J. Fluid Mech.*, 456:239–275, 2002.

J. F. Brady, A. S. Khair, and M. Swaroop. On the bulk viscosity of suspensions. *J. Fluid Mech.*, 554:109–123, 2006.

A. Caspi, R. Granek, and M. Elbaum. Enhanced diffusion in active intracellular transport. *Phys. Rev. Lett.*, 85:5655–5658, 2000.

J. C. Crocker, M. T. Valentine, E. R. Weeks, T. Gisler, P. D. Kaplan, A. G. Yodh, and D. A. Weitz. Two-point microrheology of inhomogeneous soft materials. *Phys. Rev. Lett.*, 84:888–891, 2000.

B. R. Daniels, B. C. Masi, and D. Wirtz. Probing single-cell micromechanics in vivo: the micorheology of *C. elegans* developing embryos. *Biophys. J.*, 90:4712–4719, 2006.

J. K. G. Dhont. *An introduction to the dynamics of colloids*. Elsevier Science, 1996.

F. Gittes, B. Schnurr, P. D. Olmsted, F. C. MacKintosh, and C. F. Schimdt. Microscopic viscoelasticity: shear moduli of soft materials determined from thermal fluctuations. *Phys. Rev. Lett.*, 79:3286–3289, 1997.

L. Joly, C. Ybert, and L. Bocquet. Probing the nanohydrodynamics at the liquid-solid interfaces using thermal motion. *Phys. Rev. Lett.*, 96:046101, 2006.

A. S. Khair. The 'Einstein correction' to the bulk viscosity in $n$ dimensions. *J. Coll. Int. Sci.*, 302:702–703, 2006.

A. S. Khair and J. F. Brady. "Microviscoelasticity" of colloidal dispersions. *J. Rheol.*, 49: 1449–1481, 2005.

A. S. Khair and J. F. Brady. Single particle motion in colloidal dispersions: A simple model for active and nonlinear microrheology. *J. Fluid Mech.*, 557:73–117, 2006.

A. S. Khair and J. F. Brady. Microrheology of colloidal dispersions: shape matters. J. Rheol. (Submitted), 2007a.

A. S. Khair and J. F. Brady. On the motion of two particles translating with equal velocities through a colloidal dispersion. *Proc. Roy. Soc. A*, 463:223–240, 2007b.

A. S. Khair, M. Swaroop, and J. F. Brady. A new resistance functon for two rigid spheres in a uniform compressible low-Reynolds-number flow. *Phys. Fluids.*, 18:043102, 2006.

F. C. MacKintosh and C. F. Schmidt. Microrheology. *Curr. Opin. Colloid Interface Sci.*, 4:300–307, 1999.

T. G. Mason, K. Ganesan, J. H. van Zanten, D. Wirtz, and S. C. Kuo. Particle tracking microrheology of complex fluids. *Phys. Rev. Lett.*, 79:3282–3285, 1997.

T. G. Mason and D. A. Weitz. Optical measurements of frequency-dependent linear viscoelastic moduli of complex fluids. *Phys. Rev. Lett.*, 74:1250–1253, 1995.

A. Meyer, A. Marshall, B. G. Bush, and E. M. Furst. Laser tweezer microrheology of a colloidal suspension. *J. Rheol.*, 50:77–92, 2006.

W. B. Russel, D. A. Saville, and W. R. Schowalter. *Colloidal Dispersions.* Cambridge University Press, 1989.

T. M. Squires and J. F. Brady. A simple paradigm for active and nonlinear microrheology. *Phys. Fluids*, 17:073101, 2005.

N. Ter-Oganessian, B. Quinn, D. A. Pink, and A. Boulbitch. Active microrheology of networks composed of semiflexible polymers: computer simulation of magnetic tweezers. *Phys. Rev. E*, 72:041510, 2005.

R. S. Tu and V. Breedveld. Microrheological detection of protein unfolding. *Phys. Rev. E.*, 72:041914, 2005.

T. A. Waigh. Microrheology of complex fluids. *Rep. Prog. Phys.*, 68:685–742, 2005.

H. H. Wensink and H. Löwen. Rhythmic cluster generation in strongly driven colloidal dispersions. *Phys. Rev. Lett.*, 97:038303, 2006.

# Chapter 2

# Single particle motion in colloidal dispersions: a simple model for active and nonlinear microrheology

## 2.1 Introduction

Colloidal dispersions composed of micrometer-sized particles suspended in a viscous fluid are ubiquitous in everyday life; paints, emulsions, inks, slurries, and foodstuffs being but a few examples. It is of particular importance to understand the mechanical response or flow behavior of these materials induced by the application of external body forces and ambient flow fields. This is a difficult task as colloidal dispersions are typically viscoelastic or non-Newtonian in nature, i.e. they exhibit both viscous (liquid-like) and elastic (solid-like) traits depending on the length and time (or frequency) scales on which they are interrogated. The experimental and theoretical study of the flow behavior of colloidal dispersions, or rheology, has traditionally focused on the measurement of bulk properties such as shear viscosity, normal stress differences, and storage and loss moduli. Experiments are conducted in rheometers (e.g. cone-and-plate, parallel-plate) where a macroscopic sample of the material is subjected to an oscillatory or steady shear flow. A review of traditional rheometry techniques may be found in Barnes et al. (1989). There are several limitations to conventional rheometry: one requires milliliter amounts of the substance under scrutiny; it is possible only to sample frequencies on the order of tens of Hertz (and hence one can not probe the short-time dynamical response of the material); and the rheometer apparatus often suffers from mechanical inertia and slip at the walls.

The past decade or so has seen the emergence of a number of experimental procedures collectively known as 'microrheology', with the ability to measure viscoelastic properties of soft heterogeneous materials at the micrometer scale. Many diverse systems such as living cells, DNA, actin networks, gelatin, and colloids near the glass transition have been investigated using microrheological techniques (for a review see MacKintosh and Schmidt 1999

and Waigh 2005). Microrheology does not suffer from several of the drawbacks that affect conventional 'macrorheology': microrheology only requires a small sample of the substance in comparison to macrorheology (a particular advantage in the case of rare biological materials); microrheology may be used to probe local viscoelastic properties (and hence serve to characterize inhomogeneous materials); and may sample frequencies up to the order of thousands of Hertz (and hence be used to study short-time dynamics of the material).

One of the most popular microrheology techniques involves the tracking of a single 'probe' particle to infer the properties of the embedding material. Typically, the probes are inert spherical beads on the order of a micrometer in radius. One may perform a *passive* tracking experiment where the change in probe location due to random thermal fluctuations of the surrounding medium is monitored (with e.g. optical microscopy, light scattering, or laser-deflection particle tracking). The experimentally observed mean-squared displacement of the probe may be used to infer the complex shear modulus of the surrounding material via application of a frequency dependent generalized Stokes-Einstein-Sutherland relation[1] (Mason and Weitz 1995; Mason et al. 1997). Although this is a fairly standard experimental procedure, the validity of using the frequency dependent generalized Stokes-Einstein-Sutherland relation has been called into question (Gittes et al. 1997). The major limitation of passive tracking experiments is that only *linear* viscoelastic properties may be ascertained. In contradistinction, *active* tracking experiments, in which the surrounding environment is driven out of equilibrium by application of an external force on the probe particle, may be used to study *nonlinear* viscoelastic properties of materials. (Note, our use

[1] Recently, our attention has been brought to a little-known paper by W. Sutherland ("A dynamical theory of diffusion for nonelectrolytes and the molecular mass of albumin." *Phil. Mag.* **6**(54), 781-785, 1905), in which he derives the relationship between the translational diffusion coefficient and hydrodynamic mobility for an isolated spherical colloidal particle, or, as it is colloquially known, the 'Stokes-Einstein relation'. As Sutherland and Einstein published this fundamental result in the same year, 1905, we feel it only proper to acknowledge Sutherland's contribution; hence, we propose to call this the 'Stokes-Einstein-Sutherland relation'.

of the word active is not to be confused with active in the sense of biologically active suspensions containing self-propelled particles.) Motion of the probe particle may be induced by application of magnetic fields, optical tweezers, or by manufacturing the probe to be of a different density than its surrounding environment. Much less work has been conducted on active microrheology as compared to its passive counterpart; it is the aim of this study to construct a simple theoretical model for active microrheology, with a view to interpreting existing experimental results and guiding the design of new active tracking experiments. Indeed, an important question to address is to what extent can (or should) the results of an active tracking experiment be interpreted as a 'viscosity'.

As mentioned above, microrheology is able to probe the viscoelastic properties of materials that cannot be produced in sufficient quantity to allow macrorheological testing. This notwithstanding, it is important to determine to what degree (if at all) are microrheological measurements representative of the macroscopic, or bulk, properties of a material. Certainly, agreement between microrheologically- and macrorheologically-measured properties would lend support to the microrheological results; however, should agreement between micro and macro be expected? Furthermore, is such agreement necessary for microrheology to be useful? To answer these questions it must be appreciated that micro- and macro-rheology probe materials on different length scales: in microrheology the material is deformed on the scale of the probe (typically on the order of a micrometer), whereas in macrorheology the deformation is on a 'macroscopic' scale (e.g. the gap spacing, typically on the order of a millimeter or more, of a parallel-plate rheometer). [Note, in this discussion we are only considering single-particle, or 'one-point', microrheology; two-point microrheology (Crocker et al. 2000), which cross-correlates the fluctuating motion of two distant probes, may induce deformations on length scales much larger than the individual probe size.] Furthermore, in

macrorheology the material is deformed using a viscometric flow field (e.g. simple shear), whilst in microrheology the flow induced by a moving probe is not viscometric. Thus, even in the large-probe (continuum) limit micro and macro measurements may not agree. On a microstructural level there are also fundamental differences: macrorheology applies an ambient flow (or stress) field — a quadrupolar forcing, whereas in microrheology a probe moves with a specified force (or velocity) — a dipolar forcing. With the above in mind, one should not expect, in general, agreement between micro- and macro-rheological measurements, and great care must be taken in the interpretation of the microrheological results and comparison with macrorheological data. To this end, it is essential to develop accurate theoretical models for active microrheology experiments. A final point: discrepancies between micro- and macro-rheological data are indicative of the fundamental differences in the two techniques; by understanding such differences one can only learn *more* information about a particular material. Thus, microrheology should be viewed as a compliment to, and not a replacement for, macrorheology.

Following the work of Squires and Brady (2005), as a model for active microrheology we consider the motion of a single spherical probe particle under the imposition of a steady external force amidst a sea of force- and torque-free spherical colloidal bath particles. For simplicity, it is assumed that the probe particle is of the same size as the bath particles. The advective relative velocity field generated by application of the external force on the probe causes the spatio-temporal configuration or *microstructure* of the dispersion to be driven out of its equilibrium state. Counteracting this is the Brownian diffusion of particles caused by random thermal fluctuations of the solvent molecules, which acts to restore the equilibrium microstructure. The degree to which the microstructure is displaced from equilibrium is governed by the ratio of the magnitude of the external force to the Brownian

force, known as the Péclet number, $Pe$. The limit $Pe \to 0$, in which the microstructure of the dispersion is primarily determined by Brownian diffusion, is the realm of passive (or linear) microrheology; when $Pe$ is not small compared to unity one is in the active (or nonlinear) regime.

The action of both advection and Brownian diffusion is strongly influenced by the hydrodynamic interactions between particles; thus, it is desirable to be able to investigate the effects of hydrodynamic interactions on the microstructure of the dispersion in a simple, systematic fashion. To this end, an interparticle excluded volume interaction is introduced, by which particles are kept at a minimum separation of $2b \geq 2a$ apart, where $a$ is the true (or hydrodynamic) radius and $b$ the excluded volume (or thermodynamic) radius of an individual particle. The same 'excluded-annulus' model was used previously by Brady and Morris (1997) and Bergenholtz et al. (2002) in investigations on the microstructure and macrorheology of sheared suspensions. By altering the ratio $\hat{b} = b/a$ one is able to move continuously from the limits of no hydrodynamic interactions, $\hat{b} \to \infty$, to full hydrodynamic interactions, $\hat{b} \equiv 1$.

In order to make analytical progress it assumed that the dispersion is dilute (i.e. the volume fraction of background colloidal particles is small compared to unity) so that only interactions between the probe and a single background particle are important in establishing the microstructure. In this limit the pair-distribution function of the dispersion obeys a two-body Smoluchowski equation. Previous investigations on related problems have only obtained solutions to this Smoluchowski equation (for finite $\hat{b}$) in the limits of near equilibrium ($Pe \ll 1$) and non-colloidal ($Pe^{-1} \equiv 0$) dispersions. For small departures from equilibrium Batchelor (1982), in a study of sedimentation in a dilute polydisperse suspension, determined the microstructure to first order in $Pe$ for $\hat{b} = 1$. Using this microstructure

he calculates the average translational velocity of a particle in the dispersion and in a subsequent paper (Batchelor 1983) exposes the relationship between the translational velocity and the self-diffusivity of a particle. At the other extreme $Pe^{-1} \equiv 0$, Batchelor (1982) found that for $\hat{b} = 1$ the pair-distribution function is spherically symmetric about a reference particle. This is somewhat paradoxical given the directionality imposed by the external force (in Batchelor's case gravity) and the absence of Brownian diffusion, but is in fact a consequence of the fore-aft symmetry of the relative trajectories for a pair of particles in Stokes flow. In the absence of hydrodynamic interactions ($\hat{b} \to \infty$) Squires and Brady (2005) have recently derived an exact solution of the Smoluchowski equation for arbitrary $Pe$. In this study the Smoluchowski equation is solved via a combination of perturbation methods and numerical computations, enabling us to determine the microstructure over the entire range of $Pe$ and $\hat{b}$.

The pair-distribution function may be used to calculate quantities such as the microstructurally averaged translational velocity of the probe particle. The average velocity is an experimentally accessible quantity, as illustrated in the study of Habdas et al. (2004), who, using confocal microscopy, delineated the relationship between the average velocity and applied force for a magnetic particle moving in a dense colloidal dispersion. To facilitate a comparison with macrorheology experiments one may interpret the average translational velocity of the probe particle in terms of a 'microviscosity' of the dispersion via application of Stokes drag law. In the case of non-colloidal suspensions such a connection has been made by Davis and Hill (1992) and Almog and Brenner (1997) to the viscosity obtained from 'Falling-Ball' rheometry experiments. Theoretical calculations of the 'macroviscosity' of a sheared colloidal suspension have been reported by Bergenholtz et al. (2002) over the entire range of $Pe$ (with $Pe$ defined with the non-dimensional shear-rate in this case) and

$\hat{b}$. In the limit $Pe \to 0$ (regardless of the value of $\hat{b}$) they find the macroviscosity attains a low-shear Newtonian plateau, which on increasing $Pe$ is followed by a decrease, or 'shear-thinning', of the macroviscosity up to $Pe \sim O(1)$. For $\hat{b} > 1.1$ this shear-thinning persists on increasing $Pe$ until a high-shear Newtonian plateau is reached in the limit $Pe \to \infty$. However, for $\hat{b} < 1.1$ the macroviscosity attains a minimum at $Pe \sim O(1)$ and proceeds to grow, or 'shear-thicken', with increasing $Pe$. Squires and Brady (2005) used their exact solution of the Smoluchowski equation in the absence of hydrodynamic interactions to compute the microviscosity of the dispersion for arbitrary $Pe$. They find that the microviscosity force-thins from a Newtonian plateau in the limit $Pe \to 0$, until a second Newtonian plateau is reached as $Pe \to \infty$, in qualitative agreement with the macroviscosity results of Bergenholtz et al. (2002). A major outcome of this work is the demonstration that the qualitative agreement between microviscosity and macroviscosity persists when the effects of hydrodynamic interactions between particles are included. Furthermore, after appropriate scaling, we are able to make a direct quantitative comparison between the micro- and macro-viscosity.

The remainder of this chapter is set out as follows. In § 2.2 we formulate the two-body Smoluchowski equation governing the spatio-temporal evolution of the nonequilibrium pair-distribution function. The separate hydrodynamic, Brownian, and interparticle-force contributions to the ensemble averaged translational velocity of the probe particle are derived in § 2.3, along with the interpretation of the translational velocity as a microviscosity of the dispersion. Small departures from the equilibrium microstructure ($Pe \ll 1$) are the subject of § 2.4. Here, in § 2.4.1 we show that the distortion of the equilibrium microstructure may be calculated through terms of $O(Pe^2)$ via a regular perturbation expansion, thereby extending the analysis of Batchelor (1982). To proceed to higher orders in $Pe$ requires the use

of matched asymptotic expansions. Subsection 2.4.2 is concerned with the linear-response (or passive) regime, where the perturbation to the equilibrium microstructure is linearly related to $Pe$. In this limit the microstructural evolution problem is identical to that for self-diffusion, at long wavelengths, (Brady 1994; Russel et al. 1989) and the microviscosity may be simply related to the long-time self-diffusivity of a particle. Moving to nonlinear response, in § 2.4.3 we consider the effect of a nonlinear deformation to the microstructure on the microviscosity of the suspension. To obtain the nonequilibrium microstructure for arbitrary $Pe$ one must solve the Smoluchowski equation numerically, as discussed in § 2.5. The results of our numerical computations are presented in § 2.6. To demonstrate the accuracy of the numerical solutions we focus first on the case of particles without hydrodynamic interactions, for which the Smoluchowski equation has been solved exactly (Squires and Brady 2005). Next, we examine the effect of hydrodynamic interactions on the microstructure and microviscosity of the suspension. It is found that the degree of 'force-thickening' at large $Pe$ may be tuned by altering $\hat{b}$, in agreement with the study of Bergenholtz et al. (2002) for the macroviscosity. Lastly, some concluding remarks are offered in § 2.7.

## 2.2 Nonequilibrium microstructure

Consider an assemblage of $N$ spherical particles of radii $a$ homogeneously dispersed in an incompressible Newtonian suspending fluid of density $\rho$ and dynamic viscosity $\eta$. An external force, $\boldsymbol{F}^{ext}$, is applied to one of the particles (the probe) whilst the other $N-1$ background particles are force- and torque-free. An alternative procedure is to fix the velocity of the probe particle rather than the force imposed on it, as discussed by Squires and Brady (2005) (see also Almog and Brenner 1997). The fixed-force and fixed-velocity problems are different in detail, although they share similar qualitative features. The Reynolds number,

$Re = \rho U a/\eta$ (with $U$ a typical velocity scale), characterizing the fluid inertia over a linear dimension of order of magnitude $a$, is assumed to be much less than unity, thus enabling use of the Stokes equations in describing the fluid flow. Our aim is to develop a theory that models the microstructure of the suspension. Specifically, it is desired to compute the pair-distribution function thus determining the probability of finding a background particle at a vector separation $\boldsymbol{r}$ from the probe.

Our point of departure is the Smoluchowski equation governing the spatio-temporal evolution of the probability distribution function $P_N(\boldsymbol{r}_N, t)$ of the $N$ particle configuration vector $\boldsymbol{r}_N$:

$$\frac{\partial P_N}{\partial t} + \sum_{i=1}^{N} \boldsymbol{\nabla}_i \cdot \boldsymbol{j}_i = 0,$$

where the sum is over all particles in the suspension. The flux of particle $i$ is given by

$$\boldsymbol{j}_i = \boldsymbol{U}_i P_N - \sum_{j=1}^{N} \boldsymbol{D}_{ij} P_N \cdot \boldsymbol{\nabla}_j \left( \ln P_N + V_N/kT \right),$$

where $\boldsymbol{U}_i$ is the hydrodynamic velocity due to the external force, $kT$ is the thermal energy, and $V_N$ is the $N$-particle interaction potential. The thermal or Brownian force acting on particle $i$ due to the random thermal fluctuations of the solvent molecules is $-kT\boldsymbol{\nabla}_i \ln P_N$. The relative Brownian diffusivity of an $ij$-pair of particles is $\boldsymbol{D}_{ij} = kT\boldsymbol{M}_{ij}^{UF}$, where $\boldsymbol{M}_{ij}^{UF}$ is the hydrodynamic mobility tensor relating the velocity of particle $i$ to the force exerted on particle $j$.

At equilibrium the absence of any external forcing implies that $\boldsymbol{U}_i = 0$ for each particle, and the probability distribution (denoted as $P_N^0$) is independent of time. This results in a balance between the interparticle potential and thermal forces, $\ln P_N^0 + V_N/kT = 0$, which is solved by the familiar Boltzmann distribution $P_N^0 \sim \exp(-V_N/kT)$. Application

of an external force to the probe particle will induce relative motion among the particles in the suspension, driving the system out of equilibrium and $P_N$ away from the Boltzmann distribution. The velocity of a particle $i$ due to such an externally imposed force on particle $j$ is given by $\boldsymbol{U}_i = \boldsymbol{M}_{ij}^{UF} \cdot \boldsymbol{F}_j^{ext}$.

To arrive at a closed equation for the pair-distribution function the $N$-particle Smoluchowski equation is integrated over the configurational degrees of freedom of $N-2$ particles, neglecting any resulting three-body interaction terms (for a detailed derivation see Squires and Brady 2005). In discarding the three-body couplings the validity of our theory is restricted to the limit of low background particle volume fraction, $\phi_a = 4\pi n a^3/3 \ll 1$ (where $n$ is the number density of background particles), with the advantage that it is possible to make analytical progress. The pair-distribution function $g(\boldsymbol{r})$, defined as $n^2 g(\boldsymbol{r}) = ((N-2)!)^{-1} \int P_N(\boldsymbol{r}_N, t) d\boldsymbol{r}_3 ... d\boldsymbol{r}_N$, satisfies a pair-level Smoluchowski equation:

$$\frac{\partial g}{\partial t} + \boldsymbol{\nabla}_r \cdot (\boldsymbol{U}_r g) = \boldsymbol{\nabla}_r \cdot \boldsymbol{D}_r \cdot (g \boldsymbol{\nabla}_r V/kT + \boldsymbol{\nabla}_r g). \tag{2.1}$$

In writing (2.1) the center-of-mass coordinate system of two particles $\boldsymbol{r} = \boldsymbol{r_2} - \boldsymbol{r_1}$ and $\boldsymbol{x} = \boldsymbol{r}_2 + \boldsymbol{r}_1$ has been adopted, with $\boldsymbol{r_1}$ denoting the probe particle. The relative hydrodynamic velocity and relative Brownian diffusivity tensor are given by $\boldsymbol{U}_r = \boldsymbol{U}_2 - \boldsymbol{U}_1$ and $\boldsymbol{D}_r = \boldsymbol{D}_{11} + \boldsymbol{D}_{22} - \boldsymbol{D}_{12} - \boldsymbol{D}_{21}$, respectively.

The character of the pair-distribution function reflects the competition between the external forcing in driving the suspension out of equilibrium and Brownian diffusion which acts to restore equilibrium; both of these effects are heavily influenced by the nature of the hydrodynamic interactions between particles. Thus, in a theoretical model it is desirable to be able to tune the strength of the hydrodynamic interactions in a simple and systematic

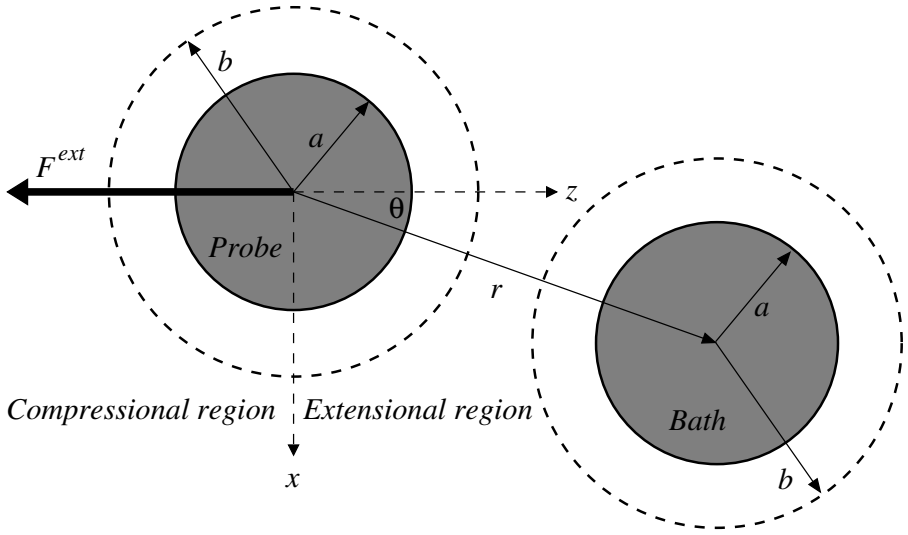


Figure 2.1: Definition sketch of the probe and background/bath particle configuration.

manner. To this end, the two-body interparticle potential $V(r)$ is chosen to be a simple 'excluded-annulus' model:

$$V(r) = \begin{cases} \infty & \text{if } r \leq 2b \\ 0 & \text{if } r > 2b. \end{cases}$$

The length $b$ ($\geq a$) is the excluded, or 'thermodynamic', radius of a particle, so that the separation between the probe particle and a background particle may be no less than $2b$. Interactions of this nature may arise from e.g. surface asperities, grafted polymer chains, or electrostatic forces. The excluded-annulus model has been employed by Brady and Morris (1997) and Bergenholtz et al. (2002) in computing the microstructure of a sheared suspension. A definition sketch of the two-sphere configuration is provided in figure 2.1. Altering the parameter $\hat{b} = b/a \in [1, \infty)$ allows one to examine the role of hydrodynamic interactions in setting the microstructure. In the limit $\hat{b} \to \infty$ the particles do not experience hydrodynamic interactions and one recovers the special case of a thermodynamic hard-sphere suspension; when $\hat{b} \equiv 1$ the particles experience full hydrodynamic interactions with one another. The diluteness assumption now requires the volume fraction based on the

excluded radius $b$ to be small, $\phi_b = 4\pi n b^3/3 \ll 1$.

The pair-level Smoluchowski equation is made dimensionless by scaling quantities as

$$\boldsymbol{r} \sim b, \quad \boldsymbol{U} \sim \frac{F_0}{6\pi\eta a}, \quad \boldsymbol{D} \sim 2D, \quad \text{and} \quad t \sim \frac{6\pi\eta a b}{F_0},$$

where $F_0$ is the magnitude of the external force $\boldsymbol{F}^{ext}$ and $D = kT/6\pi\eta a$ is the Stokes-Einstein-Sutherland diffusivity of an isolated colloidal particle of radius $a$. In this study we consider time independent microstructures for which the scaled pair-level Smoluchowski equation reads

$$Pe_b \boldsymbol{\nabla} \cdot (\boldsymbol{U} g) = \boldsymbol{\nabla} \cdot \boldsymbol{D} \cdot \boldsymbol{\nabla} g, \tag{2.2}$$

where all quantities are dimensionless, and for brevity the subscripts on $\boldsymbol{\nabla}_r, \boldsymbol{U}_r$, and $\boldsymbol{D}_r$ have been dropped. The above equation reflects the competition between advection due to the application of an external force on the probe particle (the left-hand side of (2.2)) in driving the system out of equilibrium and Brownian motion (the right-hand side of (2.2)) in attempting to restore equilibrium. The degree to which the microstructure is distorted from its equilibrium state is governed by the Péclet number, $Pe_b = F_0/(2kT/b)$, which emerges naturally from the scaling. The subscript $b$ indicates that the Péclet number is based on the excluded radius $b$ rather than the hydrodynamic radius $a$. The Péclet number may be viewed as a ratio of forces: the external force $F_0$ over the Brownian force $2kT/b$, or alternatively, as a ratio of time scales: the diffusive time $\tau_D = b^2/2D$ divided by the advective time $\tau_A = 6\pi\eta a b/F_0$. Either way, it should be clear that increasing the Péclet number corresponds to driving the system away from equilibrium.

To fully determine the pair-distribution function the Smoluchowski equation (2.2) must be accompanied by appropriate boundary conditions. It is assumed that the suspension

lacks any long-range order, which implies that

$$g(\boldsymbol{s}) \to 1 \quad \text{as} \quad s \to \infty, \tag{2.3}$$

where $s = r/b$. The effect of the interparticle potential requires that the radial component of the relative flux is zero at $r = 2b$; thus, we have

$$\boldsymbol{s} \cdot \boldsymbol{D} \cdot \boldsymbol{\nabla} g = Pe_b \, \hat{\boldsymbol{s}} \cdot \boldsymbol{U} g \quad \text{at} \quad s = 2, \tag{2.4}$$

with $\hat{\boldsymbol{s}} = \boldsymbol{s}/s$ the radial unit vector. As the pair-distribution function approaches unity at large distances it is useful to define the structural deformation function $f(\boldsymbol{s}) \equiv g(\boldsymbol{s}) - 1$. Furthermore, in the dilute limit as the equilibrium pair-distribution function is unity everywhere (i.e. for $s \geq 2$), the structural deformation function is the departure from equilibrium caused by application of the external force on the probe.

## 2.3 Average velocity of the probe particle and its interpretation as a microviscosity

At low Reynolds number the average velocity of the probe particle may be written as

$$\langle \boldsymbol{U} \rangle = \boldsymbol{U}^0 + \langle \boldsymbol{U}^H \rangle + \langle \boldsymbol{U}^P \rangle + \langle \overline{\boldsymbol{U}^B} \rangle, \tag{2.5}$$

where $\boldsymbol{U}^0 = \boldsymbol{F}^{ext}/6\pi\eta a$ is the velocity of the probe particle in isolation. The presence of background colloidal particles causes the average velocity of the probe to differ from $\boldsymbol{U}^0$. This difference may be expressed as the sum of hydrodynamic $\langle \boldsymbol{U}^H \rangle$, interparticle $\langle \boldsymbol{U}^P \rangle$,

and Brownian $\langle\overline{\boldsymbol{U}^B}\rangle$ contributions. In (2.5) the angle brackets denote an ensemble average over the admissible positions of a background particle, and the overline on $\langle\overline{\boldsymbol{U}^B}\rangle$ denotes an average over the many collisions of the probe and background particles with the surrounding solvent molecules. In this section we derive expressions for each of the three contributions.

The velocity of particle 1 ($\boldsymbol{U}_1$ say) subjected to an external force $\boldsymbol{F}_1$ in the presence of particle 2 subject to another external force $\boldsymbol{F}_2$ is

$$\boldsymbol{U}_1 = \boldsymbol{M}_{11}^{UF} \cdot \boldsymbol{F}_1 + \boldsymbol{M}_{12}^{UF} \cdot \boldsymbol{F}_2.$$

In the present case where the particles are spherical and of equal size the mobility tensors take the form

$$\boldsymbol{M}_{ij}^{UF} = \frac{1}{6\pi\eta a}\left\{A_{ij}(\hat{bs})\hat{\boldsymbol{s}}\hat{\boldsymbol{s}} + B_{ij}(\hat{bs})(\boldsymbol{I} - \hat{\boldsymbol{s}}\hat{\boldsymbol{s}})\right\},$$

where $\boldsymbol{I}$ is the identity tensor, and $A_{ij}(r)$ and $B_{ij}(r)$ are scalar mobility functions that depend on the magnitude of the dimensionless separation between the particles only. Following the notation of Batchelor (1982), the relative Brownian diffusivity tensor and relative velocity are given by

$$\begin{aligned} \boldsymbol{D} &= G(\hat{bs})\hat{\boldsymbol{s}}\hat{\boldsymbol{s}} + H(\hat{bs})\left(\boldsymbol{I} - \hat{\boldsymbol{s}}\hat{\boldsymbol{s}}\right), \\ \boldsymbol{U} &= \left[G(\hat{bs})\hat{\boldsymbol{s}}\hat{\boldsymbol{s}} + H(\hat{bs})\left(\boldsymbol{I} - \hat{\boldsymbol{s}}\hat{\boldsymbol{s}}\right)\right] \cdot \left(-\hat{\boldsymbol{F}}^{ext}\right), \end{aligned} \tag{2.6}$$

where $\hat{\boldsymbol{F}}^{ext} = \boldsymbol{F}^{ext}/F_0$. The absence of a factor of 2 multiplying the right hand side of (2.6) is due to the relative diffusivity tensor being scaled with $2D$ (the relative diffusivity of a pair of isolated spheres) rather than $D$ (the Stokes-Einstein-Sutherland diffusivity of a single isolated sphere). The hydrodynamic functions $G(r)$ and $H(r)$ describe the relative

mobility parallel and transverse to the line of centers of a pair of spheres respectively and are defined by

$$G(r) = A_{11}(r) - A_{12}(r),$$

$$H(r) = B_{11}(r) - B_{12}(r).$$

The velocity of the probe particle caused by the application of the external force is $\boldsymbol{M}_{11}^{UF} \cdot \boldsymbol{F}^{ext}$; hence, the velocity due to hydrodynamic interactions is simply

$$\boldsymbol{U}^H = \frac{\boldsymbol{F}^{ext}}{6\pi\eta a} \cdot \left\{ A_{11}(\hat{b}s)\hat{\boldsymbol{s}}\hat{\boldsymbol{s}} + B_{11}(\hat{b}s)(\boldsymbol{I} - \hat{\boldsymbol{s}}\hat{\boldsymbol{s}}) - \boldsymbol{I} \right\},$$

i.e. the difference between the total velocity $\boldsymbol{M}_{11}^{UF} \cdot \boldsymbol{F}^{ext}$ and the velocity in isolation $\boldsymbol{U}^0$. To obtain the average velocity due to hydrodynamic interactions the configuration-specific velocity $\boldsymbol{U}^H$ is weighted by the probability that the probe particle and a background particle are in a configuration characterized by the vector separation $\boldsymbol{s}$ (namely $ng(\boldsymbol{s})$) and averaged over the ensemble of all possible configurations. Following this program we have

$$\langle \boldsymbol{U}^H \rangle = \frac{3\phi_b}{4\pi} \frac{\boldsymbol{F}^{ext}}{6\pi\eta a} \cdot \int_{s\geq 2} \left\{ A_{11}(\hat{b}s)\hat{\boldsymbol{s}}\hat{\boldsymbol{s}} + B_{11}(\hat{b}s)(\boldsymbol{I} - \hat{\boldsymbol{s}}\hat{\boldsymbol{s}}) - \boldsymbol{I} \right\} g(\boldsymbol{s}) d\boldsymbol{s}. \tag{2.7}$$

It is important to note for large $s$ that $\boldsymbol{U}^H \sim O(s^{-4})$ and $g(\boldsymbol{s}) \sim O(1)$; thus, the integral in (2.7) is convergent.

Suppose that the probe particle experiences an interparticle-force interaction with a background particle specified by the interparticle force $\boldsymbol{F}^P$; the average velocity of the

probe due to this interparticle force is given by

$$\langle \boldsymbol{U}^P \rangle = \frac{1}{6\pi\eta a}\frac{3\phi_b}{4\pi}\int_{s\geq 2}\left\{G(\hat{b}s)\hat{\boldsymbol{s}}\hat{\boldsymbol{s}} + H(\hat{b}s)(\boldsymbol{I}-\hat{\boldsymbol{s}}\hat{\boldsymbol{s}})\right\}\cdot \boldsymbol{F}^P(\boldsymbol{s})g(\boldsymbol{s})d\boldsymbol{s}.$$

The excluded-annulus model is represented by a hard-sphere force $\boldsymbol{F}^P = -(kT/2b)\delta(s-2)\hat{\boldsymbol{s}}$, where $\delta(x)$ is the Dirac delta distribution. Substituting this into the above equation we have

$$\langle \boldsymbol{U}^P \rangle = -\frac{F_0}{6\pi\eta a}\frac{3\phi_b}{4\pi}\frac{2G(2\hat{b})}{Pe_b}\oint_{s=2} g(\boldsymbol{s})\hat{\boldsymbol{s}}d\Omega. \tag{2.8}$$

An immediate consequence of (2.8) is that in the limit $\hat{b}\to 1$, where $G(2\hat{b})\sim \hat{b}-1$, $\langle \boldsymbol{U}^P\rangle \to 0$. This is a statement of the fact that the hard-sphere force plays no dynamical role in the case $\hat{b}\equiv 1$: the rigidity of the particles is realized by the vanishing relative radial mobility.

Lastly, we consider the average velocity contribution of the probe particle due to Brownian motion. In appendix 2.A it is shown that

$$\overline{\boldsymbol{U}^B} = -\frac{1}{2}\boldsymbol{\nabla}\cdot\boldsymbol{D}, \tag{2.9}$$

where the divergence is taken with respect to the last index of the relative diffusivity tensor. Averaging (2.9) over the ensemble of admissible two-particle configurations yields

$$\langle\overline{\boldsymbol{U}^B}\rangle = -\frac{F_0}{6\pi\eta a}\frac{3\phi_b}{4\pi}\frac{1}{Pe_b}\int_{s\geq 2}\left(\frac{G(\hat{b}s)-H(\hat{b}s)}{s}+\frac{1}{2}\frac{dG(\hat{b}s)}{ds}\right)g(\boldsymbol{s})\hat{\boldsymbol{s}}d\boldsymbol{s}. \tag{2.10}$$

The same result may be derived if one supposes the effect of Brownian motion is equivalent to the action of equal and opposite 'thermodynamic forces' $\boldsymbol{F}_1^B = kT\boldsymbol{\nabla}\ln g(\boldsymbol{s})$ and $\boldsymbol{F}_2^B = -\boldsymbol{F}_1^B$ acting on the probe and a background particle respectively (Batchelor 1982).

Note, the integrand in (2.10) is of $O(s^{-5})$ for large $s$; hence, the integral is convergent.

Aside from the external force there are no other directional influences on $g(\boldsymbol{s})$; therefore, $g(\boldsymbol{s})$ is axially-symmetric about the orientation of $\boldsymbol{F}^{ext}$. Moreover, as $\boldsymbol{U}^0$ is parallel to $\boldsymbol{F}^{ext}$ one expects $\langle \boldsymbol{U}^H \rangle$, $\langle \boldsymbol{U}^P \rangle$, and $\langle \overline{\boldsymbol{U}^B} \rangle$ to be parallel to $\boldsymbol{F}^{ext}$ also. With this in mind, one is able to *interpret* the change in translational velocity of the probe due to the presence of the background particles as a dimensionless relative microviscosity, $\eta_r$, of the suspension. This is done by application of the Stokes drag formula $\boldsymbol{F}^{ext}/6\pi\eta a = \eta_r \langle \boldsymbol{U} \rangle$. Thus, the relative microviscosity is defined by

$$\eta_r \equiv \frac{F_0}{6\pi\eta a \hat{\boldsymbol{F}}^{ext} \cdot \langle \boldsymbol{U} \rangle}. \tag{2.11}$$

Note, the microviscosity contains (through its dependence on $\langle \boldsymbol{U} \rangle$) an *a priori* unknown dependence on the probe-to-background particle size ratio; this fact must be appreciated when analyzing results from an active tracking experiment. In our study the probe and background particles are of equal size so this is not a concern (see, however, the discussion in § 2.7 and Squires and Brady 2005).

For dilute dispersions the denominator in (2.11) can be expanded to first order in the background particle volume fraction $\phi_b$, and the relative microviscosity may be written as $\eta_r = 1 + \eta_i \phi_b$, where $\eta_i = \eta_i^H + \eta_i^P + \eta_i^B$ is the intrinsic microviscosity (i.e. the relative microviscosity minus the Newtonian solvent contribution and normalized by the background particle volume fraction); $\eta_i^H$, $\eta_i^P$, and $\eta_i^B$ are the hydrodynamic, interparticle, and Brownian contributions to the intrinsic microviscosity, respectively. A question we shall explore later is the relation between this microviscosity and the macroviscosity determined from studies on macroscopically sheared colloidal dispersions.

To highlight the role played by the nonequilibrium microstructure it is instructive to

express the intrinsic microviscosity contributions in terms of the structural deformation function $f(\boldsymbol{s})$. Firstly, for the intrinsic hydrodynamic microviscosity we have

$$\eta_i^H = \eta_{i,0}^H - \frac{3}{4\pi}\hat{\boldsymbol{F}}^{ext}\hat{\boldsymbol{F}}^{ext} : \int_{s\geq 2}\left\{A_{11}(\hat{b}s)\hat{\boldsymbol{s}}\hat{\boldsymbol{s}} + B_{11}(\hat{b}s)(\boldsymbol{I} - \hat{\boldsymbol{s}}\hat{\boldsymbol{s}}) - \boldsymbol{I}\right\} f(\boldsymbol{s})d\boldsymbol{s}, \tag{2.12}$$

where $\eta_{i,0}^H$ is the contribution to the intrinsic hydrodynamic microviscosity due to the equilibrium microstructure:

$$\eta_{i,0}^H = -\int_2^\infty (A_{11}(\hat{b}s) + 2B_{11}(\hat{b}s) - 3)s^2 ds. \tag{2.13}$$

The intrinsic interparticle microviscosity takes the form

$$\eta_i^P = \frac{3}{4\pi}\frac{2G(\hat{b}s)}{Pe_b}\hat{\boldsymbol{F}}^{ext} \cdot \oint_{s=2} f(\boldsymbol{s})\hat{\boldsymbol{s}}d\Omega, \tag{2.14}$$

from which we see the equilibrium microstructure does not affect $\eta_i^P$. For the intrinsic Brownian microviscosity we have

$$\eta_i^B = \frac{3}{4\pi}\frac{1}{Pe_b}\hat{\boldsymbol{F}}^{ext} \cdot \int_{s\geq 2}\left(\frac{G(\hat{b}s) - H(\hat{b}s)}{s} + \frac{1}{2}\frac{dG(\hat{b}s)}{ds}\right) f(\boldsymbol{s})\hat{\boldsymbol{s}}\, d\boldsymbol{s}, \tag{2.15}$$

which, as in the case of the intrinsic interparticle microviscosity, depends solely on the nonequilibrium microstructure.

## 2.4 Nonequilibrium microstructure and microrheology at small $Pe_b$

### 2.4.1 Perturbation expansion of the structural deformation

At small Péclet number, when the ratio of the external force to the restoring Brownian force is much less than unity, the suspension is only slightly displaced from its equilibrium state, enabling the pair-distribution function to be calculated via a perturbation expansion in $Pe_b$. Recalling the definition of $Pe_b$ as a ratio of timescales one anticipates that the perturbation to the equilibrium microstructure is singular, based on the general non-uniformity criterion proposed by Van Dyke (1975, pp. 80-83). Before dealing with the complicating effect of hydrodynamic interactions it is useful to examine the singular nature of the problem in their absence. Neglecting hydrodynamic interactions the pair-level Smoluchowski equation (2.2) and associated boundary conditions (2.3) and (2.4) reduce to

$$Pe_b\hat{\boldsymbol{U}}\cdot\boldsymbol{\nabla}f = \nabla^2 f, \tag{2.16}$$

$$Pe_b(\hat{\boldsymbol{s}}\cdot\hat{\boldsymbol{U}})(1+f) = \frac{df}{ds} \text{ at } s=2, \tag{2.17}$$

$$f\to 0 \quad \text{as} \quad s\to\infty, \tag{2.18}$$

where $\hat{\boldsymbol{U}} = -\hat{\boldsymbol{F}}^{ext}$. The distortion to the equilibrium microstructure is governed by a balance between isotropic diffusion and advection by a constant relative 'velocity' $\hat{\boldsymbol{U}}$. Even though the Péclet number is small from (2.16) we see that at distances $s\sim O(Pe_b^{-1})$ (where hydrodynamic interactions are unimportant anyway) the effects of advection and diffusion are of the same order of magnitude. Defining an 'outer' coordinate $\rho = sPe_b \sim O(1)$ we see

that (2.16) takes the form

$$\hat{\boldsymbol{U}} \cdot \boldsymbol{\nabla}_\rho F = \nabla_\rho^2 F, \tag{2.19}$$

in this outer region; for clarity, we denote the structural deformation in the outer region as $F$. It is required that a solution to (2.19) must vanish as $\rho \to \infty$ and match with the solution of the 'inner' equation (2.16) as $\rho \to 0$. If $Pe_b \equiv 0$ then the uniformly valid solution is simply $f = 0$, corresponding to an equilibrium microstructure.

In the inner region the first perturbation to the equilibrium microstructure is linear in the forcing $\hat{\boldsymbol{U}}$ and is given by

$$f = -Pe_b \frac{4}{s^2} \hat{\boldsymbol{s}} \cdot \hat{\boldsymbol{U}}, \tag{2.20}$$

which has the character of a diffusive dipole directed along $\hat{\boldsymbol{F}}^{ext}$. In terms of the outer variables (2.20) is

$$f = -Pe_b^3 \frac{4}{\rho^2} \hat{\boldsymbol{\rho}} \cdot \hat{\boldsymbol{U}};$$

thus, the leading order perturbation to the equilibrium microstructure is of $O(Pe_b^3)$ in the outer region. This indicates that the expansion in the inner region will be regular through terms of $O(Pe_b^2)$; specifically, we may write

$$f = f_1 Pe_b + f_2 Pe_b^2 + O(Pe_b^3),$$

where $f_1$ is given by (2.20). Now, $f_2$ must be quadratic in the forcing $\hat{\boldsymbol{U}}$ and it is a simple (if tedious) matter to show that

$$f_2 = 2\left(\frac{4}{s^3} - \frac{1}{s}\right) \hat{\boldsymbol{s}}\hat{\boldsymbol{s}} : \hat{\boldsymbol{U}}\hat{\boldsymbol{U}} - 2\left(\frac{4}{3s^3} - \frac{1}{s}\right), \tag{2.21}$$

from which it is seen that to leading order $f_2 Pe_b^2 \sim O(Pe_b^3)$ in the outer region also; hence, the first term in the outer expansion should be matched to $f_1 Pe_b + f_2 Pe_b^2$. Now, if one supposes the next term in the inner expansion to be $f_3 Pe_b^3$, then the singular nature of the expansion is revealed, because the particular solution of $f_3$ is forced by gradients in $f_2$, which from (2.21) are to leading order $O(s^{-2})$. The resulting particular solution for $f_3$ does not decay as $s \to \infty$. The matching condition for $f_3$ is: $f_1 Pe_b + f_2 Pe_b^2 + f_3 Pe_b^3 = F_1 Pe_b^3$ in the limits $\rho \to 0$ and $s \to \infty$, where $F_1$ is the first term in the outer solution. Although one may continue to higher orders in the expansion, the system (2.16)-(2.18) can be solved exactly (Squires and Brady 2005), making this unnecessary.

We now consider the effect of hydrodynamic interactions. Guided by the analysis above we propose an expansion for the structural deformation in the inner region of the form

$$f = Pe_b \hat{\boldsymbol{s}} \cdot \hat{\boldsymbol{F}}^{ext} f_1(s) + Pe_b^2 \left( \hat{\boldsymbol{s}}\hat{\boldsymbol{s}} : \hat{\boldsymbol{F}}^{ext}\hat{\boldsymbol{F}}^{ext} f_2(s) + h_2(s) \right) + O(Pe_b^3). \tag{2.22}$$

Substituting this expansion into the Smoluchowski equation (2.2) and boundary conditions (2.3) and (2.4) one obtains at $O(Pe_b)$ the system

$$\begin{aligned} \frac{d}{ds}\left( s^2 G(\hat{b}s) \frac{df_1}{ds} \right) \quad - \quad & 2H(\hat{b}s) f_1 = -s^2 W(\hat{b}s), \\ \frac{df_1}{ds} = -1 \quad & \text{at} \quad s = 2, \\ f_1 \to 0 \quad & \text{as} \quad s \to \infty, \end{aligned} \tag{2.23}$$

where $W(r) = dG/dr + 2(G - H)/r$, is proportional to the divergence of the relative

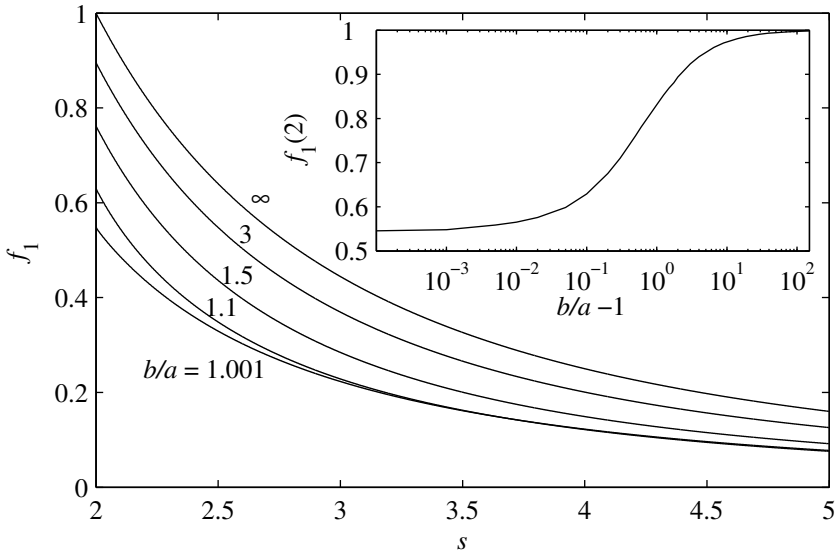


Figure 2.2: The $O(Pe_b)$ structural deformation function $f_1$ for several values of $\hat{b} = b/a$. The inset plots the contact value of $f_1$, i.e. $f_1(2)$, versus $\hat{b} - 1$. In the limit $\hat{b} \to 1$ we find $f_1(2) = 0.545$, in good agreement with Batchelor and Wen (1982) (see figure 9 in their paper).

velocity. To solve this equation we note that in the far-field

$$f_1 = \frac{f_1^\infty}{s^2} + \frac{3}{8\hat{b}}\left(3f_1^\infty - \frac{5}{\hat{b}^4}\right)\frac{1}{s^3} + \frac{9}{20\hat{b}^2}\left(3f_1^\infty - \frac{5}{\hat{b}^4}\right)\frac{1}{s^4} + O(s^{-5}), \tag{2.24}$$

reflecting the dipole nature of the disturbance. Using (2.24) as the 'initial condition' (2.23) is integrated backwards from $s = 5$ (for $s > 5$ we assume that $f_1$ is accurately represented by (2.24)) to $s = 2$. The value of the dipole strength $f_1^\infty$ is adjusted until the boundary condition at $s = 2$ is achieved. The hydrodynamic functions $G(\hat{b}s)$, $H(\hat{b}s)$, and $W(\hat{b}s)$ for $\hat{b}s > 2.01$ are computed via the twin multipole expansion of Jeffrey and Onishi (1984), whilst for $\hat{b}s < 2.01$ the lubrication theory results detailed in Kim and Karilla (1991) are used. In figure 2.2 we plot $f_1$ versus $s$ for several values of $\hat{b}$.

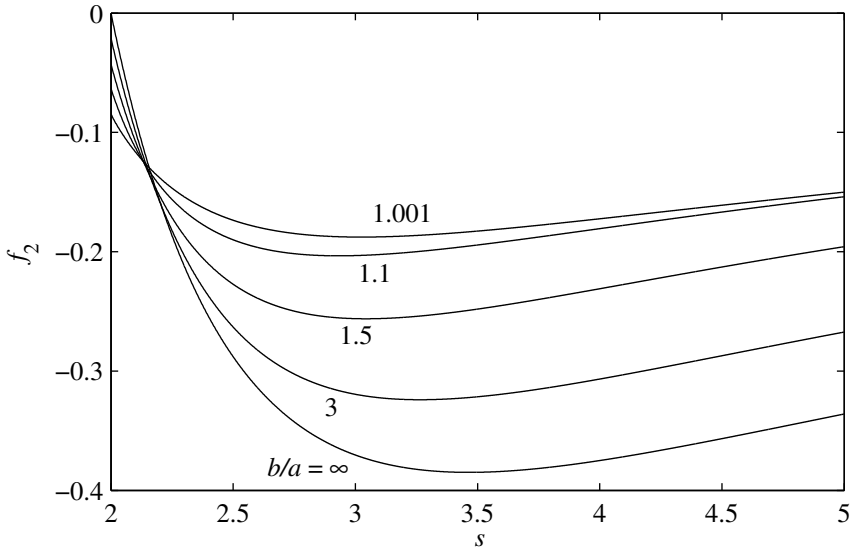


Figure 2.3: First $O(Pe_b^2)$ structural deformation function $f_2$ for several values of $\hat{b} = b/a$.

At $O(Pe_b^2)$ one obtains a system of equations for $f_2$ and $h_2$. For $f_2$ we have

$$\begin{aligned} \frac{d}{ds}\left(s^2 G(\hat{b}s)\frac{df_2}{ds}\right) - 6H(\hat{b}s)f_2 &= \left(sH(\hat{b}s) - s^2 W(\hat{b}s)\right) f_1 - G(\hat{b}s)\frac{df_1}{ds}, \\ \frac{df_2}{ds} = -f_1 \quad &\text{at} \quad s = 2, \\ f_2 \to 0 \quad &\text{as} \quad s \to \infty, \end{aligned}$$

and for $h_2$

$$\begin{aligned} \frac{d}{ds}\left(s^2 G(\hat{b}s)\frac{dh_2}{ds}\right) &= -s^2 H(\hat{b}s)f_1 - 2sH(\hat{b}s)f_2, \\ \frac{dh_2}{ds} = 0 \quad &\text{at} \quad s = 2, \\ h_2 \to 0 \quad &\text{as} \quad s \to \infty. \end{aligned}$$

To obtain $f_2$ and $h_2$ a similar procedure is adopted as in the $f_1$ problem; figures 2.3 and 2.4 plot $f_2$ and $h_2$ respectively, versus $s$ for several values of $\hat{b}$.

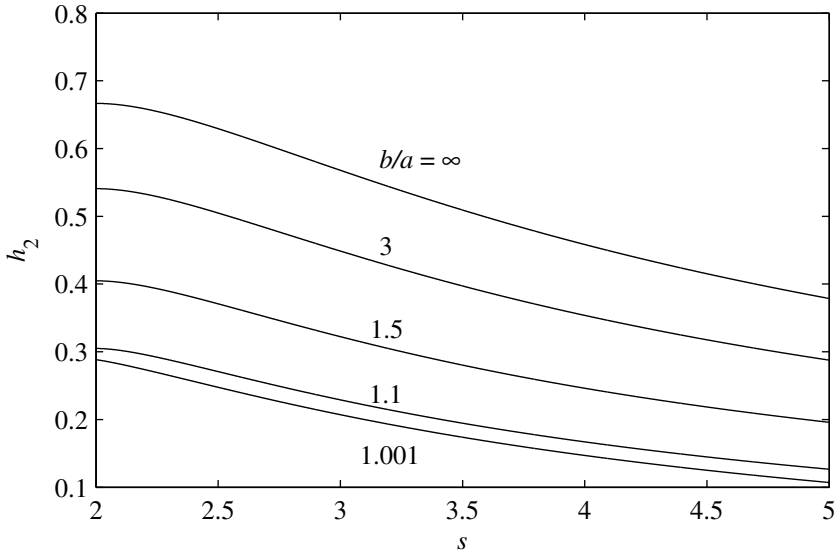


Figure 2.4: Second $O(Pe_b^2)$ structural deformation function $h_2$ for several values of $\hat{b} = b/a$.

As mentioned earlier, the $O(Pe_b)$ and $O(Pe_b^2)$ inner solutions will match to the leading order $O(Pe_b^3)$ outer solution. At distances $s \sim O(Pe_b^{-1})$ the effects of hydrodynamic interactions may be neglected in as much as the outer solution satisfies (2.19). The general solution to (2.19) may be written as (Acrvios and Taylor 1965)

$$F = \frac{\pi}{\rho} e^{-\frac{\rho}{2}(1-\mu)} \sum_{l=0}^{\infty} A_l P_l(\mu) \sum_{k=0}^{l} \frac{(l+k)!}{k!(l-k)!} \rho^{-k}, \tag{2.25}$$

where we have taken $\hat{\boldsymbol{F}}^{ext} = -\hat{\boldsymbol{z}}$, $\mu = \cos\theta$, and $P_l(\mu)$ is the Legendre polynomial of order $l$ and argument $\mu$. The expansion coefficients $A_l$ are found by matching (2.25) to the outer limit of the inner solution, which is

$$f \sim -Pe_b^3 \mu \frac{f_1^\infty}{\rho^2} + Pe_b^3 P_2(\mu) \frac{2 f_2^\infty}{3\rho} + \frac{Pe_b^3}{\rho} \left( \frac{f_2^\infty}{3} + h_2^\infty \right),$$

in terms of the outer variable $\rho$. The scalars $f_1^\infty$, $f_2^\infty$, and $h_2^\infty$ are coefficients of the

leading order terms of $f_1$, $f_2$, and $h_2$ respectively as $s \to \infty$; hence, the outer solution is indirectly influenced by hydrodynamic interactions. Matching inner and outer solutions one finds that

$$A_0 = Pe_b^3 \frac{h_2^\infty}{\pi}, \;\; A_1 = -Pe_b^3 \frac{f_1^\infty}{2\pi}, \;\; A_l = 0 \;\; \forall \, l > 1,$$

so that the outer solution to leading order is

$$F = \frac{Pe_b^3}{\rho} e^{-\frac{\rho}{2}(1-\mu)} \left\{ h_2^\infty + \mu f_2^\infty \left( 1 + \frac{2}{\rho} \right) \right\},$$

which is basically the Green's function for (2.19) with an additional term (proportional to $f_2^\infty$) accounting for the dipole structure of the leading order inner solution. Physically, on the scale of $\rho$ the probe appears to be a point source of structural deformation. At large distances ($s \sim O(Pe_b^{-1})$) the perturbation to the equilibrium microstructure produced by this point source is exponentially small everywhere except in a wake region where $\rho(1-\mu) \sim O(1)$ in which the decay is algebraic $\sim \rho^{-1}$. In the limit $\rho \to \infty$ the area of non-zero structural deformation is restricted to $\theta \sim O(\rho^{-1/2})$.

### 2.4.2 Linear response: The intrinsic microviscosity and its relation to self-diffusivity

Having analyzed the perturbation to the equilibrium microstructure we now proceed to compute the resulting intrinsic microviscosity. Firstly, we shall consider small departures from equilibrium, the so-called *linear-response* regime, where to $O(Pe_b)$ the distortion of the equilibrium microstructure is linearly related to the external force. This is the realm of passive microrheology. In addition to providing a valuable check of our numerical calculations, one can relate the intrinsic microviscosity in this limit to the long-time self-diffusivity.

There are three translational diffusive processes occurring in colloidal dispersions; each characterized with it's own diffusivity: the short-time self-diffusivity $D_0^s$; the long-time self-diffusivity $D_\infty^s$; and the collective, or down-gradient, diffusivity $D^c$. For an isolated colloidal particle all three diffusivities are identical and equal to the Stokes-Einstein-Sutherland diffusivity $D = kT/6\pi\eta a$. However, at finite particle concentrations the three diffusivities are different and correspond to distinct physical processes. Both $D_0^s$ and $D_\infty^s$ are concerned with the diffusion of a single test particle in a macroscopically quiescent dispersion (although on quite different timescales), whilst $D^c$ is the constant of proportionality relating the flux of particles down a steady small concentration gradient (see e.g. Batchelor 1976).

The short-time self-diffusivity measures the instantaneous, or local, mobility of a particle on a time interval which is large compared to the inertial, or momentum, relaxation timescale of the particle $t_I = m/6\pi\eta a$ (where $m$ is the mass of the particle) but small compared to the diffusive timescale of the particle $t_D = a^2/D$. Within this time interval the particle will have experienced many collisions from the surrounding solvent molecules without moving an appreciable fraction of its size and hence without affecting the spatial arrangement of the particles surrounding it. Thus, one defines the short-time self-diffusivity as the ensemble average of the particle mobility with respect to the *equilibrium* configuration of the dispersion. If the test particle experiences hydrodynamic interactions with surrounding particles its mobility will be decreased from its value at infinite dilution; therefore, the short-time self-diffusivity is less than the Stokes-Einstein-Sutherland diffusivity. The difference between the short-time self-diffusivity and the Stokes-Einstein-Sutherland diffusivity is nothing but the equilibrium hydrodynamic microviscosity $\eta_{i,0}^H$, defined in (2.13) as the ensemble average of the probe particle's mobility with respect to the equilibrium

pair-distribution function. Indeed, one may make the formal relationship

$$\frac{D_0^s}{D} = 1 - \eta_{i,0}^H \phi_b,$$

correct to first order in $\phi_b$ (There is also a direct relation between $D_0^s$ and $\eta_{i,0}^H$ valid for all $\phi_b$, Brady 1994).

To examine the effects of hydrodynamic interactions on $D_0^s$ we may view $\eta_{i,0}^H$ as a function of the excluded radius $\hat{b}$. In the limit of long-range excluded volume interactions ($\hat{b} \gg 1$) the asymptotic formulas for $A_{11}$ and $B_{11}$ (see e.g. Kim and Karilla 1991) may be used to show

$$\eta_{i,0}^H = \frac{15}{8\hat{b}^4} - \frac{9}{64\hat{b}^6} - \frac{1}{20\hat{b}^8} + \frac{737}{7168\hat{b}^{10}} + O(\hat{b}^{-12}). \tag{2.26}$$

For general values of $\hat{b}$ one must evaluate $\eta_{i,0}^H$ numerically. This is accomplished by splitting the range of integration $[2, \infty)$ into three regions: $2 \leq \hat{b}s < 2.01$, in which the contribution to the integral is evaluated analytically using lubrication theory results for the hydrodynamic functions; $2.01 \leq \hat{b}s < 3$, where the hydrodynamic functions are obtained via a twin multipole expansion (Jeffrey and Onishi 1984) and the integral is performed numerically; and $3 \leq \hat{b}s < \infty$, where the far-field forms of the hydrodynamic functions are used. In figure 2.5 we plot $\eta_{i,0}^H$ as a function of $\hat{b}$; the solid line in figure 2.5 is the *first* term in the series (2.26), whilst the circles represent the full numerical evaluation. The agreement between the two is excellent. For the case of full hydrodynamic interactions ($\hat{b} = 1$) we find $\eta_{i,0}^H = 1.83$ in agreement with Batchelor (1976). Note, the first term in the series (2.26) gives a value of $\eta_{i,0}^H = 1.875$ for $\hat{b} = 1$, which is remarkably close to the actual value. As $\eta_{i,0}^H$ is positive the effect of hydrodynamic interactions is to decrease $D_0^s/D$, as the motion of the probe is hindered by hydrodynamic interactions with its neighbors. Of

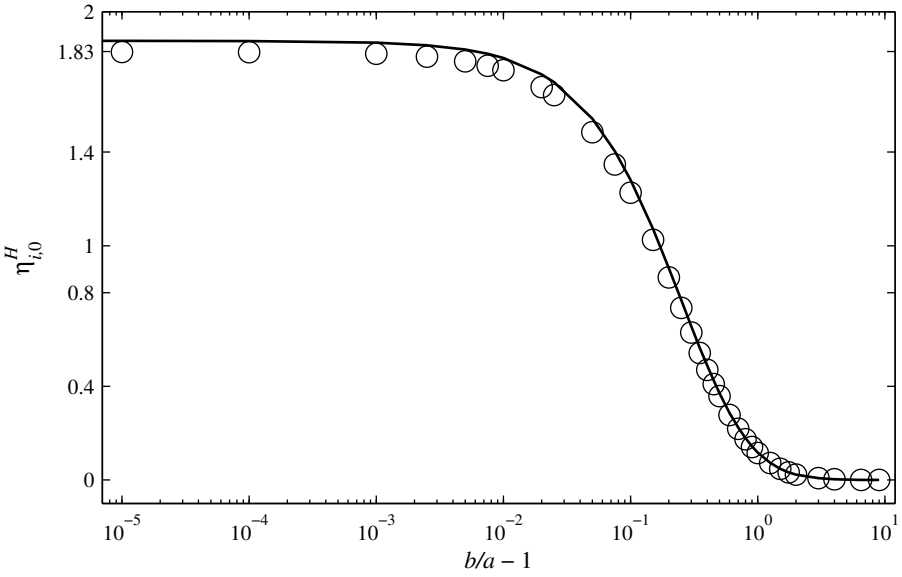


Figure 2.5: The equilibrium microstructure contribution to the intrinsic hydrodynamic microviscosity $\eta^H_{i,0}$ as a function of the excluded radius $\hat{b} = b/a$. The circles ($\circ$) are from numerical computations and the solid line is the asymptotic result $\eta^H_{i,0} = 15/8\hat{b}^4 + O(1/\hat{b}^6)$. Recall, $\eta^H_{i,0}$ is related to the short-time self-diffusivity via $D^s_0/D - 1 = -\eta^H_{i,0}\phi_b$.

course, in the limit $\hat{b} \to \infty$ the mobility of the probe is not affected by the presence of the background particles and $D^s_0/D \to 1$, i.e. the probe is isolated (in a hydrodynamic sense) from neighboring particles.

In contrast, the long-time self-diffusivity corresponds to motion on timescales much greater than the diffusive timescale $t_D$, so that the test particle will have experienced many uncorrelated encounters with surrounding particles. As it diffuses the test particle distorts its local environment from the equilibrium configuration. Brady (1994) has shown that the microstructural evolution problem for self-diffusivity (at long wavelengths) is identical to that for a probe particle moving under the action of a weak external force $\boldsymbol{F}^{ext}$. In the passive-microrheology (or linear-response) regime the distortion to the equilibrium microstructure is linear in $\boldsymbol{F}^{ext}$. Consequently, the average velocity of the probe $\langle \boldsymbol{U} \rangle$ is proportional to $\boldsymbol{F}^{ext}$, with the constant of proportionality being the time dependent self-

diffusivity $D^s(t)$ divided by $kT$. At long times ($t \gg t_D$), $D^s(t) \to D^s_\infty$, and one recovers the long-time self-diffusivity. In the linear response regime the distorted microstructure is given by $Pe_b f_1(s)\hat{\boldsymbol{s}} \cdot \hat{\boldsymbol{F}}^{ext}$. This $O(Pe_b)$ deformation of the microstructure leads to an $O(1)$ contribution to the interparticle and Brownian microviscosities as seen from (2.14) and (2.15), respectively, which we denote temporarily as $\eta^P_{i,0}$ and $\eta^B_{i,0}$ respectively. The long-time self-diffusivity may then be expressed as

$$\frac{D^s_\infty}{D} = 1 - \eta_{i,0}\phi_b, \tag{2.27}$$

where $\eta_{i,0} = \eta^H_{i,0} + \eta^P_{i,0} + \eta^B_{i,0}$, and $\eta^P_{i,0}$ and $\eta^B_{i,0}$ are given by

$$\begin{aligned} \eta^P_{i,0} &= 2G(2\hat{b})f_1(2), \\ \eta^B_{i,0} &= \int_2^\infty \left( \frac{G(\hat{b}s) - H(\hat{b}s)}{s} + \frac{1}{2}\frac{dG(\hat{b}s)}{ds} \right) f_1(s)s^2 ds. \end{aligned}$$

In figure 2.6 we plot $\eta_{i,0}$ as a function of $\hat{b}$. At the extrema of $\hat{b} = 1$ (full hydrodynamic interactions) and $\hat{b} \to \infty$ (no hydrodynamic interactions) we find that $\eta_{i,0} = 2.08$ and $\eta_{i,0} = 2$, respectively, in good agreement with Batchelor (1976) and Rallison and Hinch (1986). As $\hat{b}$ is increased hydrodynamic interactions become weaker; hence, $\eta^H_{i,0}$ and $\eta^B_{i,0}$ are monotonically decreasing functions of $\hat{b}$ (recall that the effect of Brownian motion on the velocity of the probe particle appears as a hydrodynamic coupling of the motion of two particles, see (2.9)). The decrease in $\eta^H_{i,0}$ and $\eta^B_{i,0}$ is offset by an increase in the interparticle microviscosity $\eta^P_{i,0}$, from a value of $\eta^P_{i,0} = 8(\hat{b} - 1)f_1(2)$ in the limit $\hat{b} \to 1$ to $\eta^P_{i,0} = 2$ as $\hat{b} \to \infty$. The decay of $\eta^H_{i,0}$ and $\eta^B_{i,0}$ for $\hat{b}$ slightly above unity can not be matched by the relatively small increase in $\eta^P_{i,0}$; thus, $\eta_{i,0}$ is an initially decreasing function of $\hat{b}$. This decrease persists until $\hat{b} \approx 1.6$ where $\eta_{i,0}$ exhibits a minimum. Beyond $\hat{b} \approx 1.6$ there is a

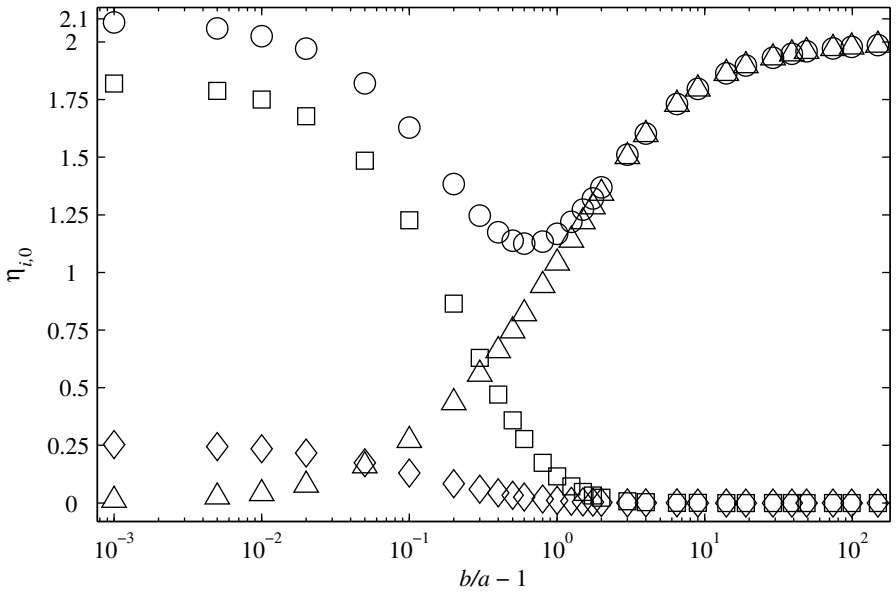


Figure 2.6: Intrinsic microviscosity contributions in the limit $Pe_b \to 0$ as a function of $\hat{b} = b/a$: $\circ$, total ($\eta_{i,0}$); $\square$, hydrodynamic ($\eta^H_{i,0}$); $\diamond$, Brownian ($\eta^B_{i,0}$); and $\triangle$, interparticle force ($\eta^P_{i,0}$). Recall, $\eta_{i,0}$ is related to the long-time self-diffusivity via $D^s_\infty/D - 1 = -\eta_{i,0}\phi_b$.

monotonic increase of $\eta_{i,0}$ to its limiting value of 2 as $\hat{b} \to \infty$.

The nonmonotonicity of $\eta_{i,0}$ is somewhat surprising and suggests the intriguing possibility of maximizing the long-time self-diffusivity of a particle through modulation of its interparticle-force interactions. If the volume fraction in (2.27) were based on the hydrodynamic radius $a$ instead of the thermodynamic radius $b$ (note that $\phi_b = \hat{b}^3\phi_a$) one must multiply $\eta_{i,0}$ by $\hat{b}^3$, implying that the long-time self-diffusivity decreases monotonically (and without bound) with increasing $\hat{b}$. However, the geometric, or excluded, radius $b$ is the correct length scale in defining the volume fraction, as particles must actually move past each other on this scale. The maximum in the long-time self-diffusivity (at $\hat{b} \approx 1.6$) arises because $\hat{b}$ is sufficiently greater than unity, so that the highly resistive hydrodynamic lubrication interactions do not hinder the motion of the probe, while $\hat{b}$ is not too large, whence the long-time self-diffusivity decreases due to the increased role of the hard sphere

interparticle-force. Although the values of long-time self-diffusivity at the extrema of $\hat{b} = 1$ and $\hat{b} \to \infty$ are similar, it is interesting to contrast the physical mechanisms at work in both limits: for $\hat{b} = 1$ the resistance to the probe motion is via hydrodynamic interactions with other particles, which are mediated through the solvent fluid, whilst in the limit $\hat{b} \to \infty$ the probe motion is hindered by the excluded volume interparticle-force, which acts at contact to provide a purely geometric resistance to the probe motion.

### 2.4.3 Weakly nonlinear theory

Our discussion of the intrinsic microviscosity and its relation to self-diffusivity took place in the regime of linear response, where the departure from the equilibrium microstructure is small and *linearly* related to the external force and $Pe_b$. The linear relationship between the distorted microstructure and the external force manifests itself in the structural deformation being fore-aft symmetric about the direction of the external force. Upon increasing $Pe_b$ one enters the nonlinear regime where the distortion to the equilibrium microstructure is no longer linearly related to $Pe_b$, and the fore-aft symmetry of the structural deformation about the external force is broken. The first nonlinear contribution to the structural deformation (in the inner region) occurs at $O(Pe_b^2)$ and was calculated in § 2.4.1. Here, we compute the effect on the intrinsic microviscosity arising from this $O(Pe_b^2)$ nonlinear deformation.

Firstly, it is readily seen from (2.22) and the symmetry of the integrals in (2.14) and (2.15) that the $O(Pe_b^2)$ structural deformation does not contribute to the Brownian and interparticle microviscosities; however, there is a contribution to the hydrodynamic micro-

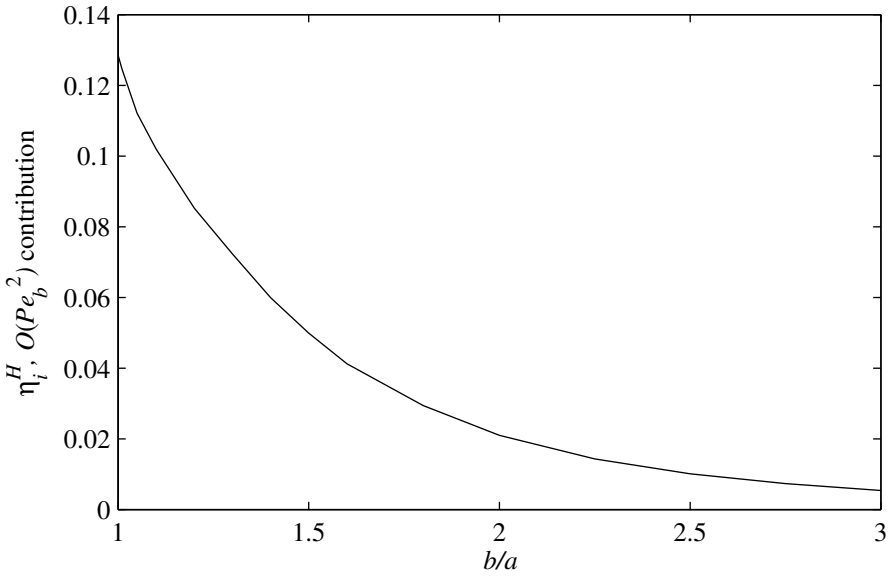


Figure 2.7: The $O(Pe_b^2)$ contribution to the intrinsic hydrodynamic microviscosity $\eta_i^H$ (2.28) as a function of $\hat{b} = b/a$.

viscosity, which is given by

$$\eta_i^H - \eta_{i,0}^H = -\frac{Pe_b^2}{5}\left(\int_2^\infty (3A_{11} + 2B_{11} - 5) f_2(s) s^2 ds + \int_2^\infty (5A_{11} + 10B_{11} - 15) h_2(s) s^2 ds\right), \tag{2.28}$$

and is evidently of $O(Pe_b^2)$. This $O(Pe_b^2)$ contribution is plotted in figure 2.7 as a function of $\hat{b}$ and is seen to be positive for finite $\hat{b}$ and approaches zero as $\hat{b} \to \infty$. Hence, the hydrodynamic microviscosity is an increasing function of $Pe_b$, for small $Pe_b$ up to $O(Pe_b^2)$. Bergenholtz et al. (2002) observed that the hydrodynamic macroviscosity of a dilute sheared suspension is an increasing function for all $Pe_b$, i.e. the hydrodynamic macroviscosity monotonically 'shear-thickens'. Our results indicate the hydrodynamic microviscosity undergoes an analogous 'force-thickening'. The persistence of this force-thickening for larger values of $Pe_b$ will be verified by the numerical calculations presented in § 2.6.

The microviscosity contributions presented above are all from the inner region, where

$s \sim O(1)$, and we must also consider the magnitude of the contributions arising from the outer region, where $s \sim O(\rho Pe_b^{-1})$. At large distances the nonequilibrium contribution to the hydrodynamic microviscosity behaves as

$$\eta_i^H - \eta_{i,0}^H \sim \int \frac{1}{s^4} f s^2 ds \sim O(Pe_b^4),$$

since $f \sim O(Pe_b^3)$ in the outer region. Hence, the $O(Pe_b^2)$ contribution to $\eta_i^H$ comes exclusively from the inner region. Similarly, the outer contribution to the Brownian microviscosity is

$$\eta_i^B \sim \frac{1}{Pe_b} \int \frac{1}{s^5} f s^2 ds \sim O(Pe_b^4).$$

However, the next term in the inner solution, $Pe_b^3 f_3$, will generate an $O(Pe_b^2)$ contribution to $\eta_i^B$ (and to $\eta_i^P$) and is therefore of lower order than the $O(Pe_b^4)$ contribution from the leading order outer solution.

## 2.5 Numerical solution of the Smoluchowski equation for arbitrary $Pe_b$

The perturbation analysis presented above sheds light on the microstructural deformation in the case of small departures from equilibrium. Attempting to continue the expansion to higher orders in $Pe_b$ is unwise as the matching of inner and outer solutions must be performed numerically (except in the absence of hydrodynamic interactions where it can be done analytically) and the algebra involved becomes rapidly intractable. Thus, to obtain the microstructure for arbitrary values of $Pe_b$ one must solve the Smoluchowski equation numerically. For $Pe_b \sim O(1)$ and higher this is a challenging task owing to the formation of

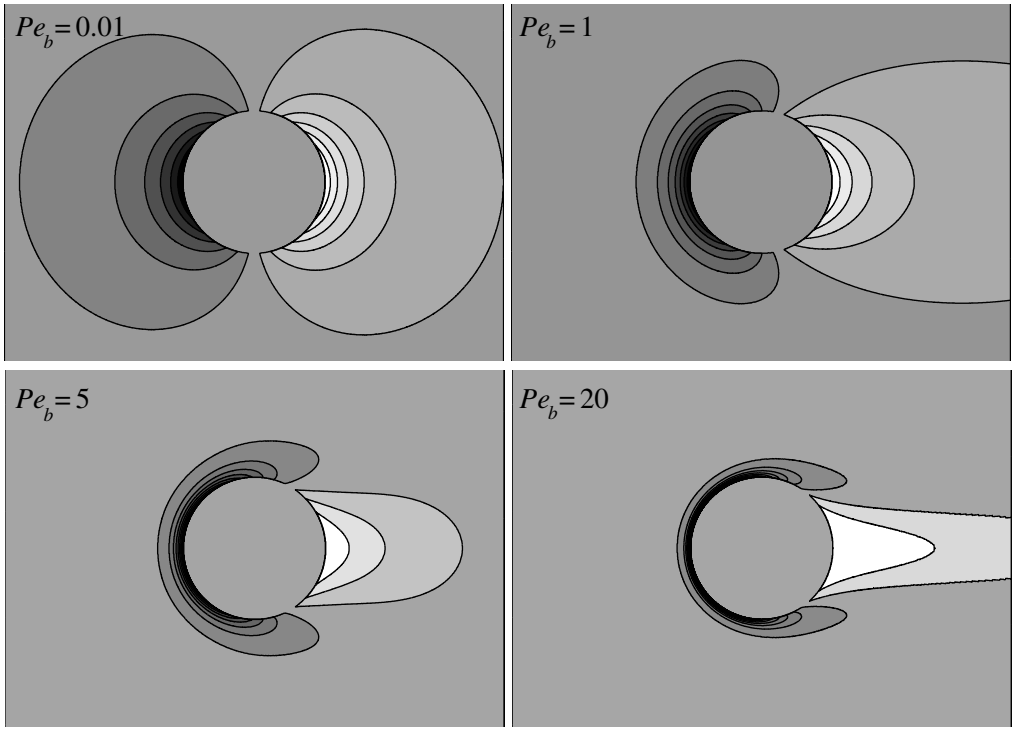


Figure 2.8: Structural deformation $f(\boldsymbol{s}) = g(\boldsymbol{s}) - 1$ in the symmetry plane of the probe particle as a function of $Pe_b$ for $\hat{b} = 1.00001$. The external force $\boldsymbol{F}^{ext}$ is from right-to-left. The test particle is shown with zero deformation $f = 0$, darker regions have positive $f$ while lighter regions have negative $f$.

a boundary layer in the compressional region (where $\hat{\boldsymbol{F}}^{ext} \cdot \hat{\boldsymbol{s}} > 0$) around the probe particle and a wake in the extensional region (where $\hat{\boldsymbol{F}}^{ext} \cdot \hat{\boldsymbol{s}} < 0$), cf. figure 2.1. In figure 2.8 we plot the structural deformation in the symmetry plane of the probe particle as a function of $Pe_b$ for $\hat{b} = 1.00001$. The formation of a boundary layer is clearly visible as is the growth of the wake with increasing $Pe_b$. In the compressional region there is an inward radial flux of background particles from upstream towards the probe particle (in a frame moving with the probe) due to advection by the relative velocity field. This flux of particles is hindered by the impenetrability of the probe, resulting in an increased probability of finding a particle in close proximity to the probe particle. The primary mechanism for a particle to pass by the probe is via Brownian diffusion whose action as $Pe_b$ is increased is confined to an ever

smaller boundary layer adjacent to the surface of the probe in the compressional region. The boundary layer signifies a balance between advection in transporting particles towards the probe and Brownian motion in enabling particles to diffuse around it. On the other hand, in the extensional region the action of the relative velocity field is to advect particles away from the probe, resulting in a decrease in the probability of finding a colloidal particle there.

To solve the Smoluchowski equation for arbitrary $Pe_b$ we utilize two methods. For $0 < Pe_b \leq 30$ an expansion of the structural deformation in a series of Legendre polynomials is employed, similar in ethos to the spherical harmonic expansions of Bergenholtz et al. (2002) and Lionberger (1998). The major limitation of the Legendre polynomial expansion is that as $Pe_b$ is increased a large number of terms in the expansion is required to faithfully represent the increasingly intricate microstructure, which is computationally taxing. Thus, to solve the Smoluchowski equation for $Pe_b > 30$ we use a finite-difference scheme which accurately captures the boundary-layer formation and wake growth.

### 2.5.1 Legendre polynomial expansion

We adopt a spherical polar coordinate system with origin at the center of the probe particle (cf. figure 2.1). In this coordinate system the Smoluchowski equation for the structural deformation function reads

$$\frac{1}{s^2}\frac{\partial}{\partial s}\left(s^2 G(\hat{b}s)\frac{\partial f}{\partial s}\right) + \frac{H(\hat{b}s)}{s^2\sin\theta}\frac{\partial}{\partial\theta}\left(\sin\theta\frac{\partial f}{\partial\theta}\right) = Pe_b\left(G(\hat{b}s)F_r^{ext}\frac{\partial f}{\partial s} + H(\hat{b}s)\frac{F_\theta^{ext}}{s}\frac{\partial f}{\partial\theta} + W(\hat{b}s)F_r^{ext}(1+f)\right), \tag{2.29}$$

where $F_r^{ext} = \hat{\boldsymbol{F}}^{ext}\cdot\hat{\boldsymbol{s}}$ and $F_\theta^{ext} = \hat{\boldsymbol{F}}^{ext}\cdot\hat{\boldsymbol{\theta}}$ are the radial and polar components of the

external force unit vector respectively. The boundary conditions on $f(s,\theta)$ are

$$\frac{\partial f}{\partial s} = -Pe_b F_r^{ext}(1+f) \qquad \text{at} \qquad s=2,$$
$$f \to 0 \qquad \text{as} \qquad s \to \infty.$$

The structural deformation may be written as an expansion in Legendre polynomials

$$f(s,\theta) = \sum_{m=0}^{\infty} q_m(s) P_m(\cos\theta),$$

where $P_m(z)$ is the Legendre polynomial of order $m$ and argument $z$ and $q_m(s)$ its expansion coefficient. The expansion is substituted into (2.29) and upon use of the orthogonality property of the Legendre polynomials on the interval $[0,\pi]$ one arrives at an infinite set of coupled ordinary differential equations for the expansion coefficients. Additionally, if one assumes (without loss of generality) that $\hat{\boldsymbol{F}}^{ext} = -\hat{\boldsymbol{z}}$, so that $F_r^{ext} = -\cos\theta$ and $F_\theta^{ext} = \sin\theta$, the set of equations take the form

$$\mathcal{D}_m q_m = Pe_b \left( W(\hat{b}s)\alpha_m + G(\hat{b}s)\beta_m + \frac{H(\hat{b}s)}{s}\gamma_m \right),$$

where the diffusion operator $\mathcal{D}_m$ is

$$\mathcal{D}_m = \frac{1}{s^2}\frac{d}{ds}\left( s^2 G(\hat{b}s)\frac{d}{ds} \right) - \frac{H(\hat{b}s)m(m+1)}{s^2},$$

and the advective coupling terms $\alpha_m$, $\beta_m$ and $\gamma_m$ are

$$\begin{aligned}
\alpha_m &= \frac{2m+1}{3}\delta_{m1} + \frac{m+1}{2m+3}q_{m+1} + \frac{m}{2m-1}q_{m-1}, \\
\beta_m &= \frac{m+1}{2m+3}\frac{dq_{m+1}}{ds} + \frac{m}{2m-1}\frac{dq_{m-1}}{ds}, ] \\
\gamma_m &= \frac{(m+1)(m+2)}{(2m+3)}q_{m+1} + \frac{m(1-m)}{2m-1}q_{m-1},
\end{aligned}$$

with $\delta_{ij}$ the Kronecker delta. The boundary conditions on the expansion coefficients are

$$\begin{aligned}
\frac{dq_m}{ds} &= Pe_b\left(\frac{2m+1}{3}\delta_{m1} + \frac{m+1}{2m+3}q_{m+1} + \frac{m}{2m-1}q_{m-1}\right) \quad \text{at} \quad s = 2, \\
q_m &\to 0 \quad \text{as} \quad s \to \infty.
\end{aligned}$$

The system of equations is solved with the *MATLAB* program *bvp4c*, which implements a collocation method for the solution of general two-point boundary value problems. An initial guess for each of the expansion coefficients on a user-defined mesh covering the domain of solution is provided as input to the program, which subsequently refines the mesh to obtain the numerical solution to a preset accuracy (usually specified in terms of the absolute tolerance). A notable feature of the *bvp4c* routine is the ability to perform parameter continuation, i.e. suppose that one has the structural deformation at some $Pe_b = Pe_{b,1}$ then this solution may be used as the initial guess for the structural deformation at $Pe_b = Pe_{b,2} > Pe_{b,1}$. This is particularly useful for $Pe_b > 10$, where the large gradients in the structural deformation encountered in the boundary layer make the choice of initial guess crucial to the convergence of the method. The expansion is truncated at $m = m_{max}$ so that $q_m = 0 \; \forall \; m > m_{max}$. The choice of $m_{max}$ for a particular $Pe_b$ is made by requiring that each of the three contributions to the intrinsic microviscosity should not differ by

more than 0.1% when computed using $m_{max}$ and $m_{max+1}$ terms. As $Pe_b$ increases so does $m_{max}$, reflecting the need for more terms in the expansion to accurately describe the microstructure. The highest value of $Pe_b$ for which a solution was obtained was $Pe_b = 30$ requiring $m_{max} = 60$.

Finally, some care needs to be taken in application of the far-field boundary condition. Here, we make the simple approximation of moving the boundary condition at infinity to a finite radial location $s = s_{far}$, taking great care to ensure the choice of $s_{far}$ does not affect the computed intrinsic microviscosity contributions. For $Pe_b < 1$ at radial distances $O(Pe_b^{-1})$ advection is comparable to diffusion, requiring $s_{far} \gg O(Pe_b^{-1})$. As a starting point $s_{far}$ is chosen to be $10^3 Pe_b^{-1}$ and increased until convergence of each of the intrinsic microviscosity contributions to eight decimal places is achieved. For $Pe_b > 1$, where, in addition to the boundary-layer structure at the front of the probe, one must also account for the wake region behind it (whose characteristic length grows linearly with $Pe_b$), we start with $s_{far} = 10^2 Pe_b$ and increase $s_{far}$ until the intrinsic microviscosity contributions converge. In § 2.6 several studies are presented that validate our approximation of the far-field boundary condition and demonstrate the accuracy of the numerical solutions.

### 2.5.2 Finite difference methods

Numerically solving the Smoluchowski equation accurately at large $Pe_b$ is a demanding task: the challenge is to capture the detailed boundary-layer structure of the pair-distribution function near contact whilst maintaining sufficient resolution in the far-field to represent the growing wake region behind the probe. In the range $2 \leq Pe_b \leq 100$ the Smoluchowski equation (2.29) is approximated by a finite difference equation, on a two-dimensional grid, which has a dense collection of nodes in the boundary layer (to capture the large gradients

in the pair-distribution function there) and nodes distributed sparsely in the far-field. Both radial and angular derivatives are approximated via central differences. Discretization of the Smoluchowski equation leads to the linear matrix equation $\boldsymbol{A} \cdot \boldsymbol{f} = \boldsymbol{w}$, where the coefficient matrix $\boldsymbol{A}$ is tridiagonal with two fringes, $\boldsymbol{f}$ is the unknown structural deformation vector, and $\boldsymbol{w}$ is the forcing vector. The matrix equation is solved iteratively using a simple Jacobi scheme, requiring computation of the inverse of the tridiagonal portion of $\boldsymbol{A}$, which is performed via a standard back-substitution algorithm (Press et al. 1992). The method is efficient in the sense that only the inverse of a tridiagonal matrix is to be computed, but inefficient (as compared to other iterative techniques such as Gauss-Seidel or SOR) as it requires a large number of iterations to converge. To reduce the number of iterations we employ the convergence acceleration scheme proposed by Ng (1974). A detailed exposition of the finite difference method is provided in appendix 2.B.

As $Pe_b$ is increased one requires a greater number of grid points (and hence iterations) for the method to converge. Beyond $Pe_b \approx 100$ the iteration diverges; at such large $Pe_b$ it is reasonable to postulate that the rheological properties of the suspension are primarily determined by the large gradients in the pair-distribution function occurring in the boundary layer. Thus, for $Pe_b > 100$ we solve a boundary-layer approximation to the full Smoluchowski equation, which is derived in appendix 2.C. This equation retains the information on the detailed structure of the boundary layer at the expense of obtaining accurate far-field behavior. The boundary-layer equation reads

$$G\frac{\partial^2 f}{\partial y^2} + Q\frac{\partial f}{\partial y} + \frac{Pe_b^{-2} H}{4\sin\theta}\frac{\partial}{\partial\theta}\left(\sin\theta\frac{\partial f}{\partial\theta}\right) = Pe_b^{-1}\left(W\cos\theta(1+f) - \frac{H}{2}\sin\theta\frac{\partial f}{\partial\theta}\right), \quad (2.30)$$

where $y = Pe_b(s-2)$ is a stretched radial coordinate, $Q = -G\cos\theta + dG/dy + Pe_b^{-1}G(1-$

$Pe_b^{-1}y/2$), and terms of $O(Pe_b^{-3})$ and greater have been discarded. The crucial distinction between (2.30) and the full Smoluchowski equation (2.29) is the absence of the $1/s^2$ factor multiplying the diffusive terms on the left-hand side of (2.30). This results in the exaggeration of diffusive effects at large $s$. Consequently, although there remains a wake behind the probe particle its size is diminished, making numerical solution of (2.30) considerably easier than that of (2.29). Strictly speaking, the structural deformation determined from (2.30) should be matched to an outer solution from the advectively dominated region. However, this is not a simple task as the radial matching length is a function of the polar angle $\theta$. Here, we assume that the solution of (2.30) is valid throughout the entire domain, specifically requiring that the solution should vanish at large radial separations. To solve the boundary-layer equation we use a finite difference method analogous to that employed for solution of the full Smoluchowski equation.

## 2.6 Results

### 2.6.1 No hydrodynamic interactions

In this subsection the microstructure and microviscosity of the dispersion are examined in the absence of hydrodynamic interactions, $\hat{b} \to \infty$. Particular attention is paid to this limit as the accuracy of our numerical calculations may be demonstrated via comparison to the exact solution of the Smoluchowski equation derived by Squires and Brady (2005) and the perturbation analysis of § 2.4.

For weak forcing it was shown in § 2.4 that to $O(Pe_b^2)$ the contact value of the structural

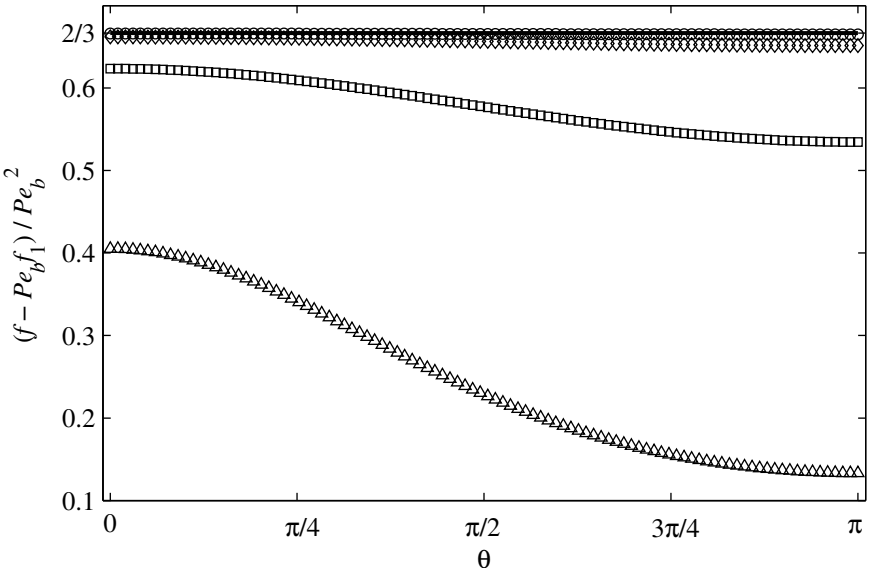


Figure 2.9: Angular dependence of the structural deformation at contact ($s = 2$) for several $Pe_b$ in the absence of hydrodynamic interactions: $Pe_b = 10^{-3}$ ($\circ$); $Pe_b = 10^{-2}$ ($\diamond$); $Pe_b = 10^{-1}$ ($\square$); and $Pe_b = 1$ ($\triangle$). The solid line is the $O(Pe_b^2)$ perturbation result $(f - Pe_b f_1)/Pe_b^2 = 2/3 + O(Pe_b)$.

deformation is

$$f(2,\theta) = -Pe_b \cos\theta f_1(2) + Pe_b^2 \left(\cos^2\theta f_2(2) + h_2(2)\right), \tag{2.31}$$

where for definiteness it is assumed $\hat{\boldsymbol{F}}^{ext} = -\hat{\boldsymbol{z}}$. Figure 2.9 compares the contact value obtained via the Legendre polynomial expansion to the perturbation theory result. In figure 2.9 the $O(Pe_b^2)$ term has been isolated by plotting $(f(2,\theta) + Pe_b \cos\theta)/Pe_b^2$ versus $Pe_b$ and comparing to the perturbation result $2/3+O(Pe_b)$. Evidently, the numerical calculations are in good agreement with the perturbation theory up to $Pe_b = 0.1$, beyond which one requires higher order terms in the expansion (2.31) to accurately represent the microstructure.

We now turn our attention to the structural deformation at large $Pe_b$, which is computed via a finite difference solution of the full Smoluchowski equation ($2 \leq Pe_b \leq 100$) and a

boundary-layer approximation of it ($20 \leq Pe_b \leq 1000$). In the absence of hydrodynamic interactions there is no reduction in the relative mobility as a force-free particle approaches the probe particle. Thus, at large $Pe_b$ the strong inward advective flux of force-free particles (in a reference frame moving with the probe) in the compressional region (upstream) leads to a large accumulation of pair density in a boundary layer at the surface of the probe particle. The probe acts as an obstruction around which the force-free particles coming from upstream must pass. The primary mechanism of passing is via Brownian diffusion, which is driven by the large gradients of pair-density present in the boundary layer. In the extensional region (downstream) advection carries the force-free particles away from the probe and a decrease in pair density, or wake, resides there. In appendix 2.D we show that at large $Pe_b$ the pair-distribution function is given by

$$g(s,\theta) = \begin{cases} F_r^{ext} Pe_b \exp\left\{-F_r^{ext} Pe_b (s-2)\right\} + O(1) & \text{if } F_r^{ext} \geq 0 \\ 0 & \text{if } F_r^{ext} < 0 \end{cases} \tag{2.32}$$

The contact value of the pair-distribution function in the compressional region, $g(2) = F_r^{ext} Pe_b$, scales linearly with $Pe_b$. In figure 2.10 we plot the contact value as a function of the polar angle $\theta$ for several $Pe_b$. The inset shows that scaling $g(2)$ with $Pe_b$ collapses that data well, verifying the linear scaling predicted by (2.32).

In the absence of hydrodynamic interactions the intrinsic microviscosity of the suspension, $\eta_i$, is determined solely by the interparticle-force contribution (2.14), which is proportional to the contact value of the structural deformation. Figure 2.11 plots $\eta_i$ as a function of $Pe_b$. In the limit $Pe_b \to 0$, where the structural deformation is linear in the external force, there is a Newtonian plateau at which $\eta_i = 2$. On increasing $Pe_b$ the non-Newtonian character of the dispersion is evident in the decrease, or force-thinning, of $\eta_i$. The inset

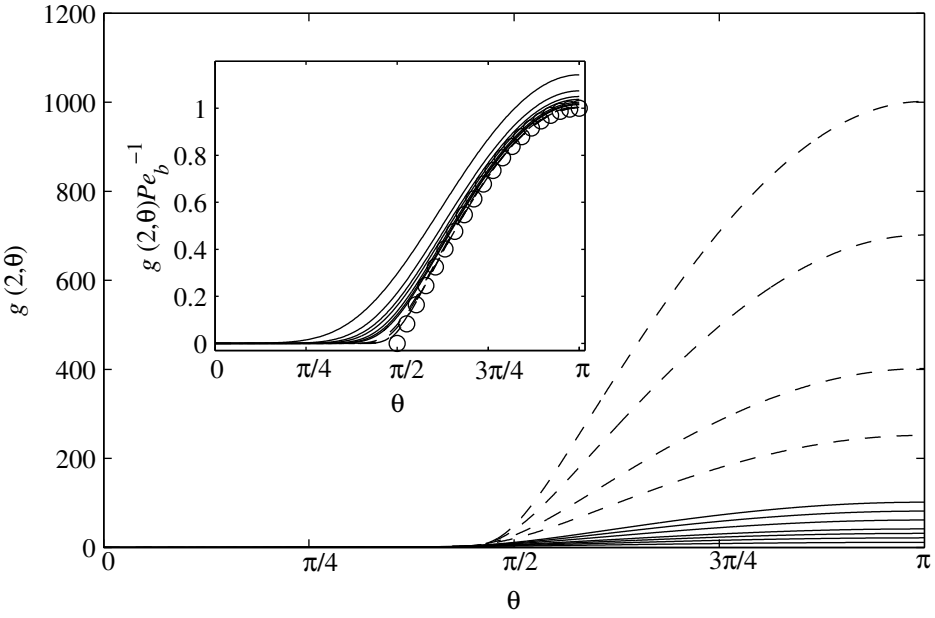


Figure 2.10: The pair-distribution function at contact as a function of the polar angle $\theta$ and $Pe_b$ in the absence of hydrodynamic interactions, $\hat{b} \to \infty$. Results from the solution of the full Smoluchowski equation are shown as solid lines whilst solutions from the boundary-layer equation are displayed as broken lines. From bottom-to-top: $Pe_b = 10, 20, 30, 40, 60, 80$, and 100; and from the boundary-layer equation $Pe_b = 250, 400, 700$, and 1000. The inset displays the same data scaled by $Pe_b$ with the addition of the asymptotic result $g(2,\theta)Pe_b^{-1} = -\cos\theta + O(Pe_b^{-1})$ ($\circ$) (see appendix 2.D) valid in the limit $Pe_b \to \infty$.

reveals that the initial portion of the force thinning is proportional to $Pe_b^2$, arising from the $O(Pe_b^3)$ structural deformation, $Pe_b^3 f_3$, which via (2.14) produces an $O(Pe_b^2)$ contribution to the microviscosity. For $Pe_b \gg 1$ the microviscosity exhibits a Newtonian plateau with $\eta_i$ slightly above unity (for $Pe_b = 10^3$ we compute $\eta_i = 1.004$). The boundary-layer analysis in appendix 2.D predicts $\eta_i = 1$ at infinite $Pe_b$. The intrinsic microviscosity calculated by Squires and Brady (2005) using the exact solution of the Smoluchowski equation is in quantitative agreement with our numerical calculations over the entire range of $Pe_b$ studied.

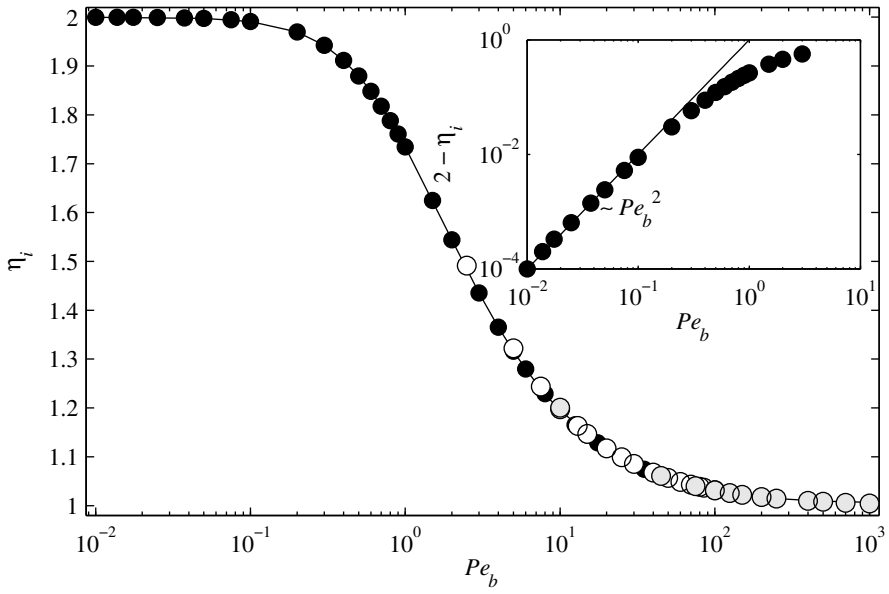


Figure 2.11: The intrinsic microviscosity $\eta_i$ as a function of $Pe_b$ in the absence of hydrodynamic interactions. The numerical method is indicated by the fill pattern: black-fill, Legendre polynomial expansion; no-fill, finite-difference solution of full Smoluchowski equation; and gray-fill, finite-difference solution of boundary-layer equation. The solid line is the intrinsic microviscosity computed from the exact solution of the Smoluchowski equation by Squires and Brady (2005). The inset shows that the initial microviscosity variation is proportional to $Pe_b^2$.

### 2.6.2 The effect of hydrodynamic interactions

Having investigated in detail the special case of particles without hydrodynamic interactions, we now consider the effect of hydrodynamic interactions on the microstructure and microrheology of the dispersion, starting at small $Pe_b$.

In the limit $Pe_b \to 0$ the intrinsic microviscosity for $\hat{b} = 1.00001$ is calculated as $\eta_i = 2.084$, being comprised of the $O(\phi_b)$ short-time self-diffusivity coefficient $\eta_{i,0}^H = 1.828$ and the Brownian contribution $\eta_i^B = 0.256$. (For $\hat{b} = 1.00001 \approx 1$ the interparticle-force plays essentially no role in determining the microrheology of the dispersion and $\eta_i^P$ is negligible as compared to the hydrodynamic and Brownian microviscosities.) To focus on the small $Pe_b$ behavior of the intrinsic microviscosity we introduce the microviscosity variations: $\Delta\eta_i =$

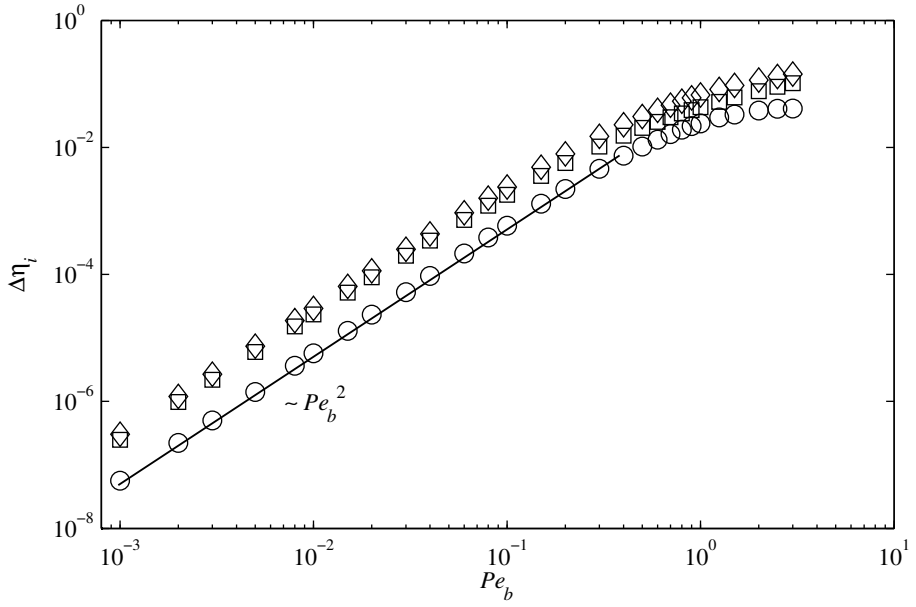


Figure 2.12: Small $Pe_b$ variation of the intrinsic microviscosity for $\hat{b} = 1.00001$. The following contributions are shown: $\Delta\eta_i = 2.084 - \eta_i$, $\circ$; $\Delta\eta_i^H = \eta_i^H - 1.828$, $\square$; and $\Delta\eta_i^B = 0.256 - \eta_i^B$, $\diamond$. The solid line indicates that the initial variation is proportional to $Pe_b^2$.

$2.084 - \eta_i$ (total); $\Delta\eta_i^H = \eta_i^H - 1.828$ (hydrodynamic); and $\Delta\eta_i^B = 0.256 - \eta_i^B$ (Brownian). The variations are defined to be positive and are plotted in figure 2.12 as a function of $Pe_b$. The hydrodynamic variation is a monotonically increasing function of $Pe_b$, as in the macroviscosity results of Bergenholtz et al. (2002). This fact is taken as further confirmation of the validity of our low $Pe_b$ results in the context of applying the outer boundary at a finite distance $s_{far}$.

The increase in the Brownian microviscosity variation outweighs that of the hydrodynamic variation resulting in a force-thinning intrinsic microviscosity at small $Pe_b$. Figure 2.12 shows that the initial force-thinning is proportional to $Pe_b^2$: this scaling arises from a combination of the $O(Pe_b^2)$ perturbation to the inner structural deformation, $Pe_b^2(\hat{\boldsymbol{s}}\hat{\boldsymbol{s}} : \hat{\boldsymbol{F}}^{ext}\hat{\boldsymbol{F}}^{ext} f_2(s) + h_2(s))$, which produces a hydrodynamic variation of $O(Pe_b^2)$ and the $O(Pe_b^3)$ perturbation to the inner structure, $Pe_b^3 f_3$, giving a Brownian variation of $O(Pe_b^2)$. Although

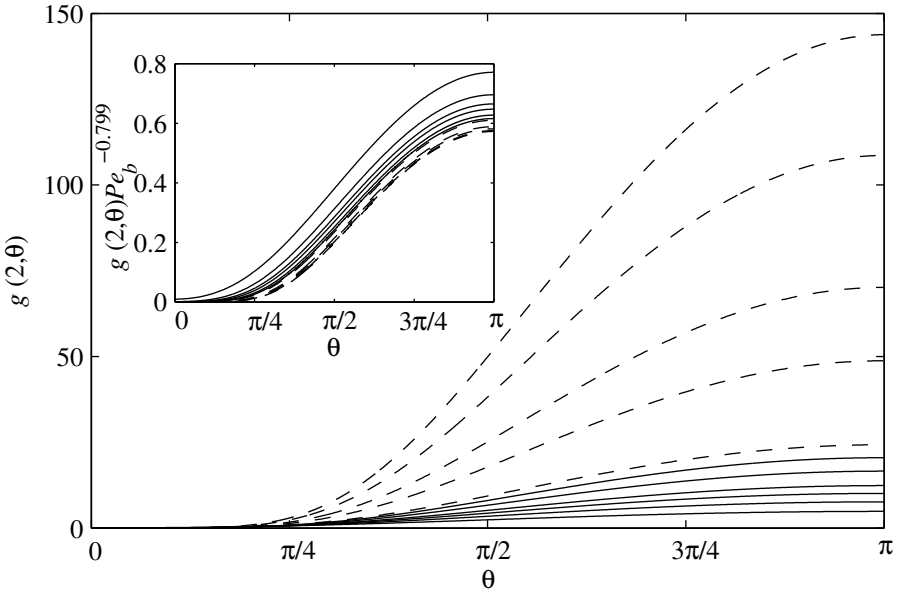


Figure 2.13: The pair-distribution function at contact as a function of the polar angle $\theta$ and $Pe_b$ in the case of near-full hydrodynamic interactions $\hat{b} = 1.00001$. Results from the solution of the full Smoluchowski equation are shown as solid lines whilst solutions from the boundary-layer equation are displayed as broken lines. From bottom-to-top: $Pe_b = 10, 20, 30, 40, 60, 80$, and 100; and from the boundary-layer equation $Pe_b = 250, 400, 700, 850$, and 1000. The inset displays the same data scaled by the theoretical prediction $g(2,\theta) \sim Pe_b^{0.799}$ (see appendix 2.E), which is seen to collapse the data well.

the analysis above has been restricted to $\hat{b} = 1.00001$ we find the microviscosity force-thins proportional to $Pe_b^2$ for all values of $\hat{b}$ studied.

We now turn to the microstructure at high $Pe_b$. In figure 2.13 the contact value of the pair-distribution function is plotted versus the polar angle $\theta$ at several $Pe_b$ for the case of particles with almost full hydrodynamic interactions, $\hat{b} = 1.00001$. The boundary-layer structure is broadly similar to the case with no hydrodynamic interactions (cf. figure 2.10), with a large accumulation of pair-density in the compressional region and a depletion of pair density in the extensional region. As $Pe_b$ is increased the accumulation and depletion become more pronounced; however, there are some subtle differences in the detailed boundary-layer characteristics. For a given value of $Pe_b$ the contact value of the

pair-distribution function in the compressional region is markedly smaller than for particles with no hydrodynamic interactions. This may be understood in terms of the hydrodynamic lubrication forces: in the compressional region the coming together of a force-free particle and the probe particle is hampered by the need to expel the solvent fluid from the narrow gap separating them. As is well known, as the gap becomes smaller the force required to remove the remaining solvent diverges. This reduction in relative mobility at small inter-particle separations (which is not present in the absence of hydrodynamic interactions) is responsible for the smaller accumulation of pair-density in the compressional region. In the extensional region the pulling apart of a force-free particle from the probe by the advective velocity field is resisted by the flow of solvent into the increasing gap between the particles, which leads to an increase in the pair-density in the extensional region.

Another important consequence of hydrodynamic interactions is that the contact value of the pair-distribution function does not scale linearly with $Pe_b$, as was the case for $\hat{b} \to \infty$. In figure 2.14 we plot $\ln(g_{max})$ (where $g_{max} = g(2,\pi)$ is the maximum contact value of the pair-distribution function) versus $\ln(Pe_b)$ and determine a sublinear scaling of $g(2) \sim Pe_b^{0.773}$ for $\hat{b} = 1.00001$. The exponent 0.773 may be predicted by a boundary-layer analysis of the Smoluchowski equation in the limit $Pe_b \to \infty$ for the case $\hat{b} \equiv 1$. In appendix 2.E it is shown that in this limit the pair-distribution function in the boundary layer is given by

$$g(s,\theta) = g_0 \Gamma \left(\frac{H_0}{G_1}\right) \left(\frac{-\alpha Pe_b}{Y(\theta)}\right)^{W_0/G_1} M\left(\frac{W_0}{G_1}, 1, \frac{\alpha Pe_b (s-2)}{Y(\theta)}\right), \tag{2.33}$$

where $H_0 = 0.402$, $G_1 = 2$, and $W_0 = 1.598$ are leading order expansions of the hydrodynamic mobility functions $H(s)$, $G(s)$, and $W(s)$ about $s = 2$, respectively. In (2.33), $g_0$ is a constant which is determined by matching to the advective outer solution, $\alpha$ is a constant

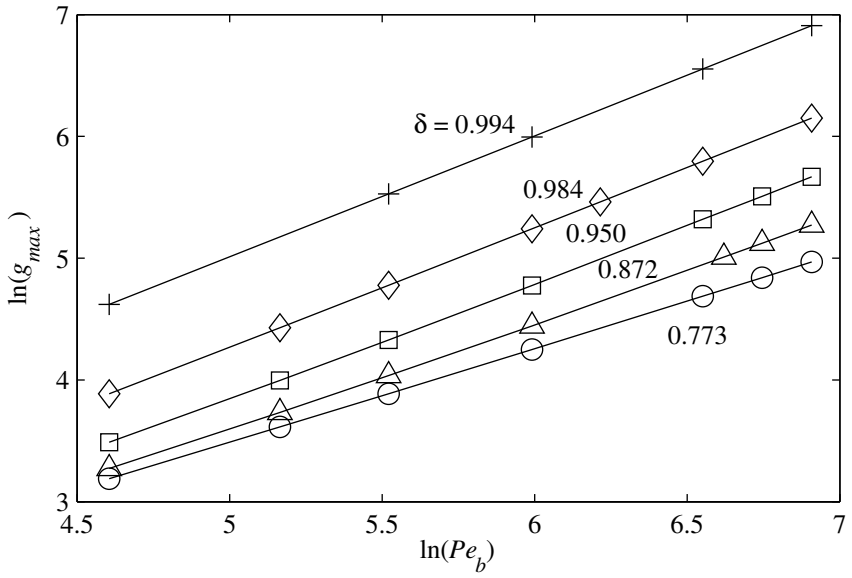


Figure 2.14: Determination of the scaling exponent $\delta$ relating the pair-distribution function at contact to $Pe_b$ for various $\hat{b}$: $\circ$, $\hat{b} = 1.00001$; $\triangle$, $\hat{b} = 1.001$; $\square$, $\hat{b} = 1.01$; $\diamond$, $\hat{b} = 1.1$; and $+$, $\hat{b} \to \infty$. Here, $g_{max} = g(2, \pi)$ denotes the maximum value of the pair-distribution function at contact.

of arbitrary magnitude but of negative sign, $Y(\theta)$ represents the boundary-layer thickness (cf. (2.E-9)), $\Gamma$ is the Gamma function, and $M$ is the first confluent hypergeometric function (Kummer's function). At contact ($s = 2$) we find $g(2, \theta) \sim Pe_b^{W_0/G_1} = Pe_b^{0.799}$, in good agreement with the numerically determined exponent of 0.773 from figure 2.14. The small discrepancy between the two exponents may be explained by noting that the theoretical exponent is strictly only valid in the asymptotic limit $Pe_b \to \infty$, whilst the numerical exponent is determined using contact value data in the range $100 \leq Pe_b \leq 1000$. Nevertheless, as shown in the inset of figure 2.13 the theoretical scaling prediction performs admirably in collapsing the numerical data.

The discussion presented above raises the interesting question of how the scaling of the contact value of the pair-distribution function with $Pe_b$ varies with $\hat{b}$. In a study of the microstructure of a sheared suspension at large $Pe_b$ Brady and Morris (1997) conclude,

via an analytical boundary-layer study of the appropriate Smoluchowski equation, that $g(2) \sim Pe_b$ for all $\hat{b}$ except in the so-called case of 'pure-hydrodynamics' $\hat{b} \equiv 1$, where $g(2) \sim Pe_b^{0.78}$. Stokesian Dynamics simulations of concentrated Brownian suspensions (at volume fractions of $\phi = 0.30$ and $\phi = 0.45$) in simple-shear flow performed by Morris and Katyal (1995) indicate that $g(2) \sim Pe_b^{0.70}$ for $\hat{b} = 1.00025$ in the range $1 \leq Pe_b \leq 1000$, as opposed to the linear scaling predicted by Brady and Morris (1997). This discrepancy in the two studies may be attributed to the neglect of the divergence of the relative-velocity field of two particles by Brady and Morris (1997), which plays a crucial role in setting the microstructure at small interparticle separations for suspensions possessing very short-range excluded volume interactions ($\hat{b} - 1 \ll 1$). Mathematically, the non-zero divergence of the relative-velocity field states that the phase space of pair-trajectories is not volume conserving; physically, it acts as a source of pair-density in the compressional regions of the flow and a sink in the extensional regions. (Note, although the relative-velocity field of two particles has a non-zero divergence, the Newtonian suspending fluid is, of course, incompressible.) Let us define the exponent $\delta = \delta(\hat{b})$ such that $g(2) \sim Pe_b^{\delta}$. In figure 2.14 the exponent $\delta$ is determined for several values of $\hat{b}$ using data from our numerical solution of the Smoluchowski equation in the range $100 \leq Pe_b \leq 1000$. We find that $\delta$ changes continuously between the limits of $\delta = 0.773$ at $\hat{b} = 1.00001$ to $\delta = 1$ as $\hat{b} \to \infty$. Whether this continuous change may be predicted by an analytical boundary-layer theory of the Smoluchowski equation for arbitrary $\hat{b}$ is left as a future study.

In addition to affecting the microstructure of the dispersion hydrodynamic interactions play a profound role in setting its microrheology. Let us first consider the microrheology of the suspension for $\hat{b}$ close to unity, where the thermodynamic radius $b$ is only slightly larger than the hydrodynamic radius $a$, so that the particles experience nearly full hydrodynamic

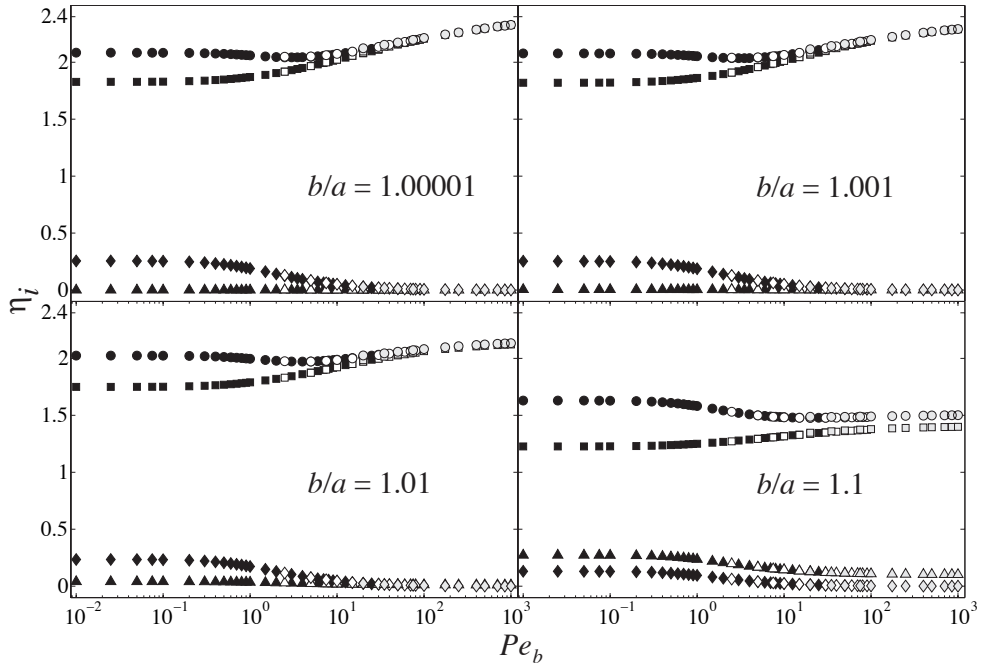


Figure 2.15: Contributions to the intrinsic microviscosity $\eta_i$ as a function of $Pe_b$ for various $\hat{b}$: $\circ$, total; $\square$, hydrodynamic; $\diamond$, Brownian; and $\triangle$, interparticle force. The numerical method is indicated by the fill pattern: black-fill, Legendre polynomial expansion; no-fill, finite-difference solution of full Smoluchowski equation; and gray-fill, finite-difference solution of the boundary-layer equation.

interactions. In figure 2.15 we plot the intrinsic microviscosity and its three constituents as a function of $Pe_b$ for $\hat{b} = 1.00001$, $\hat{b} = 1.001$, $\hat{b} = 1.01$, and $\hat{b} = 1.1$. For $\hat{b} = 1.00001$ and $\hat{b} = 1.001$ it is observed that the interparticle contribution to the intrinsic microviscosity is essentially negligible as compared to the Brownian and hydrodynamic components. For small $Pe_b$ the intrinsic viscosity exhibits a Newtonian plateau which is primarily determined by the hydrodynamic contribution although a smaller, yet significant, Brownian contribution is present. Of course, the value of the intrinsic microviscosity at this plateau is nothing but the $O(\phi_b)$ correction to the long-time self-diffusivity, as discussed in § 2.4.2. On increasing $Pe_b$ to $O(1)$ the Brownian and hydrodynamic microviscosities decrease and increase, respectively. The decrease in the Brownian contribution outweighs the increase in the hydrodynamic contribution (cf. figure 2.12) causing the intrinsic microviscosity to

force-thin up to $Pe_b \approx 3$ for $\hat{b} = 1.00001$ and $Pe_b \approx 3.5$ for $\hat{b} = 1.001$, at which point it attains a minimum. Beyond this minimum the Brownian contribution becomes negligible and the hydrodynamic contribution increases steadily, which has the net effect of making the intrinsic microviscosity force-thicken. As $Pe_b$ is increased the advective flux (set up through the relative velocity field induced by the external force on the probe) of force-free particles towards the probe particle becomes stronger. For large $Pe_b$ this advective flux 'squeezes' particles into close-contact with the probe, where they experience highly resistive lubrication forces, which is, in part, the cause of continuous force-thickening for $Pe_b \sim O(1)$ and beyond. However, this is not the whole story: the moving probe not only 'pushes' background particles (leading to a high probability-density in the boundary layer at the front of the probe), but also 'drags' background particles that are immediately behind it, as these particles are 'stuck' to the probe due to the lubrication forces (cf. the higher probability-density downstream of the probe with hydrodynamics (figure 2.13) as compared to without hydrodynamics (figure 2.10)). Indeed, this 'dragging' effect contributes significantly to the microviscosity at large $Pe_b$. In table 2.1 we split the intrinsic microviscosity at $Pe_b = 1000$ into equilibrium $\eta^H_{i,0}$; compressional (or pushing) $\eta_{i,c}$; and extensional (or dragging) $\eta_{i,e}$ contributions for full hydrodynamics ($\hat{b} = 1.00001 \approx 1$) and no hydrodynamics ($\hat{b} \to \infty$). For full hydrodynamics $\eta_{i,e}/(\eta_{i,e} + \eta_{i,c}) = 0.351$, whilst without hydrodynamics, for which there is no dragging effect (as the particles do not experience lubrication forces), $\eta_{i,e}/(\eta_{i,e} + \eta_{i,c}) = 0.001$. The qualitative picture of the microviscosity as a function of $Pe_b$ agrees with that of Bergenholtz et al. (2002) and the Stokesian Dynamics simulations of concentrated sheared suspensions of Foss and Brady (2000) for the macroviscosity.

On increasing $\hat{b}$ the qualitative description presented above changes; for $\hat{b} = 1.1$ (again, see figure 2.15) the intrinsic microviscosity has significant contributions from all three of

| | $\eta_i$ | $\eta_{i,0}^H$ | $\eta_{i,c}$ | $\eta_{i,e}$ | $\eta_{i,e}/(\eta_{i,e}+\eta_{i,c})$ |
|---|---|---|---|---|---|
| $\hat{b}=1.00001$ | 2.3275 | 1.8280 | 0.3244 | 0.1751 | 0.351 |
| $\hat{b}\to\infty$ | 1.0043 | 0 | 1.0032 | 0.0011 | 0.001 |

Table 2.1: Total $\eta_i$; equilibrium $\eta_{i,0}^H$; compressional ($F_r^{ext}>0$) $\eta_{i,c}$; and extensional ($F_r^{ext}<0$) $\eta_{i,e}$ contributions to the intrinsic microviscosity at $Pe_b=1000$ for full hydrodynamics ($\hat{b}=1.00001\approx 1$) and without hydrodynamics ($\hat{b}\to\infty$).

its constituents. The interparticle-force contribution is now greater than the Brownian contribution for all $Pe_b$. Hydrodynamic interactions directly influence the Brownian microviscosity, (2.15), in the coupling of the diffusive motion of a pair of spheres. As the effect of hydrodynamic interactions diminishes with increasing $\hat{b}$ so does the Brownian microviscosity. (In the limit $\hat{b}\to\infty$ the diffusive motion of a pair of spheres is uncoupled, the relative diffusivity being simply a sum of their individual Stokes-Einstein-Sutherland diffusivities; consequently, the Brownian microviscosity vanishes). For $Pe_b\ll 1$ the intrinsic microviscosity again attains a Newtonian plateau, whose major contribution is from the hydrodynamic microviscosity. As $Pe_b$ is increased the thinning of the interparticle and Brownian microviscosities is greater than the thickening of the hydrodynamic microviscosity, causing the intrinsic microviscosity to force-thin up to about $Pe_b\approx 5$. Beyond this the weak force-thickening of the hydrodynamic microviscosity is balanced by the force-thinning of the interparticle microviscosity (the Brownian microviscosity being essentially negligible for $Pe_b>5$), resulting in a near-Newtonian high $Pe_b$ plateau. The level of force-thickening of the hydrodynamic microviscosity is less than for the cases $\hat{b}=1.00001$ and $\hat{b}=1.001$ as the particles no longer experience the highly resistive lubrication forces when in close 'contact' (contact in a *thermodynamic* sense with respect to the excluded radius $b$).

Viewing $Pe_b$ as the ratio of diffusion ($\tau_D$) to advection ($\tau_A$) timescales, the monotonic decay of the Brownian microviscosity with increasing $Pe_b$ may be understood as follows: at

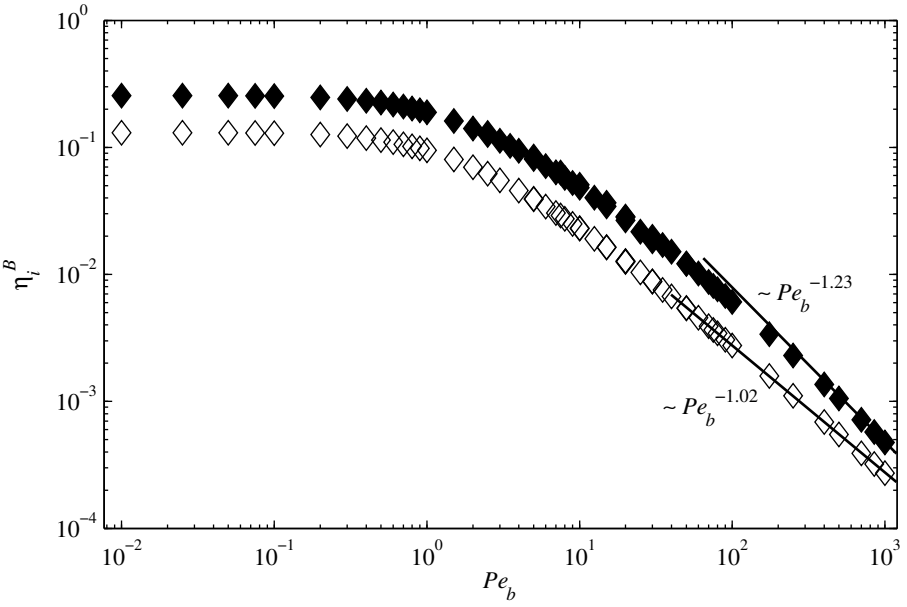


Figure 2.16: The Brownian intrinsic microviscosity $\eta_i^B$ as a function of $Pe_b$ for $\hat{b} = 1.00001$ (filled diamonds) and $\hat{b} = 1.1$ (empty diamonds). The two solid lines are the high $Pe_b$ scaling predictions $\eta_i^B \sim Pe_b^{\delta-2}$ for each value of $\hat{b}$.

low $Pe_b$ we have $\tau_D/\tau_A \ll 1$, so that Brownian diffusion acts 'quickly' against the perturbation caused by the external force to restore a near-equilibrium microstructure throughout the suspension (up until distances of $O(Pe_b^{-1})$). However, on increasing $Pe_b$ the equilibrating effect of Brownian diffusion is restricted to smaller distances and thus the Brownian microviscosity force-thins. For $Pe_b \gg 1$ the action of Brownian diffusion is confined to an $O(Pe_b^{-1})$ thin boundary layer and the Brownian microviscosity follows an asymptotic force-thinning regime. From the expression (2.15) for $\eta_i^B$ and the scaling result $g(2) \sim Pe_b^{\delta}$ at high $Pe_b$ we see that the scaling of the Brownian microviscosity with $Pe_b$ in the asymptotic force-thinning regime is $\eta_i^B \sim Pe_b^{\delta-2}$. Figure 2.16 plots the Brownian microviscosity versus $Pe_b$ for $\hat{b} = 1.00001$ and $\hat{b} = 1.1$. It is seen that the high $Pe_b$ thinning regime is well described by the scaling prediction in both cases. Similarly, from the expression (2.14) for the interparticle microviscosity one obtains the high $Pe_b$ asymptotic behavior

$\eta_i^P \sim G(2\hat{b})Pe_b^{\delta-1}$. This implies that for all finite $\hat{b}$ (for which $\delta < 1$) the interparticle microviscosity should be a weakly decaying function $Pe_b$ at large $Pe_b$. Only in the absence of hydrodynamic interactions ($\hat{b} \to \infty$, where $\delta = 1$) does the interparticle microviscosity attain a true high $Pe_b$ Newtonian plateau.

Unlike the Brownian and interparticle microviscosities, which for $Pe_b \gg 1$ are determined primarily by the boundary-layer structure, the hydrodynamic microviscosity has contributions arising throughout the entire domain $s \geq 2$. The boundary layer has a characteristic size of $O(Pe_b^{-1})$ and contains an $O(Pe_b^{\delta})$ buildup of pair-density, which from (2.12) implies an $O(Pe_b^{\delta-1})$ contribution to $\eta_i^H$. The $O(1)$ pair-density in the advective 'outer' region ($s-2 \gg O(Pe_b^{-1})$) yields an $O(1)$ (i.e. independent of $Pe_b$) contribution to $\eta_i^H$. Thus, in the limit $Pe_b \to \infty$ the hydrodynamic microviscosity takes the form $\eta_i^H \sim \alpha + \beta Pe_b^{\delta-1}$, where $\alpha$ and $\beta$ are functions of $\hat{b}$ only. This asymptotic form may be used to extrapolate the large $Pe_b$ results for $\eta_i^H$ to the $Pe_b \to \infty$ limit. The coefficients $\alpha$ and $\beta$ are determined from a nonlinear regression analysis of $\eta_i^H$ versus $Pe_b$ plots, using $\eta_i^H$ data for $Pe_b \geq 200$. Figure 2.17 displays an extrapolation of the intrinsic microviscosity $\eta_i$ for $\hat{b} = 1.00001$, for which $\eta_i^H \sim 2.511 - 0.879Pe_b^{-0.227}$ (recall that for $\hat{b} = 1.00001$ at large $Pe_b$ both $\eta_i^B$ and $\eta_i^P$ are negligible as compared to $\eta_i^H$). At infinite $Pe_b$ the extrapolation predicts $\eta_i = 2.511$, in good agreement with the studies of Batchelor and Wen (1982) and Almog and Brenner (1997) who both find that $\eta_i = 2.52$ for $\hat{b} \equiv 1$ in the 'Falling-Ball' limit $Pe_b^{-1} \equiv 0$. Furthermore, for $\hat{b} \equiv 1$ and $Pe_b^{-1} \equiv 0$ the pair-distribution function is spherically symmetric (cf. (2.E-1)), i.e. for a given radial separation there is an equal probability of finding a background particle in the compressional or extensional regions around the probe. Hence, $\eta_i$ must have equal compressional/pushing ($\eta_{i,c}$) and extensional/dragging ($\eta_{i,e}$) contributions. As the equilibrium contribution $\eta_{i,0}^H = 1.83$ for $\hat{b} \equiv 1$ this gives $\eta_{i,c} = \eta_{i,e} = 0.35$ at

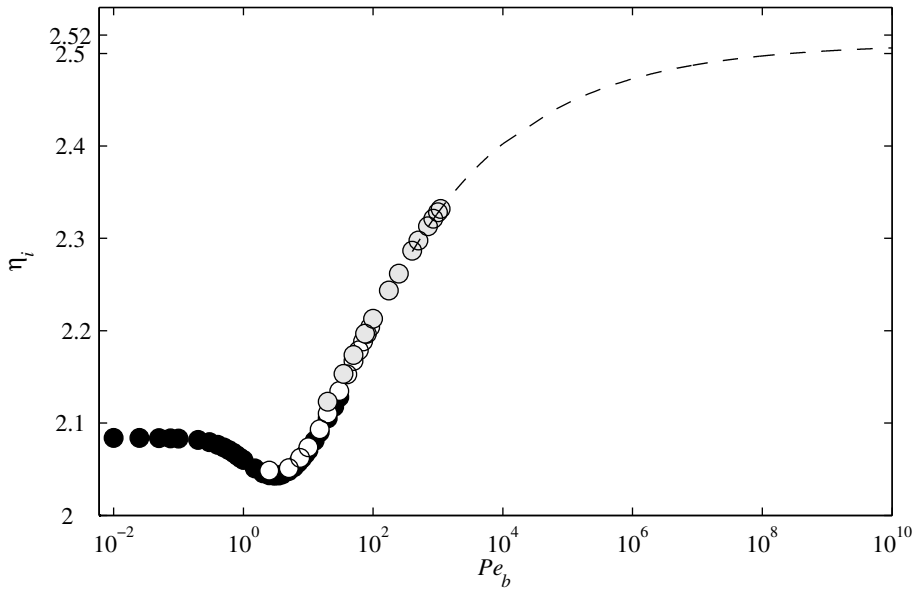


Figure 2.17: The intrinsic microviscosity for $\hat{b} = 1.00001$ as a function of $Pe_b$. The legend is the same as in figure 2.15, with the addition of a dashed line indicating the extrapolation to infinite $Pe_b$: $\eta_i^H \sim 2.511 - 0.879 Pe_b^{-0.227}$.

$Pe_b^{-1} \equiv 0$. Now, at $Pe_b = 1000$ for $\hat{b} = 1.00001 \approx 1$ (see table 2.1) we have $\eta_{i,c} = 0.3244$ and $\eta_{i,e} = 0.1751$, indicating that beyond $Pe_b = 1000$ force-thickening of the microviscosity is primarily due to the increasing accumulation of background particles in the extensional (downstream) region, until one attains a spherically symmetric microstructure in the limit $Pe_b \to \infty$ (at which point $\eta_{i,c} = \eta_{i,e}$).

## 2.7 Discussion

The work presented in the previous sections attempts to offer a simple paradigm for active and nonlinear particle tracking microrheology experiments. As a model system we choose to study the motion an externally forced Brownian probe particle in a dilute colloidal dispersion of force- and torque-free particles. In particular, it has been shown how the average translational velocity of the probe may be used to define the microviscosity of the

dispersion via application of Stokes drag law. Whilst being sufficiently simplistic to allow analytical and numerical treatment the model nevertheless exhibits non-trivial rheological properties. It is of interest to contrast the results of this investigation to those obtained from a conventional macrorheological study, such as performed by Bergenholtz et al. (2002), who examined the microstructure and macrorheology of a dilute colloidal dispersion in an ambient shear flow. In figure 2.18 we compare the intrinsic microviscosity obtained in this work with the intrinsic macroviscosity computed by Bergenholtz et al. (2002) as a function of $Pe_b$ for $\hat{b} = 1.00001$. The intrinsic macroviscosity $\eta_i$ is defined as the $O(\phi_b^2)$ coefficient of the relative macroviscosity: $\eta_r = 1 + \frac{5}{2}\phi + \eta_i \phi_b^2$ (the $O(\phi)$ term of the relative macroviscosity is, of course, the single particle Einstein correction, which scales with the hydrodynamic radius $a$), whereas the intrinsic microviscosity is defined as the $O(\phi_b)$ coefficient of the relative microviscosity (cf. 2.11). To aid in the comparison the intrinsic viscosity for both sets of data is normalized by its limiting value as $Pe_b \to 0$, which in our case is the $O(\phi_b)$ correction to the long-time self-diffusivity and for the macrorheology problem is the low-frequency dynamic, or steady shear, macroviscosity. The general functional behavior of the intrinsic viscosity is seen to be similar for the two cases. In the limit $Pe_b \to 0$ the intrinsic viscosity exhibits a Newtonian low-force(shear) plateau, which on increasing $Pe_b$ is succeeded by a force(shear)-thinning regime, caused by a decreasing Brownian contribution that outweighs the increasing hydrodynamic contribution. This force(shear)-thinning is initially proportional to $Pe_b^2$ and persists until $Pe_b \sim O(1)$, where the intrinsic viscosity attains a minimum value. The minimum occurs at $Pe_b \approx 3$ for both the microviscosity and macroviscosity. Beyond this minimum the Brownian contribution is negligible and the intrinsic viscosity is determined primarily by the hydrodynamic contribution. Since the hydrodynamic viscosity is a monotonically increasing function of $Pe_b$ the viscosity force(shear)-thickens: the degree

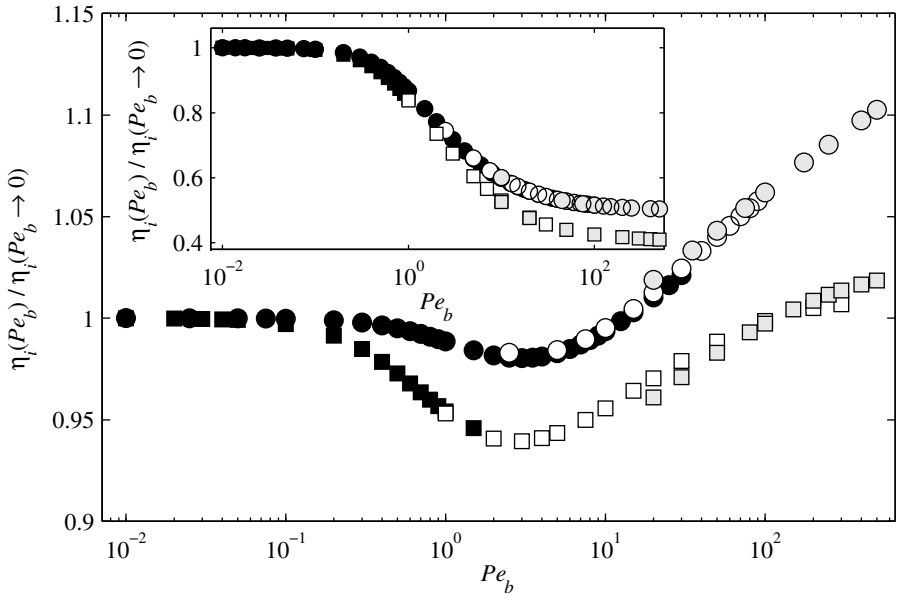


Figure 2.18: Comparison of the intrinsic microviscosity as a function of $Pe_b$ for $\hat{b} = 1.00001$ obtained in this investigation (○) with the intrinsic macroviscosity results of Bergenholtz et al. (2002) (□). The filling pattern indicates the method of numerical solution as in figure 2.11. The inset shows a comparison of the intrinsic viscosities in the absence of hydrodynamic interactions $\hat{b} \to \infty$. For the microviscosity the Péclet number is defined as $Pe_b = F_0/(2kT/b)$, whilst for the macroviscosity $Pe_b = 6\pi\eta ab\dot{\gamma}/(2kT/b)$, where $\dot{\gamma}$ is the shear-rate of the imposed shear flow.

of thickening is significantly greater for the microviscosity ($\eta_i/\eta_{i,0} \approx 1.10$ at $Pe_b = 500$) as compared to the macroviscosity ($\eta_i/\eta_{i,0} \approx 1.02$ at $Pe_b = 500$). Our results support the claim of Bergenholtz et al. (2002) that shear-thickening of the macroviscosity of colloidal dispersions at high $Pe_b$ is a two-body (or dilute) effect, which arises as a consequence of the boundary-layer formation at small interparticle separations.

When the particles do not experience hydrodynamic interactions ($\hat{b} \to \infty$) the intrinsic microviscosity and intrinsic macroviscosity are determined exclusively from the interparticle-force contribution. It was found that the microviscosity thins monotonically with increasing $Pe_b$ from a Newtonian plateau in the limit $Pe_b \to 0$ to a second Newtonian plateau at infinite $Pe_b$. Qualitatively similar behavior is seen for the intrinsic macroviscosity, as shown by the

inset of figure 2.18.

The comparison of micro- and macro-viscosity raises several issues that warrant further elaboration. As noted above, the micro- and macro-viscosity scale differently with the background particle volume fraction $\phi_b$: the microstructurally-dependent contribution (which has hitherto been termed the intrinsic viscosity) to the microviscosity is $O(\phi_b)$, whilst for the macroviscosity it is $O(\phi_b^2)$. Knowing these scalings *in advance* allows one to compare the micro- and macro-viscosity in a consistent manner. However, for more complicated (or unknown) materials such scalings may not be known *a priori*, and the comparison between micro and macro may not be so agreeable. Nonetheless, as mentioned in § 2.1, disparities between micro- and macro-rheological measurements are denotive of the fundamental physical differences in the two techniques. Therefore, such discrepancies do not render the microrheological data invalid; on the contrary, one should strive to understand the *additional* information contained in them, and, to this end, it is essential to develop detailed theoretical models for active microrheology experiments.

The comparison in figure 2.18 is between the microviscosity at fixed force and the macroviscosity at fixed shear rate. Properly, one should compared the fixed force microviscosity to the fixed stress macroviscosity (and, likewise, fixed velocity micro to fixed shear rate macro). However, in the dilute limit it is easy to show that the fixed stress and fixed shear rate macroviscosities are identical. Thus, the comparison in figure 2.18 is legitimate. In contrast, as demonstrated by Squires and Brady (2005) and discussed below, the fixed force and fixed velocity microviscosities are different in the dilute limit. Furthermore, in the fixed velocity mode the probe does not move diffusively, and the relative diffusivity is the background particle (Stokes-Einstein-Sutherland) diffusivity $D$. In fixed force mode the probe moves deterministically and diffusively; thus, the relative diffusivity is $2D$. Therefore,

the Péclet number for fixed velocity ($F_0/(kT/b)$) is twice that for fixed force ($F_0/(2kT/b)$). Lastly, although one can compare the micro- and macro-viscosity, microrheology can only determine a scalar viscosity (at least for a single spherical probe: a non-spherical probe or two spherical probes may yield more information), whereas in macrorheology the full stress tensor is obtainable, including normal stress differences and an isotropic osmotic pressure (Bergenholtz et al. 2002).

In this study it was assumed (for simplicity) that the probe particle is of the same size as the background particles; in practice, this is not always the case. For instance, Habdas et al. (2004) in their investigation of the forced motion of a magnetic bead in a dense colloidal dispersion used bead particles of roughly twice the size of the dispersion particles. A natural question to pose is: how does the calculated microviscosity of the dispersion vary with the size of the probe particle? Almog and Brenner (1997) have addressed this question in the so-called 'Falling-Ball' limit, $Pe^{-1} \equiv 0$, for $\hat{b} \equiv 1$. They find that when the probe sphere is much larger than the suspended spheres one recovers Einstein's viscosity correction $\eta_i = 2.5$. On the other hand, when the probe is much smaller than the suspended spheres they observe $\eta_i \to \infty$. In the absence of hydrodynamic interactions ($\hat{b} \to \infty$) Squires and Brady (2005) have solved the pair problem for all $Pe_b$ and all size ratios. They show that $\eta_i \sim (1+\lambda)^2/2$, where $\lambda$ is the size ratio of probe particle to background particle. It would be of interest to examine how the microviscosity varies with the size of the probe particle at finite $Pe_b$ and whether or not the scaling results of Squires and Brady (2005) hold as hydrodynamic interactions are brought in.

An alternative to fixing the force on the probe is to fix its velocity. In this case the ensemble averaged force on the probe may now be related to the suspension's microviscosity via the Stokes drag formula. A natural question arises as to whether the fixed force and fixed

velocity procedures give the same intrinsic microviscosity. Almog and Brenner (1997) have shown in the 'Falling-Ball' limit ($Pe_b \to \infty$) that the intrinsic microviscosity does differ when calculated using fixed-force or fixed-velocity probe particles. In fact, the intrinsic viscosity measured using the fixed-velocity probe is always greater than that obtained for the fixed-force probe, except in the limit where the probe particle is much larger than the suspended spheres for which one recovers Einstein's viscosity correction in both cases. In the absence of hydrodynamic interactions and for all $Pe_b$, Squires and Brady (2005) find that the ratio of fixed-velocity to fixed-force intrinsic microviscosities is $(1 + \lambda)/\lambda$. Once again, the fixed-velocity microviscosity is always greater than the fixed-force microviscosity except in the limit where the probe is much larger than the background particles, where they are equal. Physically speaking, the fixed-velocity probe expends more energy in pushing surrounding particles out of its path than the fixed-force probe which may pass around any obstructing particles. Almog and Brenner (1997) state the discrepancy between the fixed-force and fixed-velocity microviscosities to be indicative of the fundamentally non-continuum nature of the suspension. Whether this discrepancy persists for finite $Pe_b$ is not known (except in the special case $\hat{b} \to \infty$, Squires and Brady 2005) and is clearly a question of interest as it suggests the intriguing possibility of applying microrheological techniques to study the non-continuum nature of soft heterogeneous materials.

In conclusion, one may view this investigation as a step towards laying a theoretical foundation for active and nonlinear microrheology. Adopting the forced motion of a single probe particle in an otherwise quiescent colloidal dispersion as a simple paradigm for active tracking experiments, we have shown that, when appropriately scaled, the microviscosity of the dispersion is in qualitative agreement with the macroviscosity. However, for more complex materials, where the relevant micro and macro scalings are not known *a priori*,

micro- and macro-rheological data may not be in such good agreement, and great care is to be taken in the interpretation of the microrheology experiments. Nevertheless, our study suggests that active microrheology has the potential to be a valuable tool with which to explore the rich nonlinear rheology of complex fluids.

## 2.8 Bibliography

M. Abramowitz and I. Stegun. *Handbook of mathematical functions.* Dover, 1972.

A. Acrvios and T. D. Taylor. Heat and mass transfer from single spheres in Stokes flow. *Phys. Fluids*, 5:387–394, 1965.

Y. Almog and H. Brenner. Non-continuum anomalies in the apparent viscosity experienced by a test sphere moving through an otherwise quiescent suspension. *Phys. Fluids*, 9: 16–22, 1997.

H. A. Barnes, J. F. Hutton, and K. Walters. *An Introduction to Rheology.* Elsevier, 1989.

G. K. Batchelor. Brownian diffusion of particles with hydrodynamic interaction. *J. Fluid Mech.*, 74:1–29, 1976.

G. K. Batchelor. Sedimentation in a dilute polydisperse system of interacting spheres. Part 1. General theory. *J. Fluid Mech.*, 119:379–408, 1982.

G. K. Batchelor. Diffusion in a dilute polydisperse system of interacting spheres. *J. Fluid Mech.*, 131:155–176, 1983.

G. K. Batchelor and C. S. Wen. Sedimentation in a dilute polydisperse system of interacting spheres. Part 2. Numerical results. *J. Fluid Mech.*, 124:495–528, 1982.

J. Bergenholtz, J. F. Brady, and M. Vicic. The non-Newtonian rheology of dilute colloidal suspensions. *J. Fluid Mech.*, 456:239–275, 2002.

J. F. Brady. The long-time self-diffusivity in concentrated colloidal dispersions. *J. Fluid Mech.*, 272:109–133, 1994.

J. F. Brady and J. F. Morris. Microstructure of strongly sheared suspensions and its impact on rheology and diffusion. *J. Fluid Mech.*, 348:103–139, 1997.

J. C. Crocker, M. T. Valentine, E. R. Weeks, T. Gisler, P. D. Kaplan, A. G. Yodh, and D. A. Weitz. Two-point microrheology of inhomogeneous soft materials. *Phys. Rev. Lett.*, 84:888–891, 2000.

R. H. Davis and N. A. Hill. Hydrodynamic diffusion of a sphere sedimenting through a dilute suspension of neutrally buoyant spheres. *J. Fluid Mech.*, 236:513–533, 1992.

D. R. Foss and J. F. Brady. Structure, diffusion and rheology of Brownian suspensions by Stokesian Dynamics simulation. *J. Fluid Mech.*, 407:167–200, 2000.

F. Gittes, B. Schnurr, P. D. Olmsted, F. C. MacKintosh, and C. F. Schimdt. Microscopic viscoelasticity: shear moduli of soft materials determined from thermal fluctuations. *Phys. Rev. Lett.*, 79:3286–3289, 1997.

P. Habdas, D. Schaar, A. C. Levitt, and E. R. Weeks. Forced motion of a probe particle near the colloidal glass transition. *Europhys. Lett.*, 79:477–483, 2004.

D. J. Jeffrey and Y. Onishi. Calculation of the resistance and mobility functions of two unequal rigid spheres in low-Reynolds-number flow. *J. Fluid Mech.*, 139:261–290, 1984.

S. Kim and S. J. Karilla. *Microhydrodynamics: Principles and Selected Applications.* Butterworth-Heinemann, 1991.

R. A. Lionberger. Shear thinning of coloidal dispersions. *J. Rheol.*, 42:843–863, 1998.

F. C. MacKintosh and C. F. Schmidt. Microrheology. *Curr. Opin. Colloid Interface Sci.*, 4:300–307, 1999.

T. G. Mason, K. Ganesan, J. H. van Zanten, D. Wirtz, and S. C. Kuo. Particle tracking microrheology of complex fluids. *Phys. Rev. Lett.*, 79:3282–3285, 1997.

T. G. Mason and D. A. Weitz. Optical measurements of frequency-dependent linear viscoelastic moduli of complex fluids. *Phys. Rev. Lett.*, 74:1250–1253, 1995.

J. F Morris and B. Katyal. Microstructure from simulated Brownian suspension flows at large shear rate. *Phys. Fluids*, 14:1920–1937, 1995.

K. C. Ng. Hypernetted chain solution for the classical one component plasma up to $\gamma = 7000$. *J. Chem. Phys*, 61:2680–2689, 1974.

W. H. Press, S. A. Teukolsky, W. Vetterling, and B. P. Flannery. *Numerical recipes in FORTRAN*. Cambridge University Press, 1992.

J. M. Rallison and E. J. Hinch. The effect of particle interactions on dynamic light scattering from a dilute suspension. *J. Fluid Mech.*, 167:131–168, 1986.

W. B. Russel, D. A. Saville, and W. R. Schowalter. *Colloidal Dispersions*. Cambridge University Press, 1989.

T. M. Squires and J. F. Brady. A simple paradigm for active and nonlinear microrheology. *Phys. Fluids*, 17:073101, 2005.

M. Van Dyke. *Perturbation Methods in Fluid Mechanics*. Parabolic Press, 1975.

T. A. Waigh. Microrheology of complex fluids. *Rep. Prog. Phys.*, 68:685–742, 2005.

# Appendices to chapter 2

## 2.A The Brownian velocity contribution

In this appendix the result (2.9) for the Brownian velocity contribution is derived. We consider a collection of colloidal particles subjected to a stochastic Brownian force $\boldsymbol{F}^B$. In what follows there is an implicit summation over all particles in the suspension.

The Brownian force is characterized by the usual statistical properties

$$\overline{\boldsymbol{F}^B(t')} = 0, \text{ and } \overline{\boldsymbol{F}^B(t')\boldsymbol{F}^B(t'')} = \boldsymbol{\mathcal{F}}\delta(t' - t''), \tag{2.A-1}$$

where the overline denotes an average over the many collisions of the solvent molecules with the suspended particles. The appropriate timescale for this average is $t_s = m_s/6\pi\eta a_s$ (where $m_s$ and $a_s$ are the mass and radius of a solvent molecule respectively), i.e. the vorticity diffusion, or inertial relaxation, time of a solvent molecule. The amplitude of correlation of the Brownian force at times $t'$ and $t''$ is given by the fluctuation-dissipation theorem as $\boldsymbol{\mathcal{F}} = 2kT\boldsymbol{R}^{FU}$, with $\boldsymbol{R}^{FU}$ the multiparticle resistance tensor relating the forces on the particles to their velocities. This resistance tensor is a function of the instantaneous configuration, say $\boldsymbol{X}(t)$, of all the particles.

From low Reynolds number fluid dynamics the instantaneous velocity of the particles due to the Brownian force is $\boldsymbol{U}^B = \boldsymbol{M}^{UF} \cdot \boldsymbol{F}^B$, where $\boldsymbol{M}^{UF} = (\boldsymbol{R}^{FU})^{-1}$ is the multiparticle mobility tensor that relates the velocities of the particles to the forces acting on them. We need to average this velocity over a time step $\Delta t$, which is long compared to the inertial relaxation time of a particle, $t_I = m/6\pi\eta a$, but much smaller than the diffusive timescale,

$t_D = a^2/D$, characterizing changes in the configuration of the particles. Doing so we find

$$\begin{aligned}\frac{1}{\Delta t}\int_t^{t+\Delta t} U_i^B dt' &= \frac{1}{\Delta t}\int_t^{t+\Delta t} M_{ij}^{UF}(t')F_j(t')dt' \\ &= M_{ij}^{UF}(t)\frac{1}{\Delta t}\int_t^{t+\Delta t} F_j(t')dt' + \frac{\partial M_{ij}^{UF}(t)}{\partial x_k}\frac{1}{\Delta t}\int_t^{t+\Delta t}\Delta X_k(t')F_j(t')dt',\end{aligned} \tag{2.A-2}$$

where the summation convention is applied to repeated indices, and the configuration displacement is to leading order $\Delta X_k(t') = M_{kl}^{UF}(t)\int_0^{t'} F_l(t'')dt''$. Averaging (2.A-2) over many solvent collisions and using (2.A-1) we obtain

$$\overline{\boldsymbol{U}^B} = kT\boldsymbol{\nabla}\cdot\boldsymbol{M}^{UF},$$

where the divergence is taken with respect to the last index of the mobility tensor. The velocity of an individual particle $\alpha$ is given by $\overline{\boldsymbol{U}_\alpha^B} = kT\sum_{\beta=1}^{N}\boldsymbol{\nabla}_\beta\cdot\boldsymbol{M}_{\alpha\beta}^{UF}$, where the index $\beta$ runs over all $N$ particles. In the case of just two particles (say 1 and 2) we have $\overline{\boldsymbol{U}_1^B} = kT(\boldsymbol{\nabla}_1\cdot\boldsymbol{M}_{11}^{UF} + \boldsymbol{\nabla}_2\cdot\boldsymbol{M}_{12}^{UF})$. Employing a center-of-mass coordinate system ($\boldsymbol{\nabla}_r = \boldsymbol{\nabla}_2 = -\boldsymbol{\nabla}_1$) the result (2.9) is recovered.

## 2.B Finite difference method

In this appendix we describe in detail the finite difference solution of the Smoluchowski equation that was outlined in § 2.5.2. The finite difference solution is used for $Pe_b \geq 2$, for which one expects a boundary layer adjacent to the probe in the compressional region of the relative-velocity field in which there are large gradients in the pair-distribution function. To accurately capture the behavior of the pair-distribution function in the boundary layer we

stretch the radial coordinate via the transformation $y = Pe_b(s-2)$. Thus, the Smoluchowski equation (2.29) becomes (with $\hat{\boldsymbol{F}}^{ext} = -\hat{\boldsymbol{z}}$)

$$\begin{aligned} G\cos\theta\frac{\partial f}{\partial y} &- \frac{Pe_b^{-1}H\sin\theta}{2x}\frac{\partial f}{\partial\theta} + W\cos\theta(1+f) \\ &= G\frac{\partial^2 f}{\partial y^2} + Pe_b^{-1}\left(\frac{dG}{ds}+\frac{G}{x}\right)\frac{\partial f}{\partial y} + \frac{Pe_b^{-2}H}{4x^2\sin\theta}\frac{\partial}{\partial\theta}\left(\sin\theta\frac{\partial f}{\partial\theta}\right), \end{aligned}$$

where $x = 1+Pe_b^{-1}y/2$. Whilst paying careful attention to the boundary-layer structure it is also important to correctly describe the far-field behavior of $f(\mathbf{s})$. To this end, we perform a second radial coordinate transformation to go from the semi-infinite domain $y \in [0,\infty)$ to the finite domain $t \in [0,1]$ via the mapping

$$t = \exp\left(-\left\{\omega + \frac{1-\omega}{1+y}\right\}y\right),$$

where $\omega$ is an adjustable parameter. The Smoluchowski equation now reads

$$\begin{aligned} G\cos\theta\frac{dt}{dy}\frac{\partial f}{\partial t} &- \frac{Pe_b^{-1}H\sin\theta}{2x}\frac{\partial f}{\partial\theta} + W\cos\theta(1+f) \\ &= G\left(\frac{dt}{dy}\right)^2\frac{\partial^2 f}{\partial t^2} + \left(G\frac{d^2t}{dy^2}Pe_b^{-1}\left\{\frac{dG}{ds}+\frac{G}{x}\right\}\frac{dt}{dy}\right)\frac{\partial f}{\partial t} \\ &+ \frac{Pe_b^{-2}H}{4x^2\sin\theta}\frac{\partial}{\partial\theta}\left(\sin\theta\frac{\partial f}{\partial\theta}\right), \end{aligned}$$

with the boundary conditions

$$\begin{aligned} \left(\frac{dt}{dy}\right)\frac{\partial f}{\partial t} = \cos\theta(1+f) \qquad &\text{at} \qquad t=1, \\ f = 0 \qquad &\text{at} \qquad t=0. \end{aligned}$$

The Smoluchowski equation is discretized by approximating the radial and angular

derivatives by central differences

$$\begin{aligned}\frac{\partial f}{\partial t} &= \frac{f_{j+1,k}-f_{j-1,k}}{2\Delta t}, \quad \frac{\partial^2 f}{\partial t^2} = \frac{f_{j+1,k}-2f_{j,k}+f_{j-1,k}}{\Delta t^2},\\ \frac{\partial f}{\partial \theta} &= \frac{f_{j,k+1}-f_{j,k-1}}{2\Delta \theta}, \quad \frac{\partial^2 f}{\partial \theta^2} = \frac{f_{j,k+1}-2f_{j,k}+f_{j,k-1}}{\Delta \theta^2},\end{aligned}$$

where $j = 1, 2, ..., J$ and $k = 0, 1, ..., K$. The interior domain of solution is $0 < t < 1$ with $t = j/(J+1)$ (the points $t = 0$ and $t = 1$ are excluded as the radial boundary conditions must be applied there) and $0 \leq \theta \leq \pi$ with $\theta = k\pi/K$. Thus, the node spacings are $\Delta\theta = \pi/K$ and $\Delta t = 1/(J+1)$. Note, though the node spacing is constant in $t$-space it is not so in $s$-space, and via the adjustment of $\omega$ one can place a large number of nodes near $s = 2$ to accurately model the boundary layer. One can make a vector comprising the unknown structural deformation at each grid point, $f_{j,k}$, by defining an index $i = j + kJ$ running from 1 to $J(K+1)$. This enables the discretized Smoluchowski equation to be written as the matrix equation $\boldsymbol{A} \cdot \boldsymbol{f} = \boldsymbol{w}$, with $\boldsymbol{f}$ the unknown structural deformation vector. The coefficient matrix $\boldsymbol{A}$ is tridiagonal with two fringes, so we may write $\boldsymbol{T}\cdot\boldsymbol{f} = \boldsymbol{w}-(\boldsymbol{F_1}+\boldsymbol{F_2})\cdot\boldsymbol{f}$, where $\boldsymbol{T}$ is the tridiagonal part of $\boldsymbol{A}$, and $\boldsymbol{F_1}$ and $\boldsymbol{F_2}$ are the fringes. (Here, the term fringe is used to denote a matrix whose tridiagonal elements are zero.) The matrix equation is solved by constructing the Jacobi iteration

$$\boldsymbol{f}^{(n+1)} = \boldsymbol{T}^{-1} \cdot \left(\boldsymbol{w} - (\boldsymbol{F_1} + \boldsymbol{F_2}) \cdot \boldsymbol{f}^{(n)}\right),$$

where $n$ is the iteration number. For a particular value of $Pe_b$ ($Pe_{b,2}$ say) the iteration input $\boldsymbol{f}^{(0)}_{Pe_{b,2}}$ is the converged result $\boldsymbol{f}_{Pe_{b,1}}$ for the structural deformation at $Pe_{b,1} < Pe_{b,2}$, i.e. a parameter continuation in $Pe_b$ is performed. The iteration is deemed to have converged if the norm $\|\mathbf{f}^{(n+1)} - \mathbf{f}^{(n)}\| < \epsilon$, where the tolerance $\epsilon$ is typically $10^{-14}$. Alternatively, the

matrix equation may be written in component form as

$$a_i f_{i-1} + b_i f_i + c_i f_{i+1} + d_i f_{i-J} + e_i f_{i+J} = w_i,$$

where the vectors constituting the tridiagonal matrix $\boldsymbol{T}$ are

$$\begin{aligned}
a_i &= G\left(\frac{dt}{dy}\right)^2 \Delta t^{-2} - \frac{1}{2}\left(G\frac{d^2t}{dy^2}Pe_b^{-1}\left\{\frac{dG}{ds}+\frac{G}{x}\right\}\frac{dt}{dy}\right)\Delta t^{-1} + \frac{G}{2}\cos\theta\left(\frac{dt}{dy}\right)\Delta t^{-1},\\
b_i &= -2G\left(\frac{dt}{dy}\right)^2 \Delta t^{-2} - \frac{Pe_b^{-2}H}{2x^2}\Delta\theta^{-2} - Pe_b^{-1}W\cos\theta,\\
c_i &= G\left(\frac{dt}{dy}\right)^2 \Delta t^{-2} + \frac{1}{2}\left(G\frac{d^2t}{dy^2}Pe_b^{-1}\left\{\frac{dG}{ds}+\frac{G}{x}\right\}\frac{dt}{dy}\right)\Delta t^{-1} - \frac{G}{2}\cos\theta\left(\frac{dt}{dy}\right)\Delta t^{-1},
\end{aligned}$$

the fringe vectors are

$$\begin{aligned}
d_i &= -\frac{Pe_b^{-1}H\sin\theta}{4x}\Delta\theta^{-1} + \frac{Pe_b^{-2}H}{4x^2}\Delta\theta^{-2} - \frac{Pe_b^{-2}H}{8x^2}\cot\theta\Delta\theta^{-1},\\
e_i &= \frac{Pe_b^{-1}H\sin\theta}{4x}\Delta\theta^{-1} + \frac{Pe_b^{-2}H}{4x^2}\Delta\theta^{-2} + \frac{Pe_b^{-2}H}{8x^2}\cot\theta\Delta\theta^{-1},
\end{aligned}$$

and the forcing vector is simply $w_i = Pe_b^{-1}W\cos\theta$. It appears from the above that $d_i$ and $e_i$ are infinite at $\theta = 0$ and $\theta = \pi$; however, this is just a coordinate singularity and can easily be eliminated by imposing a natural symmetry boundary condition $\partial f/\partial\theta = 0$ (in finite difference terms $f_{j,k+1} = f_{j,k-1}$) at $\theta = 0$ and $\theta = \pi$.

## 2.C Boundary-layer equation

Our point of departure is the Smoluchowski equation in spherical polar coordinates (2.29). To focus on the details of the boundary layer in the high $Pe_b$ limit we introduce the stretched

radial coordinate $y = Pe_b(s-2)$, yielding the following equation

$$G\frac{\partial^2 f}{\partial y^2} + Q\frac{\partial f}{\partial y} + \frac{Pe_b^{-2}H}{4\sin\theta}\frac{\partial}{\partial\theta}\left(\sin\theta\frac{\partial f}{\partial\theta}\right) = -Pe_b^{-1}\left(\frac{H}{2}F_\theta^{ext}\frac{\partial f}{\partial\theta} + WF_r^{ext}(1+f)\right), \quad \text{(2.C-1)}$$

where terms of $O(Pe_b^{-3})$ and higher have been neglected. The smallest term discarded is $O(y^2 Pe_b^{-3})$ which indicates that (2.C-1) is not uniformly valid. However, the loss of uniformity occurs at $y \sim O(Pe_b^{1/2})$ and hence should not affect the boundary-layer structure (for which $y \sim O(1)$) of the pair-distribution function at large $Pe_b$. The function $Q$ is given by

$$Q = F_r^{ext}G + \frac{dG}{dy} + Pe_b^{-1}G\left(1 - \frac{Pe_b^{-1}y}{2}\right).$$

The boundary conditions on $f(y,\theta)$ are

$$\frac{\partial f}{\partial y} = -F_r^{ext}(1+f) \qquad \text{at} \qquad y = 0,$$

$$f \to 0 \qquad \text{as} \qquad y \to \infty.$$

If it is assumed that $\hat{\boldsymbol{F}}^{ext} = -\hat{\boldsymbol{z}}$, so that $F_r^{ext} = -\cos\theta$ and $F_\theta^{ext} = \sin\theta$, we recover the boundary-layer equation (2.30) presented in § 2.5.2.

## 2.D Boundary-layer analysis of the pair-distribution function at high $Pe_b$ in the absence of hydrodynamic interactions

Here, we derive the expression (2.32) for the pair-distribution function, $g(\boldsymbol{s})$, at high $Pe_b$ in the absence of hydrodynamic interactions. Without hydrodynamics $g(\boldsymbol{s})$ satisfies

$$\begin{aligned} -Pe_b\hat{\boldsymbol{F}}^{ext}\cdot\boldsymbol{\nabla}\quad g &= \nabla^2 g, \\ -Pe_b\hat{\boldsymbol{s}}\cdot\hat{\boldsymbol{F}}^{ext} g &= \frac{\partial g}{\partial s} \text{ at } s=2, \\ g\to 1 \quad \text{as} \quad s\to\infty. \end{aligned} \tag{2.D-1}$$

For $Pe_b \gg 1$ advection dominates the microstructural deformation and, except near the probe, (2.D-1) reduces to $\hat{\boldsymbol{F}}^{ext}\cdot\boldsymbol{\nabla}g = 0$. This simply states that along a 'streamline' $g$ is constant, and the far-field boundary condition dictates the constant to be unity. However, this constant solution does not satisfy the no-flux boundary condition at contact and near the probe there exists a boundary layer in which Brownian diffusion balances advection. To focus on the boundary layer we introduce the stretched, or inner, coordinate $y = Pe_b(s-2)$. The Smoluchowski equation now reads

$$\begin{aligned} Pe_b^2(1-Pe_b^{-2}y^2)\frac{\partial^2 g}{\partial y^2} &+ Pe_b(1-Pe_b^{-1}y)\frac{\partial g}{\partial y} + \frac{1-Pe_b^{-1}y}{4\sin\theta}\frac{\partial}{\partial\theta}\left(\sin\theta\frac{\partial g}{\partial\theta}\right) \\ &= -Pe_b^2 F_r^{ext}\frac{\partial g}{\partial y} - \frac{Pe_b F_\theta^{ext}}{2}\left(1-\frac{Pe_b^{-1}y}{2}\right)\frac{\partial g}{\partial\theta}, \end{aligned} \tag{2.D-2}$$

the boundary conditions on $g$ are

$$-F_r^{ext} g = \frac{\partial g}{\partial y} \quad \text{at} \quad y = 0,$$
$$g \to 1 \quad \text{as} \quad y \to \infty.$$

Inside the boundary layer we pose the expansion $g(y, \theta; Pe_b) = g_1(y, \theta) Pe_b + g_2(y, \theta) + O(Pe_b^{-1})$. Inserting the expansion into (2.D-2) yields equations for $g_1$ and $g_2$. For $g_1$ we have

$$\begin{aligned} \frac{\partial^2 g_1}{\partial y^2} &+ F_r^{ext} \frac{\partial g_1}{\partial y} = 0, \\ \frac{\partial g_1}{\partial y} + F_r^{ext} g_1 &= 0 \ \text{ at } \ y = 0, \\ g_1 \to 0 \quad &\text{as} \quad y \to \infty, \end{aligned}$$

which has the solution

$$g_1(y, \theta) = A(\theta) e^{-F_r^{ext} y},$$

where the angular function $A(\theta)$ will be found at the next order. This solution is only valid in the compressional region around the probe particle ($F_r^{ext} > 0$), in which inward radial advection ($F_r^{ext} \partial g_1 / \partial y$) balances Brownian diffusion ($\partial^2 g_1 / \partial y^2$) leading to an $O(Pe_b)$ build-up of pair-density in the $O(Pe_b^{-1})$ thin boundary layer. In the extensional region, $F_r^{ext} < 0$, force-free particles are advected away from the probe and there exists a wake in which $g \approx 0$.

The equation for $g_2$ is

$$\begin{aligned} \frac{\partial^2 g_2}{\partial y^2} + F_r^{ext}\frac{\partial g_2}{\partial y} &= -\frac{\partial g_1}{\partial y} - \frac{F_\theta^{ext}}{2}\frac{\partial g_1}{\partial \theta}, \\ \frac{\partial g_2}{\partial y} + F_r^{ext} g_2 &= 0 \ \text{ at } \ y = 0, \\ g_2 \to 1 \quad &\text{as} \quad y \to \infty. \end{aligned}$$

The far-field condition on $g_2$ ensures correct matching to the constant outer solution of unity. Some straightforward working gives

$$g_2(y,\theta) = \left(\beta_1(\theta) + \beta_2(\theta) y + \beta_3(\theta) y^2\right) e^{-F_r^{ext} y} - \frac{\beta_2(\theta)}{F_r^{ext}},$$

where

$$\begin{aligned} \beta_1(\theta) &= \frac{F_\theta}{2(F_r^{ext})^2}\frac{dA(\theta)}{d\theta} - \frac{A(\theta)}{F_r^{ext}}\left(1 + \frac{F_\theta}{2(F_r^{ext})^2}\frac{dF_r^{ext}}{d\theta}\right) - \frac{B(\theta)}{F_r^{ext}}, \\ \beta_2(\theta) &= \frac{F_\theta^{ext}}{2F_r^{ext}}\frac{dA(\theta)}{d\theta} - A(\theta)\left(1 + \frac{F_\theta}{2(F_r^{ext})^2}\frac{dF_r^{ext}}{d\theta}\right), \\ \beta_3(\theta) &= -\frac{F_\theta^{ext}}{4F_\theta^{ext}}\frac{dF_r^{ext}}{d\theta} A(\theta). \end{aligned}$$

To determine the angular function $B(\theta)$ the perturbation expansion must be continued to the next order in $Pe_b$; however, this is not important for our current purposes. The far-field boundary condition on $g_2$ is satisfied if $\beta_2(\theta) = -F_r^{ext}$, which yields an equation for $A(\theta)$

$$\frac{F_\theta^{ext}}{2F_r^{ext}}\frac{dA(\theta)}{d\theta} - A(\theta)\left(1 + \frac{F_\theta}{2(F_r^{ext})^2}\frac{dF_r^{ext}}{d\theta}\right) = -F_r^{ext},$$

which has the solution $A(\theta) = F_r^{ext}$. Thus, the pair-distribution function in the boundary layer is $g(y,\theta;Pe_b) = Pe_b F_r^{ext} e^{-F_r^{ext} y} + O(1)$, which shows that there is an $O(Pe_b)$ excess of

force-free particles in the compressional region around the probe. From (2.14) we see that at high $Pe_b$ the intrinsic microviscosity is

$$\eta_i = \frac{3}{4\pi}\frac{2}{Pe_b}\hat{\boldsymbol{F}}^{ext} \cdot \oint_{s=2} g(\boldsymbol{s})\hat{\boldsymbol{s}}d\Omega = \frac{3}{2\pi}\int_{F_r^{ext}>0} F_r^{ext}F_r^{ext}d\Omega + O(Pe_b^{-1}).$$

Taking $\hat{\boldsymbol{F}}^{ext} = -\hat{\boldsymbol{z}}$ (so that $F_r^{ext} = -\cos\theta$) gives $\eta_i^P = 1 + O(Pe_b^{-1})$ as $Pe_b \to \infty$.

## 2.E Boundary-layer analysis of the pair-distribution function at high $Pe_b$ for $\hat{b} \equiv 1$

In this appendix we derive the scaling result $g(2) \sim Pe_b^{0.799}$ used in § 2.6.2 in discussing the contact value of the pair-distribution function at high $Pe_b$ in the limit $\hat{b} \to 1$.

For large $Pe_b$ the Smoluchowski equation (2.29) displays the familiar trait of a small parameter multiplying the highest order derivative of a differential equation. Thus, we expect the solution about $Pe_b^{-1} \equiv 0$ to be singular with an 'inner' region (or boundary layer) adjacent to the probe particle in which the effects of Brownian motion and advection are of comparable magnitude. Outside the boundary layer, where advection is dominant, Batchelor (1982) finds that the pair-distribution function is

$$\ln g(s) = \int_s^\infty \left(\frac{2(G-H)}{zG} + \frac{1}{G}\frac{dG}{dz}\right)dz, \tag{2.E-1}$$

which is spherically symmetric and satisfies the boundary condition at infinity. However, in the limit $s \to 2$

$$g(\xi) \sim g_0\xi^{H_0/G_1-1}(\ln(\xi^{-1}))^{-H_1/G_1}, \tag{2.E-2}$$

where $\xi = s - 2$, $g_0$ is a constant, and $H_0 = 0.402$ and $G_1 = 2$ are leading order

terms in the expansion of the hydrodynamic functions $H(s)$ and $G(s)$ respectively about $s = 2$. This expression is singular as $s \to 2$ and one must take into account the effects of Brownian diffusion to satisfy the inner boundary condition. Balancing terms in (2.29) suggests that diffusion balances advection when $s \sim O(Pe_b^{-1})$; defining an inner radial coordinate $y = Pe_b(s-2)$ we obtain to leading order in $Pe_b$ the boundary-layer equation

$$\frac{\partial}{\partial y}\left(G_1 y \frac{\partial g}{\partial y}\right) - G_1 \cos\theta y \frac{\partial g}{\partial y} + \frac{H_0}{2}\sin\theta \frac{\partial g}{\partial \theta} - W_0 \cos\theta g = 0, \tag{2.E-3}$$

where $W_0 = G_1 - H_0$. The first term in (2.E-3) represents radial diffusion of pair-density with a linearly increasing diffusivity $G_1 y$. The second and third terms denote the radial and angular advection of pair-density respectively via the relative velocity field. Finally, the last term corresponds to a dipole source of pair-density. The boundary conditions that a solution of (2.E-3) must satisfy are

$$\begin{aligned} g(y,\theta) \quad &\to \quad g_0 Pe_b^{W_0/G_1} y^{-W_0/G_1} \quad \text{as} \quad y \to \infty, \\ y\frac{\partial g}{\partial y} \quad &= 0 \qquad \text{at} \quad y = 0. \end{aligned} \tag{2.E-4}$$

The right hand side of (2.E-4) is the inner limit of Batchelor's solution at infinite Péclet number (2.E-2), modulo a weak multiplicative correction of $O((\ln(Pe_b/y))^{-H_1/G_1})$ to which it is not possible to match at this order. To solve the boundary-layer problem we propose the similarity solution $g(y,\theta) = h(\theta)p(\eta)$, where $\eta = y/Y(\theta)$ is the similarity variable. Substituting this ansatz into (2.E-3) one finds that

$$\eta \frac{d^2 p}{d\eta^2} + \left\{1 - \left(\cos\theta Y + \frac{H_0}{2G_1}\sin\theta \frac{dY}{d\theta}\right)\eta\right\}\frac{dp}{d\eta} + \left(\frac{H_0}{2G_1}\sin\theta Y \frac{d\ln h}{d\theta} - \frac{W_0}{G_1}\cos\theta Y\right)p = 0,$$

subject to the boundary conditions

$$\begin{aligned} h(\theta)p(\eta) \quad &\rightarrow \quad g_0 Pe_b^{W_0/G_1} y^{-W_0/G_1} \quad \text{as} \quad \eta \rightarrow \infty, \\ \eta \frac{\partial g}{\partial \eta} \quad &= 0 \qquad \text{at} \quad \eta = 0. \end{aligned} \tag{2.E-5}$$

For the similarity transformation to be successful we require that

$$\frac{H_0}{2G_1} \sin\theta \frac{dY}{d\theta} + \cos\theta Y = \alpha, \tag{2.E-6}$$

$$\frac{H_0}{2G_1} \sin\theta Y \frac{d\ln h}{d\theta} - \frac{W_0}{G_1} \cos\theta Y = \beta, \tag{2.E-7}$$

for constants $\alpha$ and $\beta$. Setting $\theta = \pi$ in the above equations one finds that $\alpha/\beta = -G_1/W_0$. The equation for the similarity function $p$ then becomes

$$\bar{\eta} \frac{d^2 p}{d\bar{\eta}^2} + (1 - \bar{\eta}) \frac{dp}{d\bar{\eta}} - \frac{W_0}{G_1} g = 0, \tag{2.E-8}$$

with $\bar{\eta} = \alpha\eta$. The solution to (2.E-8) is

$$p(\eta) = c_1 M\left(\frac{W_0}{G_1}, 1, \alpha\eta\right) + c_2 U\left(\frac{W_0}{G_1}, 1, \alpha\eta\right),$$

where $M(a, b, z)$ (the Kummer function) and $U(a, b, z)$ (the Tricomi function) are confluent hypergeometric functions. For a second argument of unity the function $U$ is logarithmically singular at $\eta = 0$ and hence is discarded. To satisfy the far-field condition (2.E-5) we note that for $|z| \rightarrow \infty$ and $\mathrm{Re}(z) < 0$ (which restricts $\alpha$ to be negative, Abramowitz and Stegun 1972)

$$M(a, b, z) = \frac{\Gamma(b)}{\Gamma(b-a)} (-z)^{-a} \left(1 + O(|z|^{-1})\right),$$

where $\Gamma(z)$ is the Gamma function. From (2.E-5) we find

$$c_1 = g_0\Gamma\left(\frac{H_0}{L_1}\right)(-\alpha Pe_b)^{W_0/G_1}\frac{Y^{-W_0/G_1}}{h},$$

which, for $c_1$ to indeed be a constant requires $h(\theta) = Y^{-W_0/G_1}$, compatible with (2.E-6) and (2.E-7). Thus, we arrive at the boundary-layer solution for the pair-distribution function

$$g(y,\theta) = g_0\Gamma\left(\frac{H_0}{G_1}\right)\left(\frac{-\alpha Pe_b}{Y(\theta)}\right)^{W_0/G_1} M\left(\frac{W_0}{G_1}, 1, \frac{\alpha y}{Y(\theta)}\right).$$

Evidently, the function $Y(\theta)$ plays the role of the boundary-layer thickness and is found to be

$$Y(\theta) = \frac{-2\alpha G_1}{H_0}(\sin\theta)^{-2G_1/H_0}\int_\theta^\pi (\sin\phi)^{2G_1/H_0-1}\,d\phi. \tag{2.E-9}$$

One may show that $-Y/\alpha = 1$ at $\theta = \pi$ and that $Y > 0$ for $0 < \theta \leq \pi$ so that the boundary layer starts smoothly at $\theta = \pi$ and is well behaved for $0 < \theta \leq \pi$. As $\theta \to 0$ the boundary-layer thickness diverges as $Y \sim \theta^{-2G_1/H_0}$. This breakdown of the boundary-layer solution may be traced to the neglect of angular diffusion terms in (2.E-3), which are expected to be important near $\theta = 0$ in describing the coalescence of the boundary layer into a wake behind the probe. Simple scaling arguments indicate that to retain the angular diffusion terms one must introduce the variable $x = Pe_b^{1/2}\theta$ in addition to the radial boundary-layer coordinate $y = Pe_b(s-2)$. This suggests that the coalescence region is of size $O(Pe_b^{-3/2})$ and hence 'smaller' than the $O(Pe_b^{-1})$ boundary layer.

Finally, we note that the contact ($y = 0$) value of the pair-distribution function is

$$g(0,\theta) = g_0\Gamma\left(\frac{H_0}{G_1}\right)\left(\frac{-\alpha Pe_b}{Y(\theta)}\right)^{W_0/G_1},$$

from which we obtain the important scaling relation $g \sim Pe_b^{0.799}$ in the boundary layer. This is in good agreement with the numerical scaling relation $g \sim Pe_b^{0.773}$ determined from the finite difference solution of the Smoluchowski equation at $\hat{b} = 1.00001$ (cf. figure 2.14).

# Chapter 3

# "Microviscoelasticity" of colloidal dispersions

## 3.1 Introduction

The experimental measurement and theoretical prediction of the transport properties of materials is a major preoccupation for engineers and scientists alike. For the traditional states of matter: solids, liquids, and gases, this is a relatively straightforward task, with well-established techniques based on statistical mechanics (McQuarrie 2000) and kinetic theory (Chapman and Cowling 1970). On the other hand, for complex or non-Newtonian fluids, such as polymer solutions, colloidal dispersions, and biological materials, the situation is rather more complicated (see e.g. Bird et al. 1988 and Russel et al. 1989). This increase in difficulty stems from the *viscoelastic* nature of complex fluids: they exhibit both elastic (solid-like) and viscous (liquid-like) behavior, depending on the length and time (or frequency) scales on which they are scrutinized. In turn, the viscoelasticity of complex fluids is due to their inherently intricate *microstructure*; here, microstructure refers to the spatio-temporal evolution of the macromolecular constituents of the complex fluid. As an example, for colloidal dispersions the configuration of the (sub) micrometer-sized colloidal particles in the suspending fluid constitutes the microstructure. It is of particular importance to understand how the microstructure is affected by external forcing and ambient flow-fields.

Traditionally, experimental measurements are conducted in mechanical rheometers (e.g. cone-and-plate, parallel-plate), on milliliter amounts of sample, by application of oscillatory- or steady-shear flow. Through adjustment of the amplitude and time-dependence of the imposed flow it is possible to investigate linear rheological properties, such as storage and loss moduli (using small-amplitude oscillatory flow), or nonlinear properties, such as normal stress differences, shear-thinning, and shear-thickening (with finite-amplitude steady flow).

For a review of traditional rheology or, as we shall refer to it henceforth, 'macrorheology' see Barnes et al. (1989). However, macrorheological techniques have several limitations; for instance, they do not allow for the measurement of local viscoelastic properties, which can be important in the characterization of microscopically inhomogeneous materials (such as cell cytoplasm). The requirement of milliliter amounts of sample precludes the use of macrorheology to study rare or precious materials, including biological substances that are difficult to obtain in macroscopic quantities. Furthermore, rheometers often suffer from slip at the walls and inertial effects; the latter places a limit on the order of hundreds of Hertz for the maximum accessible frequencies in small-amplitude oscillatory-flow experiments.

Over the last ten years microrheology (Mason and Weitz 1995, see MacKintosh and Schmidt 1999 for a review) has burst onto the scene as an alternative to macrorheology. The term microrheology encompasses many experimental techniques that are tailored specifically to study the viscoelastic properties of complex fluids and biological materials at the microscopic scale. Living cells (Bausch et al. 1999), actin networks (Gittes et al. 1997), colloidal dispersions (Sohn and Rajagopalan 2004), polymer gels (Mahaffy et al. 2000), and DNA solutions (Mason et al. 1997) are but a few of the many systems that have been investigated using microrheological techniques (a comprehensive review is contained in Waigh 2005). The principle advantages of microrheology over macrorheology are that microrheology requires only microliter amounts of sample and may be used to study local properties of rheologically inhomogeneous materials. Also, when combined with various optical probes (e.g. confocal microscopy) one can obtain simultaneous rheological and microstructural information.

A cornerstone of microrheology is the tracking of colloidal probe particles embedded in the material under examination, and it is through the motion of the probe that one infers

the viscoelastic nature of the material. In *passive* tracking experiments the probe motion is induced by random thermal fluctuations of the surrounding environment. The location of the probe is monitored using e.g. confocal microscopy (Habdas et al. 2004), diffusing-wave spectroscopy (Mason and Weitz 1995), or laser deflection particle tracking (Mason et al. 1997). The mean-squared displacement of the probe is measured, from which the complex, or frequency-dependent, shear modulus of the surrounding material is inferred via application of a generalized Stokes-Einstein-Sutherland[1] relation (GSESR) (Mason and Weitz 1995). By its very nature, passive microrheology yields information on linear viscoelastic properties only. Nonlinear viscoelastic properties may be investigated via *active* tracking experiments, in which the material sample is driven out of equilibrium by application of an external force on the probe. Methods of probe manipulation include magnetic tweezers (Bausch et al. 1998), optical-traps (Velegol and Lanni 2001), and placement of the probe on an atomic force microscope tip (Mahaffy et al. 2000). In analogy to macrorheology, depending on the amplitude and time-dependence of the external force on the probe, the linear or nonlinear response of the material may be ascertained.

In this study we consider small-amplitude oscillatory probe motion, as a technique for determining linear viscoelastic properties of complex fluids at the microscale. Aside from the advantages of microrheology over macrorheology already mentioned, the use of small colloidal probes (which are typically on the order of a micron in diameter) allows the measurement of viscoelastic properties up to frequencies on the order of $10^6$ Hertz, approximately three decades greater than the maximum accessible frequency in macrorheology experiments. Nevertheless, an important question we shall address is to what extent, if at

[1]It has recently been brought to the attention of the scientific community that Sutherland (1905) derived and published the relationship between diffusion and hydrodynamic mobility in the same year, 1905, as Einstein. Thus, we feel it only proper to henceforth denote this as the Stokes-Einstein-Sutherland relation.

all, do the results from a small-amplitude oscillatory-force microrheology experiment mirror those from the macrorheological equivalent of small-amplitude oscillatory-flow rheometry?

As microrheology is a relatively young field (as compared to macrorheology), it is only natural that one should set macrorheology as the standard to which it is compared. Whilst agreement between microrheologically- and macrorheologically-measured properties would give credence to the microrheological results, it is prudent to ask if such an agreement is expected and necessary for microrheology to be considered useful. Indeed, microrheology and macrorheology probe the rheological properties of complex materials on fundamentally different length scales: in macrorheology the material is deformed over a 'macroscopic' (or global) length scale (e.g. the spacing between the plates of a rheometer), whilst in microrheology the deformation occurs at a 'microscopic' (or local) level, on the scale of a probe particle. Micro- and macro-rheology are also distinct from a microstructural perspective: in macrorheology a material is subjected to ambient flow (or stress) field — a quadrupolar forcing, whilst in microrheology the material is disturbed by an externally forced probe — a dipolar forcing.[2] Furthermore, in macrorheology the microstructure is deformed using a viscometric flow (e.g. simple shear), whereas the flow induced by an externally forced probe is not viscometric. It is for this reason that even in the large-probe (or continuum) limit micro- and macro-rheology may not give identical results. With the above in mind, it seems, in general, that one should not expect agreement between micro- and macro-rheology, and an instance in which the two do agree may be considered somewhat remarkable. Note, however, that any differences in micro- and macro-rheological measurements are indicative of the physically distinct manner by which the two techniques probe complex materials;

[2] In macro the forcing is with the imposed flow (with rate of strain $\boldsymbol{E}$, say); in the small-amplitude limit the microstructural deformation is linear in $\boldsymbol{E}$ (i.e. $\boldsymbol{r}\cdot\boldsymbol{E}\cdot\boldsymbol{r}$, with $\boldsymbol{r}$ the position vector), which is characteristic of a quadrupole. In micro the forcing is by the imposed force on the probe ($\boldsymbol{F}^{ext}$); in the small-amplitude limit the deformation is linear in $\boldsymbol{F}^{ext}$ (i.e. $\boldsymbol{r}\cdot\boldsymbol{F}^{ext}$), yielding a dipolar disturbance.

by investigating and understanding these differences one can only learn more about the viscoelastic response of the material. Thus, one should view microrheology as a companion (rather than a replacement) for macrorheology. Given the significant differences between micro- and macro-rheology, it is important to develop theoretical models for microrheological experiments: so that they may be interpreted correctly and compared in a consistent fashion to macrorheological data.

Following our previous work on active microrheology (Khair and Brady 2006), as a model system we consider the motion of a colloidal probe particle under the action of an oscillatory external force amidst a dispersion of monodisperse force-free colloidal 'bath' particles. It is assumed, for simplicity, that the probe and bath particles are spherical and of equal size. Imposition of an external force on the probe generates relative motion between the probe and bath particles; consequently, the microstructure of the dispersion is driven away from its equilibrium state. Opposing this is the Brownian diffusion of the probe and bath particles, induced by the random thermal movements of the solvent molecules, which serves to equilibrate the microstructure. It is the ratio of the magnitude of the external force to the Brownian (or entropic) force that dictates the extent to which the microstructure is displaced from equilibrium: this ratio is expressed as a Péclet number, $Pe$. Small-amplitude oscillatory-force microrheology corresponds to the limit $Pe \ll 1$, for which the microstructure is only slightly disturbed from its equilibrium configuration. There is, of course, no such restriction on the magnitude of (the appropriately non-dimensionalized) frequency of oscillation; indeed, our goal is to compute the viscoelastic response of the dispersion as a function of the oscillation frequency of the probe.

The macroscale viscoelastic, or 'macroviscoelastic', nature of colloidal dispersions is heavily influenced by hydrodynamic interactions between particles. Nowhere is this more

evident than in the high-frequency behavior of the elastic modulus of the dispersion. Theoretical macroviscoelasticity studies (Brady 1993; Lionberger and Russel 1994) find that the elastic modulus diverges at high-frequency for particles that interact only through hard-sphere repulsion on contact. For particles that experience 'full hydrodynamic interactions' (a term that will be made precise below) the elastic modulus attains a finite value, or plateau, in the limit of infinite frequency; furthermore, if the particles interact with a 'soft' (or continuous) potential the elastic modulus is also found to be finite at high-frequency. A major part of this study is to predict the high-frequency behavior of the elastic modulus from a microscale viscoelastic, or 'microviscoelastic', approach; therefore, it is crucial to investigate the effects of hydrodynamic interactions in a simple, systematic manner. To this end, we employ a hard-sphere like interparticle force, in which the minimum center-to-center separation between the probe and a bath particle is $2b \geq 2a$, where $a$ is the hydrodynamic (or 'true') radius and $b$ is the excluded-volume (or thermodynamic) radius of an individual particle. Interactions of this nature may arise from e.g. surface roughness, grafted polymer chains, or electrostatic repulsion. This same 'excluded-annulus' model was employed in previous work on the nonlinear microrheology of colloidal dispersions (Khair and Brady 2006; Squires and Brady 2005). Through variation of the ratio $\hat{b} \equiv b/a$ we are able to move continuously from the extremes of no hydrodynamic interactions, $\hat{b} \to \infty$, to full hydrodynamic interactions, $\hat{b} \equiv 1$.

The random nature of the Brownian force acting on the probe and bath particles necessitates a probabilistic description of the dispersion microstructure. To make analytical progress we assume the dispersion is dilute, i.e. the bath particle volume fraction is much less than unity, so that interactions between the probe and a single bath particle determine the microstructure. At this level of approximation the pair-distribution function, which

gives the probability of finding a bath particle at a vector location from the probe, satisfies a two-body Smoluchowski equation. From knowledge of the pair-distribution function it is possible to calculate many microstructurally averaged quantities; for our purposes the most important such quantity is the average translational velocity of the probe, which may be interpreted as a 'microviscosity' of the dispersion via application of Stokes drag law. For a given frequency, the microviscosity has, in general, real and imaginary parts: the real part corresponds to viscous dissipation, and the imaginary part to elasticity; hence, computing the microviscosity over a wide range of oscillation frequencies serves to delineate the viscoelastic response of the dispersion.

The rest of the chapter is organized as follows. In § 3.2.1 we present the two-body Smoluchowski equation governing the spatio-temporal evolution of the pair-distribution function in response to the application of an external force, of *arbitrary magnitude*, to the probe. The microstructurally averaged velocity of the probe is calculated in § 3.2.2 as a sum of hydrodynamic, interparticle-force, and Brownian contributions. In § 3.3 we focus on small-amplitude oscillations of the probe and demonstrate that the average velocity of the probe may be interpreted as a (complex) microviscosity of the dispersion. The microviscosity is intimately related to the self-diffusivity of the probe (as measured in passive microrheology experiments) and we discuss their connection in § 3.4. In § 3.5 we study the microstructural evolution problem in the absence of hydrodynamic interactions: in this limit the Smoluchowski equation may be solved exactly and used to derive a closed form expression for the microviscosity. Hydrodynamic interactions are considered in § 3.6, which requires numerical solution of the Smoluchowski equation. Particular attention is paid to the high-frequency behavior of the elastic modulus; importantly, we find that by including full hydrodynamic interactions the elastic modulus attains a plateau at high frequencies, in

agreement with the macroviscoelasticity studies of Brady (1993) and Lionberger and Russel (1994). In § 3.7 we discuss how to scale-up our dilute-limit results to more concentrated dispersions, and the results of the scaling analysis are employed in § 3.8 where our theoretical microviscosity calculations are compared to experimental micro- and macro-viscosity data. Finally, concluding remarks and suggestions for future investigations are offered in § 3.9.

## 3.2 Governing equations

### 3.2.1 Smoluchowski equation

Consider a dispersion comprised of $N$ neutrally buoyant spherical particles of radii $a$ homogeneously dispersed in an incompressible Newtonian fluid of density $\rho$ and dynamic viscosity $\eta$. An oscillatory external force, $\boldsymbol{F}^{ext} = \boldsymbol{F}e^{i\omega t}$ ($\omega$ is the frequency of oscillation), is applied to one of the particles (the probe), and the other $N-1$ bath particles are force- and torque-free. The Reynolds number, $Re = \rho U a/\eta$ ($U$ is a typical velocity scale) characterizing the fluid inertia over a linear dimension of order of magnitude $a$, is assumed to be much less than unity; additionally, it is assumed that the frequency non-dimensionalized on the vorticity diffusion time scale $\rho a^2/\eta$, or Strouhal number, $St = \rho\omega a^2/\eta$ is much less than unity, enabling use of the *quasi-steady* Stokes equations in describing the fluid flow.

Let us denote the probability density for finding the colloidal particles in a given configuration at time $t$ by $P_N(\boldsymbol{x}_1, \boldsymbol{x}_2, \ldots, \boldsymbol{x}_N, t)$: label 1 refers to the probe and labels 2 through $N$ refer to the bath particles. The spatio-temporal evolution of $P_N(\boldsymbol{x}_1, \boldsymbol{x}_2, \ldots, \boldsymbol{x}_N, t)$ is governed by the $N$-particle Smoluchowski equation:

$$\frac{\partial P_N}{\partial t} + \sum_{i=1}^{N} \boldsymbol{\nabla}_i \cdot \boldsymbol{j}_i = 0,$$

with the sum being over all particles in the dispersion. The flux of particle $i$ is

$$\boldsymbol{j}_i = \boldsymbol{U}_i^H P_N - \sum_{j=1}^{N} \boldsymbol{D}_{ij} P_N \cdot \boldsymbol{\nabla}_j \left( \ln P_N + V_N/kT \right),$$

where $kT$ is the thermal energy, and $V_N$ is the $N$-particle interaction potential. The hydrodynamic velocity of particle $i$ is $\boldsymbol{U}_i^H = \sum_{j=1}^{N} \boldsymbol{M}_{ij}^{UF} \cdot \boldsymbol{F}_j^{ext}$, where $\boldsymbol{M}_{ij}^{UF}$ is the configuration-dependent mobility tensor relating the velocity of particle $i$ to the external force imposed on particle $j$. The Brownian/entropic force acting on particle $i$ due to the random thermal fluctuations of the solvent molecules is $-kT\boldsymbol{\nabla}_i \ln P_N$, and the relative diffusivity of an $ij$-pair of particles is $\boldsymbol{D}_{ij} = kT\boldsymbol{M}_{ij}^{UF}$.

To obtain a closed equation for the pair-distribution function the $N$-particle Smoluchowski equation is integrated over the configurational degrees of freedom of $N-2$ bath particles, neglecting any resulting three-body interaction terms (a systematic derivation is presented in Squires and Brady 2005). By neglecting the three-body couplings the validity of our theory is restricted to the limit of small bath particle volume fraction, $\phi_a = 4\pi n a^3/3 \ll 1$ (where $n$ is the number density of bath particles), with the advantage that it is possible to make analytical progress. The pair-distribution function $g(\boldsymbol{r}, t)$ is defined as $ng(\boldsymbol{r}, t) = P_{1/1}(\boldsymbol{r}, t)$, with $P_{1/1}(\boldsymbol{r}, t)$ the conditional probability of finding a bath particle at a separation $\boldsymbol{r}$ from the probe located at $\boldsymbol{x}_1$, and satisfies a pair-level Smoluchowski equation:

$$\frac{\partial g}{\partial t} + \boldsymbol{\nabla}_r \cdot (\boldsymbol{U}_r^H g) = \boldsymbol{\nabla}_r \cdot \boldsymbol{D}_r \cdot (g\boldsymbol{\nabla}_r V/kT + \boldsymbol{\nabla}_r g). \tag{3.1}$$

In (3.1) the relative coordinate system $\boldsymbol{r} = \boldsymbol{x_2} - \boldsymbol{x_1}$ and $\boldsymbol{z} = \boldsymbol{x}_2 + \boldsymbol{x}_1$ has been introduced, where 1 denotes the probe and 2 the bath particle. The relative hydrodynamic velocity and

relative Brownian diffusivity tensor are given by $\boldsymbol{U}_r^H = \boldsymbol{U}_2^H - \boldsymbol{U}_1^H$ and $\boldsymbol{D}_r = \boldsymbol{D}_{11} + \boldsymbol{D}_{22} - \boldsymbol{D}_{12} - \boldsymbol{D}_{21}$, respectively.

The two-body interparticle potential $V(r)$ is chosen to be a simple hard-sphere 'excluded-annulus' model:

$$V(r) = \begin{cases} \infty & \text{if } r \leq 2b \\ 0 & \text{if } r > 2b. \end{cases}$$

The diluteness assumption now requires the volume fraction based on the excluded-volume radius $b$ to be small, i.e. $\phi_b = 4\pi n b^3/3 \ll 1$.

Quantities are made dimensionless by scaling as

$$\boldsymbol{r} \sim b, \quad \boldsymbol{U}^H \sim \frac{F_0}{6\pi\eta a}, \quad \boldsymbol{D} \sim 2D, \quad \text{and} \quad t \sim \frac{b^2}{2D}, \tag{3.2}$$

where $D = kT/6\pi\eta a$ is the Stokes-Einstein-Sutherland diffusivity for an isolated colloidal particle of radius $a$, and $F_0$ is the magnitude of the external force $\boldsymbol{F}^{ext}$. The scaled pair-level Smoluchowski equation reads

$$\frac{\partial g}{\partial t} + Pe_b \boldsymbol{\nabla} \cdot (\boldsymbol{U} g) = \boldsymbol{\nabla} \cdot \boldsymbol{D} \cdot \boldsymbol{\nabla} g, \tag{3.3}$$

and to simplify notation the subscripts and superscripts on $\boldsymbol{\nabla}_r, \boldsymbol{U}_r^H$, and $\boldsymbol{D}_r$ have been discarded. A Péclet number, $Pe_b = F_0/(2kT/b)$, emerges naturally from the scaling and may be viewed as the ratio of the external force $F_0$ to the Brownian force $2kT/b$: the subscript $b$ indicates that the Péclet number is based on the excluded-volume radius $b$ rather than the hydrodynamic radius $a$.

At large distances it is assumed that the suspension attains a disordered structure:

$$g(\boldsymbol{s}) \to 1 \quad \text{as} \quad s \to \infty, \tag{3.4}$$

with $s = r/b$. At $r = 2b$ the radial component of the relative flux vanishes due to the excluded-volume interparticle-force interaction:

$$\hat{\boldsymbol{s}} \cdot (\boldsymbol{D} \cdot \boldsymbol{\nabla} g - Pe_b \boldsymbol{U} g) = 0 \quad \text{at} \quad s = 2, \tag{3.5}$$

where $\hat{\boldsymbol{s}} = \boldsymbol{s}/s$ is the radial unit vector.

In the dilute limit the mobility tensors $\boldsymbol{M}_{ij}^{UF}$ take the explicit form

$$\boldsymbol{M}_{ij}^{UF}(\boldsymbol{s}; \hat{b}) = \frac{1}{6\pi\eta a} \left\{ A_{ij}(\hat{b}s) \hat{\boldsymbol{s}}\hat{\boldsymbol{s}} + B_{ij}(\hat{b}s)(\boldsymbol{I} - \hat{\boldsymbol{s}}\hat{\boldsymbol{s}}) \right\},$$

where $\boldsymbol{I}$ is the identity tensor, and $A_{ij}(r)$ and $B_{ij}(r)$ are two-body scalar mobility functions. The relative hydrodynamic velocity and relative Brownian diffusivity tensor may be written in the form

$$\begin{aligned} \boldsymbol{D} &= G(\hat{b}s) \hat{\boldsymbol{s}}\hat{\boldsymbol{s}} + H(\hat{b}s) \left(\boldsymbol{I} - \hat{\boldsymbol{s}}\hat{\boldsymbol{s}}\right), \\ \boldsymbol{U} &= \left[ G(\hat{b}s) \hat{\boldsymbol{s}}\hat{\boldsymbol{s}} + H(\hat{b}s) \left(\boldsymbol{I} - \hat{\boldsymbol{s}}\hat{\boldsymbol{s}}\right) \right] \cdot \left( -\hat{\boldsymbol{F}}^{ext} \right), \end{aligned}$$

with $\hat{\boldsymbol{F}}^{ext} = \boldsymbol{F}^{ext}/F_0$. The hydrodynamic functions $G(r) = A_{11}(r) - A_{12}(r)$ and $H(r) = B_{11}(r) - B_{12}(r)$ describe the relative mobility parallel and transverse to line of centers of a pair of spheres, respectively, and can be found in Kim and Karilla (1991).

### 3.2.2 Average probe velocity

In the limit of vanishing Reynolds number the velocity of the probe particle is given by

$$\boldsymbol{U}_1 = \boldsymbol{M}_{11}^{UF} \cdot \boldsymbol{F}^{ext} + \sum_{j=1}^{N} \boldsymbol{M}_{1j}^{UF} \cdot \boldsymbol{F}_j^P - kT \sum_{j=1}^{N} \boldsymbol{M}_{1j}^{UF} \cdot \boldsymbol{\nabla}_j \ln P_N. \tag{3.6}$$

The first term on the right-hand side of (3.6), to be denoted as $\boldsymbol{U}^H$, is the hydrodynamic contribution to the probe velocity arising from application of the external force. The second term, to be denoted as $\boldsymbol{U}^P$, is the interparticle-force contribution: $\boldsymbol{F}_j^P = -\boldsymbol{\nabla}_j V_N$ is the interparticle-force acting on particle $j$. Lastly, the third term, to be denoted as $\boldsymbol{U}^B$, is the Brownian contribution: $-kT\boldsymbol{\nabla}_j \ln P_N$ is the entropic, or thermal, force exerted on particle $j$. The average velocity of the probe is obtained by averaging the configuration-specific velocity (3.6) over the admissible positions of the $N-1$ bath particles (see Squires and Brady 2005 for a detailed derivation). In the dilute limit the three contributions to the average probe velocity are given by

$$\langle \boldsymbol{U}^H \rangle = \frac{\boldsymbol{F}^{ext}}{6\pi\eta a} \cdot \left( \boldsymbol{I} + \frac{3\phi_b}{4\pi} \int_{s\geq 2} \left\{ A_{11}(\hat{b}s)\hat{\boldsymbol{s}}\hat{\boldsymbol{s}} + B_{11}(\hat{b}s)(\boldsymbol{I} - \hat{\boldsymbol{s}}\hat{\boldsymbol{s}}) - \boldsymbol{I} \right\} g(\boldsymbol{s}) d\boldsymbol{s} \right), \tag{3.7}$$

$$\langle \boldsymbol{U}^P \rangle = -\frac{F_0}{6\pi\eta a} \frac{3\phi_b}{4\pi} \frac{2G(2\hat{b})}{Pe_b} \oint_{s=2} g(\boldsymbol{s})\hat{\boldsymbol{s}} d\Omega, \tag{3.8}$$

$$\langle \boldsymbol{U}^B \rangle = -\frac{F_0}{6\pi\eta a} \frac{3\phi_b}{4\pi} \frac{1}{Pe_b} \int_{s\geq 2} \left( \frac{G(\hat{b}s) - H(\hat{b}s)}{s} + \frac{1}{2} \frac{dG(\hat{b}s)}{ds} \right) g(\boldsymbol{s})\hat{\boldsymbol{s}} d\boldsymbol{s}, \tag{3.9}$$

with the angle brackets denoting an average over the $N-1$ bath particle positions.

## 3.3 Small-amplitude oscillations

The pair-level Smoluchowski equation (3.3) describes the spatio-temporal evolution of the dispersion microstructure in response to the imposition of an oscillatory external force of

*arbitrary* amplitude (compatible with quasi-inertia-free Brownian motion and creeping fluid flow) on the probe particle. Here, we apply the restriction that the forcing amplitude be small; consequently, the perturbation to the equilibrium microstructure is linear in the external force:

$$g(\boldsymbol{s}) = 1 + Pe_b f(s;\alpha) e^{i\alpha t}\hat{\boldsymbol{s}}\cdot\hat{\boldsymbol{F}}, \tag{3.10}$$

where $\hat{\boldsymbol{F}} = \boldsymbol{F}/F_0$, and $\alpha = \omega b^2/2D$ is the oscillation frequency $\omega$ non-dimensionalized by the diffusive timescale $b^2/2D$. The small amplitude of the external force requires that $Pe_b \ll 1$: the dispersion microstructure is only slightly displaced from its equilibrium state. Substituting (3.10) into the pair-level Smoluchowski equation (3.3) and associated boundary conditions (3.4) and (3.5) leads to an equation for the radial structural deformation $f(s;\alpha)$:

$$\frac{1}{s^2}\frac{d}{ds}\left(s^2 G(\hat{b}s)\frac{df}{ds}\right) - \frac{2H(\hat{b}s)f}{s^2} - i\alpha f = -W(\hat{b}s), \tag{3.11}$$

$$\frac{df}{ds} = -1 \qquad \text{at} \qquad s = 2, \tag{3.12}$$

$$f \to 0 \qquad \text{as} \qquad s \to \infty. \tag{3.13}$$

The hydrodynamic function $W = dG/ds + 2(G-H)/s$ arises from the divergence of the relative velocity, viz. $\boldsymbol{\nabla}\cdot\boldsymbol{U} = -W\hat{\boldsymbol{s}}\cdot\hat{\boldsymbol{F}}^{ext}$.

In the small-amplitude limit the three probe velocity contributions are strictly proportional to the external force $\boldsymbol{F}^{ext}$, as may be seen by substituting (3.10) into (3.7)-(3.9) and performing the necessary angular integrations. Through application of the Stokes drag law, $\boldsymbol{F}^{ext}/6\pi\eta a = \langle \boldsymbol{U}_1\rangle\eta_r$, one may *interpret* the three velocity contributions as increments to the relative microviscosity $\eta_r$ of the dispersion above the solvent viscosity (which has a dimensionless value of unity). To first order in the volume fraction of bath particles the

relative microviscosity may be written as

$$\eta_r = 1 + \eta_H + \eta_B + \eta_P : \tag{3.14}$$

$\eta_H$, $\eta_P$, and $\eta_B$ are the hydrodynamic, interparticle-force, and Brownian microviscosity increments to the relative microviscosity, respectively. The three increments are given by

$$\begin{aligned}
\eta_H &= \phi_b \int_2^\infty \left(3 - A_{11}(\hat{b}s) - 2B_{11}(\hat{b}s)\right) s^2 ds, \\
\eta_P &= 2\phi_b G(2\hat{b}) f(2;\alpha), \\
\eta_B &= \frac{\phi_b}{2} \int_2^\infty W(\hat{b}s) f(s;\alpha) s^2 ds.
\end{aligned}$$

The hydrodynamic increment involves an average over the equilibrium microstructure (which, in the dilute limit, is unity); hence, $\eta_H$ is a purely real quantity. In contrast, the interparticle-force and Brownian increments involve weighting over the radial microstructural deformation $f(s;\alpha)$ which is, in general, a complex function. As a result, the interparticle-force and Brownian increments will have real and imaginary components: the imaginary part corresponds to elasticity and the real part corresponds to viscous dissipation; therefore, it is useful to separate the relative microviscosity into real and imaginary parts:

$$\eta_r(\omega) = \eta'(\omega) - i\,\eta''(\omega),$$

where the frequency dependence of the microviscosity is noted explicitly. The real part of the relative microviscosity is

$$\eta'_r(\omega) = 1 + \eta_H + \eta'_P(\omega) + \eta'_B(\omega),$$

and $\eta'_P$ and $\eta'_B$ are the real parts of $\eta_P$ and $\eta_B$, respectively. The imaginary part of the relative microviscosity is

$$\eta''_r(\omega) = \eta''_P(\omega) + \eta''_B(\omega),$$

where $\eta''_P$ and $\eta''_B$ are the imaginary parts of $\eta_P$ and $\eta_B$, respectively.

To compute the relative microviscosity for arbitrary frequencies it is necessary to calculate $f(s;\alpha)$ explicitly. Before doing so, let us first consider the limiting cases of high- and low-frequency oscillations. The high-frequency limit is achieved when $\omega \to \infty$ on the scale of the diffusive time $b^2/2D$, which corresponds to $\alpha \to \infty$. The solution for $f$ is then simply $f = 0$: the forcing is of such a high frequency that the dispersion is not perturbed from its equilibrium state; consequently, the interparticle-force and Brownian contributions to the probe velocity are identically zero, and the high-frequency microviscosity is simply

$$\eta_r(\infty) = \eta'(\infty) \equiv \eta'_\infty = 1 + \eta_H.$$

The high-frequency microviscosity is purely real and therefore dissipative in nature. Khair and Brady (2006) have computed $\eta_H$ over the entire range of $\hat{b}$; therefore, we take $\eta_H$ to be known here (see below).

The low-frequency limit corresponds to the probe moving under the action of a steady external force, in which case $f$ is purely real; again, there is no elastic contribution to the microviscosity. The low-frequency microviscosity is dissipative and given by

$$\eta_r(0) = \eta'(0) \equiv \eta'_0 = 1 + \eta_H + \eta'_P(0) + \eta'_B(0).$$

For steady forcing, $\alpha = 0$, Batchelor (1983) solved the Smoluchowski equation (3.11)

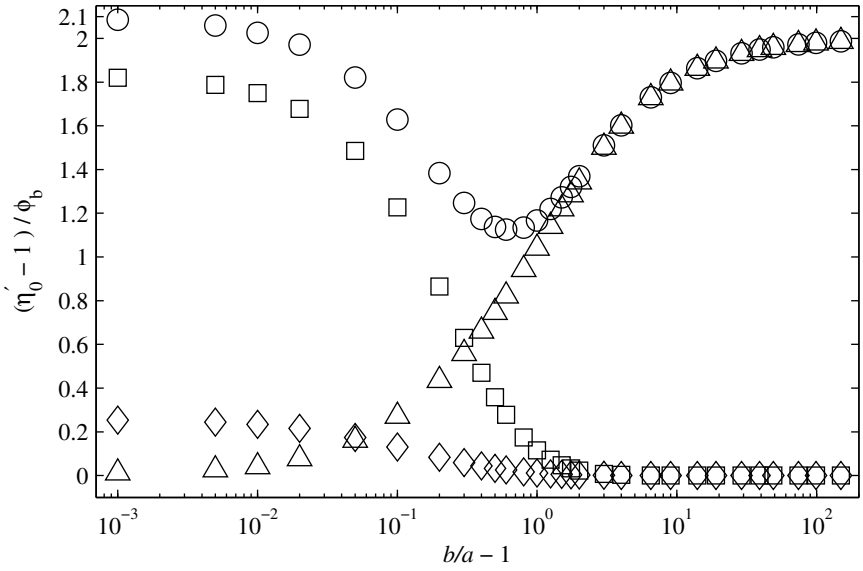


Figure 3.1: $O(\phi_b)$ coefficient of the low-frequency microviscosity $\eta_0'$ versus $\hat{b} = b/a$: total $(\eta_0' - 1)/\phi_b$, $\circ$; hydrodynamic $\eta_H/\phi_b$, $\square$; Brownian $\eta_B'(0)/\phi_b$, $\diamond$; and interparticle-force $\eta_P'(0)/\phi_b$, $\triangle$. Data taken from Khair and Brady (2006).

for $\hat{b} \equiv 1$ in computing the $O(\phi_b)$ correction to the long-time self-diffusivity. More recently, Khair and Brady (2006) have solved (3.11) for steady forcing over the entire range of $\hat{b}$ and calculated the low-frequency microviscosity $\eta_0'$. Figure 3.1 plots the $O(\phi_b)$ coefficient of $\eta_0'$ (i.e. $(\eta_0' - 1)/\phi_b$) as a function of $\hat{b}$, along with it's hydrodynamic $(\eta_H/\phi_b)$, interparticle-force $(\eta_P'(0)/\phi_b)$, and Brownian $(\eta_B'(0)/\phi_b)$ constituents. (Recall that the high-frequency microviscosity $\eta_\infty'$ is 1 plus the hydrodynamic microviscosity $\eta_H$.) At the extrema of $\hat{b} = 1$ (full hydrodynamic interactions) and $\hat{b} \to \infty$ (no hydrodynamic interactions) we find that $\eta_0' = 1 + 2.08\phi_b$ and $\eta_0' = 1 + 2\phi_b$, respectively. However, $\eta_0'$ is a non-monotonic function of $\hat{b}$: it has a minimum of $\eta_0' = 1 + 1.13\phi_b$ occurring at $\hat{b} \approx 1.6$. The minimum in $\eta_0'$ arises because $\hat{b}$ is sufficiently greater than unity, so that the highly resistive hydrodynamic lubrication interactions (which are present only for $\hat{b} - 1 \ll 1$) do not hinder the motion of the probe, but $\hat{b}$ is also not too large, whence $\eta_0'$ increases due to the prominent role of

the hard-sphere interparticle force (which provides a purely geometrical resistance to the probe's motion).

To emphasize the influence of frequency dependent microstructural deformation it is useful to define reduced microviscosity functions: for the real part of the microviscosity we define the reduced function as

$$\frac{\eta_r'(\omega) - \eta_\infty'}{\eta_0' - \eta_\infty'} = \frac{\eta_P'(\omega) + \eta_B'(\omega)}{\eta_P'(0) + \eta_B'(0)}, \tag{3.15}$$

and for the imaginary part of the microviscosity the reduced function is

$$\frac{\eta_r''(\omega)}{\eta_0' - \eta_\infty'} = \frac{\eta_P''(\omega) + \eta_B''(\omega)}{\eta_P'(0) + \eta_B'(0)}. \tag{3.16}$$

Both reduced microviscosities are functions of the dimensionless frequency $\alpha$ only; the explicit volume fraction dependence has been removed by the scaling.

## 3.4 Connection between microviscosity and self-diffusivity of the probe particle

Here, we elucidate the intimate relationship between the microviscosity of the dispersion and the self-diffusivity of the probe particle. Recall, in passive microrheology one measures the mean-squared displacement of the probe (i.e. its self-diffusivity) and relates this to the complex modulus of the material through a GSESR. There are several methods (see figure 2 of Waigh 2005) to convert the mean-squared displacement of the probe (a purely real quantity) into a complex modulus. For example, one can take the Laplace transform of the mean-squared displacement and apply a Laplace-space GSESR to obtain the (Laplace

transformed) relaxation modulus; the complex modulus is then obtained via an analytic continuation of the Laplace transformed relaxation modulus into Fourier space. Alternatively, one may take the Fourier transform of the mean-squared displacement and apply a Fourier-space GSESR (Mason 2000), thereby directly obtaining the complex modulus. In what follows we demonstrate that the small-amplitude oscillatory motion of an active (as opposed to passive) probe fundamentally relates the microviscosity to self-diffusion.

For sufficiently high frequencies, on the scale of the diffusive time $b^2/2D$, the oscillation of the probe does not distort the microstructure of the dispersion from its equilibrium state. Thus, the average velocity of the probe is $\langle \boldsymbol{U}_1 \rangle = \langle \boldsymbol{M}_{11}^{UF} \rangle_{eq} \cdot \boldsymbol{F}^{ext}$ (where $\langle \cdots \rangle_{eq}$ denotes an average over the equilibrium microstructure), and the microviscosity is equal to the high-frequency microviscosity $\eta'_\infty$. On the other hand, the short-time self-diffusivity tensor $\boldsymbol{D}_0^s$ is defined as $kT\langle \boldsymbol{M}_{11}^{UF} \rangle_{eq}$. For an isotropic equilibrium microstructure $\boldsymbol{D}_0^s = D_0^s \boldsymbol{I}$; therefore, the (scalar) short-time self-diffusivity is related to the high-frequency microviscosity via the identity $\eta'_\infty \equiv D/D_0^s$ (recall, $D$ is the Stokes-Einstein-Sutherland diffusivity, and $\eta'_\infty$ has already been made dimensionless by the solvent viscosity $\eta$).

A probe executing oscillations of lower frequency does disturb the microstructure in its surroundings. In the small-amplitude regime, to leading order in $Pe_b$, the disturbance is proportional to $\boldsymbol{F}^{ext} = \boldsymbol{F} e^{i\omega t}$, due to the linearity of the Smoluchowski equation. Consequently, $\langle \boldsymbol{U}_1 \rangle$ is also linearly dependent on $\boldsymbol{F}^{ext}$, and the complex proportionality constant defines the frequency-dependent self-diffusivity, $D^s(\omega)$, divided by $kT$. The frequency-dependent self-diffusivity is equal to the Fourier transform of $dD^s(t)/dt$ (Cichocki and Felderhof 1991), where $D^s(t)$ is the time-dependent self-diffusivity, which is simply the time derivative of the mean-squared displacement of the probe. Thus, the complex microviscosity is equal to the inverse of the frequency-dependent self-diffusivity: $\eta_r(\omega) \equiv D/D^s(\omega)$.

In the limit of zero-frequency oscillations, where the probe moves under a steady external force, the (purely real) proportionality constant between $\langle \boldsymbol{U}_1 \rangle$ and $\boldsymbol{F}^{ext}$ is the long-time self-diffusivity, $D^s_\infty$, divided by $kT$. Thus, the zero-frequency or steady-force microviscosity is related to the long-time self-diffusivity via $\eta'_0 \equiv D/D^s_\infty$.

In fact, in the linear-response regime the (Fourier transformed) microstructural evolution equation for self-diffusion (Brady 1994), at long wavelengths, is identical to that of our oscillatory probe problem. Note, however, that beyond the linear-response regime there is no such simple relationship, if indeed a relationship exists at all, between the self-diffusion problem and the finite-amplitude oscillatory motion of an active probe.

With the above in mind, the scaled transition from low- to high-frequency microviscosity is equivalent to the scaled transition from long- to short-time self-diffusivity:

$$\frac{\eta_r(\omega) - \eta'_\infty}{\eta'_0 - \eta'_\infty} = \frac{1/D^s(\omega) - 1/D^s_0}{1/D^s_\infty - 1/D^s_0},$$

Thus, in the linear-response regime the connection between the mean-squared displacement ($D^s(\omega)$) and the microviscosity ($\eta_r(\omega)$) is fundamentally exact *by definition*; the connection between the microviscosity and the macroviscosity is not obvious, however, and needs to be addressed.

## 3.5 Microstructure & microrheology: No hydrodynamic interactions

Before dealing with the complicating effect of hydrodynamic interactions it is instructive to consider the microstructural deformation problem in their absence. In terms of the excluded-annulus model neglecting hydrodynamic interactions corresponds to the limit $\hat{b} = b/a \to \infty$:

the excluded-volume radius $b$ is much larger than the hydrodynamic radius $a$. In the absence of hydrodynamic interactions ($G = 1$, $H = 1$, and $W = 0$) the Smoluchowski equation reads

$$\frac{1}{s^2}\frac{d}{ds}\left(s^2\frac{df}{ds}\right) - \frac{2f}{s^2} - i\alpha f = 0, \tag{3.17}$$

$$\frac{df}{ds} = -1 \qquad \text{at} \qquad s = 2, \tag{3.18}$$

$$f \to 0 \qquad \text{as} \qquad s \to \infty, \tag{3.19}$$

and admits the exact solution (Brady 1994)

$$f = \frac{4}{s^2}\left(\frac{1 + z_0 s/2}{1 + z_0 + z_0^2/2}\right) e^{z_0(1-s/2)} \quad ,$$

where $z_0 = 2(i\alpha)^{1/2}$. Without hydrodynamic interactions the Brownian $\eta_B$ and hydrodynamic $\eta_H$ microviscosity increments are both identically zero, and the relative microviscosity is simply 1 plus the interparticle-force component $\eta_P = 2f(2;\alpha)\phi_b$. The solution to (3.17) for $\alpha = 0$, corresponding to a steady force on the probe, is $f(s;0) = 4/s^2$; thus, the low-frequency microviscosity is $\eta_0' = 1 + 2\phi_b$. Of course, in the absence of hydrodynamic interactions the high-frequency microviscosity is simply equal to solvent viscosity, i.e. $\eta_\infty' = 1$.

After a little algebra, the contact value of the structural deformation may be separated into real and imaginary parts, giving the reduced microviscosity functions

$$\frac{\eta_r'(\omega) - \eta_\infty'}{\eta_0' - \eta_\infty'} = \Re f(2;\alpha) = \frac{1 + \beta + \beta^2}{(1+\beta)(1+\beta^2)},$$

and

$$\frac{\eta_r''(\omega)}{\eta_0' - \eta_\infty'} = -\Im f(2;\alpha) = \frac{\beta^2}{(1+\beta)(1+\beta^2)},$$

where $\beta = (2\alpha)^{1/2}$.

Although we have an exact solution for $f(2;\alpha)$ for arbitrary $\alpha$, it is useful to examine the asymptotic limits of small and large $\alpha$. At small $\alpha$ the contact value of the structural deformation has the asymptotic form

$$f(2;\alpha) \sim 1 - (2\alpha)^{3/2} + (2\alpha)^2 - i(2\alpha - (2\alpha)^{3/2}) + O(\alpha^3).$$

The first departure from the steady solution, which is of $O(\alpha)$, is purely imaginary and therefore elastic in nature. Interestingly, the first frequency correction to the real part of $f(2;\alpha)$ is $O(\alpha^{3/2})$, a non-analytic dependence, which is due to singular nature of the Smoluchowski equation for small $\alpha$: Brownian diffusion dominates the microstructural deformation, except at distances $s \sim O(\alpha^{-1/2})$ where it is balanced by unsteadiness/oscillatory forcing.

In the limit of infinite frequency $f = 0$, which satisfies the far-field condition (3.19) but not the no-flux condition at contact (3.18). The perturbation about infinite frequency is therefore singular, with a boundary layer adjacent to the probe particle in which diffusion balances oscillatory forcing. Defining the stretched coordinate $y = \alpha^{1/2}(s-2)$ leads to the boundary-layer equation $d^2f/dy^2 = if$, which has the solution

$$f = \frac{1}{(i\alpha)^{1/2}} e^{-i^{1/2}y} + \frac{i}{2\alpha}\left(1 + i^{1/2}y\right) e^{-i^{1/2}y} + O(\alpha^{-3/2}). \tag{3.20}$$

To leading order, the real and imaginary parts of $f(2;\alpha)$, and hence $\eta_r$, vanish like $\alpha^{-1/2}$ as $\alpha \to \infty$. The elastic modulus of the dispersion $G'$ is related to the imaginary part of the microviscosity by $G'(\omega) = \omega\eta''(\omega)$. A microviscosity decaying as $\alpha^{-1/2}$ gives an elastic modulus that diverges as $\alpha^{1/2}$ at high frequency. The unbounded growth of

$G'$ with $\alpha$ is clearly unphysical, and in § 3.6 it is shown that including full hydrodynamic interactions ($\hat{b} = 1$) removes the divergence. In terms of self-diffusion, the $\alpha^{-1/2}$ decay in $f(2;\alpha)$ incorrectly predicts a *short-time* temporal response proportional to $t^{1/2}$; again, by including full hydrodynamic interactions we shall resolve this issue.

It is interesting to compare the complex viscosity obtained from our microrheological study with that from macrorheology. In macrorheology a colloidal dispersion is subjected to an oscillatory linear flow of the form $\boldsymbol{E}e^{i\omega t}$, where $\boldsymbol{E}$ is a constant traceless tensor detailing the flow type (simple shear, elongational etc.). (In macrorheology there is no probe particle, and all particles have the same hydrodynamic radii $a$ and excluded-volume radii $b$). For small-amplitude oscillations, which requires the Péclect number based on the excluded-volume radius $b$: $Pe_b = \dot{\gamma}b^2/2D$ (where $\dot{\gamma} = |\boldsymbol{E}|$), to be much less than unity, the microstructural deformation is linear in $\boldsymbol{E}$. Hence, the average stress in the dispersion will be strictly proportional to $\boldsymbol{E}$, and the coefficient of proportionality defines the complex macroviscosity. In analogy to the complex microviscosity, the real part of the complex macroviscosity corresponds to viscous dissipation, and the imaginary part corresponds to elasticity. There is, however, an important distinction between the micro- and macro-viscosity: the microstructurally-dependent contribution to the microviscosity is $O(\phi_b)$, whilst for the macroviscosity it is $O(\phi_b^2)$ (the $O(\phi_b)$ contribution to the relative macroviscosity is, of course, the single particle Einstein correction $\frac{5}{2}\phi$). Nevertheless, using reduced viscosity functions we are able to scale out the explicit volume fraction dependencies and make a direct comparison between the microstructurally-dependent contributions to the micro- and macro-viscosities. In figures 3.2 and 3.3 we compare the reduced complex microviscosity to the reduced complex macroviscosity (as computed by Brady 1993) for dilute dispersions in the absence of hydrodynamic interactions, as a function of the

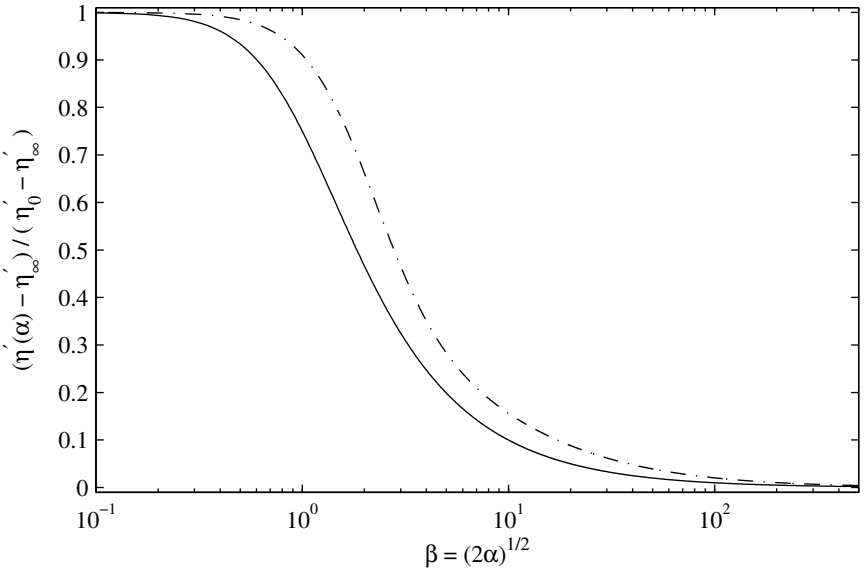


Figure 3.2: Real part of the reduced complex viscosity in the absence of hydrodynamic interactions as a function of dimensionless frequency $\alpha$. The solid line is the microviscosity and the broken line is the macroviscosity (from Brady 1993). In the limit $\alpha \to 0$ the microviscosity and macroviscosity share the asymptotic form $1 - O(\alpha^{3/2})$. At high frequencies the common asymptotic decay scales like $\alpha^{-1/2}$.

scaled frequency $\alpha$. Figure 3.2 compares the real parts of the microviscosity and macroviscosity, which are seen to be in qualitative agreement over the entire frequency range. Qualitative agreement is also observed between the imaginary parts of the microviscosity and macroviscosity, as shown in figure 3.3. Of particular importance is the congruence in the high-frequency asymptotic forms of the micro- and macro-viscosity: both decay like $\alpha^{-1/2}$ as $\alpha \to \infty$; therefore, the elastic modulus obtained from the complex macroviscosity also diverges like $\alpha^{1/2}$ at high frequency. Furthermore, by including full hydrodynamic interactions in the macrorheology problem Brady (1993) and Lionberger and Russel (1994) have shown that one obtains an elastic modulus that is finite as $\alpha \to \infty$.

Before continuing, some subtleties regarding the micro-macro comparison need to be highlighted. The comparison is between oscillatory-force microrheology and oscillatory-

flow macrorheology. Strictly, one should compare oscillatory-force microrheology with oscillatory-stress macrorheology (or, likewise, oscillatory-velocity microrheology with oscillatory-flow macrorheology). However, in the dilute limit, i.e. to leading order in $\phi_b$, oscillatory-stress macrorheology and oscillatory-flow macrorheology yield the same macroviscosity;[3] therefore, the comparison in figures 3.2 and 3.3 is valid. In contrast, the oscillatory-velocity and oscillatory-force microviscosities are different at leading order in $\phi_b$, as demonstrated by Squires and Brady (2005) and discussed in § 3.9. In the linear-response regime although there is a direct proportionality between probe velocity and force there can nevertheless be a scale factor difference between the two situations. In the plot of the reduced viscosities, figures 3.2 and 3.3, this scale factor difference is accounted for in the normalization. Moreover, in oscillatory-velocity mode the probe experiences no diffusive motion; thus, the relative diffusivity is equal to the bath particle (Stokes-Einstein-Sutherland) diffusivity $D$. In oscillatory-force mode the probe moves deterministically and diffusively, and the relative diffusivity is then the sum of probe and bath diffusivities, $2D$. Therefore, the dimensionless frequency for oscillatory velocity ($\omega b^2/D$) is twice that for oscillatory force ($\omega b^2/2D$). This would shift the microviscosity curves in figures 3.2 and 3.3 to the right by a factor of $\sqrt{2}$.

In macrorheology the Cox-Merz rule (Cox and Merz 1958) enables one to glean information on the *nonlinear* rheological response of a colloidal dispersion (or, in general, other complex fluids) from small-amplitude oscillatory-flow experiments. The Cox-Merz rule is an empirical rule (although Renardy 1997 provides a theoretical argument for its use in the case of polymer melts) which states that the dependence of the steady-shear macroviscosity

[3] In fact, in the dilute limit the two macrorheology modes yield equal macroviscosities even in the nonlinear regime (i.e. when the Péclet number is not small compared to unity). Additionally, in the linear-response regime it can be shown that oscillatory stress and oscillatory force give the same macroviscosity regardless of the concentration.

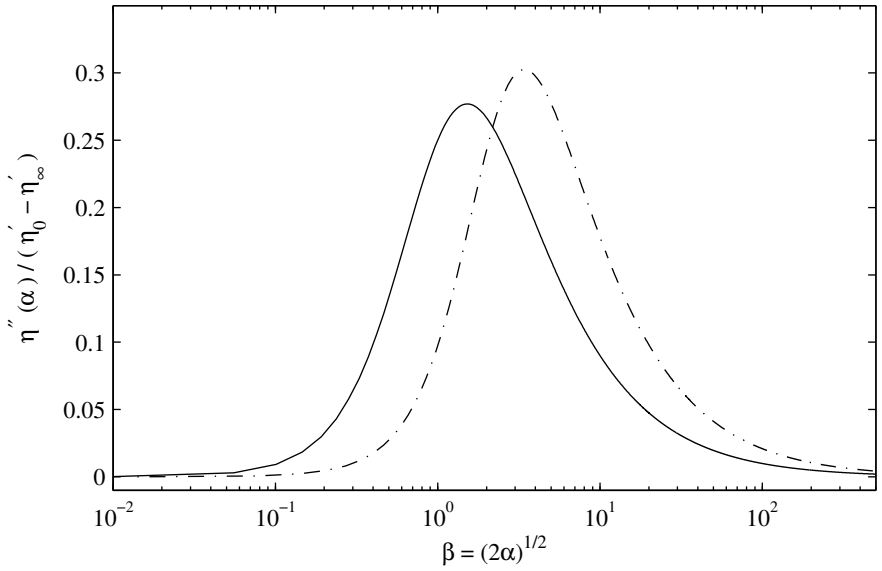


Figure 3.3: Imaginary part of the reduced complex viscosity in the absence of hydrodynamic interactions as a function of dimensionless frequency $\alpha$. The solid line is the microviscosity and the broken line is the macroviscosity (from Brady 1993). The maximum in the microviscosity occurs at $\beta = (1-(26/27)^{1/2})^{1/3}+(1+(26/27)^{1/2})^{1/3} = 1.52...$, and the maximum in the macroviscosity occurs at $\beta = 3.41$ (to two decimal places). In the limit of $\alpha \to 0$ the microviscosity and macroviscosity share the asymptotic form $O(\alpha)+O(\alpha^{3/2})$. At high frequencies the common asymptotic decay scales like $\alpha^{-1/2}$.

$\eta(\dot{\gamma})$ on the shear-rate $\dot{\gamma}$ can be estimated from the modulus of the complex macroviscosity $\eta(\omega)$ as a function of frequency $\omega$, as the two functions should be almost identical, i.e. $\eta(\dot{\gamma}) = |\eta(\omega)|$. This observation has important practical applications as it is often easier to acquire data over a wide range of oscillation frequencies as compared to shear rates. A natural question to pose is whether the Cox-Merz rule also applies for the microviscosity. For microrheology the relevant nonlinear rheological property is the microviscosity as a function of the *steady* external force $\boldsymbol{F}^{ext}$, which should be compared to the frequency dependence of the complex microviscosity. In figure 3.4 we plot the reduced steady-force microviscosity increment, $(\Delta\eta_r(Pe_b)-\Delta\eta_r(\infty))/(\Delta\eta_r(0)-\Delta\eta_r(\infty))$, as a function of the non-dimensional external force, or Péclet number, $Pe_b$. (Recall that the microviscosity increment is defined

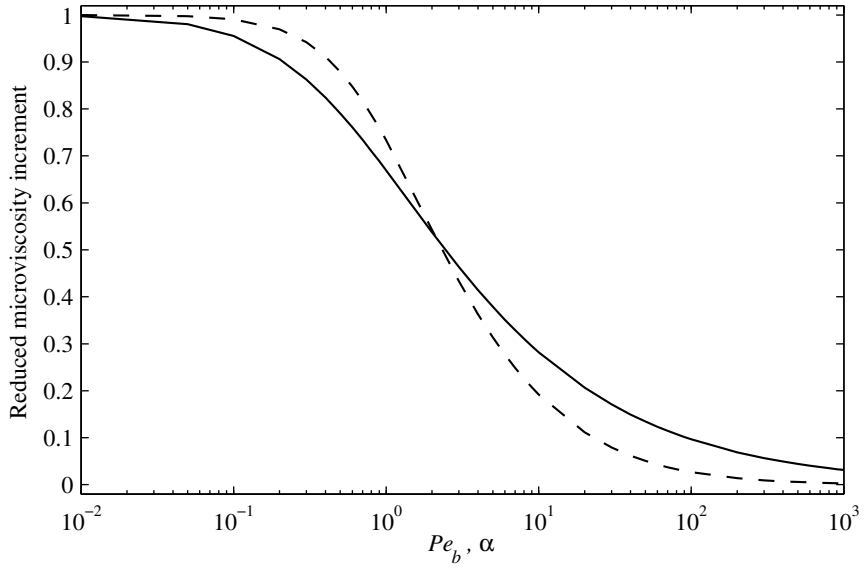


Figure 3.4: Cox-Merz relationship between the frequency $\omega$ and external force $\boldsymbol{F}^{ext}$ dependence of the relative microviscosity increment, $\Delta\eta_r = \eta_r - 1$. The reduced steady-force microviscosity increment, $(\Delta\eta_r(Pe_b) - \Delta\eta_r(\infty))/(\Delta\eta_r(0) - \Delta\eta_r(\infty))$, is plotted as a function of non-dimensional external force, or Péclet number, $Pe_b = F_0/(2kT/b)$ (broken line). The reduced complex microviscosity increment, $(|\Delta\eta_r(\alpha)| - |\Delta\eta_r(\infty)|)/(|\Delta\eta_r(0)| - |\Delta\eta_r(\infty)|)$, is plotted versus the dimensionless frequency, $\alpha = 6\pi\eta ab\omega/(2kT/b)$ (solid line). Hydrodynamic interactions are neglected.

as $\Delta\eta_r = \eta_r - 1$.) The data are taken from the analytical solution to the steady-state Smoluchowski equation derived by Squires and Brady (2005). In figure 3.4 we also show the reduced complex microviscosity increment, $(|\Delta\eta_r(\alpha)| - |\Delta\eta_r(\infty)|)/(|\Delta\eta_r(0)| - |\Delta\eta_r(\infty)|)$, versus the dimensionless frequency $\alpha$. The two curves are in good agreement over the entire range of $(\alpha, Pe_b)$, suggesting that the Cox-Merz rule is applicable to the microviscosity; whether, and how, this applicability holds when hydrodynamic interactions are included is discussed in the next section.

## 3.6 Microstructure & microrheology: Hydrodynamic interactions

In the absence of hydrodynamic interactions the microstructural evolution equation was solved exactly, which lead to an analytical expression for the complex microviscosity. Here, we wish to compute the complex microviscosity in the presence of hydrodynamic interactions over the entire range of $\hat{b} \equiv b/a \in [1, \infty)$. The inclusion of hydrodynamics entails a numerical solution of the Smoluchowski equation; we proceed by separating the structural deformation into real and imaginary parts: $f(s;\alpha) = f'(s;\alpha) + if''(s;\alpha)$. The functions $f'(s;\alpha)$ and $f''(s;\alpha)$ are real-valued and satisfy

$$\begin{aligned}
\frac{1}{s^2}\frac{d}{ds}\left(s^2 G(\hat{b}s)\frac{df'}{ds}\right) - \frac{2H(\hat{b}s)f'}{s^2} \quad &+ \quad \alpha f'' = -W(\hat{b}s), \\
\frac{1}{s^2}\frac{d}{ds}\left(s^2 G(\hat{b}s)\frac{df''}{ds}\right) - \frac{2H(\hat{b}s)f''}{s^2} \quad &- \quad \alpha f' = 0, \\
\frac{df'}{ds} = -1 \quad , \quad \frac{df''}{ds} = 0 \qquad &\text{at} \qquad s = 2, \\
f' \to 0 \quad , \quad f'' \to 0 \qquad &\text{as} \qquad s \to \infty.
\end{aligned}$$

This coupled system of equations is solved with the *MATLAB* program *bvp4c*, which implements a collocation method for the solution of general two-point boundary value problems. The mobility functions $G(\hat{b}s)$, $H(\hat{b}s)$, and $W(\hat{b}s)$ for $\hat{b}s > 2.01$ are computed via the twin multipole expansion of Jeffrey and Onishi (1984), whilst for $\hat{b}s < 2.01$ the lubrication theory results detailed in Kim and Karilla (1991) are used.

In figure 3.5 we plot the real part of the reduced complex microviscosity (3.15) as a function of dimensionless frequency $\alpha$ for $\hat{b} = 1.00001$, 1.01, 1.1, 1.5, and $\infty$. Qualitatively similar behavior is observed for each of the $\hat{b}$ values studied: the reduced microviscosity

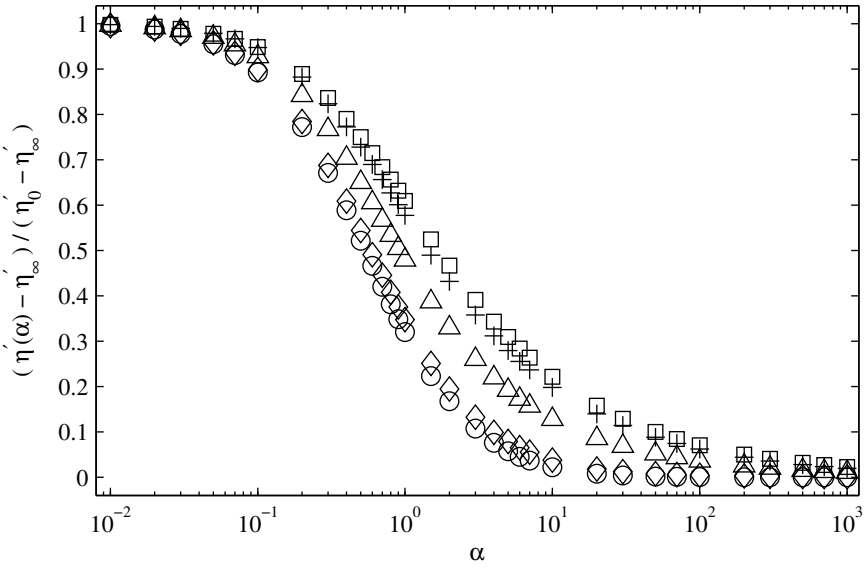


Figure 3.5: Real part of the reduced complex viscosity versus dimensionless frequency $\alpha$ for various $\hat{b} = b/a$: $\hat{b} = 1.00001$, $\circ$; $\hat{b} = 1.01$, $\diamond$; $\hat{b} = 1.1$, $\triangle$; $\hat{b} = 1.5$, $+$; and $\hat{b} \to \infty$, $\square$. Recall, $\hat{b}$ is the ratio of excluded-volume to hydrodynamic radii.

exhibits a low-frequency plateau at $\alpha = 0$, undergoes a regime of 'frequency-thinning' as $\alpha$ is increased, and asymptotes to zero as $\alpha \to \infty$. At high frequencies the motion of the probe does not perturb the dispersion from its equilibrium microstructure, and the only reduction in the probe's mobility, or increase in $\eta'$ above unity, is due to hydrodynamic interactions with the bath particles (which are in their equilibrium configuration). On the other hand, at low frequencies the motion of the probe does cause microstructural deformation to the dispersion, and in addition to hydrodynamic interactions with bath particles the probe's motion is retarded by the reactive Brownian/entropic force of the dispersion, which acts to heal the microstructural 'wound' caused by the probe. Therefore, the resistance to the probe's motion is greater at low frequencies than at high frequencies; consequently, the real part of the complex microviscosity decreases, or exhibits 'frequency-thinning', as the frequency of oscillation is increased.

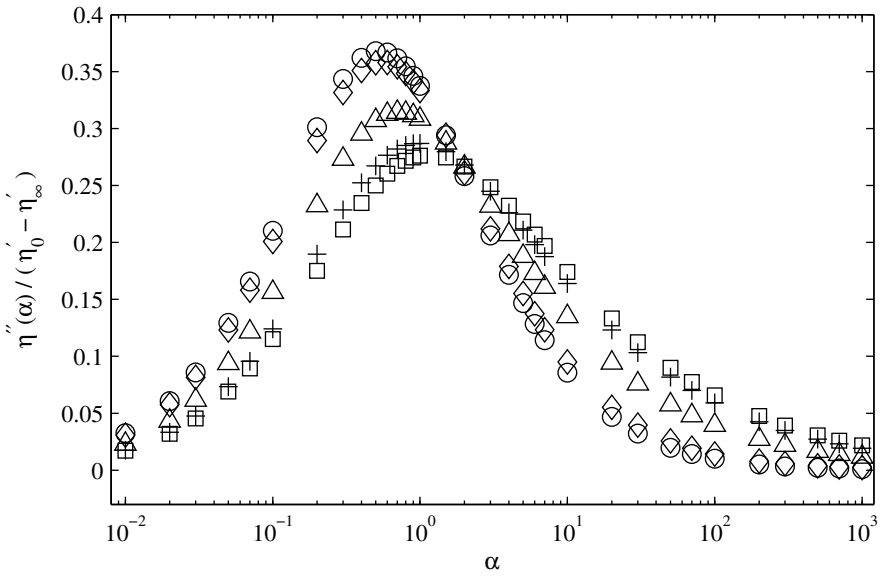


Figure 3.6: Imaginary part of the reduced complex viscosity versus dimensionless frequency $\alpha$ for various $\hat{b} = b/a$. The legend is the same as in figure 3.5.

Figure 3.6 plots the imaginary part of the reduced complex microviscosity (3.16) versus $\alpha$ for $\hat{b} = 1.00001$, 1.01, 1.1, 1.5, and $\infty$; again, qualitative agreement is seen between each of the $\hat{b}$ values displayed. Recall, the imaginary part of the microviscosity describes the elastic response of the dispersion, which is driven by microstructural deformations that are out of phase with the oscillatory forcing. In the limit of infinite-frequency forcing the microstructure is at equilibrium; hence, the imaginary microviscosity is zero. At low frequencies the microstructural deformation inflicted by the probe is predominantly in phase with the forcing; therefore, the imaginary microviscosity vanishes as $\alpha \to 0$. Between these high- and low-frequency limits the dispersion exhibits an elastic response, and the imaginary viscosity attains a maximum value, for all values of $\hat{b}$. The frequency at which the maximum in the imaginary microviscosity occurs, say $\alpha_{max}$, decreases monotonically as hydrodynamic interactions become more important: in the absence of hydrodynamics ($\hat{b} \to \infty$) $\alpha_{max} = 1.16$ and for full hydrodynamics ($\hat{b} = 1.00001 \approx 1$) $\alpha_{max} \approx 0.53$. Similarly,

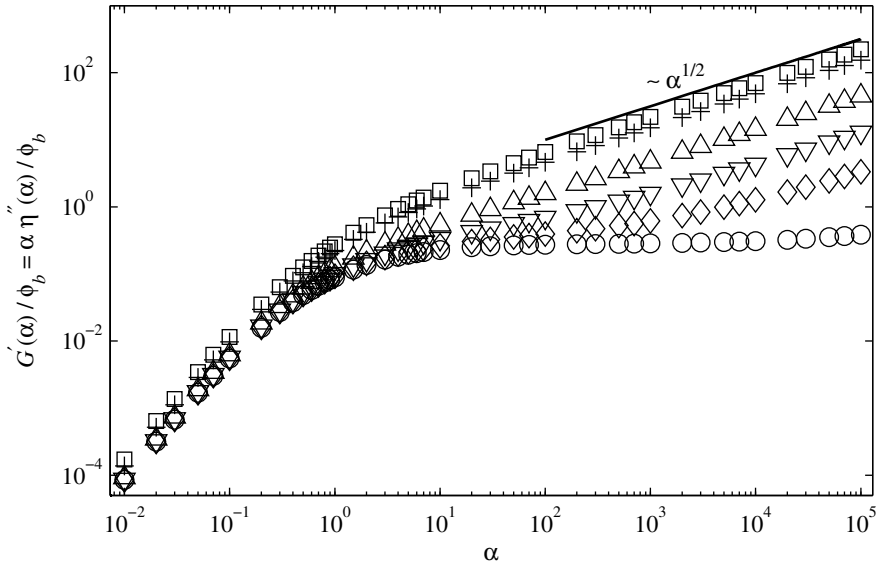


Figure 3.7: Elastic modulus $G'(\alpha)/\phi_b = \alpha\eta''(\alpha)/\phi_b$ versus dimensionless frequency $\alpha$ for various $\hat{b} = b/a$. The legend is the same as in figure 3.5, with the addition of $\bigtriangledown$ representing $\hat{b} = 1.03$.

the 'half-value' in the real part of the reduced microviscosity in figure 3.5 (defined as the frequency, $\alpha_{half}$, at which $(\eta'(\alpha_{half}) - \eta'_\infty)/(\eta'_0 - \eta'_\infty) = 1/2$) decreases monotonically as hydrodynamics become stronger: in the absence of hydrodynamics $\alpha_{half} = 1.69$ and for full hydrodynamics $\alpha_{half} \approx 0.53$. Importantly, both $\alpha_{max}$ and $\alpha_{half}$ are close to unity, for all values of $\hat{b}$. We shall return to this issue in § 3.8 where our theoretical calculations are compared to experimental data.

From the discussion above, one might be lead to believe that hydrodynamic interactions play only a quantitative role in the viscoelasticity of the dispersion; however, as we shall see below, this is not the case.

Further insight into the effect of hydrodynamic interactions on the viscoelasticity of the dispersion may be acquired by examination of the elastic modulus $G'(\alpha)$. Recall, in the absence of hydrodynamic interactions $G' \sim \alpha^{1/2}$ as $\alpha \to \infty$. In figure 3.7 the elastic

modulus is plotted as a function of $\alpha$ for $\hat{b} = 1.00001$, 1.01, 1.03, 1.1, 1.5, and $\infty$. With the exception of $\hat{b} = 1.00001$, it is seen that $G' \sim \alpha^{1/2}$ as $\alpha \to \infty$, for all values of $\hat{b}$ shown. To understand this behavior it is necessary to examine the high-frequency asymptotics of the Smoluchowski equation.

We proceed with a regular perturbation expansion of the structural deformation in inverse powers of $\alpha$. To leading order the Smoluchowski equation (3.11) reflects a balance between oscillatory forcing and advection, with the asymptotic solution $f \equiv F = -iW(\hat{b}s)/\alpha$. At large distances $W(\hat{b}s) \sim O(\hat{b}s)^{-5}$; thus, $F$ satisfies the zero deformation condition (3.13), but does not satisfy the no-flux boundary condition at contact (3.12). The perturbation about infinite frequency is singular: near contact there exists a boundary layer of $O(\alpha^{-1/2})$ in which (radial) Brownian diffusion balances unsteady effects. In appendix 3.A we show that in the boundary layer the structural deformation is

$$\begin{aligned} f(y;\alpha) &= \left(\frac{G_0}{i\alpha}\right)^{1/2} e^{-(i/G_0)^{1/2}y} + \frac{i}{4\alpha}\left(2G_0 + G_1\right)\left(1 + \left(\frac{i}{G_0}\right)^{1/2} y\right) e^{-(i/G_0)^{1/2}y} \\ &+ \frac{G_1}{4\alpha G_0} y^2 e^{-(i/G_0)^{1/2}y} - \frac{iW_0}{\alpha} + O(\alpha^{-3/2}), \end{aligned}$$

where $y = \alpha^{1/2}(s-2)$ is a boundary-layer coordinate, $G_0 = G(2\hat{b})$, $G_1 = dG/ds|_{2\hat{b}}$, and $W_0 = W(2\hat{b})$. As $y \to \infty$, $f \to -iW_0/\alpha$, which is precisely the inner limit of the outer solution $F = -iW(\hat{b}s)/\alpha$. After a little work (again, see Appendix 3.A for the details) the interparticle-force $G'_P$ and Brownian $G'_B$ contributions to the elastic modulus $G'$ are found as

$$\frac{G'_P}{\phi_b} = \left(2G_0^3\alpha\right)^{1/2} - G_0\left(G_0 + \frac{G_1}{2} - 2W_0\right) + O(\alpha^{-1/2}), \tag{3.21}$$

$$\frac{G'_B}{\phi_b} = 2W_0G_0 + \frac{1}{2}\int_2^\infty [W(\hat{b}s)]^2 s^2 ds + O(\alpha^{-1/2}). \tag{3.22}$$

The dominant contribution to the elastic modulus comes from $G'_P$, which diverges like $\alpha^{1/2}$ to leading order. The first term on the right-hand side of (3.22) is the contribution to $G'_B$ from the boundary layer, and the second term is the contribution from an integral over the 'outer' region, in which $f \equiv F = -iW(\hat{b}s)/\alpha$. The $\alpha^{1/2}$ divergence of $G'$ is clearly seen for all values of $\hat{b}$ shown in figure 3.7, with the exception of $\hat{b} = 1.00001$. To understand this we must examine the asymptotic formulae for $G'_P$ and $G'_B$ in the limit $\hat{b} \to 1$. For $\hat{b} \approx 1$ the mobility functions take the form $G_0 \approx 2(\hat{b}-1)$, $G_1 \approx 2$, and $W_0 \approx 1.598$, and the outer solution contribution to $G'_B$ is 0.264 (to three decimal places); thus, as $\hat{b} \to 1$ we have

$$\frac{G'_P}{\phi_b} \sim 4\left((\hat{b}-1)^3\alpha\right)^{1/2} - 2(\hat{b}-1)\left(2(\hat{b}-1) - 2.196\right) + O(\alpha^{-1/2}), \tag{3.23}$$

$$\frac{G'_B}{\phi_b} \sim 6.392(\hat{b}-1) + 0.264 + O(\alpha^{-1/2}). \tag{3.24}$$

From (3.23) we see that $G'_P \sim (4(\hat{b}-1)^3\alpha)^{1/2}$, i.e. whilst the $\alpha^{1/2}$ scaling persists its coefficient vanishes as $\hat{b} \to 1$; indeed, all the boundary-layer contributions to $G'$ vanish as $\hat{b} \to 1$, and the only finite contribution is from the integral over the outer solution in $G'_B$, which equals 0.264. Thus, for $\hat{b} \approx 1$ to observe an $\alpha^{1/2}$ divergence in $G'$ requires sampling frequencies much greater than the 'threshold frequency' $\alpha_t \approx 1/(\hat{b}-1)^3$. At frequencies below $\alpha_t$, for which the dominant contribution to $G'$ comes from the integral over the outer solution (which is independent of $\alpha$), one would (erroneously) conclude that $G'$ reaches a finite value as $\alpha \to \infty$; this behavior is seen in figure 3.7 for $\hat{b} = 1.00001$, in which case $\alpha_t \approx 10^{15}$, some ten decades greater in frequency than the largest numerical computation of $G'$ at $\alpha = 10^5$.

It is only in the special case of 'full hydrodynamics', where $G'_P \equiv 0$, that the elastic modulus attains a high-frequency plateau. When $\hat{b} \equiv 1$ the normal component of the relative

velocity between the probe and bath particle is zero at contact; consequently, the inner boundary condition on the Smoluchowski equation is $\hat{\boldsymbol{s}}\cdot\boldsymbol{D}\cdot\boldsymbol{\nabla}g=0$, and for small-amplitude forcing this implies $(s-2)df/ds=0$ at $s=2$. The outer solution of $f\equiv F=-iW(s)/\alpha$ is uniformly valid, i.e. it satisfies the boundary condition at $s=2$; hence, there is no boundary layer near contact. This is consistent with (3.23) and (3.24), which indicate that the boundary-layer contributions to $G'$ vanish as $\hat{b}\to 1$. The numerical value of the high-frequency plateau for $\hat{b}\equiv 1$, denoted as $G'_\infty$, is

$$G'_\infty=-\frac{\alpha\phi_b}{2}\int_2^\infty W(s)\Im f(s;\alpha)s^2ds=\frac{\phi_b}{2}\int_2^\infty [W(s)]^2s^2ds=0.264\phi_b.$$

Theoretical macrorheology studies by Brady (1993) and Lionberger and Russel (1994) find that the elastic modulus attains a high-frequency plateau for $\hat{b}\equiv 1$, in agreement with our results; in the absence of hydrodynamic interactions ($\hat{b}\to\infty$) they both observe that $G'$ grows like $\alpha^{1/2}$ as $\alpha\to\infty$, in accordance with the findings of § 3.5. Between these two limiting cases it is expected that the elastic modulus obtained from macrorheology should also diverge like $\alpha^{1/2}$ as $\alpha\to\infty$ (or, more precisely, for frequencies greater than a macrorheology threshold frequency analogous to $\alpha_t$) as per the microviscosity (3.23). However, at the present time, the numerical solution of the macrorheology Smoluchowski equation at finite $\hat{b}$ has yet to be determined.

The divergence of $G'$ as $\alpha\to\infty$ originates from the excluded-annulus model of interparticle-force interactions, which implements a hard-sphere repulsion between the probe and a bath particle, acting at a distance $b$ greater than the true radius $a$ of the probe. If the colloidal particles experience a *soft* interparticle-force interaction Brady (1993) has shown that the elastic modulus determined from macrorheology attains a high-frequency plateau. One

should observe an analogous plateau in the microrheological elastic modulus, although we leave this for future study. Finally, we note the implications for self-diffusivity: for full hydrodynamics the $1/\alpha$ decay of $f(y;\alpha)$ predicts a short-time temporal response proportional to $t$.

In § 3.5 (see also figure 3.4) we demonstrated that in the absence of hydrodynamic interactions the microviscosity obeys, to a good degree, the Cox-Merz rule. (Recall, the Cox-Merz rule states $\eta(\boldsymbol{F}^{ext}) = |\eta(\omega)|$, where $\eta(\boldsymbol{F}^{ext})$ is the *nonlinear* microviscosity obtained from a steady-force experiment, and $|\eta(\omega)|$ is the *linear* microviscosity from an small-amplitude, oscillatory-force experiment.) In the presence of hydrodynamic interactions the application of the Cox-Merz rule needs to be modified. In steady-force microrheology the microviscosity increment, $\Delta\eta_r = \eta_r - 1$, is a sum of hydrodynamic, Brownian, and interparticle-force contributions: the hydrodynamic contribution is a monotonically increasing function of the non-dimensional force (or Péclet number, $Pe_b$), whilst the Brownian and interparticle-force contributions are monotonically decreasing functions of $Pe_b$ (Khair and Brady 2006). If hydrodynamic interactions are sufficiently strong, i.e. $\hat{b} \approx 1$, the increase in the hydrodynamic contribution outweighs the decrease in the Brownian and interparticle-force contributions, and the microviscosity 'force-thickens', in analogy to macrorheological shear-thickening, at large $Pe_b$. For small-amplitude oscillatory-force experiments the microviscosity increment is again comprised of hydrodynamic, Brownian, and interparticle-force constituents; however, the hydrodynamic contribution, to leading order in the oscillation amplitude $Pe_b$, is not a function of the oscillation frequency and merely sets the bath particle contribution to the high-frequency dynamic microviscosity. The Brownian and interparticle-force microviscosity contributions are, of course, frequency-dependent. Therefore, when hydrodynamic interactions are present the Cox-Merz is understood to mean $\eta_T(\boldsymbol{F}^{ext}) = |\eta_T(\omega)|$, where the

subscript $T$ denotes the *thermodynamic* (i.e. Brownian plus interparticle-force) contribution to the microviscosity.

One can measure $\eta_T$ via so-called stress-jump (or flow-cessation) experiments. In macrorheological stress-jump experiments the dispersion is sheared at a constant rate until a steady-state microstructure is attained (in which the colloidal particles are subject to hydrodynamic and thermodynamic forces), and the shear is then stopped suddenly: the hydrodynamic contribution to the macroviscosity vanishes instantly, allowing one to isolate the thermodynamic contribution $\eta_T$ (which decays on the diffusive microstructural relaxation time scale). It is possible to formulate a microrheological analog of the stress-jump experiment (as discussed in § 3.9), so that one may verify the Cox-Merz relationship with experimental microviscosity data.

In figure 3.8 we plot the reduced steady-force microviscosity increment, $(\Delta_T\eta_r(Pe_b) - \Delta_T\eta_r(\infty))/(\Delta_T\eta_r(0) - \Delta_T\eta_r(\infty))$, as a function of $Pe_b$; here, $\Delta_T\eta_r(Pe_b) = \eta_r(Pe_b) - (1 + \eta_H(Pe_b))$ is the thermodynamic contribution to the microviscosity increment. The data are taken from the numerical solution of the Smoluchowski equation by Khair and Brady (2006). The reduced complex microviscosity increment, $(|\Delta_T\eta_r(\alpha)| - |\Delta_T\eta_r(\infty)|)/(|\Delta_T\eta_r(0)| - |\Delta_T\eta_r(\infty)|)$, is also plotted in figure 3.8, versus the dimensionless frequency $\alpha$. For both sets of data $\hat{b} = 1.00001$. Reasonable agreement (the half-value, $\alpha_{half}$, of the steady-force increment is approximately three times that of the complex increment) between the steady-force microviscosity increment and the complex microviscosity increment is observed over the entire range of $(\alpha, Pe_b)$, indicating that the Cox-Merz rule may be applicable to the (thermodynamic contribution of the) microviscosity when hydrodynamic interactions are present.

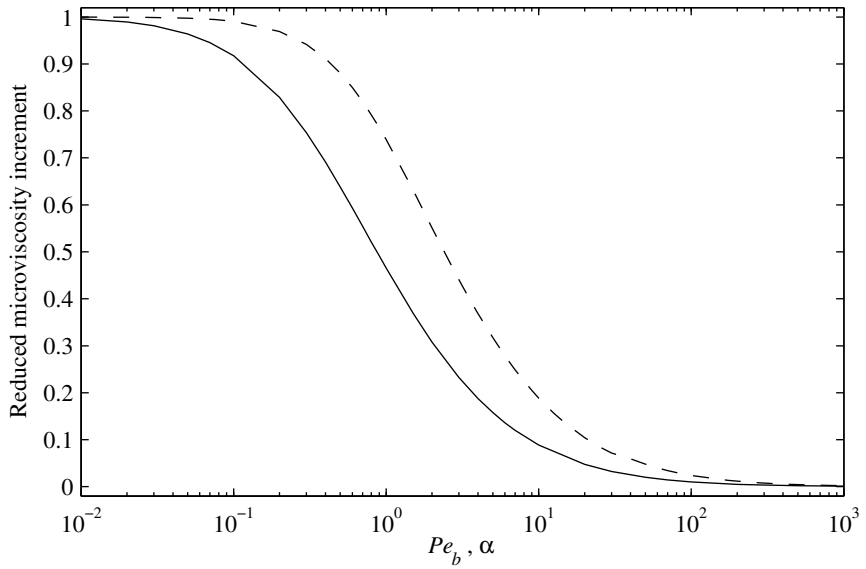


Figure 3.8: Cox-Merz relationship between the frequency $\omega$ and external force $\boldsymbol{F}^{ext}$ dependence of the relative microviscosity increment, $\Delta_T\eta_r = \eta_r - (1+\eta_H)$. The reduced steady-force microviscosity increment, $(\Delta_T\eta_r(Pe_b) - \Delta_T\eta_r(\infty))/(\Delta_T\eta_r(0) - \Delta_T\eta_r(\infty))$, is plotted as a function of non-dimensional external force, or Péclet number, $Pe_b = F_0/(2kT/b)$ (broken line). The reduced complex microviscosity increment, $(|\Delta_T\eta_r(\alpha)| - |\Delta_T\eta_r(\infty)|)/(|\Delta_T\eta_r(0)| - |\Delta_T\eta_r(\infty)|)$, is plotted versus the dimensionless frequency, $\alpha = 6\pi\eta ab\omega/(2kT/b)$ (solid line). For both sets of data $\hat{b} \equiv b/a = 1.00001$.

## 3.7 Scale-up of results to more concentrated dispersions

The results presented in previous sections are valid for *dilute* dispersions, for which the volume fraction of bath particles is small compared to unity. Here, using simple, intuitive arguments, we scale-up our findings to more concentrated systems. Squires and Brady (2005) have conducted a thorough scaling analysis of the nonlinear microviscosity calculated from steady probe motion (at fixed force or fixed velocity); we tailor their analysis of the small-amplitude fixed-force regime to our problem of oscillatory motion.

Firstly, note that two quantities need to be scaled: the microviscosity, $\eta_r$, and the oscillation frequency, $\omega$. In § 3.4 it was demonstrated that the transition from low- to high-frequency microviscosity is equivalent to the transition from long- to short-time self-

diffusivity. The self-diffusivity transition may be expressed in dimensional form as (Cichocki and Felderhof 1991)

$$D^s_\infty - D^s_0 = \frac{1}{3}\int_0^\infty \langle \boldsymbol{v}(t)\cdot\boldsymbol{v}(0)\rangle dt,$$

where $\langle \boldsymbol{v}(t)\cdot\boldsymbol{v}(0)\rangle$ is the velocity autocorrelation function. Here, $\langle\cdots\rangle$ denotes an ensemble average over all particles in the dispersion and $\boldsymbol{v}(t)$ is the regular part of the velocity of a 'tagged' particle (that is, only the part which fluctuates due to microstructural fluctuations caused by Brownian motion) measured on the diffusive, or Smoluchowski, time scale $b^2/D$. The 'relaxation' time scale characterizing the self-diffusivity transition is simply defined by

$$\tau_D(\phi_b) = \frac{\int_0^\infty \langle t\boldsymbol{v}(t)\cdot\boldsymbol{v}(0)\rangle dt}{\int_0^\infty \langle \boldsymbol{v}(t)\cdot\boldsymbol{v}(0)\rangle dt}.$$

We define a dimensionless oscillation frequency $\alpha^*(\phi_b) = \omega\tau_D(\phi_b)$. In the dilute limit, $\phi_b \ll 1$, and in the absence of hydrodynamic interactions, $\hat{b} \to \infty$, Cichocki and Felderhof (1993) calculate $D\tau_D/b^2 = 1$. Therefore, $\alpha^*(\phi_b \ll 1) = 2\times(\omega b^2/2D)$, which is a factor of two greater than our 'naive' scaling of $\alpha = \omega b^2/2D$ (see equation (3.2)). Little appears to be known about the behavior of $\tau_D$ beyond the dilute limit. The Brownian Dynamics (BD) simulations of Cichocki and Hinsen (1992) suggest that $D\tau_D/b^2$ decreases with increasing $\phi_b$ until $\phi_b \approx 0.46$, where it attains a minimum value of $D\tau_D/b^2 \approx 0.06$, and then increases. Unfortunately, Cichocki and Hinsen (1992) do not present data beyond $\phi_b = 0.50$, and it is not known how $\tau_D$ behaves as the limit of random close packing, $\phi_m \approx 0.63$, is approached. Intuitively, one would expect that $\tau_D$ diverges as $\phi_b \to \phi_m$: a particle becomes trapped in a 'cage' formed by other particles and can only escape the cage (and hence lose correlation with its initial velocity) on times much larger than $b^2/D$. With full hydrodynamic interactions, $\hat{b} = 1$, all that is known about $\tau_D$, to our knowledge, is the dilute-limit result $D\tau_D/b^2 = 1.868$

(Cichocki and Felderhof 1993). In § 3.8, where our theoretical calculations are compared to experimental micro- and macro-viscosity data, we propose a simple model for the volume fraction dependence of $\tau_D$.

Finally, the microviscosity itself must be scaled, or, more precisely, the contribution to the microviscosity arising from microstructural deformations $\Delta\eta \equiv \eta_r - \eta'_\infty$ (recall, the high-frequency dynamic microviscosity $\eta'_\infty$ is a function of the equilibrium microstructure). As mentioned above, for small-amplitude forcing the average velocity of the probe is proportional to the long-time self-diffusivity; thus, the appropriate scale for $\Delta\eta$ is $D/D^s_\infty$. Brady (1994) has shown that the long-time self-diffusivity may be approximated as $D^s_\infty = D^s_0 \times \hat{D}^{s,nohydro}_\infty$, where $\hat{D}^{s,nohydro}_\infty$ is the dimensionless long-time self-diffusivity in the absence of hydrodynamic interactions; furthermore, Brady (1994) notes that $\hat{D}^{s,nohydro}_\infty$ scales approximately like $1/\phi_b g_{eq}(2;\phi_b)$, where $g_{eq}(2;\phi_b)$ is the contact-value of the equilibrium pair-distribution function (which may be obtained from the Carnahan-Starling equation of state).

Putting this together suggests the microviscosity to scale like

$$\Delta\eta \sim \frac{D}{D^s_\infty}\Upsilon(\alpha^*;\hat{b}) \approx \frac{\phi_b g_{eq}(2;\phi_b)}{D^s_0/D}\Upsilon(\alpha^*;\hat{b}),$$

where the dimensionless (complex) function $\Upsilon(\alpha^*;\hat{b})$ details the frequency response for a particular value of $\hat{b}$. Interestingly, starting from the $N$-particle Smoluchowski equation, Brady (1993) demonstrates that the macroviscosity scales in the same manner as the microviscosity (aside from an extra factor of $\phi_b$ for the macroviscosity).

## 3.8 Comparison with experimental data

In § 3.5 (see also figures 3.2 and 3.3) we showed in the dilute limit and in the absence of hydrodynamic interactions that the complex microviscosity compares favorably with the complex macroviscosity over the entire range of oscillation frequencies. Here, with the aid of the scaling arguements developed in § 3.7, we compare our microviscosity results to experimental micro- and macro-viscosity data for concentrated dispersions.

The appropriate time scale for macroviscoelastic response arises from consideration of the transition from low- to high-frequency macroviscosity, which is given by the following dimensional Green-Kubo formula (Nägele and Bergenholtz 1998)

$$\eta_0' - \eta_\infty' = \frac{V}{kT}\int_0^\infty \langle \sigma_{xy}^T(t)\sigma_{xy}^T(0)\rangle dt,$$

where $V$ is the volume, $\langle \sigma_{xy}^T(t)\sigma_{xy}^T(0)\rangle$ is the shear stress autocorrelation function, and $\sigma_{xy}^T(t)$ denotes the instantaneous thermodynamic shear stress (due to interparticle-forces and/or Brownian diffusion) arising from fluctuations in the dispersion microstructure about its equilibrium configuration. (The subscript $xy$ is used for definiteness, but since there is no preferred direction at equilibrium we could have used $xz$ or $yz$.) In analogy to $\tau_D$, we define a macroviscosity relaxation time

$$\tau_\eta(\phi_b) = \frac{\int_0^\infty \langle t\sigma_{xy}^T(t)\sigma_{xy}^T(0)\rangle dt}{\int_0^\infty \langle \sigma_{xy}^T(t)\sigma_{xy}^T(0)\rangle dt}.$$

In the dilute limit and in the absence of hydrodynamic interactions $D\tau_\eta/b^2 = 2/9$ (Cichocki and Felderhof 1993). For higher concentrations much more is known about $\tau_\eta$ as compared to $\tau_D$. The mode coupling theory (MCT) calculations of Banchio et al. (1999)

show that $\tau_\eta$ decreases on increasing $\phi_b$ (MCT predicts $D\tau_\eta/b^2 = 0.19$ in the dilute limit) until $\phi_b \approx 0.3$, at which point it attains a minimum of $D\tau_\eta/b^2 \approx 0.08$. This initial decrease in $\tau_\eta$ is due to the increasing number of collisions as $\phi_b$ increases past the dilute limit, which leads to faster relaxation of the shear stress. Beyond $\phi_b \approx 0.3$, $\tau_\eta$ increases and diverges in the limit $\phi_b \to \phi_m$. In analogy to $\tau_D$, the increase in $\tau_\eta$ for $\phi_b > 0.3$ is due to the caging of particles in concentrated dispersions, which leads to a slower relaxation of the shear stress. The MCT description of $\tau_\eta$ as a function of $\phi_b$ is confirmed by the BD study of Foss and Brady (2000); interestingly, both Foss and Brady (2000) and Banchio et al. (1999) find that the product $D_\infty^{s,nohydro}(\phi_b)\tau_\eta(\phi_b)/b^2$ is approximately constant over a wide range of $\phi_b$. In particular, $\tau_\eta(\phi_b)$ scales like $b^2/D_\infty^{s,nohydro}(\phi_b)$ as $\phi_b \to \phi_m$ (here, $D_\infty^{s,nohydro} = D \times \hat{D}_\infty^{s,nohydro}$ is the dimensional long-time self-diffusivity in the absence of hydrodynamic interactions).

With full hydrodynamic interactions and in the dilute limit $D\tau_\eta/b^2 = 0.4892$ (Cichocki and Felderhof 1993), which is approximately double the value of $D\tau_\eta/b^2$ in the absence of hydrodynamic interactions. Beyond the dilute limit nothing, to our knowledge, is known theoretically about $\tau_\eta$ in the presence of hydrodynamic interactions, although Van der Werff et al. (1989) have measured this quantity experimentally. The 'simplest' way to account for the effect of hydrodynamic interactions on $\tau_\eta$ (and, for that matter, $\tau_D$) is in an averaged, or mean-field like, approach by replacing the solvent viscosity with the high-frequency dynamic macroviscosity: it is as if two particles are in a suspending fluid of effective viscosity $\eta'_\infty$. As the high-frequency dynamic macroviscosity is inversely proportional to the short-time self-diffusivity (Brady 1994) one may equivalently multiply $D_\infty^{s,nohydro}$ by $D_0^s/D$; thus, in the presence of hydrodynamic interactions we propose that $\tau_\eta(\phi_b)$ scales like $b^2/D_\infty^s(\phi_b)$, where $D_\infty^s = D_0^s \times \hat{D}_\infty^{s,nohydro}$ is the long-time self-diffusivity in the presence of hydrodynamic interactions. To test the accuracy of this assumption one could calculate $\tau_\eta$ from Stokesian

| | System | Method |
|---|---|---|
| Van der Werff et al. (1989) | Silica particles sterically stabilized by octadecyl chains in cyclohexane. | Torsion pendulum and Nickel-tube resonator. |
| Shikata and Pearson (1994) | Silica particles in ethylene glycol (EG) or EG/glycerin mixture. | Concentric-cylinder and cone-and-plate rheometers with time-temperature superposition of data. |
| Sohn and Rajagopalan (2004) | Silica probes in a dispersion comprised of PMMA particles in cycloheptyl alcohol. | Dynamic light scattering to measure mean-squared displacement of probes. Infer complex modulus through generalized Stokes-Einstein-Sutherland relation. |

Table 3.1: Brief description of the experimental investigations discussed in § 3.8.

Dynamics simulations of Brownian dispersions at equilibrium.

Therefore, for the macroviscosity we define a dimensionless frequency $\alpha^*_{macro}(\phi_b) = \omega\tau_\eta(\phi_b) = \lambda_\eta\omega b^2/2D^s_\infty(\phi_b)$, where $\lambda_\eta$ is the value of ratio $2D^s_\infty(\phi_b)\tau_\eta(\phi_b)/b^2$ (which according to Banchio et al. 1999 and Foss and Brady 2000 is a constant over a wide range of $\phi_b$, at least in the absence of hydrodynamic interactions). Likewise, we assume that $\tau_D$ also scales as $b^2/D^s_\infty$ and write the dimensionless frequency for the microviscosity as $\alpha^*_{micro}(\phi_b) = \omega\tau_D(\phi_b) = \lambda_D\omega b^2/2D^s_\infty(\phi_b)$, where $\lambda_D$ is the value of the ratio $2D^s_\infty(\phi_b)\tau_D(\phi_b)/b^2$.

The BD simulations of Foss and Brady (2000) (see their table 1) suggest that $\lambda_\eta \approx 0.1$ in the absence of hydrodynamic interactions; however there is no reason to believe that this value of $\lambda_\eta$ holds in the presence of hydrodynamic interactions. Furthermore, from the results of Cichocki and Hinsen (1992) it is not possible to obtain a reliable value of $\lambda_D$, even in the absence of hydrodynamic interactions. Therefore, due to lack of available data and in the interests of consistency, we shall simply take $\lambda_\eta = \lambda_D = 1$, knowing full well that these are overestimates. Hence, $\alpha^*_{micro} = \alpha^*_{macro} = \omega b^2/2D^s_\infty$. For the long-time self-diffusivity

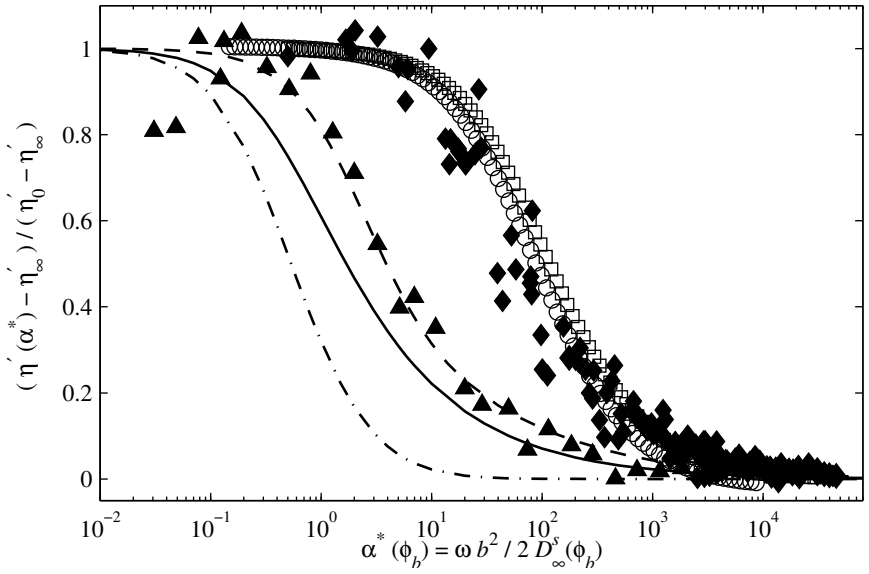


Figure 3.9: Comparison of theoretical calculations and experimental data for the real part of the reduced complex viscosity, $(\eta'(\alpha^*) - \eta'_\infty)/(\eta'_0 - \eta'_\infty)$, versus dimensionless frequency $\alpha^*(\phi_b) = \omega b^2/2D^s_\infty(\phi_b)$. Experimental data: filled triangles are the macroviscosity data of Shikata and Pearson (1994) ($\phi_b = 0.37$); filled diamonds are the macroviscosity data of Van der Werff et al. (1989) ($\phi_b = 0.42 \rightarrow 0.58$); and the unfilled circles ($\phi_b = 0.37$) and unfilled squares ($\phi_b = 0.44$) are the microviscosity data of Sohn and Rajagopalan (2004). Theoretical calculations: solid line is the microviscosity in the absence of hydrodynamic interactions ($\hat{b} \rightarrow \infty$); dot-dashed line is the microviscosity for full hydrodynamic interactions ($\hat{b} = 1.00001 \approx 1$); and the dashed line is the macroviscosity in the absence of hydrodynamic interactions (from Brady 1993).

we shall use the following simple analytical estimate derived by Brady (1994)

$$D^s_\infty(\phi_b) = D^s_0(\phi_b)[1 + 2\phi_b g_{eq}(2;\phi_b)]^{-1}, \tag{3.25}$$

which is in good agreement with experimental data over a wide range of $\phi_b$ (see figures 2 and 3 of Brady 1994).

In figures 3.9 and 3.10 we compare our theoretical microviscosity calculations (for full hydrodynamics, $\hat{b} = 1.00001 \approx 1$, and no hydrodynamics, $\hat{b} \rightarrow \infty$) to the experimental microviscosity data of Sohn and Rajagopalan (2004) and the experimental macroviscosity

data of Van der Werff et al. (1989) and Shikata and Pearson (1994) (see table 3.1 for a brief description of each experimental study). Figure 3.9 plots the real part of the reduced viscosity, $(\eta'(\alpha^*)-\eta'_\infty)/(\eta'_0-\eta'_\infty)$, versus dimensionless frequency, $\alpha^* = \omega b^2/2D^s_\infty$. Although the shape of each experimental reduced viscosity data set as a function of $\alpha^*$ is in qualitative agreement with our theoretical microviscosity calculations, the experimental data are shifted to higher $\alpha^*$ as compared to the theoretical curves: for the data of Van der Werff et al. (1989) and Sohn and Rajagopalan (2004) the shift is by approximately two decades in $\alpha^*$. One should, however, not be alarmed by this shift of the experimental data since in the comparison, due to the lack of available data, we took $\lambda_\eta = \lambda_D = 1$. Van der Werff et al. (1989) observe that $G'(\omega) \sim \omega^{1/2}$ at high frequencies, which indicates that short-range hydrodynamic lubrication interactions may not be important in their dispersions; the BD simulations of Foss and Brady (2000) suggest that $\lambda_\eta \approx 0.1$, which would shift the data of Van der Werff et al. (1989) a decade lower in $\alpha^*$, as compared to figure 3.9. Furthermore, if lubrication interactions are not present the simple formula (3.25) underestimates the long-time self-diffusivity, and this may also contribute to the discrepancy between their data and the theoretical curves. Similarly, before drawing conclusions concerning the comparison of our microviscosity calculations with the data of Shikata and Pearson (1994) and Sohn and Rajagopalan (2004), which both exhibit a high-frequency plateau in the elastic modulus, one needs to calculate $\lambda_\eta$ and $\lambda_D$ in the presence of full hydrodynamic interactions. Additionally, Sohn and Rajagopalan (2004) used probe particles approximately twice as large as their bath particles; therefore, properly, one should define a dimensionless frequency for their data as $\omega b^2/D^r_\infty$, where $D^r_\infty$ is the long-time relative diffusivity, rather than $\omega b^2/D^s_\infty$. Whilst $D^r_\infty$ and $D^s_\infty$ should share the same dependence on bath particle concentration, $D^r_\infty$ is also a function of the ratio of probe size to bath particle size. Furthermore, the theoretical

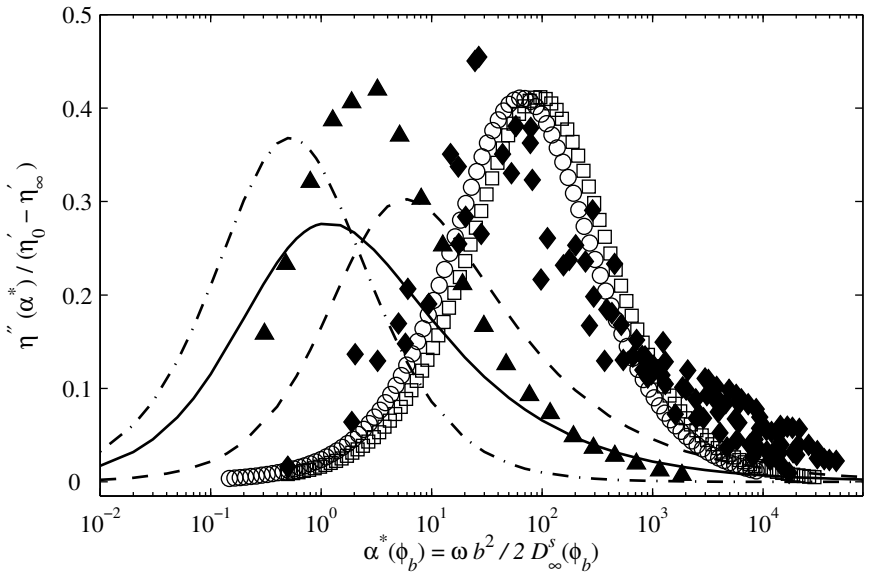


Figure 3.10: Comparison of theoretical calculations and experimental data for the imaginary part of the reduced complex viscosity, $\eta''(\alpha^*)/(\eta_0' - \eta_\infty')$, versus dimensionless frequency $\alpha^*(\phi_b) = \omega b^2/2D_\infty^s(\phi_b)$. The legend is the same as in figure 3.9.

microviscosity curves are for probe and bath particles of equal size; although the qualitative nature of the reduced microviscosity as a function of $\alpha^*$ should not be altered by a disparity in probe and bath particle sizes (provided that the ratio of sizes is neither much larger nor much smaller than unity) there will, nevertheless, be quantitative differences.

Figure 3.10 plots the imaginary part of the reduced viscosity, $\eta''(\alpha^*)/(\eta_0' - \eta_\infty')$, versus dimensionless frequency, $\alpha^* = \omega b^2/2D_\infty^s$. Again, whilst the shape of each experimental data set is in qualitative agreement with the theoretical predictions, they are shifted to higher $\alpha^*$, for the reasons explained above. Lastly, we note that the theoretical curves have $\alpha^*_{max}$ (the frequency at which the maximum in the imaginary reduced viscosity occurs) and $\alpha^*_{half}$ (the frequency at which the half-value in the real reduced viscosity occurs) approximately equal to unity. The experimental data should also, which suggests that $\lambda_\eta \approx \lambda_D \approx 0.01$.

Rather than the quantitative comparison shown in figures 3.9 and 3.10 the discussion

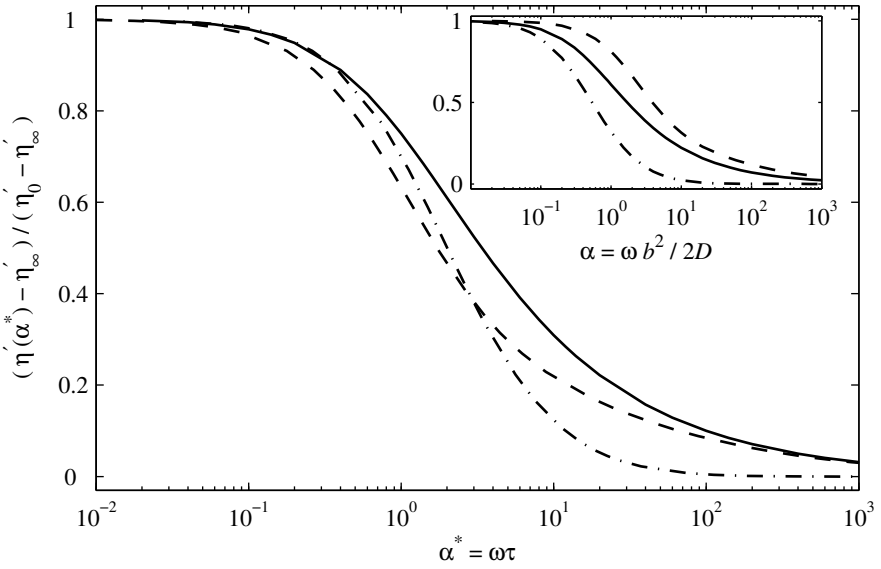


Figure 3.11: Real part of the reduced complex viscosity versus dimensionless 'rescaled' frequency $\alpha^* = \omega\tau$: the solid line is the microviscosity in the absence of hydrodynamic interactions ($\hat{b} \to \infty$), for which $\alpha^* = \omega\tau_D = 2 \times (\omega b^2/2D)$; the dot-dashed line is the microviscosity for full hydrodynamic interactions ($\hat{b} = 1.00001 \approx 1$), for which $\alpha^* = \omega\tau_D = 3.736 \times (\omega b^2/2D)$; and the dashed line is the macroviscosity in the absence of hydrodynamic interactions (from Brady 1993), for which $\alpha^* = \omega\tau_\eta = (4/9) \times (\omega b^2/2D)$. The inset displays the same three sets of viscosity data plotted against the dimensionless 'bare' frequency $\alpha = \omega b^2/2D$.

above is perhaps more valuable in *identifying* $\tau_D$ and $\tau_\eta$ as the appropriate, and distinct, relaxation time scales for micro- and macro-viscoelastic response, respectively. To make a 'true' comparison between micro- and macro-viscoelastic data requires calculation of $\tau_D$ and $\tau_\eta$ as a function of volume fraction, both with and without hydrodynamic interactions. Nonetheless, we can illustrate the importance of the disparity in micro- and macro-viscoelastic relaxation time scales by considering the dilute limit, $\phi_b \ll 1$, in which $\tau_D$ and $\tau_\eta$ are known (Cichocki and Felderhof 1993). In figure 3.11 we plot the real part of the reduced viscosity, $(\eta'(\alpha^*) - \eta'_\infty)/(\eta'_0 - \eta'_\infty)$, versus the 'rescaled' dimensionless frequency $\alpha^* = \omega\tau$ for three cases: (i) microviscosity in the absence of hydrodynamic interactions ($\hat{b} \to \infty$), for which $\tau = \tau_D = 2 \times (\omega b^2/2D)$; (ii) microviscosity with full hydrodynamic

interactions ($\hat{b} = 1.00001 \approx 1$), for which $\tau = \tau_D = 3.736 \times (\omega b^2/2D)$; and (iii) macroviscosity in the absence of hydrodynamic interactions, for which $\tau = \tau_\eta = (4/9) \times (\omega b^2/2D)$. Plotting the three viscosity curves versus the rescaled frequency is seen to collapse them quite well at low frequencies ($\alpha^* \leq 1$), as can be appreciated by comparing to the inset of figure 3.11, which displays the same three curves as a function of the 'bare' dimensionless frequency $\alpha = \omega b^2/2D$. However, the collapse of the three curves fails for $\alpha^* = \omega\tau \gg 1$, where the reduced microviscosity with full hydrodynamics decays to zero faster than the micro- and macro-viscosities in the absence of hydrodynamic interactions (which both decay like $(\alpha^*)^{-1/2}$). This is indicative of the fundamental influence of hydrodynamic interactions and interparticle-forces on the high-frequency viscoelasticity of colloidal dispersions: without hydrodynamics the hard-sphere-like interparticle force sets up a boundary layer adjacent to the probe (in which oscillatory forcing balances Brownian diffusion), and it is the microstructural deformation inside the boundary layer that determines the viscoelastic response, whilst with full hydrodynamic interactions there is no such boundary layer as the hard-sphere interparticle-force plays no dynamical role (the rigidity of the particles is realized by the vanishing relative radial mobility of two particles at contact).

## 3.9 Discussion

The last decade has witnessed the emergence of a new paradigm in rheology: the interrogation of complex fluids at the microscopic scale. In that spirit, the work presented here offers a perspective on the viscoelasticity of colloidal dispersions from a microscale viewpoint (or, as we call it, the 'microviscoelasticity' of colloidal dispersions). As a model system, the small-amplitude oscillatory motion of an externally forced probe particle in a quiescent colloidal dispersion (consisting of monodisperse hard-spheres suspended in a Newtonian fluid)

was investigated. By calculating the average velocity of the probe it was possible to infer the (complex) microviscosity of the dispersion, through application of Stokes drag law. The hard-sphere colloidal dispersion is perhaps the simplest of complex fluids, yet we have shown it exhibits significantly non-trivial microviscoelastic response. However, a criticism often leveled at microrheology is that the results from a single particle tracking experiment may bear little resemblance to the macroscopic, or 'true', properties of the material; indeed, two-point microrheology (Crocker et al. 2000), which cross-correlates the fluctuating motion of two distant probes, was designed to provide an accurate description of the rheology of microscopically heterogeneous materials. It is encouraging then that our microviscosity is in qualitative agreement with the shear-viscosity or 'macroviscosity' from macrorheology studies (see figures 3.2 and 3.3), at least in the absence of hydrodynamic interactions. However, as noted in § 3.5, the micro- and macro-viscosity scale differently with the bath particle volume fraction $\phi_b$: the microstructurally-dependent contributions to the micro- and macro-viscosity are $O(\phi_b)$ and $O(\phi_b^2)$, respectively. It is only through knowledge of these scalings that one can compare the micro- and macro-viscosity in a meaningful and consistent manner. For more complex (or unknown) materials, where such scalings may not be known *a priori*, micro- and macro-rheological measurements should not be expected to be in agreement in general. Nevertheless, as discussed in § 3.1, differences between micro- and macro-rheological data originate from the fundamentally different physical mechanisms the two methods employ to probe materials. Thus, any disagreement between the micro- and macro-rheological results should not devalue the microrheological data. Indeed, it should act as a spur to develop theoretical microrheology models to decipher the *additional* information encoded in the disparity between the micro- and macro-rheological measurements.

It would be interesting to see if the qualitative similarities between microviscosity and

macroviscosity persists when hydrodynamic interactions are considered, i.e. over the entire range of $\hat{b}$. It is not possible to make this comparison at the present time as the complex macroviscosity has only been computed for the limiting cases of $\hat{b} \to \infty$ (for all $\omega$, Brady 1993) and $\hat{b} \equiv 1$ (for $\omega \gg 1$, Brady 1993; Lionberger and Russel 1994). Nevertheless, Khair and Brady (2006) demonstrate, in the presence of hydrodynamic interactions, that the nonlinear microviscosity and nonlinear macroviscosity are qualitatively similar functions of the Péclet number; consequently, (by our verification of the Cox-Merz rule in § 3.6) we expect the frequency dependence of the complex macroviscosity and complex microviscosity to be in qualitative agreement when hydrodynamic interactions are present.

A significant portion of this work was devoted to elucidating the behavior of the elastic modulus in the limit of high-frequency oscillations. It was found that the elastic modulus diverges like $\omega^{1/2}$ as $\omega \to \infty$ for particles experiencing hard-sphere interparticle-force interactions, regardless of at what distance the interaction occurs (i.e. for all $b/a > 1$). On the other hand, in the absence of hard-sphere interparticle forces ($b/a \equiv 1$) the effect of hydrodynamic interactions yields an elastic modulus that is finite as $\omega \to \infty$. These conclusions agree with the macrorheology studies of Brady (1993) and Lionberger and Russel (1994); furthermore, Brady (1993) and Lionberger and Russel (1994) suggest that dispersions in which the particles experience soft interparticle-force interactions exhibit a high-frequency plateau in the elastic modulus. The two-body Smoluchowski formulation may easily be extended to more specific, or realistic, interparticle-force laws, making it possible to test the claims of Brady (1993) and Lionberger and Russel (1994), from a microrheological viewpoint. As a first step it would be prudent to consider the microstructural evolution problem in the absence of hydrodynamic interactions: in order to isolate the effect of a particular interparticle-force law on microstructural deformation.

With the exception of the *a posteriori* scaling analysis in § 3.7 and comparison with experimental data in § 3.8, the dispersion was assumed to be dilute. One possible approach in modeling more concentrated systems is to introduce conditionally averaged hydrodynamic interactions within the framework of the two-body Smoluchowski equation. Although relatively straightforward from a technical standpoint, it may be that correctly capturing the many-body particle interactions for concentrated dispersions requires consideration of higher-order distribution functions (three-body, four-body etc.), beyond our pair-level (or two-body) theory. Whilst it is possible to formulate a hierarchy of equations for these distribution functions one is faced with the problem of closure (in our theory the hierarchy is closed, with an $O(\phi_b)$ error, by the assumption of diluteness) and the complicated (integro-differential) nature of the equations themselves. Of course, as an alternative to theoretical analyses one could employ Stokesian Dynamics simulations to study probe motion in concentrated dispersions.

Several variations on the present theme are possible. For simplicity, and in keeping with macrorheology practices, the probe particle and bath particles were assumed to be of equal size. It would be interesting to see what effect varying the size ratio of probe particle to bath particle has on the complex microviscosity. Batchelor (1983) has considered this problem in the context of diffusion in a polydisperse suspension: he calculates the short- and long-time self-diffusivities for varying size ratios of particles; however, the frequency response of the self-diffusivity (or, equivalently, complex microviscosity) as a function of size ratio is an open problem. A similar extension is to impose an oscillatory velocity on the probe, rather than an oscillatory force. Squires and Brady (2005) have computed the nonlinear microviscosity as a function of $Pe_b$, in the absence of hydrodynamic interactions, from fixed-force and fixed-velocity probe motion. They find that the ratio of fixed-velocity to

fixed-force microviscosity is $(1+\lambda)/\lambda$, where $\lambda$ is the ratio of probe size to bath particle size; thus, the fixed-velocity microviscosity is always greater than the fixed-force microviscosity: the fixed-velocity probe expends more energy in 'bulldozing' bath particles out of its path than the fixed-force probe which may move around any obstructing bath particles. Thus, it is expected (at least in the absence of hydrodynamic interactions) that the complex microviscosity should be greater for an oscillatory-velocity probe than an oscillatory-force probe. How the inclusion of hydrodynamic interactions affects the situation is not known.

The present theoretical framework may be used to study microrheology equivalents of other macrorheology techniques, such as flow-cessation (or stress-jump), start-up flow, creep tests, and step-strain experiments. For instance, in the microrheology analog of flow-cessation the probe moves under a steady external force, so that a steady-state microstructure has been established, for times $t < 0$. At $t = 0$ the external force on the probe is removed, and the relaxation of the microstructure towards its equilibrium state is monitored. In the absence of an external force the microstructural relaxation is diffusive; thus, the 'force-cessation' (or 'velocity-jump') experiment provides a method of separating the hydrodynamic and thermodynamic contributions to the microviscosity. In 'start-up force' experiments a steady external force is applied to the probe at $t = 0$ (for $t < 0$ the dispersion is in equilibrium), and one observes the evolution of the microstructure towards it's nonequilibrium steady-state form. The time-dependence of the hydrodynamic and Brownian contributions to the microviscosity can be studied in such an experiment.

## 3.10 Bibliography

A. J. Banchio, G. Nägele, and J. Bergenholtz. Viscoelasticity and generalized Stokes-Einstein relations of colloidal dispersions. *J. Chem. Phys.*, 111:8721–8740, 1999.

H. A. Barnes, J. F. Hutton, and K. Walters. *An Introduction to Rheology.* Elsevier, 1989.

G. K. Batchelor. Diffusion in a dilute polydisperse system of interacting spheres. *J. Fluid Mech.*, 131:155–176, 1983.

A. R. Bausch, W. Möller, and E. Sackmann. Measurement of local viscoelasticity and forces in living cells by magnetic tweezers. *Biophys. J.*, 76:573–579, 1999.

A. R. Bausch, F. Ziemann, A. A. Boulbitch, K. Jacobson, and E. Sackmann. Local measurement of viscoelastic parameters of adherent cell membranes by magnetic bead microrheometry. *Biophys. J.*, 75:2038–2049, 1998.

R. B. Bird, O. Hassager, R. C. Armstrong, and C. F. Curtiss. *Dynamics of Polymeric Liquids, Kinetic Theory.* Wiley, 1988.

J. F. Brady. The rheological behavior of concentrated colloidal dispersions. *J. Chem. Phys.*, 99:567–581, 1993.

J. F. Brady. The long-time self-diffusivity in concentrated colloidal dispersions. *J. Fluid Mech.*, 272:109–133, 1994.

S. Chapman and T. G. Cowling. *The Mathematical Theory of Nonuniform Gases.* Cambridge University Press, 1970.

B. Cichocki and B. U. Felderhof. Time-dependent self-diffusion coefficient of interacting Brownian particles. *Phys. Rev. A*, 44:6551–6558, 1991.

B. Cichocki and B. U. Felderhof. Influence of hydrodynamic interactions on self-diffusion and stress relaxation in a semidilute suspension of hard spheres. *Physica A*, 198:423–440, 1993.

B. Cichocki and K. Hinsen. Dynamic computer simulation of concentrated hard sphere suspensions. II. Re-analysis of mean square displacement data. *Physica A*, 187:133–144, 1992.

W. P. Cox and E. H. Merz. Correlation of dynamic and steady flow viscosities. *J. Polym. Sci.*, 28:619–622, 1958.

J. C. Crocker, M. T. Valentine, E. R. Weeks, T. Gisler, P. D. Kaplan, A. G. Yodh, and D. A. Weitz. Two-point microrheology of inhomogeneous soft materials. *Phys. Rev. Lett.*, 84:888–891, 2000.

D. R. Foss and J. F. Brady. Brownian dynamics simulation of hard-sphere colloidal dispersions. *J. Rheol.*, 44:629–651, 2000.

F. Gittes, B. Schnurr, P. D. Olmsted, F. C. MacKintosh, and C. F. Schimdt. Microscopic viscoelasticity: shear moduli of soft materials determined from thermal fluctuations. *Phys. Rev. Lett.*, 79:3286–3289, 1997.

P. Habdas, D. Schaar, A. C. Levitt, and E. R. Weeks. Forced motion of a probe particle near the colloidal glass transition. *Europhys. Lett.*, 79:477–483, 2004.

D. J. Jeffrey and Y. Onishi. Calculation of the resistance and mobility functions of two unequal rigid spheres in low-Reynolds-number flow. *J. Fluid Mech.*, 139:261–290, 1984.

A. S. Khair and J. F. Brady. Single particle motion in colloidal dispersions: A simple model for active and nonlinear microrheology. *J. Fluid Mech.*, 557:73–117, 2006.

S. Kim and S. J. Karilla. *Microhydrodynamics: Principles and Selected Applications*. Butterworth-Heinemann, 1991.

R. A. Lionberger and W. B. Russel. High frequency modulus of hard sphere colloids. *J. Rheol.*, 38:1885–1908, 1994.

F. C. MacKintosh and C. F. Schmidt. Microrheology. *Curr. Opin. Colloid Interface Sci.*, 4:300–307, 1999.

R. E. Mahaffy, C. K. Shih, F. C. MacKintosh, and J. Käs. Scanning probe-based frequency dependent microrheology of polymer gels and biological cells. *Phys. Rev. Lett.*, 85:880–883, 2000.

T. G. Mason. Estimating the viscoelastic moduli of complex fluids using the generalized Stokes-Einstein equation. *Rheol. Acta.*, 39:371–378, 2000.

T. G. Mason, K. Ganesan, J. H. van Zanten, D. Wirtz, and S. C. Kuo. Particle tracking microrheology of complex fluids. *Phys. Rev. Lett.*, 79:3282–3285, 1997.

T. G. Mason and D. A. Weitz. Optical measurements of frequency-dependent linear viscoelastic moduli of complex fluids. *Phys. Rev. Lett.*, 74:1250–1253, 1995.

D. A. McQuarrie. *Statistical Mechanics*. University Science Books, 2000.

G. Nägele and J. Bergenholtz. Linear viscoelasticity of colloidal mixtures. *J. Chem. Phys*, 108:9893–9904, 1998.

M. Renardy. Qualitative correlation between viscometric and linear viscoelastic functions. *J. Non-Newtonian Fluid Mech.*, 68:133–135, 1997.

W. B. Russel, D. A. Saville, and W. R. Schowalter. *Colloidal Dispersions*. Cambridge University Press, 1989.

T. Shikata and D. S. Pearson. Viscoelastic behavior of concentrated spherical suspensions. *J. Rheol.*, 38:601–616, 1994.

I. S. Sohn and R. Rajagopalan. Microrheology of model quasi-hard-sphere dispersions. *J. Rheol.*, 48:117–140, 2004.

T. M. Squires and J. F. Brady. A simple paradigm for active and nonlinear microrheology. *Phys. Fluids*, 17:073101, 2005.

W. Sutherland. A dynamical theory of diffusion for nonelectrolytes and the molecular mass of albumin. *Phil. Mag.*, 6:781–785, 1905.

J. C. Van der Werff, C. G. de Kruif, C. Blom, and J. Mellema. Linear viscoelastic behavior of dense hard-sphere dispersions. *Phys. Rev. A*, 39:795–807, 1989.

D. Velegol and F. Lanni. Cell traction forces on soft biomaterials. 1: Microrheology of type 1 collagen gels. *Biophys. J.*, 81:1786–1792, 2001.

T. A. Waigh. Microrheology of complex fluids. *Rep. Prog. Phys.*, 68:685–742, 2005.

# Appendix to chapter 3

## 3.A High-frequency asymptotics with hydrodynamic interactions

Here, we consider the high-frequency asymptotics of the Smoluchowski equation in the presence of hydrodynamic interactions. At high frequencies the Smoluchowski equation (3.11) reflects a balance between oscillatory forcing and advection, and the solution is $f \equiv F = -iW(\hat{b}s)/\alpha$; whilst satisfying the far-field condition (3.13) this solution does not meet the no-flux boundary condition at contact (3.12). Therefore, near contact there exists an 'inner' region, or boundary layer, of $O(\alpha^{-1/2})$ in which Brownian diffusion balances oscillatory forcing. We introduce the boundary-layer coordinate $y = \alpha^{1/2}(s-2)$ and expand the mobility functions $H(\hat{b}s), G(\hat{b}s)$, and $W(\hat{b}s)$ about $s = 2$. The Smoluchowski equation then reads

$$\begin{aligned} &\left(G_0 + G_1\alpha^{-1/2}y\right)\alpha\frac{d^2f}{dy^2} + \left(\left(1-\alpha^{-1/2}y/2\right)\left(G_0 + G_1\alpha^{-1/2}y\right) + G_1\right)\alpha^{1/2}\frac{df}{dy} - i\alpha f \\ = \;& \frac{1}{2}\left(1-\alpha^{-1/2}y\right)\left(H_0 + H_1\alpha^{-1/2}y\right)f - \left(W_0 + W_1\alpha^{-1/2}y\right) + O(\alpha^{-3/2}), \end{aligned} \tag{3.A-1}$$

with $X_0 = X(2\hat{b})$ and $X_1 = dX/ds|_{2\hat{b}}$, for $X = G$, $H$, or $W$. The boundary conditions on $f(y;\alpha)$ are

$$\begin{aligned} \frac{df}{dy} &= -\frac{1}{\alpha^{1/2}} \qquad \text{at} \qquad y = 0, \\ f &\to -\frac{iW_0}{\alpha} \qquad \text{as} \qquad y \to \infty. \end{aligned}$$

To satisfy the boundary condition at contact $f(y;\alpha)$ must scale like $\alpha^{-1/2}$ to leading order; hence, we pose the expansion $f(y;\alpha) \sim f_0(y)/\alpha^{1/2} + f_1(y)/\alpha + O(\alpha^{-3/2})$. Inserting

this expansion into (3.A-1) yields equations for $f_0(y)$ and $f_1(y)$. For $f_0$ we have

$$\begin{aligned} G_0 \frac{d^2 f_0}{dy^2} \quad - \quad & i f_0 = 0, \\ \frac{df_0}{dy} = -1 \qquad & \text{at} \qquad y = 0, \\ f_0 \to 0 \qquad & \text{as} \qquad y \to \infty, \end{aligned}$$

which has the solution

$$f_0 = \left( \frac{G_0}{i} \right)^{1/2} e^{-(i/G_0)^{1/2} y}. \tag{3.A-2}$$

The equation for $f_1$ is

$$\begin{aligned} G_0 \frac{d^2 f_1}{dy^2} - i f_1 \quad = \quad & -W_0 - G_1 y \frac{d^2 f_0}{dy^2} - (G_0 + G_1) \frac{df_0}{dy}, \\ \frac{df_1}{dy} = 0 \qquad & \text{at} \qquad y = 0, \\ f_1 \to -iW_0 \qquad & \text{as} \qquad y \to \infty. \end{aligned}$$

The far-field condition on $f_1$ ensures correct matching with the outer solution $F = -iW(\hat{b}s)/\alpha$. Some straightforward algebra gives

$$f_1 = \frac{i}{4} (2G_0 + G_1) \left( 1 + \left( \frac{i}{G_0} \right)^{1/2} y \right) e^{-(i/G_0)^{1/2} y} + \frac{G_1}{4G_0} y^2 e^{-(i/G_0)^{1/2} y} - iW_0. \tag{3.A-3}$$

In the absence of hydrodynamic interactions ($G_0 = 1, G_1 = 0$, and $W_0 = 0$) the expression (3.20) for the structural deformation is recovered. All terms in the inner expansion of the structural deformation (with the exception of the $-iW_0/\alpha$ matching term) are proportional to $e^{-(i/G_0)^{1/2} y}$: these terms decay exponentially fast with increasing radial distance $y$. The length scale of the decay is $G_0^{1/2}$, which vanishes like $(\hat{b} - 1)^{1/2}$ as $\hat{b} \to 1$. In fact, for

the special case of full hydrodynamic interactions ($\hat{b} \equiv 1$, where the terms proportional to $e^{-(i/G_0)^{1/2}y}$ decay on an infinitesimally small length scale) there is no boundary layer and $f \equiv F = -iW(s)/\alpha$ is a uniformly valid asymptotic solution to the Smoluchowski equation. (When $\hat{b} = 1$ the inner boundary condition at $s = 2$ is now $\hat{\boldsymbol{s}} \cdot \boldsymbol{D} \cdot \boldsymbol{\nabla} g = 0$, which for small-amplitude forcing implies $(s-2)df/ds = 0$ at $s = 2$.) Thus, it should be appreciated that the presence of the boundary layer at high frequencies is solely due to the hard-sphere interparticle-force interaction.

From the contact value of the structural deformation, $f(0;\alpha) \sim f_0(0)/\alpha^{1/2} + f_1(0)/\alpha + O(\alpha^{-3/2})$, the real and imaginary parts of the interparticle-force microviscosity, $\eta_P(\alpha) = 2G_0 f(0;\alpha)$, are found as

$$\begin{aligned} \frac{\eta_P'}{\phi_b} &= \left(\frac{2G_0^3}{\alpha}\right)^{1/2} + O(\alpha^{-3/2}), \\ \frac{\eta_P''}{\phi_b} &= \left(\frac{2G_0^3}{\alpha}\right)^{1/2} - \frac{G_0}{\alpha}\left(G_0 - \frac{G_1}{2} - 2W_0\right) + O(\alpha^{-3/2}),. \end{aligned}$$

The $O(1/\alpha)$ contribution to the contact value of the structural deformation is purely imaginary; hence, there is no $O(1/\alpha)$ term in the high-frequency expansion of $\eta_P'$. For full hydrodynamic interactions ($\hat{b} \equiv 1$ and $G_0 = 0$) the interparticle-force microviscosity vanishes, as expected. By multiplying the imaginary part of the interparticle-force microviscosity by $\alpha$ we recover the expression for interparticle-force contribution to the elastic modulus (3.21).

To arrive at an asymptotic expression for the Brownian microviscosity $\eta_B$ requires a little more work. Recall, the definition of $\eta_B$:

$$\frac{\eta_B}{\phi_b} = -\frac{1}{2}\int_2^\infty W(\hat{b}s) f(s;\alpha) s^2 ds. \tag{3.A-4}$$

We proceed by constructing the composite expansion, denoted as $f_c$, of the inner and outer expansions for the structural deformation:

$$f_c = \frac{f_0}{\alpha^{1/2}} + \frac{f_1 + iW_0}{\alpha} + F. \tag{3.A-5}$$

Inserting (3.A-5) into (3.A-4) we find

$$\frac{\eta_B}{\phi_b} = -\frac{1}{2}\int_2^\infty W(\hat{b}s)\left(\frac{f_0}{\alpha^{1/2}} + \frac{f_1 + iW_0}{\alpha}\right)s^2 ds + \frac{i}{2\alpha}\int_2^\infty [W(\hat{b}s)]^2 s^2 ds + O(\alpha^{-3/2}). \tag{3.A-6}$$

The first term on the right-hand side of (3.A-6) is the contribution to $\eta_B$ from the boundary layer, and the second term is the contribution from the outer region. Using expressions (3.A-2) and (3.A-3) for $f_0$ and $f_1$ respectively the boundary-layer contribution to $\eta_B$ is $2iW_0G_0/\alpha + O(\alpha^{-3/2})$; thus, the Brownian microviscosity is

$$\frac{\eta_B}{\phi_b} = \frac{2iW_0G_0}{\alpha} + \frac{i}{2\alpha}\int_2^\infty [W(\hat{b}s)]^2 s^2 ds + O(\alpha^{-3/2}),$$

which to leading order in $\alpha$ is purely imaginary. Multiplying the above expression by $\alpha$ we recover the Brownian contribution to the high-frequency elastic modulus (3.22) .

# Chapter 4

# Microrheology of colloidal dispersions: shape matters

## 4.1 Introduction

Over the past decade, a number of experimental techniques have emerged with the ability to infer rheological properties of complex fluids and biological materials at the micrometer scale. Collectively, they have come to be known as 'microrheology' (for reviews see MacKintosh and Schmidt 1999; Waigh 2005). The name microrheology was adopted, perhaps, to distinguish these techniques from more traditional (macro-) rheological procedures (e.g., mechanical rheometry), which typically operate on much larger (millimeter or more) length scales. Therein lies the main advantage of micro- over macro-rheology: it requires much smaller (microliter) amounts of sample. This is a particular advantage for rare, expensive, or biological substances that one simply cannot produce or procure in quantities sufficient for macrorheological testing.

At the heart of microrheology is the use of colloidal 'probe' particles embedded in the material of interest. Through tracking the motion of the probe (using, e.g., light scattering, diffusing-wave spectroscopy, or laser-deflection particle tracking) it is possible to infer the viscoelastic properties of the material. In *passive* tracking experiments the probe moves diffusively due to the random thermal fluctuations of its surrounding environment. The mean-squared displacement of the probe is measured, from which the complex, or frequency-dependent, shear modulus of the material is inferred via a generalized Stokes-Einstein-Sutherland relation (Mason and Weitz 1995; Mason et al. 1997). Many diverse systems, such as polymer gels (Mahaffy et al. 2000), single cells (Daniels et al. 2006), colloidal dispersions (Sohn and Rajagopalan 2004), and actin networks (Gittes et al. 1997), have been studied using passive microrheology. One should not think, however, that the use of thermally diffusing probes is limited to ascertaining viscoelastic moduli: recent studies have employed

them to study protein folding (Tu and Breedveld 2005), liquid-solid interfaces (Joly et al. 2006), and vortices in non-Newtonian fluids (Atakhorammi et al. 2005).

In passive microrheology the probe only slightly disturbers its surroundings; consequently, one can infer only the near-equilibrium, or linear-response, properties of a material. In contradistinction, *active* microrheology, in which the material is pushed out of equilibrium by driving the probe through it (using, for instance, optical traps or magnetic tweezers), can be used to determine nonlinear viscoelastic properties. Colloids near the glass transition (Habdas et al. 2004); suspensions of rod-like particles (Wensink and Löwen 2006); semiflexible polymer networks (Ter-Oganessian et al. 2005a,b); and colloidal dispersions (Meyer et al. 2006), are but a few of the systems that have been investigated using actively driven probe particles.

Our own recent work (Squires and Brady 2005; Khair and Brady 2005, 2006) has focused on developing theoretical paradigms for active-microrheology experiments, by studying possibly the simplest of scenarios: an externally driven spherical probe in a monodisperse hard-sphere colloidal dispersion. The moving probe pushes the microstructure of the colloidal 'bath' particles out of equilibrium. In turn, the progress of the probe is retarded by the presence of the bath particles, which, through Brownian diffusion, act to restore equilibrium. The relative magnitude of the probe's externally driven motion to the thermal restoring force of the bath particles sets the degree of microstructural distortion and is known as the Péclet number, $Pe$.

One can interpret the retardation of the probe's motion in terms of a 'microviscosity' of the dispersion via application of Stokes drag law. As shown by Squires and Brady (2005), the computed value of the microviscosity depends on the whether the probe is driven at fixed force or fixed velocity, and on the probe to bath particle size ratio. Nevertheless, after

scaling appropriately for these effects, Squires and Brady (2005) demonstrate qualitative agreement between the microviscosity and the shear, or macro-, viscosity from macrorheology. Further work (Khair and Brady 2006) investigated the role of hydrodynamic interactions between the probe and bath particles: in particular, when the particles experience short-range lubrication forces the microviscosity 'force-thickens' at large $Pe$, in analogy to the 'shear-thickening' of the macroviscosity (Bergenholtz et al. 2002). Note, however, this near-quantitative agreement between micro- and macro-viscosity is only possible as the relevant scalings for both are known *a priori*, allowing for a direct and meaningful comparison of the two. For more complex (or unknown) materials, where this is not the case, one should not expect micro and macro to agree, in general.

In the present work, we examine a facet of active microrheology that has hitherto been unexplored; namely, what role does the *shape* of the probe play? One might ask if it is worthwhile to address this issue since, after all, the symmetry of a spherical probe greatly simplifies experimental design and theoretical analysis. Unfortunately, this symmetry can also be viewed as a drawback: one can infer only a scalar (micro-) viscosity from a (single) spherical probe, whereas in macrorheology the full stress tensor is obtainable, including normal stress differences and an isotropic osmotic pressure (Bergenholtz et al. 2002). Naturally, this leads one to ask if a non-spherical probe might give more than just a microviscosity. For example, could it be used to infer normal stress differences? In this (first) study, however, we shall ask the simpler question of how the shape of the probe affects the computed value of the microviscosity. Certainly, this is an issue of experimental significance as one expects the probe to have some degree of non-sphericity, as result of the manufacturing process or due to surface asperities, for instance.

As a variation of the model system used in our previous work, we consider a non-spherical

probe translating at constant velocity through a dispersion of spherical bath particles. The probe is a body of revolution with major and minor semiaxes $a$ and $b$, respectively, and the bath particles are spheres of radii $b$. The probe's shape is such that when its major(minor) axis is the axis of revolution the excluded-volume, or contact, surface between the probe and a bath particle is a prolate(oblate) spheroid.[1] To facilitate an analytical treatment we assume the volume fraction of bath particles is small compared to unity and neglect solvent-mediated hydrodynamic interactions between the probe and bath particles. In this limit, the pair-distribution function, which represents the likelihood of finding a bath particle at a particular location from the probe (and hence is a measure of the nonequilibrium microstructure), satisfies a two-body Smoluchowski equation. Our main focus in this chapter is on a (prolate or oblate) probe moving along its symmetry axis, for which the pair-distribution function is axisymmetric about the direction of motion. From the pair-distribution function we calculate the average external force required to sustain the probe's motion, which can be interpreted in terms of a microviscosity via application of Stokes law. Our aim is to calculate the nonequilibrium microstructure and microviscosity over a wide range of probe aspect ratio $\hat{a} = a/b$ and $Pe$ (here, $Pe$ is the dimensionless velocity of the probe).

The rest of this chapter is organized as follows. In § 4.2 we present the Smoluchowski equation governing the non-equilibrium microstructure of the dispersion. Details of the coordinate systems used for modeling a prolate and oblate probe translating along its symmetry axis are given in § 4.2.1 and § 4.2.2, respectively. In § 4.3 we demonstrate how the average external force on the probe can be interpreted as a microviscosity of the dispersion.

[1] The reader may wonder why we did not simply take the probe to be an prolate(oblate) spheroid. It is, of course, possible to do this, but the resulting excluded-volume shape is rather complicated: specifically, it is not a coordinate surface in prolate(oblate) spheroidal coordinates, making the ensuing analysis far more difficult.

In § 4.4 we present a perturbation analysis of the Smoluchowski equation in the limits of small ($Pe \ll 1$) and large ($Pe \gg 1$) departures from equilibrium. For arbitrary $Pe$ the Smoluchowski equation is solved numerically, and the techniques used for doing so are explained in § 4.5. Results for the microstructure and microviscosity are detailed in § 4.6. In § 4.7 we offer some concluding remarks, including a preliminary analysis of a prolate probe translating at an angle $\beta$ to its symmetry axis. In this case, one must apply an external torque to prevent the probe from rotating, and we suggest how the torque may be indicative of the normal stress differences of the dispersion.

## 4.2 Nonequilibrium microstructure

Consider a probe particle traveling at constant velocity through a dispersion of colloidal bath particles suspended in a Newtonian fluid of shear viscosity $\eta$. The probe is a body of revolution with major and minor semiaxes $a$ and $b$, respectively, and the bath particles are spheres of radii $b$. To develop an analytical description of the microstructural deformation caused by the driven probe, we assume the volume fraction of bath particles, $\phi = 4\pi n b^3/3$ (with $n$ the number density of bath particles), is much less than unity. In this (dilute) limit the microstructure is determined by interactions between the probe and a single bath particle, and the pair-distribution function $g(\boldsymbol{r})$ [defined as $ng(\boldsymbol{r}) = P_{1/1}(\boldsymbol{r})$, with $P_{1/1}(\boldsymbol{r})$ the conditional probability of finding a bath particle at a separation $\boldsymbol{r}$ from the probe] satisfies a two-body Smoluchowski equation, viz.

$$D\nabla_r^2 g + \boldsymbol{U}\cdot\nabla_r g = 0, \tag{4.1}$$

where $D = kT/6\pi\eta b$ is the Stokes-Einstein-Sutherland diffusivity of a bath particle ($kT$

being the thermal energy), and $\boldsymbol{U}$ is the probe velocity. [For a systematic derivation of (4.1), starting from the $N$-body Smoluchowski equation, see Squires and Brady (2005).] In writing (4.1) the relative coordinate system $\boldsymbol{r} = \boldsymbol{x_2} - \boldsymbol{x_1}$ and $\boldsymbol{z} = \boldsymbol{x}_2 + \boldsymbol{x}_1$ is employed, where $\boldsymbol{x}_1$ and $\boldsymbol{x}_2$ denote the probe and bath particle positions, respectively.

To non-dimensionalize the Smoluchowski equation we scale lengths with $b$ and velocities by $U = |\boldsymbol{U}|$, which gives

$$\nabla^2 g + Pe\hat{\boldsymbol{U}}\cdot\nabla g = 0, \tag{4.2}$$

where $\hat{\boldsymbol{U}} = \boldsymbol{U}/U$, and we have dropped the subscript $r$ for brevity. A Péclet number, $Pe = Ub/D$, arises from the scaling and may be thought of as a ratio of advective ($U$) to diffusive ($D/b$) 'velocities'. Far from the probe, it is assumed that the dispersion has no long-range order:

$$g(\boldsymbol{s}) \to 1 \quad \text{as} \quad |\boldsymbol{s}| \to \infty, \tag{4.3}$$

with $\boldsymbol{s} = \boldsymbol{r}/b$. The rigidity of the particles is represented by a no-flux condition:

$$\boldsymbol{n}\cdot(\boldsymbol{\nabla} g + Pe\hat{\boldsymbol{U}} g) = 0 \quad \text{on} \quad S_e, \tag{4.4}$$

where $S_e$ is the excluded-volume, or contact, surface between the probe and bath particle. Clearly, the form of $S_e$ is dependent on the shape of the probe. In this study, we take the probe shape to be that which results in a prolate(oblate) spheroidal $S_e$ when the probe's axis of revolution is its major(minor) axis. In both cases, when the probe moves along its symmetry axis the microstructure is axisymmetric about the direction of motion; however, the two situations require different coordinate systems with which to solve the Smoluchowski equation, as discussed next.

### 4.2.1 Prolate probe

We consider the probe to move along its major axis, which is taken as the $z$-axis of a cylindrical $[\rho, z]$ coordinate system, whose origin is at the center of the probe (see figure 4.1). The probe's shape is such that the excluded-volume surface $S_e$ is a prolate spheroid with major and minor semiaxes $a_e = 1 + \hat{a}$ and $b_e = 2$, respectively, where $\hat{a} = a/b$ is the aspect ratio of the probe. (Recall, all lengths are made dimensionless with the bath particle radius $b$.) Let us introduce the prolate spheroidal coordinates $\xi$ and $\eta$ defined by

$$\rho = c \sinh\xi \sin\eta \ \ , \ \ z = c \cosh\xi \cos\eta,$$

where $c$ is a scale factor; $0 \leq \xi < \infty$; and $0 \leq \eta \leq \pi$. The coordinate surface $\xi = \xi_0$ is a prolate spheroid (centered at the origin) with major and minor semiaxes $a_0 = c\cosh\xi_0$ and $b_0 = c\sinh\xi_0$, respectively. Thus, we find

$$c = \sqrt{(\hat{a}+1)^2 - 4} \ \ , \ \ \xi_e = \frac{1}{2}\ln\left(\frac{\hat{a}+3}{\hat{a}-1}\right), \tag{4.5}$$

with $\xi_e$ the coordinate surface corresponding to $S_e$. In cylindrical coordinates $S_e$ is represented as $[\rho_e = 2\sin\eta, z_e = (1+\hat{a})\cos\eta]$, and the probe itself is

$$\left[\rho_p = \rho_e - \frac{\cosh\xi_e \sin\eta}{(\sinh^2\xi_e + \sin^2\eta)^{1/2}} \ \ , \ \ z_p = z_e - \frac{\sinh\xi_e \sin\eta}{(\sinh^2\xi_e + \sin^2\eta)^{1/2}}\right]. \tag{4.6}$$

Note, when $\hat{a} = 1$ the probe and excluded-volume surfaces degenerate to spheres, of radii 1 and 2, respectively.

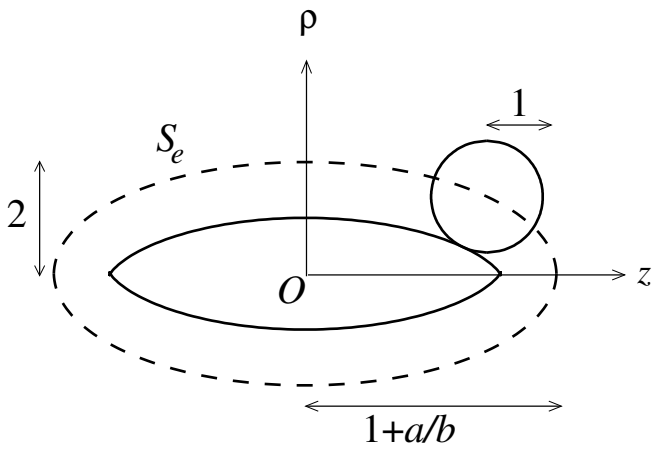


Figure 4.1: Definition sketch for the prolate probe. Here, the aspect ratio $\hat{a} = a/b = 3.5$. The circle of radius unity represents a bath particle, which is contacting the probe. The probe moves at constant velocity along its axis of revolution, the $z$-axis. The excluded-volume surface $S_e$ (broken curve) is formed by 'rolling' the bath particle over the probe's surface.

In prolate spheroidal coordinates, the Smoluchowski equation (4.2) becomes

$$\frac{1}{\sinh\xi}\frac{\partial}{\partial\xi}\left(\sinh\xi\frac{\partial g^{pr}}{\partial\xi}\right)+\frac{1}{\sin\eta}\frac{\partial}{\partial\eta}\left(\sin\eta\frac{\partial g^{pr}}{\partial\eta}\right)=cPe\left(\cosh\xi\sin\eta\frac{\partial g^{pr}}{\partial\eta}-\sinh\xi\cos\eta\frac{\partial g^{pr}}{\partial\xi}\right), \tag{4.7}$$

subject to the boundary conditions

$$\frac{\partial g^{pr}}{\partial\xi}=-cPe\sinh\xi_e\cos\eta g^{pr} \qquad \text{at} \qquad \xi=\xi_e,$$

$$g^{pr}\to 1 \qquad \text{as} \qquad \xi\to\infty.$$

The superscript *pr* has been added to the pair-distribution function to make clear these are equations are for the prolate probe. Equations pertaining to the oblate probe will have attached the superscript *ob*.

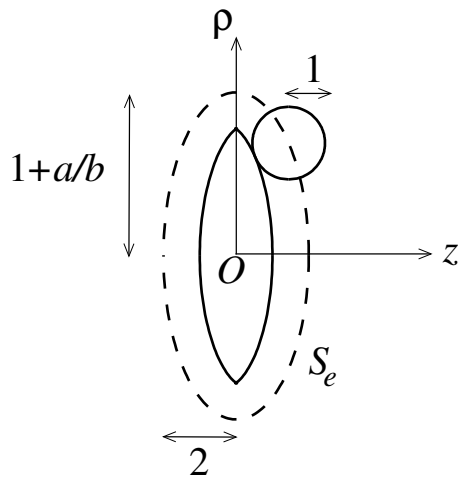


Figure 4.2: Definition sketch for the oblate probe. Here, the aspect ratio $\hat{a} = a/b = 3.5$, and the legend is the same as in figure 4.1. Again, the probe moves along its axis of revolution (the $z$-axis) at constant velocity.

### 4.2.2 Oblate probe

In this case, the probe moves along its minor axis, which is the $z$-axis of a cylindrical $[\rho, z]$ coordinate system. The shape of $S_e$ is an oblate spheroid, with the same major and minor semiaxes as in the prolate case (see figure 4.2). We define the oblate spheroidal coordinates $\xi$ and $\eta$ by

$$\rho = c \cosh\xi \sin\eta \quad , \quad z = c \sinh\xi \cos\eta,$$

where $\xi$ and $\eta$ have the same ranges as before; moreover, the scale factor $c$ and the excluded-volume coordinate surface $\xi_e$ are again given by (4.5). In fact, one can transform from prolate to oblate coordinates via the transformation

$$c \to -ic \quad , \quad \cosh\xi \to i \sinh\xi, \tag{4.8}$$

where $i = \sqrt{-1}$ (Morse and Feshbach 1953). Therefore, in the interests of brevity, rather than state explicitly the excluded-volume shape, probe shape, and Smoluchowski equation

in oblate spheroidal coordinates, we note that they can be obtained by applying (4.8) to the relevant prolate spheroidal equations. Furthermore, in the what follows we perform detailed calculations for the prolate probe and, wherever possible, employ (4.8) to obtain results for the equivalent oblate probe.

## 4.3 Microviscosity

From the pair-distribution function it is possible to calculate many microstructurally-averaged properties. In the present context, the most interesting is the average external force on the probe $\langle \boldsymbol{F}^{ext} \rangle$, which, as derived by Squires and Brady (2005), is given by

$$\langle \boldsymbol{F}^{ext} \rangle = M^{-1}\boldsymbol{U} + nkT \oint \boldsymbol{n} g(\boldsymbol{r}) dS_e, \tag{4.9}$$

where $M = 1/6\pi\eta b K$ is the mobility of the probe, and $dS_e$ is the differential area element of the excluded-volume surface. The mobility factor $K$ accounts for the non-sphericity of the probe. For the rather complicated probe shape represented by (4.6) evaluation of $K$ is nontrivial. Therefore, we make the assumption that (for purposes of computing the mobility only) the probe itself may be approximated as a spheroid with the same major and minor semiaxes. Thus, the mobility factors are (Happel and Brenner 1965)

$$\begin{aligned} K^{pr} &= \frac{4}{3}\left(\tau_p^2 - 1\right)^{-1/2}\left[(\tau_p^2+1)\coth^{-1}\tau_p - \tau_p\right]^{-1}, \\ K^{ob} &= \frac{4\hat{a}}{3}\left(\lambda_p^2 + 1\right)^{-1/2}\left[\lambda_p - (\lambda_p^2-1)\cot^{-1}\lambda_p\right]^{-1}, \end{aligned} \tag{4.10}$$

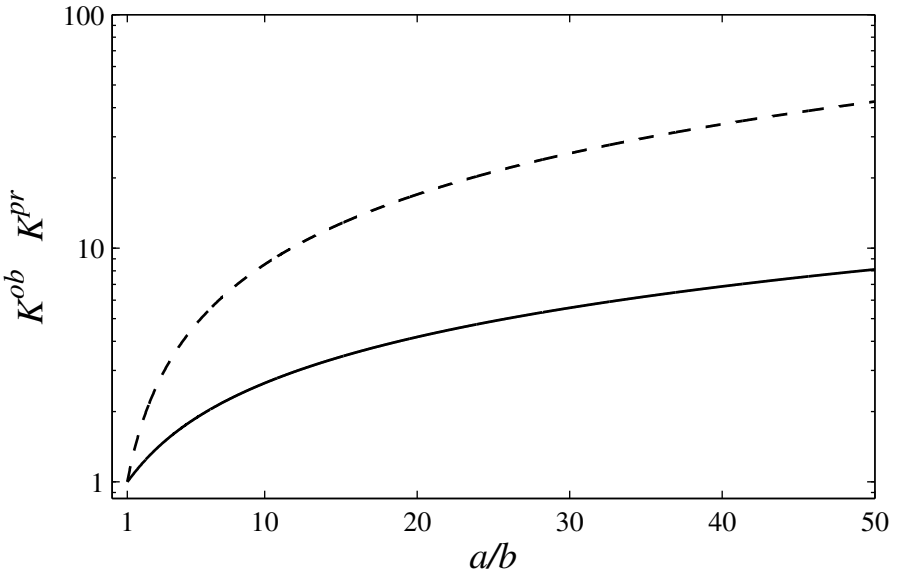


Figure 4.3: Plot of the mobility factors versus probe aspect ratio $\hat{a} = a/b$. The broken line is the oblate factor $K^{ob}$ and the solid line is the prolate factor $K^{pr}$.

where $\tau_p = \cosh \xi_p$ and $\lambda_p = \sinh \xi_p$, and

$$\xi_p = \frac{1}{2} \ln \left( \frac{\hat{a}+1}{\hat{a}-1} \right),$$

is the coordinate surface of the 'spheroidal' probe. In figure 4.3 we plot $K^{pr}$ and $K^{ob}$ as a function of the aspect ratio $\hat{a} = a/b$. In the limit of a spherical probe, $\hat{a} = 1$, both $K^{pr}$ and $K^{ob}$ approach unity, as expected. When $\hat{a} \gg 1$ the prolate probe resembles a long thin rod and $K^{pr} \sim 2\hat{a}/[3\ln(2\hat{a}) - 3/2]$ (cf. equation 4-31.4 of Happel and Brenner 1965). The oblate probe in the limit $\hat{a} \gg 1$ degenerates to a thin circular disk, for which $K^{ob} \sim 8\hat{a}/3\pi$ (cf. equation 4-27.2 of Happel and Brenner 1965).

As the probe translates, there is an accumulation(deficit) of bath particles on its upstream(downstream) side, resulting in an 'osmotic pressure' imbalance [the integral in (4.9) is simply the average of this imbalance over the excluded-volume surface], which provides an entropic force resisting the probe's motion. As such, the average external force on the

probe required to maintain its velocity at $\boldsymbol{U}$ is greater than if the probe were traveling in the absence of bath particles. One can interpret the increase in external force as an increment to a 'microviscosity' of the dispersion: from Stokes drag law, $\langle F_z^{ext} \rangle = 6\pi\eta bKU\eta_r$ (the external force is, by symmetry, directed solely along the $z$-axis), a dimensionless relative microviscosity $\eta_r$ is defined

$$\eta_r = 1 + \frac{nkT}{6\pi\eta bKU} \oint n_z g dS_e,$$

where $n_z = \boldsymbol{n}\cdot\hat{\boldsymbol{U}}$. It is natural to define a microviscosity increment, $\Delta\eta_r$, as

$$\Delta\eta_r = \frac{nkT}{6\pi\eta bKU} \oint n_z g dS_e,$$

representing the contribution to the microviscosity due to the interaction of the probe with bath particles. For the prolate probe the increment may be written as

$$\Delta\eta_r^{pr} = \frac{6\phi}{K^{pr}Pe} \int_0^{\pi} g^{pr} \cos\eta \sin\eta d\eta. \tag{4.11}$$

Recall, $\phi = 4\pi nb^3/3$ is the volume fraction of bath particles. In the oblate case the increment is

$$\Delta\eta_r^{ob} = \frac{3(1+\hat{a})^2\phi}{2K^{ob}Pe} \int_0^{\pi} g^{ob} \cos\eta \sin\eta d\eta. \tag{4.12}$$

## 4.4 Analytical results

### 4.4.1 Near equilibrium $Pe \ll 1$

For small $Pe$ the Brownian diffusion of bath particles dominates over advection by the moving probe; the microstructure is only slightly perturbed from its equilibrium state. This is the passive-microrheology, or linear-response, regime in which the microstructural deformation is proportional to the probe velocity. Therefore, we write the pair-distribution function as $g = 1 + Pef$, where $f$ satisfies Laplace's equation and must vanish at large distances. In the prolate case the no-flux condition on the excluded-volume surface reads

$$\frac{\partial f^{pr}}{\partial \xi} = -c \sinh \xi_e \cos \eta \quad \text{at} \quad \xi = \xi_e,$$

representing a dipolar forcing. The solution for $f^{pr}$ is found to be

$$f^{pr} = \frac{c(\tau_e^2 - 1)}{\coth^{-1} \tau_e - \tau_e(\tau_e \coth^{-1} \tau_e - 1)} (\tau \coth^{-1} \tau - 1) \cos \eta, \tag{4.13}$$

where $\tau = \cosh \xi$ and $\tau_e = \cosh \xi_e$. We note the 'angular' dependence of $\cos \eta$, giving $f^{pr}$ the structure a diffusive dipole directed along $\hat{\boldsymbol{U}}$. From (4.11), the microviscosity increment is calculated as

$$\Delta \eta_r^{pr} = \frac{1}{K^{pr}} \left[ \frac{8(\tau_e^2 - 1)^{1/2} (\tau_e \coth^{-1} \tau_e - 1)}{\coth^{-1} \tau_e - \tau_e(\tau_e \coth^{-1} \tau_e - 1)} \right] \phi,$$

where we have used $c(\tau_e^2 - 1)^{1/2} = 2$. Using the transformation (4.8) on (4.13), we find in the oblate case

$$f^{ob} = \frac{c(\lambda_e^2 + 1)}{\lambda_e(1 - \lambda_e \cot^{-1} \lambda_e) - \cot^{-1} \lambda_e} (\lambda \cot^{-1} \lambda - 1) \cos \eta,$$

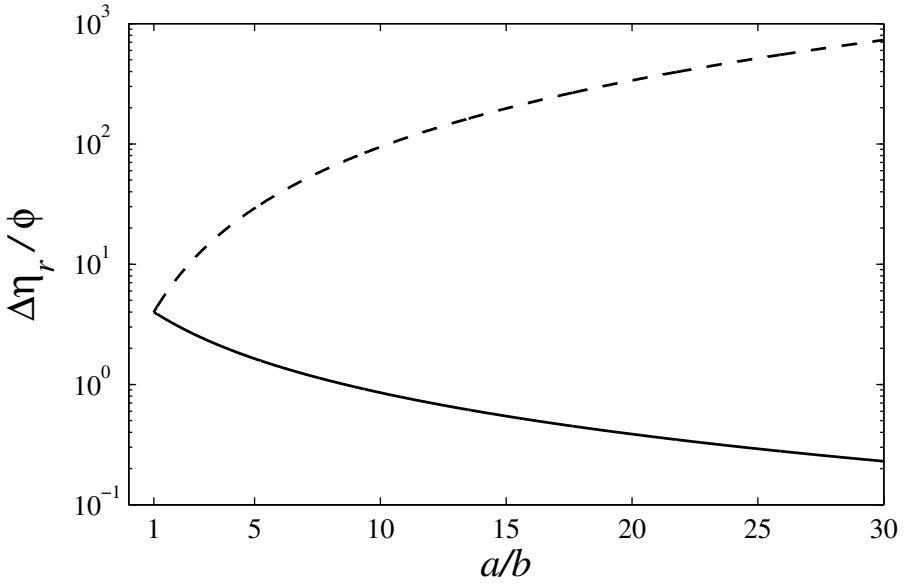


Figure 4.4: Microviscosity increments at small $Pe$ as a function of probe's aspect ratio $\hat{a} = a/b$. The broken line is the oblate increment $\Delta\eta_r^{ob}$ and the solid line is the prolate increment $\Delta\eta_r^{pr}$.

where $\lambda = \sinh\xi$ and $\lambda_e = \sinh\xi_e$. From (4.12) the microviscosity increment is calculated as

$$\Delta\eta_r^{ob} = \frac{(1+\hat{a})^3}{K^{ob}} \left[ \frac{(1+\lambda_e^2)^{1/2}(\lambda_e \coth^{-1}\lambda_e - 1)}{\lambda_e(1 - \lambda_e \coth^{-1}\lambda_e) - \coth^{-1}\lambda_e} \right] \phi,$$

where have used $c(\lambda_e^2+1)^{1/2} = \hat{a}+1$

Figure 4.4 plots the prolate ($\Delta\eta_r^{pr}$) and oblate ($\Delta\eta_r^{ob}$) microviscosity increments at small $Pe$ as a function of the aspect ratio $\hat{a} = a/b$. For $\hat{a} = 1$ both increments approach the value $4\phi$, which is the microviscosity increment for a spherical probe at small $Pe$ (Squires and Brady 2005). On increasing the aspect ratio the prolate(oblate) increment decays(grows) monotonically and vanishes(diverges) in the limit $\hat{a} \to \infty$. We defer a physical explanation of these trends until presentation of our numerical computations at arbitrary $Pe$ (see § 4.6).

### 4.4.2 Far from equilibrium $Pe \gg 1$

For large $Pe$ advection dominates the microstructure, and Brownian diffusion is important only in a thin boundary layer on the upstream side of the probe. The boundary layer represents (in a frame fixed on the moving probe) a balance between the strong advection of bath particles (with velocity $-\hat{\boldsymbol{U}}$) towards the probe and diffusion, which enables the bath particles to pass around the (impenetrable) probe. As a result, there is a large accumulation of bath particles ($g \gg 1$) in the boundary layer. Downstream of the probe advection carries bath particles away: a region of low-particle density ($g \approx 0$), or wake, is present. In this subsection, we present a simple physical argument to calculate the boundary-layer microstructure. However, note that (as shown in appendix 4.B) the same conclusions may be obtained from a rigorous asymptotic analysis. In what follows, we examine the oblate and prolate cases separately.

#### 4.4.2.1 Oblate probe

As mentioned above, the boundary layer signifies a balance between 'radial' diffusion ($D\nabla_\xi^2 g$) and advection ($\boldsymbol{U}_\perp \cdot \nabla_\xi g$) with the perpendicular component of the probe velocity ($U_\perp = \boldsymbol{U}\hat{\boldsymbol{\xi}}$). Equating these two terms gives an approximate (first order) model for the microstructure in the boundary layer, which, in *dimensional* terms, reads

$$D\frac{\partial^2 g^{ob}}{\partial t^2} + Uc\cosh\xi_e \cos\eta \frac{\partial g^{ob}}{\partial t} = 0, \tag{4.14}$$

where $t = \xi - \xi_e$ is a dimensionless coordinate perpendicular to the (local) excluded-volume surface ($S_e$), and $c\cosh\xi_e = a + b$ is the major semiaxis of $S_e$. The solution of (4.14)

is

$$g^{ob} \sim A^{ob}(\eta) e^{-U(a+b)t\cos\eta/D}. \tag{4.15}$$

Clearly, this solution is valid only upstream of the probe, $0 \leq \eta \leq \pi/2$; downstream there is a wake in which $g \approx 0$. We integrate across the boundary layer to obtain the local surface density $\sigma$:

$$\sigma = \int_0^\infty A^{ob}(\eta) e^{-U(a+b)t\cos\eta/D} dt = \frac{D A^{ob}(\eta)}{U(a+b)\cos\eta}. \tag{4.16}$$

At steady state $\sigma$ must be independent of the angular coordinate $\eta$, to ensure there is no accumulation of bath particles on $S_e$; thus, $A^{ob} \sim \cos\eta$. The constant of proportionality can be determined through a flux balance on the boundary layer. In general, the oblate shape of the probe leads to a complicated boundary-layer geometry. However, we can make progress in the limit $a \gg b$, where $S_e$ degenerates to a circular disk of radius $a+b$ and thickness $4b$ (see figure 4.5). The flux of bath particles $Q_{in}$ towards the disk is simply

$$Q_{in} = \pi(a+b)^2 g^\infty U,$$

where $g^\infty (= 1)$ is the far-field value of the pair-distribution function. At steady state, $Q_{in}$ is balanced by a flux $Q_{out}$ of particles exiting the boundary layer. The bath-particle surface density $\sigma$ is advected around $S_e$ with the parallel component of velocity $U_{||} = \boldsymbol{U}\cdot\hat{\boldsymbol{\eta}} = -U\sinh\xi_e \sin\eta/(\cosh^2\xi_e - \sin^2\eta)^{1/2}$ and finally leaves the boundary layer from the edge of the disk, over a cylindrical (exit) surface of perimeter $2\pi(a+b)$ and thickness $2b$. (The thickness of the disk edge is $4b$; however the boundary layer terminates half way along the edge. Thus, the thickness of the exit surface is $2b$.) The edge corresponds to $\eta = 1/2$, for

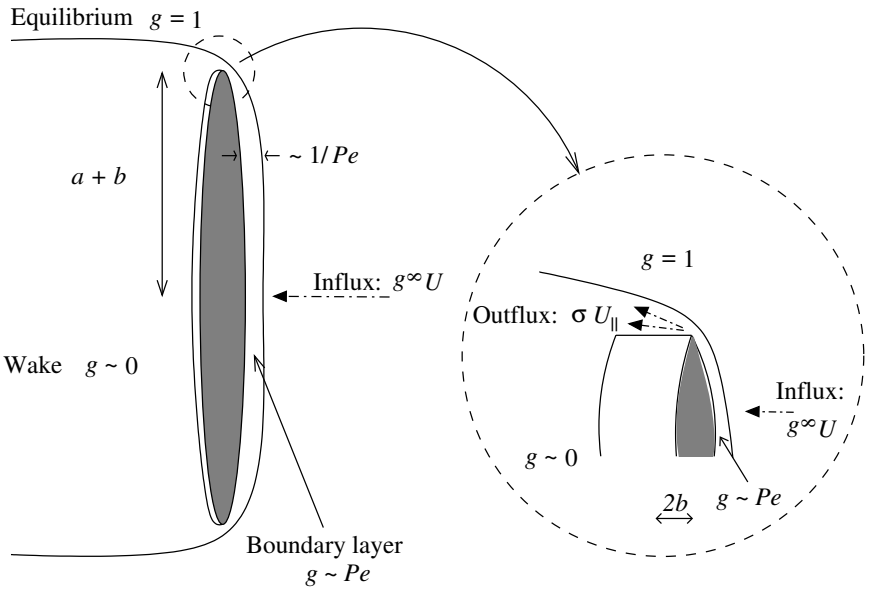


Figure 4.5: Sketch of the microstructure around a oblate probe at large $Pe$.

which $U_{||} \approx -U$. Therefore, $Q_{out}$ is

$$Q_{out} = 4\pi(a+b)b\sigma U.$$

Equating fluxes gives

$$\sigma = \frac{1}{4}\left(\frac{a+b}{b}\right) g^{\infty}. \tag{4.17}$$

From (4.15), (4.16), and (4.17) we find the boundary-layer microstructure to be (in *dimensionless* variables)

$$g^{ob}(\xi, \eta < \pi/2) \sim \frac{(\hat{a}+1)^2}{4} Pe \cos\eta e^{-(\hat{a}+1)Pe(\xi-\xi_e)\cos\eta}.$$

The pair-distribution function at contact is

$$g^{ob}(\xi_e, \eta < \pi/2) = \frac{(\hat{a}+1)^2}{4} Pe \cos\eta; \tag{4.18}$$

thus, there is a large $O(Pe = Ub/D)$ excess of bath particles in front of the probe. Moreover, this excess is amplified by a geometrical factor of $(\hat{a}+1)^2/4$. Properly, though, for the circular disk (and, actually, for all oblate probes) one should scale lengths with the disk radius $a+b$ (it being the dominant length scale in the problem), which yields

$$g^{ob}(\xi_e, \eta < \pi/2) = \frac{(\hat{a}+1)}{4} Pe_a \cos\eta,$$

where $Pe_a = U(a+b)/D$ is a Péclet number based on the major semiaxis of $S_e$, rather than the bath particle radius $b$. Now we find the $O(Pe_a)$ build-up of bath particles is amplified by $(\hat{a}+1)/4$, which is simply the ratio of the surface areas for entry $[\pi(a+b)^2]$ and exit $[4\pi b(a+b)]$ of bath particles: physically, bath particles are advected into the boundary layer through a much $[O(a+b)]$ larger area (the disk face) than from which they can escape (the disk edge), leading to large amplification of the $O(Pe)$ build-up.

Finally, from (4.12) and (4.18) (i.e., with the Péclet number based on the bath particle radius) the microviscosity increment is

$$\Delta\eta_r^{ob} = \frac{3(1+\hat{a})^2\phi}{2K^{ob}Pe}\int_0^{\pi/2} g^{ob}\cos\eta\sin\eta d\eta = \frac{(\hat{a}+1)^4}{8}\frac{\phi}{K^{ob}}.$$

#### 4.4.2.2 Prolate probe

For the prolate probe at large $Pe$ an equation for the boundary-layer microstructure may be obtained by balancing again 'radial' diffusion ($D\nabla_\xi^2 g$) and advection ($\boldsymbol{U}_\perp \cdot \nabla_\xi g$), viz.

$$D\frac{\partial^2 g^{pr}}{\partial t^2} + Uc\sinh\xi_e\cos\eta\frac{\partial g^{pr}}{\partial t} = 0, \tag{4.19}$$

where $t = \xi - \xi_e$, and $c\sinh\xi_e = 2b$ is the minor semiaxis of the excluded-volume surface.

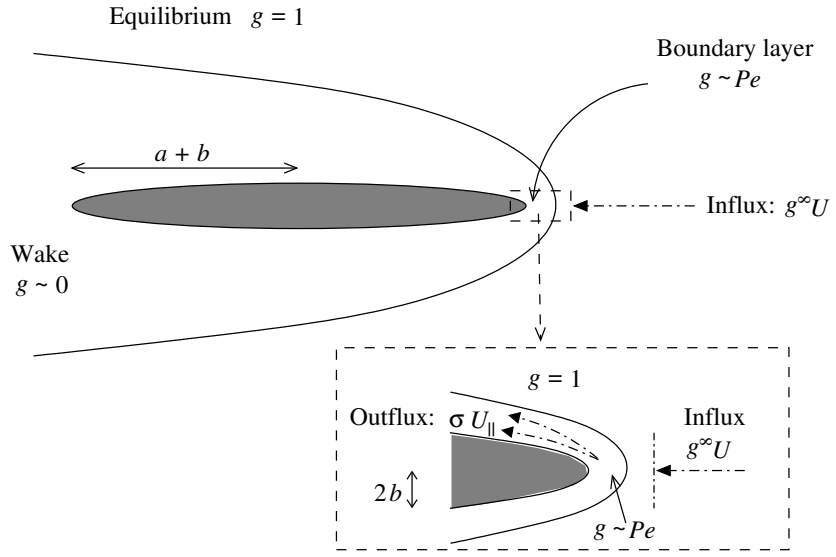


Figure 4.6: Sketch of the microstructure around an prolate probe at large $Pe$.

The solution to (4.19) is

$$g^{pr} \sim A^{pr}(\eta) e^{-2Ubt\cos\eta/D}. \tag{4.20}$$

Integrating across the boundary layer we find the surface density $\sigma$ to be

$$\sigma = \int_0^\infty A^{pr}(\eta) e^{-2Ubt\cos\eta/D} dt = \frac{DA^{pr}(\eta)}{2Ub\cos\eta}. \tag{4.21}$$

As for oblate probe, the function $A^{pr}(\eta)$ can be found through a flux balance. To make progress, we consider the limiting case $a \gg b$, where the excluded volume degenerates to a long thin rod [of length $2(a+b)$ and diameter $4b$]. A sketch of this configuration is shown in figure 4.6. The flux of bath particles $Q_{in}$ entering the boundary layer (located at the upstream tip of the rod) is

$$Q_{in} = \pi(2b)^2 g^\infty U.$$

The surface density is advected past the tip of the rod with the parallel component of

velocity $U_{||} = \boldsymbol{U}\cdot\hat{\boldsymbol{\eta}} = -U\cosh\xi_e \sin\eta/(\sinh^2\xi_e + \sin^2\eta)^{1/2}$ and leaves the boundary layer along the length of the rod, over a cylindrical (exit) surface of perimeter $4\pi b$ and length $a+b$. (The boundary layer terminates at the midpoint of the rod; hence the length of the exit surface is half that of the rod.) The long thin rod is obtained in the limit $\xi_e \to 0$, in which case $U_{||} \approx -U$. Therefore, $Q_{out}$ is

$$Q_{out} = 4\pi b(a+b)\sigma U.$$

At steady state, setting $Q_{in} = Q_{out}$ gives

$$\sigma = \left(\frac{b}{a+b}\right) g^{\infty}. \tag{4.22}$$

From (4.20), (4.21), and (4.22) the boundary layer microstructure is (in *dimensionless* variables)

$$g^{pr}(\xi, \eta < \pi/2) \sim \frac{2}{\hat{a}+1} Pe\cos\eta e^{-2Pe(\xi-\xi_e)\cos\eta},$$

and the contact value is

$$g^{pr}(\xi_e, \eta < \pi/2) = \frac{2}{\hat{a}+1} Pe\cos\eta. \tag{4.23}$$

As before, there is a large $O(Pe = Ub/D)$ excess of bath particle in front of the probe. However, in contrast to the oblate probe, the excess is attenuated by a factor of $2/(\hat{a}+1)$. Physically, bath particles exit the boundary layer through a much $[O(a+b)]$ larger area (the rod length) than from which they enter (the rod tip), leading to an attenuation of the $O(Pe)$ build-up. Again, the attenuation factor is given (modulo a factor of 2 that could, actually, be incorporated into a new Péclet number based on the minor semiaxis of $S_e$:

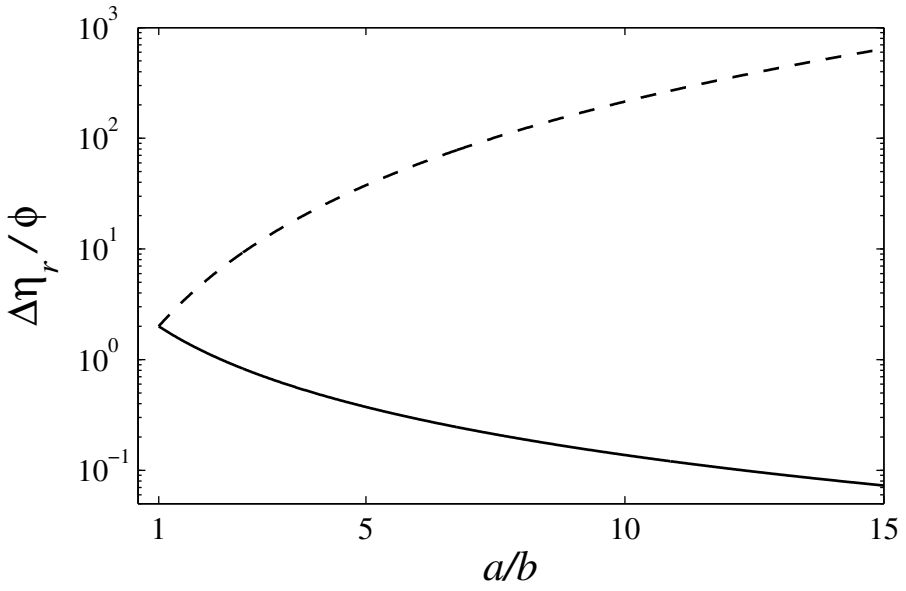


Figure 4.7: Microviscosity increments at large $Pe$ as a function of probe's aspect ratio $\hat{a} = a/b$. The legend is the same as in figure 4.4.

$Pe_b = 2bU/D$) by the ratio of the surface areas for entry $[\pi(2b)^2]$ and exit $[4\pi b(a+b)]$ of bath particles.

Lastly, from (4.11) and (4.23) the microviscosity increment is

$$\Delta\eta_r^{pr} = \frac{6\phi}{K^{pr}Pe}\int_0^{\pi/2} g^{pr}\cos\eta\sin\eta d\eta = \frac{4}{\hat{a}+1}\frac{\phi}{K^{pr}}.$$

Although our simple physical arguments are restricted to the limiting case $\hat{a} = a/b \gg 1$, for which the prolate(oblate) excluded volume degenerates to a long thin rod(thin disk), the results [(4.18) and (4.23)] are in fact valid for all $\hat{a}$ (see appendix 4.B). In figure 4.7 we plot the microviscosity increments at large $Pe$ as a function of the aspect ratio $\hat{a} = a/b$. For $\hat{a} \to 1$ both increments approach the value $2\phi$, which is the microviscosity increment for a spherical probe at large $Pe$ (Squires and Brady 2005). On increasing $\hat{a}$ the prolate(oblate) increment decays(grows) monotonically and vanishes(diverges) in the limit $\hat{a} \to \infty$.

Having determined the asymptotic values of the microviscosity for all $\hat{a}$, we now ask

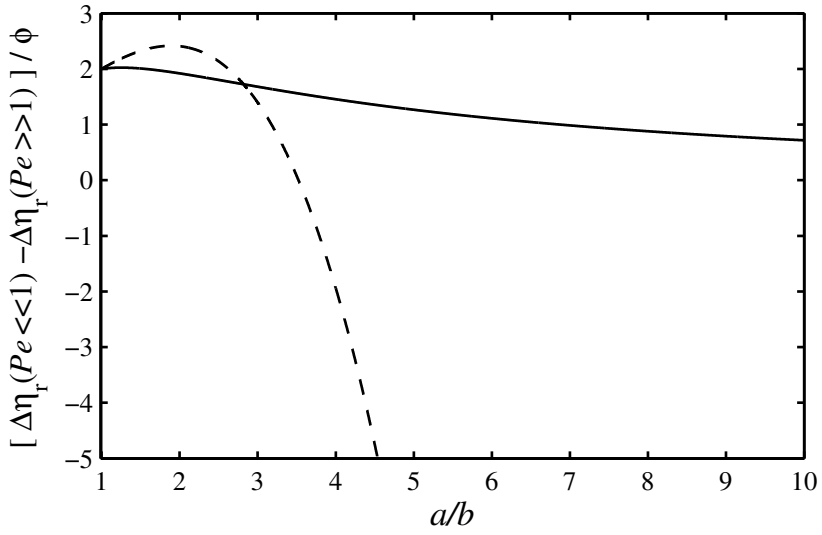


Figure 4.8: Difference in microviscosity increments at small $Pe$ and large $Pe$ as a function of probe aspect ratio $\hat{a} = a/b$. The broken(solid) line is the difference in the oblate(prolate) increment

how it transitions between these limits. To this end, it is useful to to examine the difference between the microviscosity in the limits $Pe \ll 1$ and $Pe \gg 1$ (see figure 4.8). For the prolate probe the microviscosity (for a fixed $\hat{a}$) at small $Pe$ is greater than at large $Pe$, which suggests the microviscosity decreases, or 'velocity-thins', as a function of $Pe$. However, the situation is not so simple for the oblate probe. On increasing $\hat{a}$ (above unity) the difference between small $Pe$ and large $Pe$ microviscosities is positive and growing, indicating that the microviscosity velocity-thins. This trend continues until $\hat{a} = 1.89$ (to two decimal places), at which point the difference reaches a maximum value and proceeds to decreases monotonically with increasing $\hat{a}$. The difference in microviscosities is zero for $\hat{a} = 3.52$ (to two decimal places), and for higher $\hat{a}$ it becomes increasingly negative. This behavior is rather unexpected and suggests that the microviscosity increment for the oblate probe increases, or 'velocity-thickens', as a function of $Pe$ for $\hat{a} > 3.52$. The conclusions of our asymptotic analysis will be verified by results from numerical solution of the Smoluchowski

equation and a physical explanation for this unexpected behavior will be offered. Next, we describe the methods used to perform the numerical computations.

## 4.5 Numerical methods

In the preceding section, we calculated the microstructure and microviscosity increments for small and large departures from equilibrium, using analytical perturbation methods. Here, we present numerical methods that facilitate computation of the microstructure and microviscosity at arbitrary $Pe$. One should note, however, that the Smoluchowski equation does in fact admit an exact solution in spheroidal coordinates (see appendix 4.A for details). Therefore, one could, in principle, use the exact solution to develop analytical formulas for the microviscosity valid for all $Pe$. The exact solution is found by separation of variables and takes the usual form of a eigenfunction summation; unfortunately, the complexity of the eigenfunctions coupled with the mixed (Robin) no-flux boundary condition (4.4) on $S_e$, makes numerical evaluation of the exact solution computationally prohibitive (especially at large $Pe$, where one needs to retain a large number of eigenfunctions). Therefore, we choose to solve the Smoluchowski equation numerically, using two different methods.

For $Pe < 10$ an expansion of the pair-distribution function in a series of Legendre polynomials is employed. This approach was used previously in determining the microstructure around a externally forced spherical probe (Khair and Brady 2006). As $Pe$ increases one requires more terms in the expansion to faithfully represent the increasingly complex microstructure, which is computationally taxing. Therefore, for $Pe > 10$ we solve the Smoluchowski equation using a finite-difference scheme, which accurately captures the boundary layer and wake structure present at large $Pe$. The two methods are described next.

### 4.5.1 Legendre polynomial expansion

For for the prolate probe, the pair-distribution $g^{pr}$ function is written as

$$g^{pr}(\xi,\eta) = 1 + \sum_{n=0}^{\infty} f_n^{pr}(\xi) P_n(\cos\eta), \tag{4.24}$$

where $P_n(z)$ is the Legendre polynomial of degree $n$ and argument $z$. This expansion is substituted into the Smoluchowski equation (4.7) and, after using the orthogonality property of the Legendre polynomials on the interval $[0,\pi]$, we arrive at a coupled set of ordinary differential equations for the expansion coefficients $f_n^{pr}(\xi)$:

$$\frac{1}{\sinh\xi}\left(\sinh\xi\frac{\partial f_n^{pr}}{\partial\xi}\right) - n(n+1)f_n^{pr} = -cPe\left(\alpha_n\cosh\xi + \beta_n\sinh\xi\right), \tag{4.25}$$

where the advective coupling terms are

$$\begin{aligned}
\alpha_n &= \frac{(n+1)(n+2)}{2n+3}f_{n+1}^{pr} + \frac{n(1-n)}{2n-1}f_{n-1}^{pr}, \\
\beta_n &= \frac{n+1}{2n+3}\frac{\partial f_{n+1}^{pr}}{\partial\xi} + \frac{n}{2n-1}\frac{\partial f_{n-1}^{pr}}{\partial\xi}.
\end{aligned}$$

The boundary conditions on the expansion coefficients are

$$\frac{\partial f_n^{pr}}{\partial\xi} = -c\sinh\xi_e\ Pe\left(\delta_{n1} + \frac{n+1}{2n+3}f_{n+1}^{pr} + \frac{n}{2n-1}f_{n-1}^{pr}\right) \quad \text{at} \quad \xi=\xi_e, \tag{4.26}$$

$$f_n^{pr} \to 0 \quad \text{as} \quad \xi\to\infty, \tag{4.27}$$

where $\delta_{ij}$ is Kronecker's delta. The system of equations is solved using the *Matlab* boundary-value problem solver *bvp4c*. The summation in (4.24) is truncated at $n = n_{max}$; for a given value of $Pe$, the choice of $n_{max}$ is made be requiring the resulting microviscosity

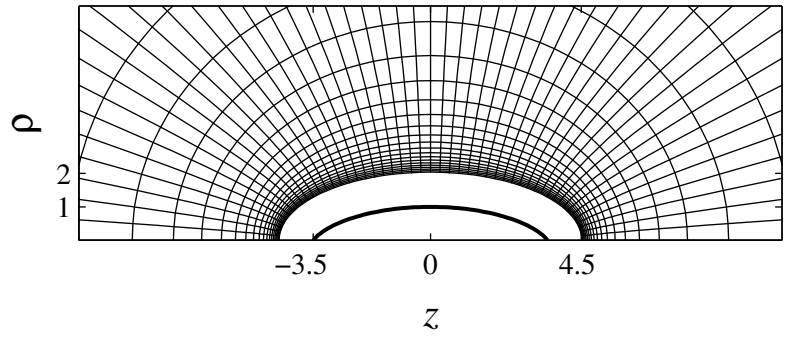


Figure 4.9: Sample finite difference gird for a prolate probe. Here, $\hat{a} = 3.5$; there are $50 \times 50$ grid points; and $Pe = 5$. Note the high density of mesh points near the excluded-volume surface.

increment not differ by more than 0.2% when computed using $n_{max}$ and $n_{max+1}$ terms. Of course, as $Pe$ increases so does $n_{max}$, which reflects the need for more terms in the expansion to capture the microstructure. The largest value for which we obtained a solution being $Pe = 10$, requiring $n_{max} = 50$.

For the oblate probe the pair-distribution function ($g^{ob}$) is expanded as per (4.24), and the differential equations for the expansion coefficients ($f_n^{ob}$, say) can be derived by applying the transformation (4.8) to (4.25) through (4.27).

### 4.5.2 Finite differences

Solving the Smoluchowski equation for $Pe > 1$ is numerically challenging: one has to capture the intricate boundary-layer structure at the front of the probe and the growing wake behind it. For $Pe > 10$ we approximate the Smoluchowski equation by a finite-difference equation (central differences are used for all derivatives) on a mesh that has a high density of grid points near the excluded-volume surface $S_e$ (to resolve the large gradients of the pair-distribution function in the boundary layer) and a lower density in the far-field. To create

this non-uniform mesh in (physical) $\xi$-space we employ a mapping from the semi-infinite domain $\xi \in [\xi_e, \infty)$ to the finite interval $p \in [0, 1]$, viz.

$$\ln p = -y \left( \omega + \frac{1-\omega}{1+y} \right),$$

where $\omega$ is a parameter and $y = Pe(\xi - \xi_e)$. Using a uniform grid in $p$-space one can (via adjustment of $\omega$) place a large number of nodes near $\xi = \xi_e$, to accurately model the near-field microstructure (e.g., see figure 4.9).

The linear system of equations resulting from discretization of the Smoluchowski equation is solved using a simple Jacobi iteration (the method closely resembles that of Khair and Brady 2006, who calculated the microstructure around a spherical probe at large $Pe$). As $Pe$ increases, one requires are greater number of grid points for the method to converge: the maximum value of $Pe$ for which a solution was obtained being $Pe = 100$.

## 4.6 Results

In this section, we present results for the microstructure and microviscosity at arbitrary $Pe$ for different values of $\hat{a}$. In figure 4.10 the microstructural deformation, $g - 1$, is plotted in the symmetry plane of a prolate probe of aspect ratio $\hat{a} = 3.5$, as a function of $Pe$. For $Pe \ll 1$ diffusion dominates: the deformation is approximately for-aft symmetric about the probe, with an $O(Pe)$ accumulation(depletion) on its upstream(downstream) side, in agreement with the linear-response analysis of § 4.4.1. Moving to $Pe \sim O(1)$ advection comes into play, and the symmetry is broken. For larger $Pe$ the probe acts as a 'bulldozer': it accumulates bath particles in a $O(Pe^{-1})$ thin boundary-layer on its upstream side and leaves a wake of bath-particle free suspending fluid behind it. Note, the 'width' of the

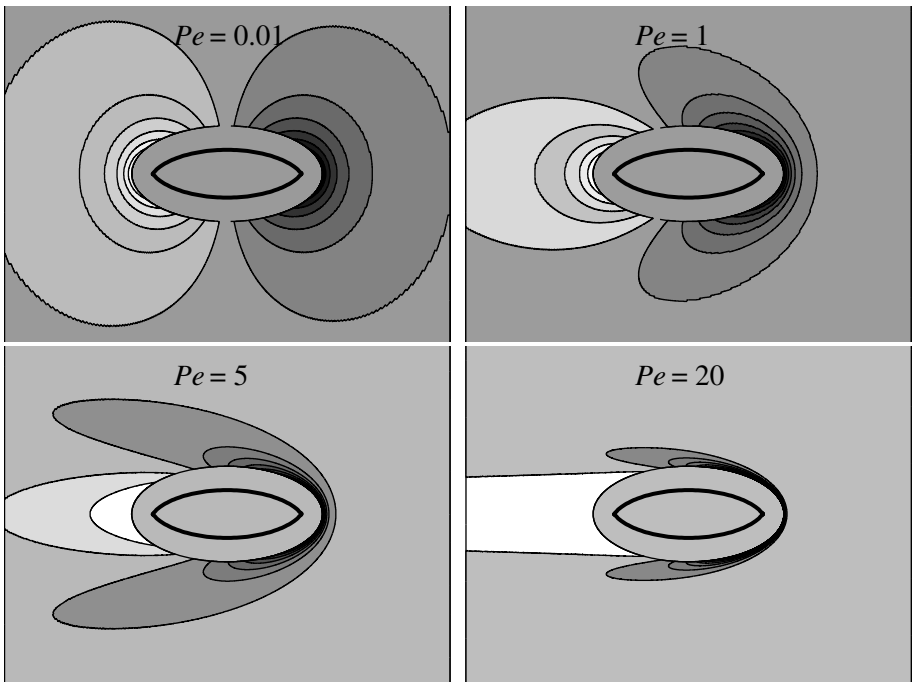


Figure 4.10: Microstructural deformation, $g-1$, in the symmetry plane of the prolate probe as a function of $Pe$. Here, $\hat{a} = 3.5$ and the probe moves from left to right. The excluded-volume surface is shown with zero deformation, $g = 1$; darker regions imply accumulation, $g > 1$; and lighter regions represent depletion, $g < 1$. The closed curve inside the excluded-volume surface is the probe itself.

boundary layer (i.e., its extent perpendicular to the probe motion) is on the order of the probe's minor semi-axis (which is equal to the bath particle radius $b$, in dimensional terms). Physically speaking, as the probe moves through the dispersion it pushes a single bath particle past it (per unit time).

In figure 4.11 we plot the microstructure around an oblate probe (again, with $\hat{a} = 3.5$) as a function of $Pe$. As per the prolate probe, the deformation is fore-aft symmetric at small $Pe$ and exhibits a boundary layer and wake structure at large $Pe$. However, the width of the boundary layer at large $Pe$ is now on the scale of the probe major semiaxis, $\hat{a}$. Physically, the oblate probe must push a greater (compared to the prolate probe) number of bath particles out of its path. Consequently, as discussed in § 4.4.2, there is a greater density of bath particles in the boundary layer for the oblate probe, $g^{ob} \sim (\hat{a}+1)^2 Pe$, than the prolate

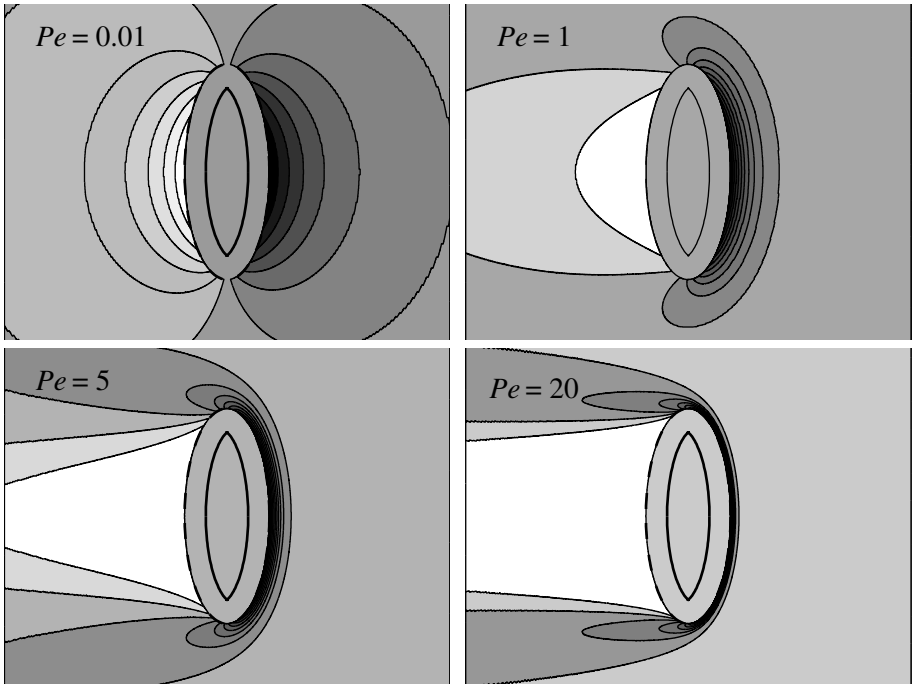


Figure 4.11: Microstructural deformation, $g-1$, in the symmetry plane of the oblate probe as a function of $Pe$. Here, $\hat{a} = 3.5$ and the probe moves from left to right. The shading scheme is the same as in figure 4.10.

probe, $g^{pr} \sim Pe/(\hat{a}+1)$. This disparity in bath-particle density affects fundamentally the microviscosity. Recall, in § 4.3 we interpreted the nonequilibrium microstructure around the probe in terms of an osmotic pressure imbalance; the microviscosity increment is the average of the imbalance over the excluded-volume surface. Now, the oblate probe has a bath-particle density of $O((\hat{a}+1)^2 Pe)$ in its boundary layer and a density of $O(1)$ in the wake behind it. The drop in density occurs over the 'edge' of the probe, which is $O(1)$ ($O(b)$ in dimensional terms). Thus, the osmotic pressure gradient that the oblate probe moves against is $O((\hat{a}+1)^2 Pe)$. In contrast, the prolate probe has a bath-particle density of $O(Pe/(\hat{a}+1))$ in its boundary layer and $O(1)$ in its wake, and the drop occurs over the $O(\hat{a}+1)$ length of the probe. Therefore, the osmotic pressure gradient for the prolate probe is $O(Pe/(\hat{a}+1)^2)$, which is far smaller than for the oblate probe. Consequently, the average additional external force imposed on the probe (to maintain its steady motion in the face of

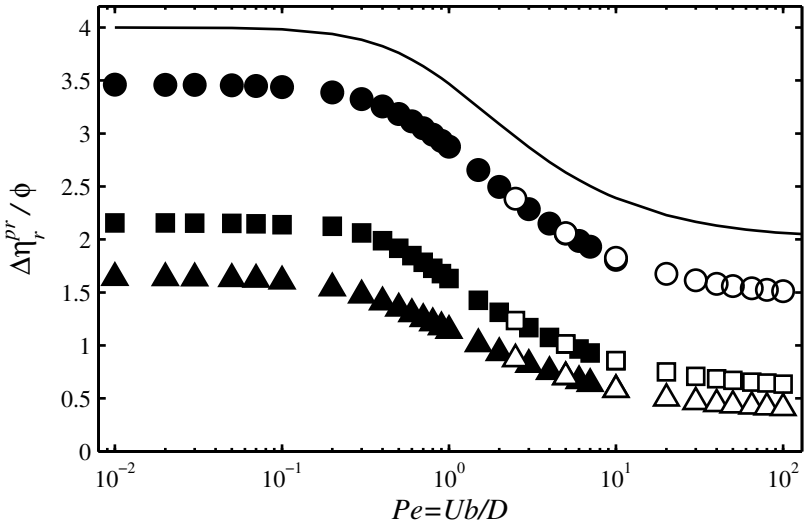


Figure 4.12: Microviscosity increment for a prolate probe, $\Delta\eta_r^{pr}$, as a function of $Pe = Ub/D$ for different $\hat{a} = a/b$: circles, $\hat{a} = 1.5$; squares, $\hat{a} = 3.5$; and triangles, $\hat{a} = 5$. The filling pattern indicates the method of numerical solution: filled, Legendre expansion; and empty, finite differences. The solid line is the microviscosity increment for a spherical probe, $\hat{a} = 1$, from Squires and Brady (2005).

the osmotic pressure gradient) is far greater in the oblate case. Thus, from the Stokes law definition of the microviscosity, the microviscosity increment inferred by the oblate probe is greater than that by the prolate probe. Next, we examine in detail the microviscosity as a function of $Pe$ and $\hat{a}$ for both prolate and oblate probes.

In figure 4.12 we plot the prolate microviscosity increment, $\Delta\eta_r^{pr}$, as a function of $Pe$ for $\hat{a} = 1.5$, 3.5, and 5. For each value of $\hat{a}$, $\Delta\eta_r^{pr}$ velocity-thins from a Newtonian plateau at small $Pe$ to a second Newtonian plateau at large $Pe$. This behavior is in qualitative agreement with the spherical probe increment calculated by Squires and Brady (2005). At a given value of $Pe$, $\Delta\eta_r^{pr}$ decreases with increasing $\hat{a}$, due to two factors: (i) the upstream contact value of the pair-distribution function decreases; and (ii) the length of the probe (i.e., parallel to the direction of motion) grows. Thus, following the arguments in the paragraph above, the osmotic pressure gradient across $S_e$ decreases with increasing $\hat{a}$; consequently,

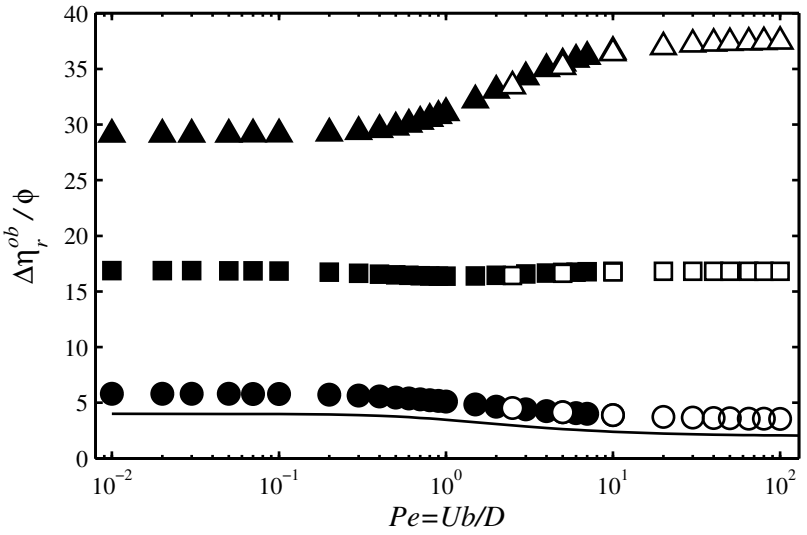


Figure 4.13: Microviscosity increment for an oblate probe, $\Delta\eta_r^{ob}$, as a function of $Pe = Ub/D$ for different $\hat{a} = a/b$. The legend is the same as in figure 4.12.

the additional external force, and hence the microviscosity, also decrease. Ultimately, as $\hat{a} \to \infty$ — a long thin rod probe — the microviscosity vanishes for all $Pe$. In this limit, the rod appears infinitely long on the scale of a bath particle; as such, the bath particles cannot 'see' the ends of the rod, and the microstructure is not disturbed by the moving rod.

Figure 4.13 plots the microviscosity increment for the oblate probe, $\Delta\eta_r^{ob}$, versus $Pe$ for $\hat{a} = 1.5$, 3.5, and 5. We note for a given value of $Pe$ that $\Delta\eta_r^{ob}$ increases with increasing $\hat{a}$, which can be explained by the following argument. As $\hat{a}$ increases the area of the excluded-volume surface upon which bath particles from upstream are incident grows ($\sim \hat{a}^2$). This leads to an increase in the contact value of the pair-distribution function on the upstream side of the probe. Moreover, unlike the prolate probe, as $\hat{a}$ increases the extent of the probe parallel to its motion (i.e., its thickness) stays fixed at 2 ($2b$ in dimensional terms). Thus, the osmotic pressure gradient of bath particles across $S_e$ increases with increasing $\hat{a}$. As a result, the average external force on the probe, and hence the microviscosity, increase. Finally, as $\hat{a} \to \infty$ — a thin circular disk probe — the microviscosity diverges for all $Pe$: essentially,

the probe must overcome an infinite osmotic pressure gradient to maintain steady motion.

The behavior of the oblate increment for a given value of $\hat{a}$ as a function of $Pe$ is far more complicated than the prolate increment. For $\hat{a} = 1.5$, in analogy to the spherical and prolate probe microviscosities, the oblate increment monotonically velocity-thins from a small $Pe$ plateau ($\Delta\eta_r^{ob}/\phi = 5.80$ at $Pe = 0.001$) to a plateau at high $Pe$ ($\Delta\eta_r^{ob}/\phi = 3.55$ at $Pe = 100$). However, for $\hat{a} = 3.5$ the increment is approximately independent of $Pe$: it undergoes a small amount of velocity-thinning initially (from $\Delta\eta_r^{ob}/\phi = 16.87$ at $Pe = 0.001$), which is recovered by velocity-thickening at $Pe \sim O(1)$ and greater (at $Pe = 100$ we find $\Delta\eta_r^{ob}/\phi = 16.81$). For $\hat{a} = 5$ the increment monotonically velocity-thickens from a small $Pe$ plateau ($\Delta\eta_r^{ob}/\phi = 29.13$ at $Pe = 0.001$) until a plateau at large $Pe$ is reached ($\Delta\eta_r^{ob}/\phi = 37.46$ at $Pe = 100$). Note, these numerical results are in agreement entirely with the asymptotic analysis presented in § 4.4. (In fact, $\hat{a} = 3.5$ was chosen for numerical calculations because it is close the value, $\hat{a} = 3.52$, at which the small and large $Pe$ microviscosities are predicted to be equal, cf. figure 4.8.)

At first glance, the transition of $\Delta\eta_r^{ob}$ from velocity-thinning to -thickening with increasing $\hat{a}$ might seem somewhat strange. There is a relatively simple explanation, however. Let us define the microstructural deformation $F^{ob} = g^{ob} - 1$. Recall, from (4.12) the microviscosity increment is directly proportional to $F^{ob}$ averaged over the excluded-volume surface, $S_e$. At small $Pe$ the deformation is forced by the no-flux condition at contact [$dF^{ob}/d\xi = -(\hat{a}+1)Pe\cos\eta$ at $\xi = \xi_e$], and the contact value of the deformation was found to be (see § 4.4.1)

$$F^{ob}(Pe \ll 1) = (\hat{a}+1)H(\lambda_e)Pe\cos\eta,$$

where

$$H(\lambda_e) = \frac{(1+\lambda_e^2)^{1/2}(\lambda_e \cot^{-1}\lambda_e - 1)}{\lambda_e(1-\lambda_e\cot^{-1}\lambda_e) - \cot^{-1}\lambda_e}.$$

The function $H(\lambda_e) = 0.5$ for $\hat{a} = 1$, and $H(\lambda_e) \to 0.64$ (to two decimal places) as $\hat{a} \to \infty$. Hence, to make progress we assume $H(\lambda_e) \approx 0.5$ for all $\hat{a}$. The microstructural deformation averaged over $S_e$ is

$$\langle F^{ob}(Pe \ll 1)\rangle_{S_e} = \int_0^\pi F^{ob}(Pe \ll 1)\cos\eta \sin\eta d\eta = 2(\hat{a}+1)H(\lambda_e)Pe \approx (\hat{a}+1)Pe.$$

At large $Pe$, from the boundary-layer analysis in § 4.4.2 we found

$$F^{ob}(Pe \gg 1) = \frac{1}{4}(\hat{a}+1)^2 Pe\cos\eta;$$

importantly, this solution is valid only upstream of the probe, $\eta \leq \pi/2$; downstream there is wake in which $g^{ob} \approx 0$. The surface-averaged deformation is

$$\langle F^{ob}(Pe \gg 1)\rangle_{S_e} = \int_0^{\pi/2} F^{ob}(Pe \gg 1)\cos\eta\sin\eta d\eta = \frac{1}{4}(\hat{a}+1)^2 Pe.$$

The small- and large-$Pe$ averaged deformations are equal, ($\langle F^{ob}(Pe \gg 1)\rangle_{S_e} = \langle F^{ob}(Pe \ll 1)\rangle_{S_e}$), at $\hat{a} = 3$, which is close to the transition point $\hat{a} = 3.52$ of $\Delta\eta_r^{ob}$ from velocity-thinning to -thickening. (Of course, using the full form of $H(\lambda_e)$ would yield the correct value of $\hat{a} = 3.52$ from our simple analysis.)

Before proceeding to the next section, we pause to make a comment about the micro-viscosity increment $\Delta\eta_r$ as a function of $Pe$. As mentioned above, $\Delta\eta_r$ is proportional to the contact value of the pair-distribution function, which is $O(Pe)$ for all $Pe$. And, since there is a factor of $1/Pe$ multiplying the microstructural integrals in (4.11) and (4.12),

$\Delta\eta_r \sim O(Pe^0)$ for all $Pe$. (The microstructural pictures at small and large $Pe$ are, of course, very different: for $Pe \ll 1$ the probe causes a small $O(Pe)$ deformation over a large $O(1/Pe)$ region; in the singular limit of $Pe \to \infty$ there is a large $O(Pe)$ deformation in a small $O(1/Pe)$ thin boundary layer.) However, while we know $\Delta\eta_r$ is of $O(Pe^0)$ at both small and large $Pe$, there is no way (without detailed calculation) of knowing in which limit it is greater (and hence if $\Delta\eta_r$ thins or thickens with increasing $Pe$). The thinning/thickening behavior is dependent on the detailed geometry — in our case the (prolate or oblate) probe shape and $\hat{a}$ — of the probe and bath particle configuration. This points up the care that must be taken when selecting a probe (in terms of its shape, size, and orientation) for use in a particular active microrheology experiment.

## 4.7 Discussion

In this study, we have developed a model for active (nonlinear) microrheology experiments using non-spherical probe particles. We consider the probe to be a body of revolution moving along its symmetry axis at constant velocity, through a colloidal dispersion of spherical bath particles. The probe's shape is such that the excluded-volume, or contact, surface between it and a bath particle is a(n) prolate(oblate) spheroid when its major(minor) axis is the axis of revolution. The average external force imposed on the probe (to maintain its steady motion) can be interpreted in terms of a microviscosity of the dispersion via application of Stokes drag law. This is, possibly, the simplest model system one could conceive; however, as shown in the preceding sections, the resulting microrheology is nontrivial.

It is instructive to determine to what extent the results from a particular microrheological experiment represent the true, or macrorheological, properties of a material. As mentioned in § 4.1, for highly complex or unknown materials it is, in general, not possible

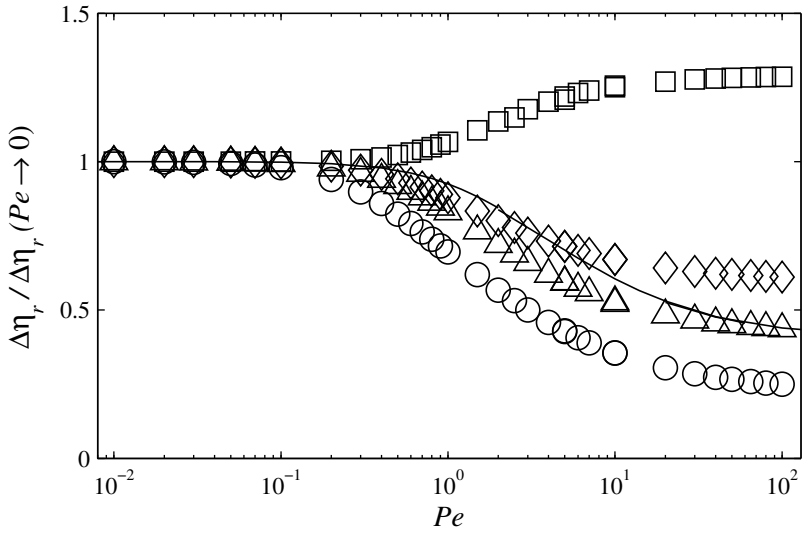


Figure 4.14: Comparison of microviscosity increments from prolate and oblate probes with the macroviscosity (from Bergenholtz et al. (2002)). Legend: diamonds, oblate $\hat{a} = 1.5$; squares, oblate $\hat{a} = 5$; triangles, prolate $\hat{a} = 1.5$; circles, prolate $\hat{a} = 5$; and the solid line is the macroviscosity. For the microviscosity $Pe = Ub/D$, and for the macroviscosity $Pe = (b\dot{\gamma})b/D$ (with $\dot{\gamma}$ the shear-rate).

to compare micro to macro, as the relevant scalings are not known *a priori*. However, for our model system the scalings are available; thus, we can make a direct, quantitative comparison between the micro- and macro-viscosity. In figure 4.14 we plot the microviscosity increments for the oblate and prolate probes (for $\hat{a} = 1.5$ and $\hat{a} = 5$) versus the macroviscosity (from Bergenholtz et al. 2002). Note, for macrorheology there is no probe particle, and all particles are spherical with equal radii, $b$. The relative macroviscosity is $\Delta\eta_r^{macro} = 1 + 5/2\phi + \Delta\eta_r^{macro}\phi^2$; the macro increment is $O(\phi^2)$, while the micro increment is $O(\phi)$. [The $O(\phi)$ contribution to the macroviscosity is, of course, the single-particle 'Einstein correction'.] Furthermore, the Péclet number for the macroviscosity is $Pe = (b\dot{\gamma})b/D$, where $\dot{\gamma}$ is the shear-rate. To aid in the comparison, the macro- and micro-viscosities have been normalized by their respective limiting values as $Pe \to 0$. For $\hat{a} = 1.5$ the oblate and prolate increments velocity-thin with increasing $Pe$, which qualitatively, and near quanti-

tatively, mimics the 'shear-thinning' of the macroviscosity. However, for $\hat{a} = 5.0$ the oblate increment velocity-thickens for all $Pe$, which is qualitatively different from the macroviscosity behavior. One should not think, though, this disagreement somehow invalidates the microrheological results. On the contrary, it simply highlights the fundamental physical differences between microrheology and macrorheology (for detailed discussions of these differences see Squires and Brady 2005; Khair and Brady 2006), and emphasizes the care that must be taken when comparing the results from a microrheology experiment using non-spherical probes to the 'equivalent' macrorheological measurements.

The theoretical framework presented in this work can be used to study other related problems. A natural extension is to consider a non-spherical (oblate or prolate) probe that is translating with fixed velocity at an angle ($\beta$, say) to its symmetry axis (see figure 4.15). In this sense, the present study considers the special case $\beta = 0$, in which the microstructure is axisymmetric about the direction of motion; however, for non-zero $\beta$ the microstructure is now fully three dimensional. Consequently, to maintain steady motion not only must an additional external force (above the Stokes drag) be imposed on the probe, but also an external torque to prevent the probe from rotating. In appendix 4.C we present a preliminary analysis of this problem for small and large $Pe$. In the linear-response regime ($Pe \ll 1$) the symmetry of the $O(Pe)$ microstructural deformation (4.C-2) dictates that the dispersion does not exert a torque on the probe. In contrast, far from equilibrium ($Pe \gg 1$) the highly nonlinear microstructure does necessitate the application an external torque. Importantly, we find that the external torque is directed perpendicular to the plane of motion; therefore, there is no tendency for the probe to rotate out of that plane or about its symmetry axis. Furthermore, for longwise, $\beta = 0$, and broadside, $\beta = \pi/2$, motion the external torque vanishes, indicating that both are steady modes of translation. However,

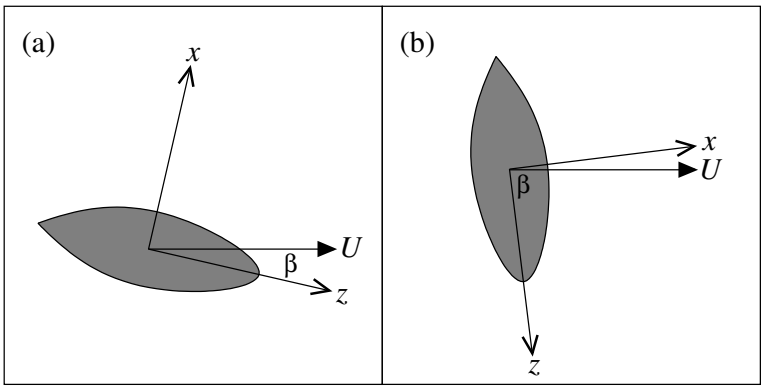


Figure 4.15: Sketch of a prolate probe translating at angle $\beta$ to its symmetry axis: (a) near-longwise motion, $\beta \ll 1$; and (b) near-broadside motion, $\pi/2 - \beta \ll 1$. Note, the $y$-axis is directed out of the page.

for near-longwise, $\beta \ll 1$, and near-broadside, $\pi/2 - \beta \ll 1$, motion the dispersion exerts a torque that generates a clockwise rotation. Therefore, the longwise(broadside) translation is an unstable(stable) equilibrium. Moreover, we conjecture that these are the only two equilibrium modes; hence, if $\beta \neq 0$ the rod will adopt a terminal broadside orientation in the absence of an external torque.

Could the external torque on the probe be used to infer more than just a microviscosity? To address this question, we note that Leal (1975) studied the motion of a slender ($\hat{a} \gg 1$) axisymmetric rod translating in a second-order fluid. The second-order fluid is the second 'term' in an asymptotic expansion of the stress of a viscoelastic fluid in the limit of slow and slowly varying flow (the first term is simply the Newtonian stress), which includes first ($N_1$) and second ($N_2$) normal stress differences. Like us, Leal (1975) finds that the second-order fluid exerts a torque that is out of the rod's plane of motion; moreover, longwise and broadside translation are the only two steady configurations — which configuration is stable depends on the normal stress differences. The direction of the torque [see equation (47) in Leal 1975] is given by the sign of the quantity $4N_1 + N_2$: if $4N_1 + N_2$ is positive(negative) the longwise(broadside) mode is stable. Recently, this result has been shown to hold for a

prolate spheroid of arbitrary $\hat{a}$ for the special case $N_1 = -2N_2$ (Galdi 2000).

Our analysis for a prolate probe gave a stable broadside orientation which, assuming that the second-order fluid model is applicable to the hard-sphere colloidal dispersion, suggests that $4N_1 + N_2 < 0$ at large $Pe$. Is this consistent with macrorheological observations? To answer this question, we note that the microstructure at large $Pe$ was found via a simple 'radial-balance approximation' of the full boundary-layer equations (see appendix 4.C for details), used originally by Brady and Morris (1997) in calculation of the microstructure of a sheared dispersion at large $Pe$. From the radial-balance microstructure Brady and Morris (1997) computed the normal stress differences of the dispersion, finding that $N_1 \equiv 0$ (by the symmetry properties of the approximate boundary-layer equations) and $N_2 < 0$ at large $Pe$. This implies that $4N_1 + N_2$ is indeed negative, in agreement with our microrheological findings that broadside translation is stable. However, note that Bergenholtz et al. (2002) solved numerically the full macrorheological boundary-layer equations and found $N_1$ to be 'small' and positive at large $Pe$; infact their results give $4N_1 + N_2 > 0$, which suggests that the longwise translation should be stable. Clearly, one needs to solve the full microrheological boundary-layer equations (4.C-3) to determine if the broadside mode is stable as a result of the radial-balance approximation (i.e., would a solution of the full equations give a stable longwise translation). Furthermore, as shown by Zarraga et al. (2000), for non-colloidal dispersions ($Pe^{-1} \equiv 0$) both $N_1$ and $N_2$ are proportional to the shear-rate $\dot{\gamma}$, whereas for the second-order fluid $N_1$ and $N_2$ scale as $\dot{\gamma}^2$. Thus, it is not clear that one can use Leal's (Leal 1975) results to infer normal stress differences from a prolate probe translating at large $Pe$.[2] Nevertheless, the discussion above has shown that microrheology

[2]However, colloidal dispersions near equilibrium ($Pe \ll 1$) posses normal stress differences, $N_1$ and $N_2$, that do scale as $\dot{\gamma}^2$ (Brady and Vicic 1995), in accordance with the second-order fluid model. Thus one can use Leal's analysis to infer normal stress differences for a prolate probe moving at small $Pe$. Of course, $Pe$ must be sufficient in magnitude such that the dispersion is out of the linear-response regime, for which there is no torque on the probe.

with non-spherical probes has the potential to give information on normal stress differences.

In this study we supposed, for simplicity, that the minor semiaxis of the probe was equal in size to the bath particle radius. This allowed the probe-bath geometry to be specified by a single quantity: the probe aspect ratio $\hat{a} = a/b$. One could, however, relax this assumption by setting the bath particle radius equal to $c$ (here, $c$ is not to be confused with the scale factor in spheroidal coordinates, of course). Now, the geometry is set by the ratios $\hat{a}_1 = a/b$ and $\hat{a}_2 = a/c$. The additional degree of freedom allows us to study several interesting limiting cases: for example, (i) $\hat{a}_1 \gg 1$ and $\hat{a}_2 \sim O(1)$ — a flat disk (oblate) / thin rod (prolate) translating past bath particles of comparable size; and (ii) $\hat{a}_1 \gg 1$ and $\hat{a}_2 \ll 1$ — a flat disk (oblate) / thin rod (prolate) moving through a dispersion of much larger bath particles. Case (i) is particularly interesting, as while the oblate probe is a flat disk, it now pushes only one bath particle out of its path (per unit time). Hence, one expects the microviscosity inferred from it may not velocity-thicken at large $Pe$.

Recently, Khair and Brady (2005) examined a spherical probe executing small-amplitude oscillations in a colloidal dispersion. The small-amplitude condition requires that the Péclet number be much less than unity; the system is in the linear-response (passive) regime. There is, however, no such restriction on the (appropriately non-dimensionalized) oscillation frequency ($\alpha$, say). In this limit, the microstructural deformation has a component that is in phase with the probe oscillation and a component that is out of phase. Through application of Stokes drag law one can define a complex microviscosity of the dispersion — the real and imaginary parts of which correspond to liquid-like and solid-like response, respectively. In that sense, the oscillating probe may be used to study the 'microviscoelasticity' of the dispersion As a variation on that (and the present) theme, one may consider a non-spherical probe moving parallel to its axis of revolution with a small-amplitude oscillatory velocity.

Again, the microstructural response will contain in-phase and out of phase components, from which a complex microviscosity can be inferred. For a spherical probe Khair and Brady (2005) demonstrated that the Cox-Merz rule is obeyed to a reasonable degree (see figure 4 in that paper). Recall, the Cox-Merz rule states that the frequency dependence of the modulus of the complex microviscosity should be almost identical to the $Pe$ dependence of the steady microviscosity. For the oblate probe, it would be interesting to see if the complex microviscosity 'frequency-thickens' at large $\alpha$, in analogy to the velocity-thickening of the nonlinear (steady) microviscosity at large $Pe$ for $\hat{a} > 3.5$ (see figure 4.13). If the complex microviscosity does not thicken this would constitute a violation of the Cox-Merz rule.

## 4.8 Bibliography

M. Atakhorammi, G. H. Koenderink, C. F. Schmidt, and F. C. MacKintosh. Short-time inertial response of viscoelastic fluids: observation of vortex propagation. *Phys. Rev. Lett.*, 95:208302, 2005.

J. Bergenholtz, J. F. Brady, and M. Vicic. The non-Newtonian rheology of dilute colloidal suspensions. *J. Fluid Mech.*, 456:239–275, 2002.

J. F. Brady and J. F. Morris. Microstructure of strongly sheared suspensions and its impact on rheology and diffusion. *J. Fluid Mech.*, 348:103–139, 1997.

J. F. Brady and M. Vicic. Normal stresses in colloidal dispersions. *J. Rheol.*, 39:545–566, 1995.

B. R. Daniels, B. C. Masi, and D. Wirtz. Probing single-cell micromechanics in vivo: the micorheology of *C. elegans* developing embryos. *Biophys. J.*, 90:4712–4719, 2006.

C. Flammer. *Spheroidal wave functions.* Stanford University Press, 1957.

G. P. Galdi. Slow steady fall of rigid bodies in a second-order fluid. *J. Non-Newtonian Fluid Mech.*, 90:81–89, 2000.

F. Gittes, B. Schnurr, P. D. Olmsted, F. C. MacKintosh, and C. F. Schimdt. Microscopic viscoelasticity: shear moduli of soft materials determined from thermal fluctuations. *Phys. Rev. Lett.*, 79:3286–3289, 1997.

P. Habdas, D. Schaar, A. C. Levitt, and E. R. Weeks. Forced motion of a probe particle near the colloidal glass transition. *Europhys. Lett.*, 79:477–483, 2004.

J. Happel and H. Brenner. *Low Reynolds number Hydrodynamics.* Prentice-Hall, 1965.

L. Joly, C. Ybert, and L. Bocquet. Probing the nanohydrodynamics at the liquid-solid interfaces using thermal motion. *Phys. Rev. Lett.*, 96:046101, 2006.

A. S. Khair and J. F. Brady. "Microviscoelasticity" of colloidal dispersions. *J. Rheol.*, 49: 1449–1481, 2005.

A. S. Khair and J. F. Brady. Single particle motion in colloidal dispersions: A simple model for active and nonlinear microrheology. *J. Fluid Mech.*, 557:73–117, 2006.

L. G. Leal. The slow motion of a slender rod-like particle in a second-order fluid. *J. Fluid Mech.*, 69:305–337, 1975.

F. C. MacKintosh and C. F. Schmidt. Microrheology. *Curr. Opin. Colloid Interface Sci.*, 4:300–307, 1999.

R. E. Mahaffy, C. K. Shih, F. C. MacKintosh, and J. Käs. Scanning probe-based frequency dependent microrheology of polymer gels and biological cells. *Phys. Rev. Lett.*, 85:880–883, 2000.

T. G. Mason, K. Ganesan, J. H. van Zanten, D. Wirtz, and S. C. Kuo. Particle tracking microrheology of complex fluids. *Phys. Rev. Lett.*, 79:3282–3285, 1997.

T. G. Mason and D. A. Weitz. Optical measurements of frequency-dependent linear viscoelastic moduli of complex fluids. *Phys. Rev. Lett.*, 74:1250–1253, 1995.

A. Meyer, A. Marshall, B. G. Bush, and E. M. Furst. Laser tweezer microrheology of a colloidal suspension. *J. Rheol.*, 50:77–92, 2006.

P. M. Morse and H. Feshbach. *Methods of theoretical physics. Part II.* McGraw-Hill, 1953.

I. S. Sohn and R. Rajagopalan. Microrheology of model quasi-hard-sphere dispersions. *J. Rheol.*, 48:117–140, 2004.

T. M. Squires and J. F. Brady. A simple paradigm for active and nonlinear microrheology. *Phys. Fluids*, 17:073101, 2005.

N. Ter-Oganessian, D. A. Pink, and A. Boulbitch. Active microrheology of networks composed of semiflexible polymers: theory and comparison with simulations. *Phys. Rev. E.*, 72:041511, 2005a.

N. Ter-Oganessian, B. Quinn, D. A. Pink, and A. Boulbitch. Active microrheology of networks composed of semiflexible polymers: computer simulation of magnetic tweezers. *Phys. Rev. E*, 72:041510, 2005b.

R. S. Tu and V. Breedveld. Microrheological detection of protein unfolding. *Phys. Rev. E.*, 72:041914, 2005.

T. A. Waigh. Microrheology of complex fluids. *Rep. Prog. Phys.*, 68:685–742, 2005.

H. H. Wensink and H. Löwen. Rhythmic cluster generation in strongly driven colloidal dispersions. *Phys. Rev. Lett.*, 97:038303, 2006.

I. E. Zarraga, D. A. Hill, and D. T. Leighton. The characterization of the total stress of concentrated suspensions of noncolloidal spheres in Newtonian fluids. *J. Rheol.*, 44: 185–220, 2000.

# Appendices to chapter 4

## 4.A Exact solution of the Smoluchowski equation

Here, we derive an exact solution to the Smoluchowski equation (4.2) in spheroidal coordinates. In the interests of brevity, we deal with the prolate probe only; however, it is possible to calculate an exact solution for the oblate probe also (either from first principles or by simply using the transformation (4.8) in the formulas below).

First, we write the pair-distribution function as

$$g^{pr} = 1 + f^{pr} e^{-c\kappa \cosh\xi \cos\eta},$$

where $\kappa = Pe/2$. Substituting this into the Smoluchowski equation (4.7) we find that $f^{pr}$ satisfies a modified Helmholtz equation:

$$\frac{1}{\sinh\xi}\frac{\partial}{\partial\xi}\left(\sinh\xi\frac{\partial f^{pr}}{\partial\xi}\right) + \frac{1}{\sin\eta}\frac{\partial}{\partial\eta}\left(\sin\eta\frac{\partial f^{pr}}{\partial\eta}\right) = c^2\kappa^2(\sinh^2\xi + \sin^2\eta) f^{pr}, \qquad (4.A\text{-}1)$$

subject to the boundary conditions

$$\begin{aligned} \frac{\partial f^{pr}}{\partial\xi} &= -2\kappa\cos\eta\left[1 + 2e^{(\hat{a}+1)\kappa\cos\eta}\right] \quad \text{at} \quad \xi = \xi_e, \\ f^{pr} &\to 0 \qquad \text{as} \quad \xi \to \infty. \end{aligned}$$

The solution to (4.A-1) is found by separation of variables (see, e.g., Flammer 1957) and can be written as an eigenfunction expansion:

$$f^{pr} = \sum_{n=0}^{\infty} A_n S_{0n}(ik,\mu) R_{0n}^{(3)}(ik,\tau),$$

where $\mu = \cos\eta$, $\tau = \cosh\xi$, $k = c\kappa$, and the $A_n$ are expansion coefficients. The function

$S_{0n}$ is the (axisymmetric) angle function of the first kind and is defined as a sum of Legendre polynomials:

$$S_{0n}(ik,\mu) = \sum_{r=0,1}^{\infty} d_r^{0n}(ik) P_r(\mu),$$

where the summation is over even(odd) values of $r$ when $n$ is even(odd). The summation coefficients $d_r^{0n}$ obey a recurrence relation — see equation 3.1.4 of Flammer (1957). The function $R_{0n}^{(3)}$ is known as the radial function of third kind, which vanishes for large $\tau$ (thus satisfying the far-field boundary condition). Formally, $R_{0n}^{(3)}$ may be written as a summation of spherical Hankel functions of the first kind (denoted as $h_r^{(1)}$)

$$R_{0n}^{(3)}(ik,\tau) = \left( \sum_{r=0,1}^{\infty} d_r^{0n}(ik) \right)^{-1} \sum_{r=0,1}^{\infty} i^{r-n} d_r^{0n}(ik) h_r^{(1)}(ik\tau).$$

To satisfy the boundary condition at contact we require

$$\sum_{n=0}^{\infty} A_n \frac{\partial R_{0n}^{(3)}}{\partial \xi}|_{\xi_e} S_{0n}(ik,\mu) = -2\kappa\mu \left[ 1 + 2e^{(\hat{a}+1)\kappa\mu} \right].$$

We note that the angle functions satisfy are orthogonal on the interval $[-1,1]$:

$$\int_{-1}^{1} S_{0n}(ik,\mu) S_{0p}(ik,\mu) d\mu = \delta_{np} N_{0n}(k);$$

the normalization constant $N_{0n}(k)$ is given by equation 3.1.33 of Flammer (1957). Hence, the constants $A_n$ are given by

$$A_n = -\frac{2\kappa}{N_{0k} \frac{\partial R_{0n}^{(3)}}{\partial \xi}|_{\xi_e}} \left[ \int_{-1}^{1} S_{0n}(ik,\mu)\mu d\mu + 2\int_{-1}^{1} S_{0n}(ik,\mu) e^{(\hat{a}+1)\kappa\mu} \mu d\mu \right]. \qquad (4.\text{A-2})$$

The first integral in (4.A-2) can be performed analytically; however, the second integral

must be computed numerically, which does, unfortunately, limit the usefulness of the exact solution.

Finally, from (4.11) the microviscosity increment is given by

$$\Delta\eta^{pr} = \frac{6\phi}{K^{pr}Pe}\sum_{n=0}^{\infty} A_n R_{0n}^{(3)}(ik,\tau_e)\int_{-1}^{1} S_{0n}(ik,\mu)e^{-(\hat{a}+1)\kappa\mu}\mu d\mu.$$

Again, this integral must be performed numerically.

## 4.B Asymptotic analysis at large $Pe$

In this appendix, we present a rigorous asymptotic analysis of the microstructure at large $Pe$, to confirm the findings of our simple physical arguments in § 4.4.2. Detailed calculations are performed for the prolate probe, and the results for the equivalent oblate probe are obtained via the transformation (4.8).

At large $Pe$ advection dominates the microstructure and, except near the probe, the Smoluchowski equation (4.2) reduces to $\hat{\boldsymbol{U}}\cdot\boldsymbol{\nabla}g = 0$, implying $g$ is constant along a 'streamline'. The far-field condition (4.3) dictates this constant to be unity; however, this solution does not satisfy the no-flux boundary condition on the excluded-volume surface $S_e$ (4.4). The Smoluchowski equation is in fact singular in the limit $Pe^{-1} \to 0$, and there exists an 'inner' region (or boundary layer) adjacent to the probe in which Brownian diffusion balances advection, thus enabling the no-flux condition on $S_e$ to be met.

To focus on the boundary layer we introduce the stretched, or inner, coordinate $y =$

$Pe(\xi - \xi_e)$. The Smoluchowski equation in prolate spheroidal coordinates (4.7) becomes

$$\begin{aligned} & \frac{Pe^2}{\sinh\xi_e + Pe^{-1} y \cosh\xi_e} \frac{\partial}{\partial y}\left[(\sinh\xi_e + Pe^{-1} y\cosh\xi_e)\frac{\partial g^{pr}}{\partial y}\right] + \frac{1}{\sin\eta}\frac{\partial}{\partial\eta}\left(\sin\eta\frac{\partial g^{pr}}{\partial\eta}\right) \\ = \quad & cPe\left[(\cosh\xi_e + Pe^{-1}y\sinh\xi_e)\sin\eta\frac{\partial g^{pr}}{\partial\eta} - Pe\left(\sinh\xi_e + Pe^{-1}y\cosh\xi_e\right)\cos\eta\frac{\partial g^{pr}}{\partial y}\right], \end{aligned} \tag{4.B-1}$$

subject to the boundary conditions

$$\begin{aligned} \frac{\partial g^{pr}}{\partial y} = -c\sinh\xi_e\cos\eta g^{pr} \qquad & \text{at} \qquad y = 0. \\ g^{pr} \to 1 \qquad & \text{as} \qquad y \to \infty, \end{aligned}$$

Inside the boundary layer we expand the pair-distribution function as $g^{pr}(y,\eta;Pe) = g_1^{pr}(y,\eta)Pe + g_2^{pr}(y,\eta) + O(Pe^{-1})$. Inserting this expansion into (4.B-1) yields equations for $g_1^{pr}$ and $g_2^{pr}$. For $g_1^{pr}$ we have

$$\begin{aligned} \frac{\partial^2 g_1^{pr}}{\partial y^2} \quad & + \quad c\sinh\xi_e\cos\eta\frac{\partial g_1^{pr}}{\partial y} = 0, \\ \frac{\partial g_1^{pr}}{\partial y} \quad & + \quad c\sinh\xi_e\cos\eta g_1^{pr} = 0 \quad \text{at} \quad y = 0, \\ g_1^{pr} \to \quad & 0 \qquad \text{as} \quad y \to \infty, \end{aligned}$$

which has the solution

$$g_1^{pr}(y,\eta) = A(\eta)e^{-cy\sinh\xi_e\cos\eta}.$$

The 'angular' function $A(\eta)$ will be found at the next order. Note, this solution is only valid upstream of the probe ($0 \le \eta \le \pi/2$), where advection balances diffusion in the

boundary layer. Downstream of the probe, $\pi/2 \leq \eta \leq \pi$, bath particles are advected away and there exists a wake in which $g \approx 0$.

The system for $g_2^{pr}$ reads

$$\begin{aligned}
\frac{\partial^2 g_2^{pr}}{\partial y^2} + c\sinh\xi_e\cos\eta\frac{\partial g_2^{pr}}{\partial y} &= c\cosh\xi_e\left(\sin\eta\frac{\partial g_1^{pr}}{\partial \eta} - y\cos\eta\frac{\partial g_1^{pr}}{\partial y}\right) - \coth\xi_e\frac{\partial g_1^{pr}}{\partial y}, \\
\frac{\partial g_2^{pr}}{\partial y} + c\sinh\xi_e\cos\eta g_2^{pr} &= 0 \quad \text{at} \quad y = 0. \\
g_2^{pr} \to 1 \qquad &\text{as} \qquad y \to \infty,
\end{aligned}$$

The far-field condition on $g_2^{pr}$ ensures correct matching to the advective outer solution of unity. Some straightforward working yields

$$g_2^{pr}(y,\eta) = [\beta_1(\eta) + \beta_2(\eta)y + \beta_3(\eta)y^2]e^{-cy\sinh\xi_e\cos\eta} - \frac{\beta_2}{c\sinh\xi_e\cos\eta},$$

where

$$\begin{aligned}
\beta_1(\eta) &= -\frac{\coth\xi_e}{c\sinh\xi_e}\left[\frac{A(\eta)}{\cos^3\eta} + \frac{\tan\eta}{\cos\eta}\frac{dA(\eta)}{d\eta}\right] - \frac{B(\eta)}{c\sinh\xi_e\cos\eta}, \\
\beta_2(\eta) &= -\coth\xi_e\left[\tan\eta\frac{dA(\eta)}{d\eta} + (1+\sec^2\eta)A(\eta)\right], \\
\beta_3(\eta) &= -\frac{c\cosh\xi_e}{2\cos\eta}A(\eta).
\end{aligned}$$

One can determine the function $B(\eta)$ by continuing the perturbation expansion to the next order in $Pe$; this is not, however, required for our current purposes. To satisfy the far-field condition on $g_2^{pr}$ requires $\beta_2(\eta) = -c\sinh\xi_e\cos\eta$, from which we obtain an equation for $A(\eta)$:

$$\tan\eta\frac{dA(\eta)}{d\eta} + (1+\sec^2\eta)A(\eta) = c\sinh\xi_e\tanh\xi_e\cos\eta,$$

which has the solution $A(\eta) = \frac{1}{2} c \sinh\xi_e \tanh\xi_e \cos\eta$. Hence, the pair-distribution function in the boundary layer may be written as

$$g^{pr}(y,\eta;Pe) = \frac{1}{2} c \sinh\xi_e \tanh\xi_e \cos\eta e^{-cPe(\xi-\xi_e)\sinh\xi_e\cos\eta} + O(1). \tag{4.B-2}$$

From (4.11) we find that at large $Pe$ the microviscosity increment is

$$\Delta\eta_r^{pr} = \frac{6\phi}{K^{pr}Pe}\int_0^{\pi/2} g^{pr}\cos\eta\sin\eta d\eta = \frac{4}{\hat{a}+1}\frac{\phi}{K^{pr}} + O(Pe^{-1}),$$

where we have used the relations $c\sinh\xi_e = 2$ and $\tanh\xi_e = 2/(\hat{a}+1)$

For the oblate probe, using the transformation (4.8) on (4.B-2), we find the pair-distribution function in the boundary layer is

$$g^{ob}(y,\eta;Pe) = \frac{1}{2} c \cosh\xi_e \coth\xi_e \cos\eta e^{-cPe(\xi-\xi_e)\cosh\xi_e\cos\eta} + O(1),$$

and from (4.12) the microviscosity increment is

$$\Delta\eta_r^{ob} = \frac{3(1+\hat{a})^2\phi}{2K^{ob}Pe}\int_0^{\pi/2} g^{ob}\cos\eta\sin\eta d\eta = \frac{(\hat{a}+1)^4}{8}\frac{\phi}{K^{ob}} + O(1).$$

where we have used $c\cosh\xi_e = \hat{a}+1$ and $\coth\xi_e = (\hat{a}+1)/2$. Note, both results above are in complete agreement with the simple geometric balance presented in § 4.4.2.

## 4.C Prolate probe translating at an angle to its symmetry axis

Here, we present an asymptotic analysis for a prolate probe translating at an angle $\beta$ to its symmetry axis (see figure 4.15). The dimensionless velocity of the probe is

$$\hat{\boldsymbol{U}} = \cos\beta\hat{\boldsymbol{z}} + \sin\beta\hat{\boldsymbol{x}}.$$

In addition to an external force $\langle \boldsymbol{F}^{ext} \rangle$ (4.9) one must, in general, apply an external torque $\langle \boldsymbol{T}^{ext} \rangle$ to maintain steady motion. The 'osmotic force' exerted *by* the bath particles *on* an infinitesimal area $dS_e$ of the probe is $-nkTg(\boldsymbol{r})\boldsymbol{n}dS_e$. Therefore, the average external torque about the center of the probe is

$$\langle \boldsymbol{T}^{ext} \rangle = nkT \oint \boldsymbol{r} \wedge \boldsymbol{n} g(\boldsymbol{r}) dS_e,$$

which for the prolate probe reduces to

$$\frac{\langle \boldsymbol{T}^{ext} \rangle}{6\eta b^2 U} = \frac{6\phi}{Pe \sinh^2 \xi_e} \int_0^{2\pi} \int_0^{\pi} g^{pr}(\boldsymbol{r})(\cos\theta\hat{\boldsymbol{y}} - \sin\theta\hat{\boldsymbol{x}}) \sin^2\eta \cos\eta d\eta d\theta. \tag{4.C-1}$$

Here, $\theta$ is the azimuthal coordinate about the $z$-axis. In the linear-response regime ($Pe \ll 1$) we write $g^{pr} = 1 + Pe f^{pr}$, where $f^{pr}$ solves Laplace's equation and vanishes at large distances. The no-flux condition on the excluded volume surface is

$$\frac{\partial f^{pr}}{\partial \xi} = -c\left(\cos\beta \sinh\xi_e \cos\eta + \sin\beta \cosh\xi_e \sin\eta \cos\theta\right) \quad \text{at} \quad \xi = \xi_e,$$

representing a weighted combination of axisymmetric (along $z$-axis) and

non-axisymmetric (along $x$-axis) forcing. The solution for $f^{pr}$ is found to be

$$f^{pr} = -\frac{2}{dQ_1^0(\tau)/d\xi|_{\xi_e}} \cos\beta \cos\eta Q_1^0(\tau) - \frac{\hat{a}+1}{dQ_1^1(\tau)/d\xi|_{\xi_e}} \sin\beta \sin\eta Q_1^1(\tau) \cos\theta, \qquad (4.C\text{-}2)$$

where $\tau = \cosh\xi$ and $Q_n^m(\tau)$ is an associated Legendre polynomial of the second kind. Using (4.C-2) with (4.C-1) we find that the external torque is identically zero — as a consequence of the symmetry of microstructure — in the linear-response regime. On increasing $Pe$ this fore-aft symmetry will be broken, resulting in a non-zero torque.

We now consider the opposite extreme, $Pe \gg 1$, where advection dominates the microstructure. As in appendix 4.B, the problem is singular in this limit with a boundary layer adjacent to the probe in which diffusion balances advection. Thus, near $S_e$ we stretch $\xi$ as $y = Pe(\xi - \xi_e)$. The Smoluchowski equation for $g^{pr}$ in stretched coordinates reads

$$\begin{aligned}
\frac{\partial^2 g^{pr}}{\partial y^2} \quad &+ \quad Pe^{-1} \coth\xi_e \frac{\partial g^{pr}}{\partial y} = Pe^{-1} c \sin\beta \frac{\sinh^2\xi_e + \sin^2\eta}{\sinh\xi_e \sin\eta} \sin\theta \frac{\partial g^{pr}}{\partial \theta} \\
&- \quad c\cos\beta \left[ (\sinh\xi_e + Pe^{-1} y \cosh\xi_e) \cos\eta \frac{\partial g^{pr}}{\partial y} - Pe^{-1} \cosh\xi_e \sin\eta \frac{\partial g^{pr}}{\partial \eta} \right] \\
&- \quad c\sin\beta \left[ (\cosh\xi_e + Pe^{-1} y \sinh\xi_e) \sin\eta \frac{\partial g^{pr}}{\partial y} + Pe^{-1} \sinh\xi_e \cos\eta \frac{\partial g^{pr}}{\partial \eta} \right] + O(Pe^{-2});
\end{aligned} \qquad (4.C\text{-}3)$$

furthermore, $g^{pr}$ must satisfy the boundary conditions

$$\frac{\partial g^{pr}}{\partial y} = -c\left(\cos\beta \sinh\xi_e \cos\eta + \sin\beta \cosh\xi_e \sin\eta \cos\theta\right) g^{pr} \quad \text{at} \quad y = 0, \qquad (4.C\text{-}4)$$

$$g^{pr} \to 1 \quad \text{as} \quad y \to \infty. \qquad (4.C\text{-}5)$$

One can, in principle, solve for $g^{pr}$ by posing the expansion $g^{pr} = Pe\, g_1^{pr} + g_2^{pr} + O(Pe^{-1})$ as per appendix 4.B; however, the resulting algebra is rather cumbersome. Instead, to find

$g^{pr}$ we invoke the 'radial-balance approximation' used by Brady and Morris (1997) for the microstructure of a sheared suspension at large $Pe$. The physical idea is that the competition between 'radial' advection and diffusion generates the large gradients of $g^{pr}$ present in the boundary layer. Thus, we form a 'leading-order' equation by retaining the $O(Pe^0)$ *and* the $O(Pe^{-1})$ radial $(\partial/\partial y)$ terms in (4.C-3), which gives

$$\frac{\partial^2 g^{pr}}{\partial y^2} + v_y \left(1 + \frac{1}{v_y} Pe^{-1} \coth \xi_e + Pe^{-1} \frac{\partial \ln v_y}{\partial \xi_e} y\right) \frac{\partial g^{pr}}{\partial y} = 0, \tag{4.C-6}$$

where $v_y$ is the 'radial' advective velocity in the boundary layer:

$$v_y(\eta, \theta) = c \left(\cos\beta \sinh \xi_e \cos\eta + \sin\beta \cosh \xi_e \sin\eta \cos\theta\right). \tag{4.C-7}$$

The solution to (4.C-6) satisfying (4.C-4) and (4.C-5) is

$$g^{pr}(y) = \frac{1 - v_y \int_0^y e^{-s(z)} dz}{1 - v_y \int_0^\infty e^{-s(z)} dz},$$

where $s(z)$ is given by

$$s(z) = v_y \left[\left(1 + \frac{1}{v_y} Pe^{-1} \coth \xi_e\right) z + \frac{1}{2} Pe^{-1} \frac{\partial \ln v_y}{\partial \xi_e} z^2\right].$$

Note, this solution is valid only if $v_y > 0$: the locus of points on the excluded-volume surface satisfying $v_y = 0$ *defines* the transition between upstream $(v_y > 0)$ and downstream $(v_y < 0)$ regions. Physically, bath particles are advected from upstream towards the probe, resulting in a boundary layer, while downstream they are advected away from it, giving a

low-density wake in which $g^{pr} \approx 0$. We can rewrite $g^{pr}$ as

$$g^{pr}(y) = g^{pr}(0)\left[1 - v_y \int_0^y e^{-s(z)} dz\right],$$

and in the limit $Pe \to \infty$ it is found that

$$\begin{aligned} g^{pr}(0) &= Pe \tanh \xi_e v_y, \\ &= \frac{2Pe}{(\hat{a}+1)} \left[2\cos\beta\cos\eta + (\hat{a}+1)\sin\beta\sin\eta\cos\theta\right], \end{aligned} \tag{4.C-8}$$

showing that there is an $O(Pe)$ accumulation of bath particles in the upstream boundary layer. Note that for $\beta = 0$ we recover, modulo a factor of 2, the contact value for a probe translating along its symmetry axis, cf. (4.23).

Substituting the above into (4.C-1) we can now evaluate the external torque. However, there is a subtlety: the range of $\eta$ in (4.C-1) is formally between 0 to $\pi$ (from the upstream to downstream end of the probe), while the contact value (4.C-8) is valid only in the upstream region, from $\eta = 0$ to $\eta = \eta_l$, where $v_y(\eta_l, \theta) = 0$. (The interval $\eta < \eta_l < \pi$ corresponds to the downstream region in which $g^{pr} \approx 0$.) From (4.C-7), $\eta_l$ satisfies the equation

$$2\cos\beta\cos\eta_l + (\hat{a}+1)\sin\beta\sin\eta_l\cos\theta = 0. \tag{4.C-9}$$

To make progress, we focus on the limits of near-longwise ($\beta \ll 1$) and near-broadside ($\pi/2 - \beta \ll 1$) translation. For $\beta \ll 1$, the solution to (4.C-9) is

$$\eta_l = \frac{\pi}{2} + \frac{\hat{a}+1}{2}\beta\cos\theta,$$

i.e., the $O(\beta)$ tilting causes the boundary layer-wake transition to occur slightly downstream of the probe midpoint ($\eta = \pi/2$). The external torque for $\beta \ll 1$ is found to be

$$\frac{\langle \boldsymbol{T}^{ext} \rangle}{6\pi\eta b^2 U} = 3\phi\beta \left[ \left( \frac{\hat{a}+1}{2} \right)^2 - 1 \right] \hat{\boldsymbol{y}}, \tag{4.C-10}$$

where we have used $\sinh^2 \xi_e = [(\hat{a}+1)^2/4 - 1]^{-1}$. Similarly, for $\pi/2 - \beta \ll 1$ we have

$$\eta_l = \pi - \frac{\hat{a}+1}{2} \left( \frac{\pi}{2} - \beta \right) \cos\theta;$$

thus, in near-broadside translation the boundary layer occupies nearly the entire upstream-facing side of the probe, and the resulting torque is

$$\frac{\langle \boldsymbol{T}^{ext} \rangle}{6\pi\eta b^2 U} = \frac{15}{8}\phi \left( \frac{\pi}{2} - \beta \right)^4 \left( \frac{\hat{a}+1}{2} \right)^4 \left[ \left( \frac{\hat{a}+1}{2} \right)^2 - 1 \right] \hat{\boldsymbol{y}}. \tag{4.C-11}$$

From (4.C-10) and (4.C-11) one can make the following observations. First, for a spherical probe, $\hat{a} = 1$, the torque vanishes as expected. Second, the torque is directed along the positive $y$-axis; hence, there is no tendency for the probe to rotate out of its plane of motion (or about its symmetry axis). Third, for longwise, $\beta = 0$, and broadside, $\beta = \pi/2$, motion the torque vanishes, indicating that both of these are possible equilibrium modes of translation. However, by referring to figure 4.15 for near-longwise and near-broadside motion the external torque rotates the probe anticlockwise; consequently, the dispersion exerts a torque that generates a clockwise rotation. Hence, in the absence of an external torque the longwise(broadside) translation is an unstable(stable) equilibrium configuration. Furthermore, we conjecture that these are the only two equilibrium modes; hence, if $\beta \neq 0$ the rod will adopt a terminal broadside orientation.

Finally, we note that in obtaining (4.C-8) the $O(Pe^{-1})$ 'angular' terms in (4.C-3) were neglected, while the $O(Pe^{-1})$ 'radial' terms were retained, thus forming a 'radial balance' with the leading order $[O(Pe^{0})]$ terms (4.C-6). This is generally not a valid procedure, as the angular terms in (4.C-3) will affect the $O(Pe^{0})$ angular structure of the pair-distribution function at contact, $g^{pr}(0)$. However, to leading order $[O(Pe)]$ the angular structure of the contact value should not be affected by the neglect of the $O(Pe^{-1})$ angular terms, although the magnitude of $g^{pr}(0)$ might be. [Indeed, this is evident for $\beta = 0$, where the radial-balance solution (4.C-8) gives a contact value that is identical, modulo a factor of 2, to the solution of the full boundary-layer equations, (4.23).] Therefore, while a solution of the full boundary-layer equations (4.C-3) may well alter the magnitude of the torque in (4.C-10) and (4.C-11), we do not expect the sense of rotation to change.

# Chapter 5

# On the motion of two particles translating with equal velocities through a colloidal dispersion

## 5.1 Introduction

Colloidal dispersions, comprising (sub-) micrometer sized particles in a suspending fluid, occur in a variety of natural and man-made settings: inks, aerosols, foodstuffs, paints, and biological materials are but a few everyday examples. From an academic viewpoint, the length and time scales relevant to colloidal dispersions place them in a perhaps unique position at the intersection of fluid dynamics, statistical mechanics, and macromolecular chemistry. A central goal of colloid science is the calculation of the macroscopic, or effective, properties of a dispersion (e.g., diffusion coefficients, viscosity, conductivity), from interactions at the microscopic level, or microscale. In these materials, it is the interplay of hydrodynamic, interparticle, and Brownian (or thermal) forces that determines the microscale configuration, or microstructure, of the colloidal particles. In equilibrium the balance is between interparticle and Brownian forces, and the microstructure is given by the familiar Boltzmann distribution. The action of external agents, such as ambient flow-fields or body forces, drives the microstructure out of equilibrium, where hydrodynamic forces now enter the description.

In this work, we study the nonequilibrium microstructure created by two colloidal ('probe') particles translating with equal, fixed velocities through an otherwise undisturbed colloidal dispersion. The driven motion of the probes pushes the dispersion's microstructure out of equilibrium; counteracting this is the Brownian diffusion of the colloidal 'bath' particles, which acts to heal this microstructural wound. As a consequence of the microstructural deformation, the dispersion exerts an entropic, or thermal, force on each of the probes, which is a function of the separation between the probes $\boldsymbol{d}$, and the dimensionless velocity of the probes, or Péclet number, $Pe$. Our aim is to calculate the entropic forces on the probes over

the entire range of $\boldsymbol{d}$ and $Pe$, for which one must, of course, determine the nonequilibrium microstructure.

In equilibrium, it is well known that entropic forces between colloidal particles are often produced by the addition of macromolecular entities to the suspending fluid. These entities may be other (usually smaller) colloidal particles (Crocker et al. 1999), polymers (Verma et al. 1998), or stiff rods (Heldon et al. 2003). The generated forces have important physical consequences and applications, including crystallization (Anderson and Lekkerkerker 2002) and self-assembly (Yodh et al. 2001). A classic example, first noted by Asakura and Oosawa (1958), is the so-called 'depletion attraction', where two colloidal particles in a dilute bath of smaller colloids experience an attractive (depletion) force when the excluded-volume surfaces of the large particles overlap, owing to an increase in volume available to the bath particles. The depletion force can lead to depletion flocculation (Jenkins and Snowden 1996) and has been seen to promote phase separation in binary colloid mixtures (Kaplan et al. 1994). The diluteness of bath particles is crucial; for more concentrated systems interactions between the bath particles themselves can lead to a repulsive force between the two large colloids (Crocker et al. 1999; Tehver et al. 1999).

Away from equilibrium, the depletion interaction between colloidal particles must compete with external driving mechanisms. This can lead to pattern formation on macroscopic (i.e., much greater the particle size) length scales: e.g., 'lane' formation in binary mixtures of oppositely driven colloids (Dzubiella et al. 2002; Chakrabarti et al. 2004). To our knowledge, the only theoretical study of depletion forces out of equilibrium is that of Dzubiella et al. (2003), who computed the forces on two fixed colloidal particles in a drifting bath of smaller Brownian particles. As expected, for non-zero drift velocities the forces on the fixed particles are not equal, which Dzubiella et al. (2003) interpreted as a violation of

Newton's third law. Their analytical approach [Brownian Dynamics (BD) simulations were also performed] consisted of superimposing the microstructural deformations induced by a single fixed particle in the drifting bath, at the (two) locations relevant to the two-particle configuration. This is valid only if the fixed particles are widely separated and the (appropriately non-dimensionalized) drift velocity is small; somewhat surprisingly, the theoretical results are in good agreement with the BD simulations even when these two conditions are not met. In this work, subject to the assumptions listed below, we are able to avoid such approximations and restrictions in computing the microstructural deformation caused by the moving probes.

In the present study, we make four important assumptions. First, for simplicity, we take the probes and bath particles to be spherical and of equal size. However, note that the theory developed in § 5.2 for the nonequilibrium microstructure may be easily extended to different-sized probe and bath particles. Hence, we could, if desired, recover the small bath particle limit of Dzubiella et al. (2003). Second, in analogy to classic theories of depletion forces in equilibrium, we take the volume fraction of bath particles to be small, so that interactions between bath particles may be neglected. Furthermore, to facilitate an analytical treatment, we assume the microstructure is determined by interactions of the probes with a single bath particle. Third, hydrodynamic interactions mediated by the suspending fluid are neglected. While seemingly over-restrictive, this condition can be realized for particles whose excluded-volume (or hard-sphere) radii are much greater than their physical (or hydrodynamic) radii, such as present in sterically- or charge-stabilized dispersions. Fourth, we assume that the particles move along their line of centers, $\boldsymbol{d}$. Therefore, the microstructural deformation is axisymmetric about $\boldsymbol{d}$, and the (entropic) forces on the probes are directed along $\boldsymbol{d}$. With these conditions in place, we are able to derive a closed equation for the

nonequilibrium microstructure in terms of a 'conditional pair-distribution function', which gives the probability of finding a bath particle at a particular location, given the two-probe configuration.

The rest of the chapter is organized as follows. In § 5.2.1 we present the three-body Smoluchowski equation governing the spatio-temporal evolution of the nonequilibrium microstructure, and the entropic forces on the probes are derived in § 5.2.2. The Smoluchowski equation must be solved numerically and, as discussed in § 5.3, different approaches are used for overlapping and non-overlapping probe excluded-volumes. Results are presented in § 5.4 and concluding remarks offered in § 5.5.

## 5.2 Governing equations

### 5.2.1 Nonequilibrium microstructure

Consider a collection of $N$ colloidal particles of radii $a$ suspended in a Newtonian fluid of density $\rho$ and viscosity $\eta$. The $N$-particle probability density function for finding the particles in a given spatial configuration at time $t$ is $P_N(\boldsymbol{x}_1, \boldsymbol{x}_2, \boldsymbol{x}_3, \ldots, \boldsymbol{x}_N, t)$, where the labels 1 and 2 refer to the trailing and leading probes, respectively, and $3 \rightarrow N$ are the $N-2$ bath particles. The probability density satisfies an $N$-particle Smoluchowski equation:

$$\frac{\partial P_N}{\partial t} + \sum_{i=1}^{N} \boldsymbol{\nabla}_i \cdot \boldsymbol{j}_i = 0,$$

where $\boldsymbol{j}_i = \boldsymbol{U}_i P_N$ is the probability flux carried by particle $i$. Neglecting hydrodynamic interactions, the configuration-specific, or instantaneous, velocity of particle $i$, $\boldsymbol{U}_i$, is given by

$$\boldsymbol{U}_i = \frac{1}{6\pi\eta a} \left( \boldsymbol{F}_i - kT \boldsymbol{\nabla}_i \ln P_N \right), \tag{5.1}$$

where $kT$ is the thermal energy; $\boldsymbol{F}_i$ is the external force acting on particle $i$; and $-kT\boldsymbol{\nabla}_i \ln P_N$ is the thermal, or Brownian, force on particle $i$, due to random thermal fluctuations of the solvent molecules. We proceed by integrating the $N$-particle Smoluchowski equation over the configurational degrees of freedom of $N-3$ bath particles, neglecting interactions between bath particles. The neglect of such higher-order couplings restricts our theory to low bath particle volume fractions, $\phi = 4\pi n a^3/3 \ll 1$ ($n$ being the number density of bath particles), for which only one bath particle interacts with the probes. The three-particle distribution function $P_3(\boldsymbol{x}_1, \boldsymbol{x}_2, \boldsymbol{x}_3, t)$, defined as $P_3 = [(N-3)!]^{-1} \int P_N d\boldsymbol{x}_4 \dots d\boldsymbol{x}_N$, satisfies a three-body Smoluchowski equation:

$$\frac{\partial P_3}{\partial t} + \boldsymbol{\nabla}_1 \cdot \langle \boldsymbol{j}_1 \rangle_3 + \boldsymbol{\nabla}_2 \cdot \langle \boldsymbol{j}_2 \rangle_3 + \boldsymbol{\nabla}_3 \cdot \langle \boldsymbol{j}_3 \rangle_3 = 0,$$

where $\langle \cdots \rangle_3$ denotes a conditional average with the trailing probe, leading probe, and bath particle at $\boldsymbol{x}_1$, $\boldsymbol{x}_2$, and $\boldsymbol{x}_3$, respectively. For a statistically homogeneous suspension we adopt a coordinate system relative to the trailing probe; defining $\boldsymbol{r}_{1i} = \boldsymbol{x}_i - \boldsymbol{x}_1$ we have

$$\frac{\partial P_3}{\partial t} + \boldsymbol{\nabla}_{12} \cdot \langle \boldsymbol{j}_2 - \boldsymbol{j}_1 \rangle_3 + \boldsymbol{\nabla}_{13} \cdot \langle \boldsymbol{j}_3 - \boldsymbol{j}_1 \rangle_3 = 0. \tag{5.2}$$

The absolute position of the trailing probe does not matter; hence, derivatives with respect to $\boldsymbol{x}_1$ are zero. The probability fluxes in the relative coordinate system are given by

$$\langle \boldsymbol{j}_2 - \boldsymbol{j}_1 \rangle_3 = (\boldsymbol{U}_2 - \boldsymbol{U}_1) P_3 \quad , \quad \langle \boldsymbol{j}_3 - \boldsymbol{j}_1 \rangle_3 = -D_3 \boldsymbol{\nabla}_{13} P_3 - \boldsymbol{U}_1 P_3,$$

where $D_3 = kT/6\pi\eta a$ is the Stokes-Einstein-Sutherland diffusivity of the bath particle.

Thus, (5.2) becomes

$$\frac{\partial P_3}{\partial t} + (\boldsymbol{U}_2 - \boldsymbol{U}_1)\cdot\boldsymbol{\nabla}_{12}P_3 - \boldsymbol{U}_1\cdot\boldsymbol{\nabla}_{13}P_3 - D_3\nabla_{13}^2 P_3 = 0. \tag{5.3}$$

In this study, we assume that the probes translate with equal velocities; hence, the second term in (5.3) vanishes. The three-particle distribution function may be written as

$$P_3(\boldsymbol{x}_1, \boldsymbol{x}_2, \boldsymbol{x}_3) = P_{1/2}(\boldsymbol{x}_3|\boldsymbol{x}_1, \boldsymbol{x}_2)P_2(\boldsymbol{x}_1, \boldsymbol{x}_2), \tag{5.4}$$

where $P_{1/2}(\boldsymbol{x}_3|\boldsymbol{x}_1, \boldsymbol{x}_2)$ is the conditional probability of finding the bath particle at $\boldsymbol{x}_3$ given the leading and trailing probes at $\boldsymbol{x}_1$ and $\boldsymbol{x_2}$, respectively. Substituting this into (5.3) gives

$$\frac{\partial P_{1/2}}{\partial t} - \boldsymbol{U}_1\cdot\boldsymbol{\nabla}_{13}P_{1/2} - D_3\nabla_{13}^2 P_{1/2} = 0. \tag{5.5}$$

Furthermore, $P_{1/2}$ may be written as $P_{1/2}(\boldsymbol{x}_3|\boldsymbol{x}_1, \boldsymbol{x}_2) = ng(\boldsymbol{r}_{13}|\boldsymbol{r}_{12})$, where $g(\boldsymbol{r}_{13}|\boldsymbol{r}_{12})$ is the 'conditional pair-distribution function' (hereafter CPDF), which gives the probability of locating the bath particle at a separation $\boldsymbol{r}_{13}$ (henceforth $\boldsymbol{r}$) from the trailing probe, given a (fixed and finite) separation $\boldsymbol{r}_{12}$ (henceforth $\boldsymbol{d}$) between the leading and trailing probes. Thus, (5.5) becomes

$$\frac{\partial g}{\partial t} - \boldsymbol{U}_1\cdot\boldsymbol{\nabla}_{13}g - D_3\nabla_{13}^2 g = 0.$$

We make quantities dimensionless by scaling as

$$\boldsymbol{r} \sim a, \quad \boldsymbol{U}_1 \sim U, \quad t \sim \frac{a^2}{D_3},$$

with $U = |\boldsymbol{U}_1|$. In this study we consider time-independent microstructures, for which

the scaled three-body Smoluchowski equation reads

$$-Pe\,\hat{\boldsymbol{U}}\cdot\boldsymbol{\nabla}g=\nabla^2 g, \tag{5.6}$$

where $\hat{\boldsymbol{U}}=\boldsymbol{U}/U$; all quantities are dimensionless; and the subscripts on $\hat{\boldsymbol{U}}_1$ and $\boldsymbol{\nabla}_{13}$ have been dropped. Physically, (5.6) expresses a balance between advection by the moving probes, which drives the microstructure out of equilibrium, and Brownian diffusion of the bath particles, which acts to restore equilibrium. The degree to which the microstructure is distorted is given by the Péclet number, $Pe=Ua/D_3$, which emerges naturally from the scaling as a ratio of advective ($U$) to diffusive ($D_3/a$) 'velocities'. We leave the subscript on $D_3$ to emphasize that only the bath particle undergoes Brownian diffusion, whereas the motion of the probes is deterministic.

To fully determine the microstructure, the Smoluchowski equation must be accompanied with suitable boundary conditions. At large separations it is assumed the dispersion has no long-range order, which implies

$$g(\tilde{\boldsymbol{r}}|\tilde{\boldsymbol{d}})\to 1 \quad \text{as} \quad |\tilde{\boldsymbol{r}}|\to\infty, \tag{5.7}$$

where $\tilde{\boldsymbol{r}}=\boldsymbol{r}/a$ and $\tilde{\boldsymbol{d}}=\boldsymbol{d}/a$. Henceforth, we drop the tildes on $\tilde{\boldsymbol{r}}$ and $\tilde{\boldsymbol{d}}$; they are to be understood. The rigidity of the particles requires that the normal component of the relative flux vanishes when the bath particle is contacting either of the probes:

$$\boldsymbol{n}_{i3}\cdot(\boldsymbol{\nabla}g+Pe\boldsymbol{U}g)=0 \quad \text{on} \quad S_{i3}, \tag{5.8}$$

where $\boldsymbol{n}_{i3}$ is the outward unit normal from probe $i$ to the bath particle, and $S_{i3}$ is the

excluded-volume surface between probe $i$ and the bath particle.

### 5.2.2 Forces on the probes

From the CPDF it is possible to compute a variety of microstructurally-averaged properties. The most interesting in the present context is the average external force on each of the probes. The average force is computed as an integral of the configuration-specific force $\boldsymbol{F}_i$ on the probe [cf. (5.1)] weighted by the admissible positions of a bath particle, given the (fixed) locations of the probes. Formally, we have

$$\begin{aligned}\langle \boldsymbol{F}_1 \rangle_2 &= 6\pi\eta a \boldsymbol{U}_1 + kT \int \langle \boldsymbol{\nabla}_1 \ln P_N \rangle_3 P_{1/2} d\boldsymbol{x}_3, \\ \langle \boldsymbol{F}_2 \rangle_2 &= 6\pi\eta a \boldsymbol{U}_2 + kT \int \langle \boldsymbol{\nabla}_2 \ln P_N \rangle_3 P_{1/2} d\boldsymbol{x}_3,\end{aligned}$$

where $\langle \cdots \rangle_2$ denotes a conditional average with the trailing and leading probes at $\boldsymbol{x}_1$ and $\boldsymbol{x}_2$, respectively. In the relative three-particle coordinate system the difference in the forces is then

$$\langle \boldsymbol{F}_2 \rangle_2 - \langle \boldsymbol{F}_1 \rangle_2 = 6\pi\eta a(\boldsymbol{U}_2 - \boldsymbol{U}_1) + kT \int (\boldsymbol{\nabla}_{13} \ln P_3) P_{1/2} d\boldsymbol{r}_{13} + 2kT \int (\boldsymbol{\nabla}_{12} \ln P_3) P_{1/2} d\boldsymbol{r}_{13}, \tag{5.9}$$

where the first term on the right-hand side of (5.9) is the difference in the Stokes drags, which vanishes if the probes move with equal velocities (as assumed henceforth). Using (5.4), we may write (5.9) as

$$\langle \boldsymbol{F}_2 \rangle_2 - \langle \boldsymbol{F}_1 \rangle_2 = kT \frac{1}{P_2} \int \boldsymbol{\nabla}_{13} P_3 d\boldsymbol{r}_{13} + 2kT \boldsymbol{\nabla}_{12} \ln P_2.$$

Applying the divergence theorem to the volume integral in the above gives

$$\langle \boldsymbol{F}_2 \rangle_2 - \langle \boldsymbol{F}_1 \rangle_2 = kT \oint \boldsymbol{n}_{23} P_{1/2} dS_{23} - kT \oint \boldsymbol{n}_{13} P_{1/2} dS_{13} + 2kT \nabla_{12} \ln P_2,$$

where $dS_{i3}$ is the differential area element of the excluded-volume surface $S_{i3}$. In terms of the CPDF, $g(\boldsymbol{r}|\boldsymbol{d})$, we have

$$\langle \boldsymbol{F}_2 \rangle_2 - \langle \boldsymbol{F}_1 \rangle_2 = nkT \oint \boldsymbol{n}_{23} g dS_{23} - nkT \oint \boldsymbol{n}_{13} g dS_{13} + 2kT \nabla_{12} \ln P_2. \tag{5.10}$$

The two integrals in (5.10) represent the effect of a third (bath) particle, while the $2kT\nabla_{12} \ln P_2$ term is the isolated two-probe contribution. We remove this two-probe contribution by defining an 'entropic' force $\langle \Delta \boldsymbol{F} \rangle_2 = \langle \Delta \boldsymbol{F}_l \rangle_2 - \langle \Delta \boldsymbol{F}_t \rangle_2$, due solely to the presence of the bath particles, where

$$\langle \Delta \boldsymbol{F}_t \rangle_2 = -nkT \oint \boldsymbol{n}_t g dS_t, \quad \text{and} \quad \langle \Delta \boldsymbol{F}_l \rangle_2 = -nkT \oint \boldsymbol{n}_l g dS_l, \tag{5.11}$$

are the entropic forces on each probe. These forces are exerted *by* the dispersion *on* the probes, as a result of the microstructural deformation: they are simply the integral over the surface of the probe of the 'osmotic' pressure exerted by the bath particles. Thus, to ensure the probes move with constant velocities one must adjust the external forces acting on them, by an amount equal in magnitude but opposite in direction to their respective entropic forces. Above, and henceforth, we replace the probe labels 1 and 2 with $t$ (trailing) and $l$ (leading), respectively.

## 5.3 Solution of the Smoluchowski equation

Computation of the dispersion microstructure is technically challenging: one has to solve the Smoluchowski (advection-diffusion) equation (5.6) subject to the far-field constraint (5.7) and the no-flux boundary condition (5.8) on the two excluded-volume surfaces, $S_t$ and $S_l$. We assume that the probes move along their line of centers; consequently, the microstructural deformation is axisymmetric about the direction of motion, which somewhat simplifies the problem. Furthermore, the axisymmetry of $g(\boldsymbol{r}|\boldsymbol{d})$ implies that the entropic forces are directed along $\boldsymbol{d}$.

The shape of the excluded-volume surfaces $S_t$ and $S_l$, and hence the microstructural deformation, is crucially dependent on the probe spacing, $\boldsymbol{d}$. For $d = |\boldsymbol{d}| > 4$ (recall, $d$ is made dimensionless with the probe radius, $a$) $S_t$ and $S_l$ are non-intersecting spheres of radii 2 (see figure 5.1). In contrast, for $d < 4$ both $S_t$ and $S_l$ are spheres (again, of radii 2), which intersect to form a closed dumbbell (see figure 5.3). Physically, for $d > 4$ a bath particle is able to pass between the probes; for $d < 4$ it is not. Mathematically, the two scenarios require different coordinate systems in which to solve the Smoluchowski equation: for $d > 4$ we employ bispherical coordinates, and for $d < 4$ we use toroidal coordinates (see, e.g., Morse and Feshbach 1953). Note, the case $d = 4$, for which $S_t$ and $S_l$ are touching spheres, may be treated using tangent-sphere coordinates (see Moon and Spencer 1961); however, we do not study this special value here.

Before discussing the cases $d > 4$ and $d < 4$ in more detail, we simplify the mathematical complexity of the problem by following Squires and Brady (2005) in writing the CPDF as

$$g(\boldsymbol{r}|\boldsymbol{d}) = 1 + f(\boldsymbol{r}|\boldsymbol{d}) \exp\left(-\kappa \hat{\boldsymbol{U}} \cdot \boldsymbol{r}\right),$$

where $\kappa = Pe/2$. Substituting this into the Smoluchowski equation (5.6) yields

$$\nabla^2 f = \kappa^2 f, \tag{5.12}$$

i.e., a modified Helmholtz equation for $f(\boldsymbol{r}|\boldsymbol{d})$, as compared to the advection-diffusion equation for $g(\boldsymbol{r}|\boldsymbol{d})$. The far-field boundary condition on $f(\boldsymbol{r}|\boldsymbol{d})$ is

$$f(\boldsymbol{r}|\boldsymbol{d}) \to 0 \quad \text{as} \quad |\boldsymbol{r}| \to \infty,$$

and the no-flux conditions (for $i = t, l$) are

$$\boldsymbol{n}_i \cdot \left( \nabla f + \kappa \hat{\boldsymbol{U}} f \right) = -2\kappa \boldsymbol{n}_i \cdot \hat{\boldsymbol{U}} \exp\left( \kappa \hat{\boldsymbol{U}} \cdot \boldsymbol{r} \right) \quad \text{on} \quad S_i. \tag{5.13}$$

### 5.3.1 Non-intersecting excluded volumes: bispherical coordinates

We consider the probes to be moving along their line of centers, $\boldsymbol{d} = d\hat{\boldsymbol{z}}$, which is taken as the $z$-axis of a two-dimensional Cartesian $[x,z]$ coordinate system, whose origin is at the midpoint of the probes (see figure 5.1). Thus, the leading probe is at $[0,d/2]$ and the trailing probe is at $[0,-d/2]$. Let us introduce the bispherical coordinates $\mu$ and $\eta$ defined by

$$x = \frac{c \, \sin\eta}{\cosh\mu - \cos\eta} \quad , \quad z = \frac{c \, \sinh\mu}{\cosh\mu - \cos\eta},$$

where $c$ is a scale factor; $0 \leq \eta \leq \pi$; and $-\infty < \mu < \infty$. The surface $\mu = \mu_0$ is a sphere of radius $c/|\sinh\mu_0|$ centered at $[0,c\coth\mu_0]$. Thus, we find

$$c = \frac{1}{2}\sqrt{(d-4)(d+4)} \quad , \quad \cosh\mu_0 = \frac{d}{4}.$$

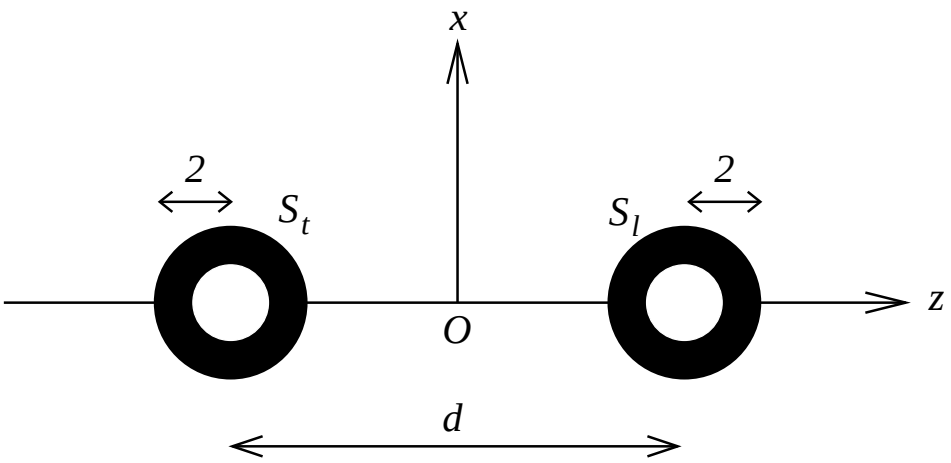


Figure 5.1: Definition sketch for non-intersecting excluded-volumes, $d > 4$. The excluded volume surfaces are shaded black, and the probes are white.

In bispherical coordinates we can further simplify the Helmholtz equation for $f(\boldsymbol{r}|\boldsymbol{d}) = f(\mu, \eta; d)$ via the substitution

$$f(\mu, \eta; d) = c\kappa\sqrt{2\cosh\mu - 2\cos\eta}\; h(\mu, \eta; d). \tag{5.14}$$

The function $h(\mu, \eta; d)$ satisfies

$$\frac{\partial^2 h}{\partial \mu^2} + \frac{\partial^2 h}{\partial \eta^2} + \cot\eta \frac{\partial h}{\partial \eta} - \frac{1}{4}h = \frac{c^2\kappa^2}{(\cosh\mu - \cos\eta)^2}h, \tag{5.15}$$

subject to the boundary conditions

$$\begin{aligned} h &\rightarrow 0 \quad \text{as} \quad |\boldsymbol{r}| \rightarrow \infty, \\ \frac{\partial h}{\partial \mu} &= \left[\frac{c\kappa(\cosh\mu\cos\eta - 1)}{(\cosh\mu - \cos\eta)^2} - \frac{\sinh\mu}{2(\cosh\mu - \cos\eta)}\right] h \\ &+ \frac{\sqrt{2}(\cosh\mu\cos\eta - 1)}{(\cosh\mu - \cos\eta)^{5/2}} \exp\left(\frac{c\kappa\ \sinh\mu}{\cosh\mu - \cos\eta}\right) \quad \text{at} \quad \mu = \pm\mu_0. \end{aligned}$$

The bispherical coordinate system maps the two-probe configuration onto the rectangle

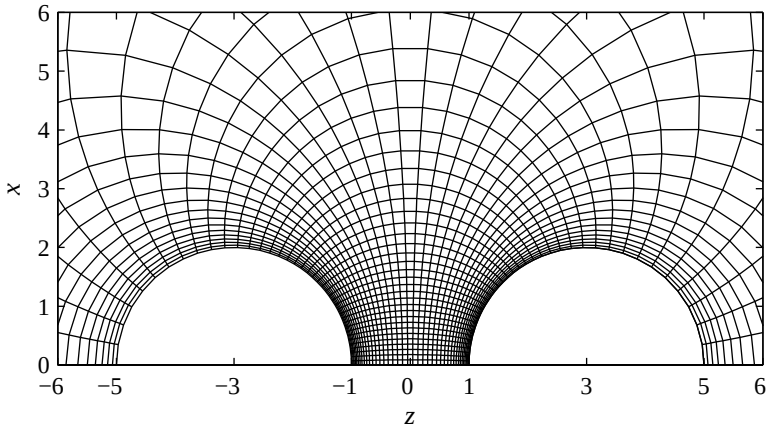


Figure 5.2: Sample finite difference grid in (transformed) bispherical coordinates $\eta$ and $\lambda$. Here, there are $50 \times 50$ grid points; $d = 6$; and $\alpha = 3$. Note, the computational domain is the entire Cartesian $[x > 0, z]$ half space.

$\{0 \leq \eta \leq \pi, -\mu_0 \leq \mu \leq \mu_0\}$. However, we gain this rectilinear geometry at the cost of losing separability in the Helmholtz equation (5.12). Therefore, to compute $h(\mu, \eta; d)$ we approximate (5.15) by a finite difference equation (central differences are used for all derivatives) on a uniform grid and solve the resulting linear system of equations by a simple Jacobi iteration. The method closely resembles that of Khair and Brady (2006), who calculated the microstructural deformation around a single forced probe. However, the bispherical geometry raises a couple of issues that warrant comment. First, to ensure axisymmetry one must impose the boundary condition $\partial h/\partial \eta = 0$ at $\eta = 0$ and $\eta = \pi$. Second, it is desirable to have a high density of grid points near the excluded-volume surfaces; to this end, we use the transformation

$$\mu = \mu_0 \frac{1 + \exp(\alpha)}{1 - \exp(\alpha)} \left[ 1 - \frac{2}{1 + \exp(-\alpha\lambda)} \right], \tag{5.16}$$

where $-1 \leq \lambda \leq 1$, and $\alpha > 0$. Increasing $\alpha$ places a larger number of grid points near the excluded-volume surfaces ( i.e., near $\mu = \pm\mu_0$). A typical grid discretization is shown

in figure 5.2.

Finally, from (5.11) the entropic forces on the probes, which are in the $z$-direction, are given by

$$\begin{aligned}\langle \Delta F_l^z \rangle_2 &= \frac{\phi kT}{a}\, 6\sinh^2\mu_0 \int_0^\pi g(\mu_0,\eta)\frac{\sin\eta(1-\cos\eta\cosh\mu_0)}{(\cosh\mu_0-\cos\eta)^3}d\eta,\\ \langle \Delta F_t^z \rangle_2 &= -\frac{\phi kT}{a}\, 6\sinh^2\mu_0 \int_0^\pi g(-\mu_0,\eta)\frac{\sin\eta(1-\cos\eta\cosh\mu_0)}{(\cosh\mu_0-\cos\eta)^3}d\eta.\end{aligned}$$

### 5.3.2 Intersecting excluded volumes: toroidal coordinates

When the probes are sufficiently close, $d < 4$, a bath particle is not able to pass between them. In this case, the excluded-volume surfaces intersect at an angle $\psi = \arccos[(d^2/8)-1]$ (see figure 5.3) to form a dumbbell shape. To solve the Smoluchowski equation in this geometry it is appropriate to use toroidal coordinates; we take the same Cartesian frame as before and define the toroidal coordinates $\mu$ and $\eta$ via

$$x = \frac{c\ \sinh\mu}{\cosh\mu-\cos\eta} \quad , \quad z = \frac{c\ \sin\eta}{\cosh\mu-\cos\eta},$$

where $c$ is a scale factor; $-\pi \le \eta \le \pi$; and $0 < \mu < \infty$. The surface $\eta = \eta_0$ ($\eta_0 > 0$) is that part of a sphere of radius $c/\sin\eta_0$, centered at $[0,c\cot\eta_0]$, which is above the $x-y$ plane (i.e, for which $z > 0$). Its mirror image about the $x-y$ plane is the surface $\eta = -\eta_0$. Hence, it is easy to show

$$c = \frac{1}{2}\sqrt{(4-d)(4+d)} \ , \ \cos\eta_0 = \frac{d}{4}.$$

Using the substitution (5.14), in toroidal coordinates the Helmholtz equation for $f(\mu,\eta;d)$

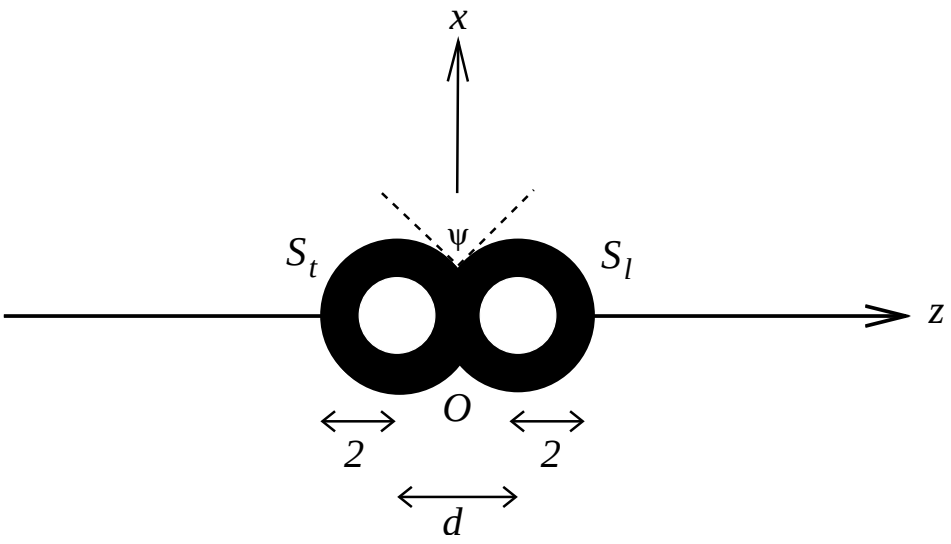


Figure 5.3: Definition sketch for intersecting excluded-volumes, $d < 4$. The excluded volume surfaces, which intersect at an angle $\psi = \arccos[(d^2/8)-1]$, are shaded black, and the probes are white.

transforms into

$$\frac{\partial^2 h}{\partial \mu^2} + \frac{\partial^2 h}{\partial \eta^2} + \coth\mu \frac{\partial h}{\partial \mu} + \frac{1}{4}h = \frac{c^2\kappa^2}{(\cosh\mu - \cos\eta)^2}h,$$

where $h(\mu, \eta; d)$ must also satisfy

$$\begin{aligned} h &\rightarrow 0 \quad \text{as} \quad |\boldsymbol{r}| \rightarrow \infty, \\ \frac{\partial h}{\partial \eta} &= -\left[\frac{c\kappa(\cosh\mu\cos\eta - 1)}{(\cosh\mu - \cos\eta)^2} + \frac{\sin\eta}{2(\cosh\mu - \cos\eta)}\right] h \\ &- \frac{\sqrt{2}(\cosh\mu\cos\eta - 1)}{(\cosh\mu - \cos\eta)^{5/2}} \exp\left(\frac{c\kappa\ \sin\eta}{\cosh\mu - \cos\eta}\right) \quad \text{at} \quad \eta = \pm\eta_0. \end{aligned}$$

In toroidal coordinates we again lose separability of the Helmholtz equation for $f(\mu, \eta; d)$; therefore, $h(\mu, \eta; d)$ is calculated using finite differences. Axisymmetry of the microstructure about the $z$-axis requires $\partial h/\partial\mu = 0$ at $\mu = 0$. The excluded-volume surfaces intersect at $\mu = \infty$, and $h(\mu, \eta; d)$ should be continuous at this point, which requires $\partial h/\partial\mu = 0$ at $\mu = \infty$. In practice, this is difficult to implement owing to the semi-infinite range of $\mu$. Thus, we move the condition to $\mu = \mu_{max}$ and increase $\mu_{max}$ until convergence of

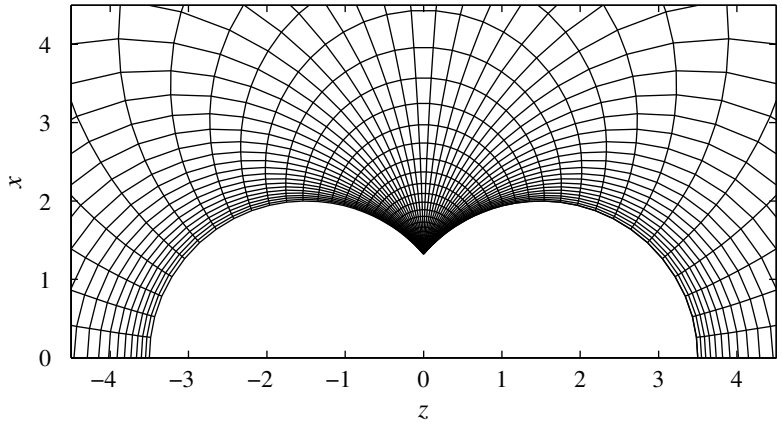


Figure 5.4: Sample finite difference grid in (transformed) toroidal coordinates $\xi$ and $\lambda$. Here, there are $50 \times 50$ grid points; $d = 3$; $\mu_{max} = 20$; and $\alpha = 3$. Again, the computational domain is the entire Cartesian $[x > 0, z]$ half space.

the entropic forces is achieved. As with bispherical coordinates, it is desirable to place a large number of grid points near the excluded-volume surfaces. Furthermore, in toroidal coordinates there is a natural clustering of grid points near the intersection point of the surfaces, $\mu = \infty$, as shown in figure 5.4. Therefore, we transform $\eta$ according to (5.16) and $\mu$ via $\mu = \exp(\beta\xi) - 1$, where $0 \leq \xi \leq 1$ and $\beta = \ln(\mu_{max} + 1)$, which places a greater density (as compared to the 'naive' toroidal discretization) of grid points near the upstream half of the leading probe $[\mu = 0, \eta = \eta_0]$ and the downstream half of the trailing probe $[\mu = 0, \eta = -\eta_0]$.

From (5.11), the entropic forces on the probes are given by

$$\begin{aligned}
\langle \Delta F_l^z \rangle_2 &= -\frac{\phi kT}{a}\, 6 \sin^2 \eta_0 \int_0^\infty g(\mu, \eta_0) \frac{\sinh \mu (1 - \cos \eta_0 \cosh \mu)}{(\cosh \mu - \cos \eta_0)^3} d\mu, \\
\langle \Delta F_t^z \rangle_2 &= \frac{\phi kT}{a}\, 6 \sin^2 \eta_0 \int_0^\infty g(\mu, -\eta_0) \frac{\sinh \mu (1 - \cos \eta_0 \cosh \mu)}{(\cosh \mu - \cos \eta_0)^3} d\mu.
\end{aligned}$$

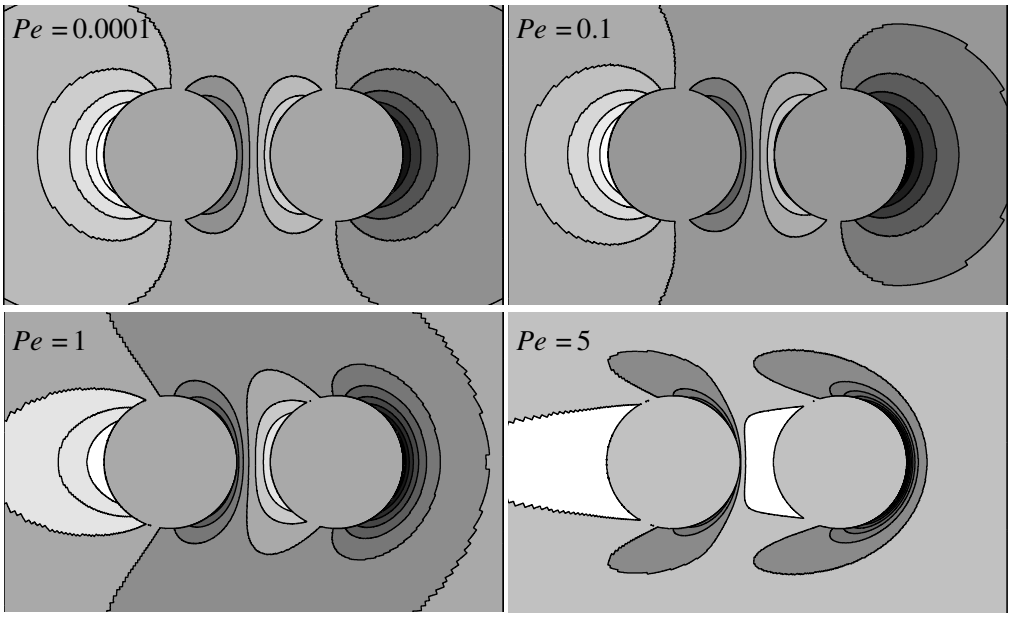


Figure 5.5: Microstructural deformation, $g-1$, in the symmetry plane of the probes as a function of $Pe$ for $d=5$. The probes move from left-to-right, and their excluded-volume surfaces are shown with zero deformation. Darker regions imply $g-1>0$ (accumulation), while lighter regions represent $g-1<0$ (deficit).

## 5.4 Results

Before presenting our results, we comment briefly on numerical details. As $Pe$ is increased the demand for grid points (and hence the number of iterations) increases, to capture accurately the boundary layers on the upstream side of the leading and, depending on the value of $d$, trailing probes (see figures 5.5 and 5.6 ). Thus, computational cost of the finite difference scheme also increases with $Pe$: the largest value for which we obtained a convergent solution being $Pe=10$. Typically, in both the toroidal and bispherical geometries, $300\times300$ grid points were used, and accuracy was tested by comparing the resulting entropic forces, $\langle\Delta F_t^z\rangle_2$ and $\langle\Delta F_l^z\rangle_2$, to those computed using a $350\times350$ grid.

In figure 5.5 we plot the microstructural deformation, $g(\boldsymbol{r}|\boldsymbol{d})-1$, as a function of $Pe$ for $d=5$. For $Pe\ll1$, where Brownian diffusion dominates advection, the deformation is proportional to $Pe$, and the probes act as a pair of diffusive dipoles, with an accumulation

of particles on their upstream sides and a deficit on their downstream sides. For sufficiently large $d$ the two dipoles do not interact, and the microstructure is fore-aft symmetric about each probe. However, for smaller $d$ (such as $d = 5$) the probes sense each other's presence; consequently, the fore-aft symmetry is broken. Moving to $Pe \approx 1$, advection now comes into play, and the deformation around the probes exhibits the beginnings of a classic boundary layer and wake structure. Physically, in a frame fixed on the probes, the advective flux of bath particles (moving with velocity $-\hat{\boldsymbol{U}}$) leads to an accumulation on the upstream sides of the (impenetrable) probes, which act as obstacles that the bath particles must navigate. The mechanism for passing around the probes is via Brownian diffusion. Thus, the boundary layers signify a balance between advection, in transporting bath particles toward the probes, and diffusion. On the downstream sides of the probes advection carries bath particles away; a region of low particle density, or wake, is formed. As $Pe$ is increased further the stronger advective flux results in thinner boundary layers and longer wakes. Note, the boundary layer on the trailing probe is significantly less particle-rich as compared to the leading probe [which has an $O(Pe)$ accumulation], as the trailing probe travels in the (low particle density) wake created by the leading probe, while the leading probe moves through the undisturbed dispersion. Of course, for $d$ much larger than the characteristic wake length (which grows as $Pe$) one expects the boundary layers on the trailing and leading probes to be almost identical. Conversely, for $d$ much smaller than the wake length the boundary layer on the trailing probe disappears; essentially, it moves through a particle-free tunnel of suspending fluid.

In figure 5.6 we plot the microstructural deformation as a function of $Pe$ for $d = 3$. In this case, and for all $d < 4$, the excluded-volume surfaces, $S_t$ and $S_l$, of the probes join and, from the bath particle's viewpoint, form a single dumbbell shaped obstacle. At small $Pe$

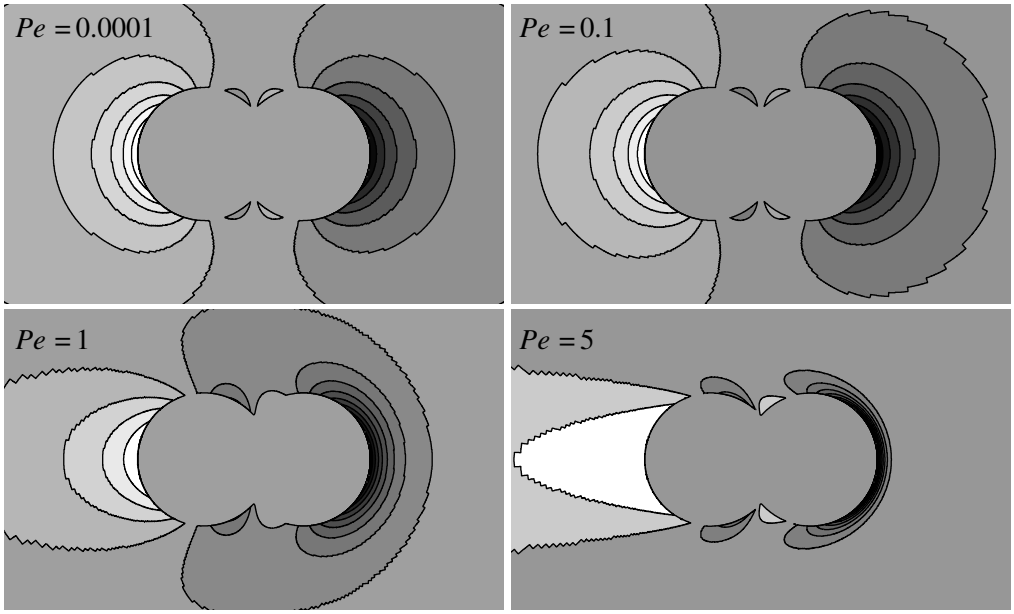


Figure 5.6: Microstructural deformation, $g - 1$, in the symmetry plane of the probes as a function of $Pe$ for $d = 3$. The color scheme is the same as in figure 5.5

this dumbbell acts as a diffusive dipole, which is approximately fore-aft symmetric about the intersection point of the two excluded-volume surfaces (save for a small accumulation of particles on the upstream side of the trailing probe and a small deficit on the downstream side of the leading probe). For larger $Pe$ we again see the formation of a boundary layer on the upstream side of the leading probe. As bath particles can not reside in the overlap of $S_t$ and $S_l$, there is neither a wake on the downstream side of the leading probe nor a boundary layer on the upstream side of the trailing probe. There is, however, a wake on the downstream side of the trailing probe, as bath particles are transported away from the rear of the dumbbell by advection.

Having discussed the dispersion microstructure, we move to the entropic forces on the probes. Figure 5.7 plots the scaled difference in entropic forces, $-(\langle \Delta F_l^z \rangle_2 - \langle \Delta F_t^z \rangle_2)/(\phi kT/a)$, as a function of $Pe$ for various $d$. For $Pe \ll 1$ and large $d$ (take the data for $d = 25$, say) the difference in entropic forces is small $[O(Pe^2)]$; this scaling arises since to $O(Pe)$ the probes

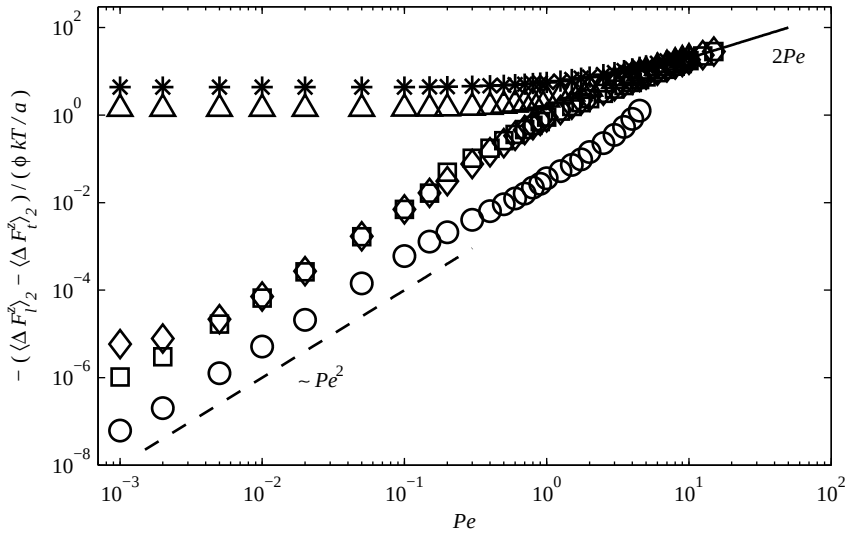


Figure 5.7: Difference in entropic forces, $-(\langle\Delta F_l^z\rangle_2 - \langle\Delta F_t^z\rangle_2)/(\phi kT/a)$, versus $Pe = Ua/D_3$ for various $d$: $d = 2.1$, $*$; $d = 3.5$, $\triangle$; $d = 4.25$, $\diamond$; $d = 5$, $\square$; and $d = 25$, $\bigcirc$. The dashed line indicates for large $d$ the differences in forces is proportional to $Pe^2$ at small $Pe$. The solid line is the large $Pe$ asymptote.

act as identical diffusive dipoles; thus, the $O(Pe)$ contributions to their respective entropic forces are equal. However, as mentioned above and shown in figure 5.8, for smaller $d$ the diffusive dipoles interact, and the difference in entropic forces grows [i.e., it is no longer $O(Pe^2)$]. In fact, for $d < 4$ the entropic forces on the probes have opposite signs: $\langle\Delta F_t^z\rangle_2$ and $\langle\Delta F_l^z\rangle_2$ are directed along $\boldsymbol{d}$ and $-\boldsymbol{d}$, respectively, and are both $O(1)$ in magnitude, resulting in an $O(1)$ difference. By construction, the velocity of each probe is fixed at $\boldsymbol{U}$. The microstructure around the leading probe consists of an accumulation of particles on its upstream side and a deficit on what is left of its downstream portion (before the intersection of $S_t$ and $S_l$). Thus, the leading probe is retarded by the net accumulation of particles on its excluded-volume surface; the dispersion exerts an $O(1)$ entropic force opposite to the direction of motion. Hence, the additional external force on the leading probe (which is equal in magnitude to the entropic force on it) is in the direction of motion, thereby maintaining the probe velocity at $\boldsymbol{U}$. Conversely, the deformation about the trailing probe is a deficit of

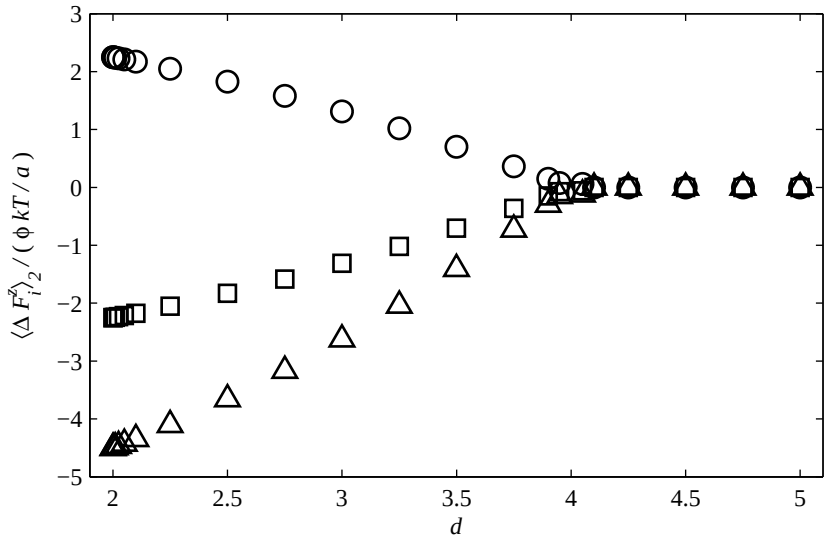


Figure 5.8: Entropic forces, $\langle \Delta F_i^z \rangle_2 / (\phi kT/a)$, versus $d$ for $Pe = 0.0001$: □, leading probe; ◯, trailing probe; and △, leading minus trailing.

particles on its downstream side and an accumulation on what is left of its upstream side. Hence, there is a net deficit of bath particles around the trailing probe, and the dispersion exerts an entropic force in the direction of motion. To ensure the trailing probe velocity remains equal to $\boldsymbol{U}$, the additional external force applied to it must be opposite to the direction of motion.

At large $Pe$ for all values of $d$ the differences in entropic forces approaches a common asymptote, $(\langle \Delta F_l^z \rangle_2 - \langle \Delta F_t^z \rangle_2)/(\phi kT/a) \to -2Pe$, as $Pe \to \infty$. As shown by Khair and Brady (2006), this is nothing but the entropic force on a single probe at high $Pe$, the dominant contribution to which is from the large $O(Pe)$ build-up of bath particles in the thin $O(Pe^{-1})$ upstream boundary layer. For two probes at high $Pe$ there is still a boundary layer on the upstream side of the leading probe (almost identical to that for a single probe); however, the trailing probe moves through the wake of the leading probe. Moreover, the trailing probe generates its own wake; effectively, then, it moves through a tunnel of suspending fluid, and hence there is a much smaller (as compared to the leading probe) entropic

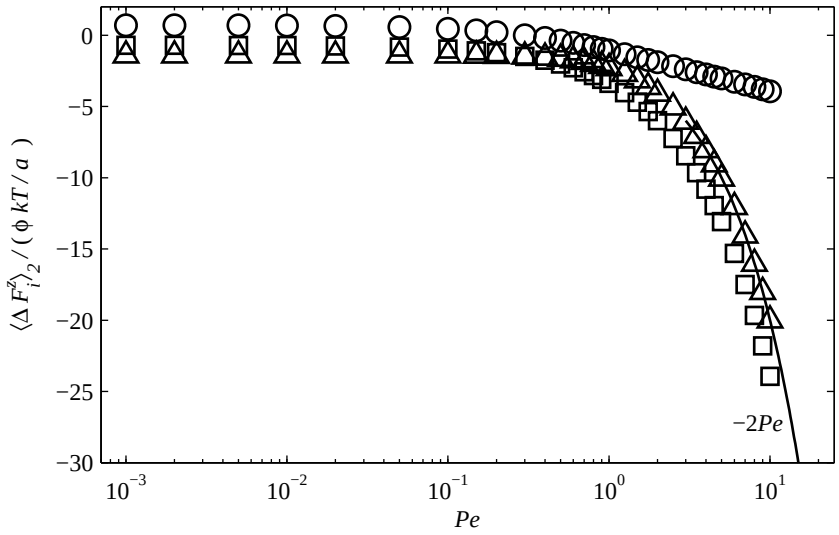


Figure 5.9: Entropic forces, $\langle \Delta F_i^z \rangle_2 / (\phi kT/a)$, versus $Pe$ for $d = 3.5$: legend is the same as in figure 5.8. Solid line is the large $Pe$ asymptote for the difference between leading and trailing forces.

force exerted on it. In figure 5.9 we plot the individual entropic forces as a function of $Pe$ for $d = 3.5$, where the behavior described above is clearly seen. Furthermore, as shown in figure 5.10, for a given value of $Pe(> 1)$ the magnitude of the entropic force on the trailing probe monotonically decreases with decreasing $d$; the force on the leading probe is almost constant over the entire range of $d$. This is readily understood as the force on the leading probe is determined by the boundary-layer structure, which is relatively insensitive to $d$, whereas decreasing $d$ places the trailing probe deeper in the wake of the leading probe, thus decreasing the magnitude of the entropic force on it.

## 5.5 Discussion

We have calculated the entropic forces acting on two colloidal (probe) particles moving with fixed, equal velocities through a dispersion of colloidal bath particles. It is well known that the presence of such bath, or contaminant, particles can generate forces between col-

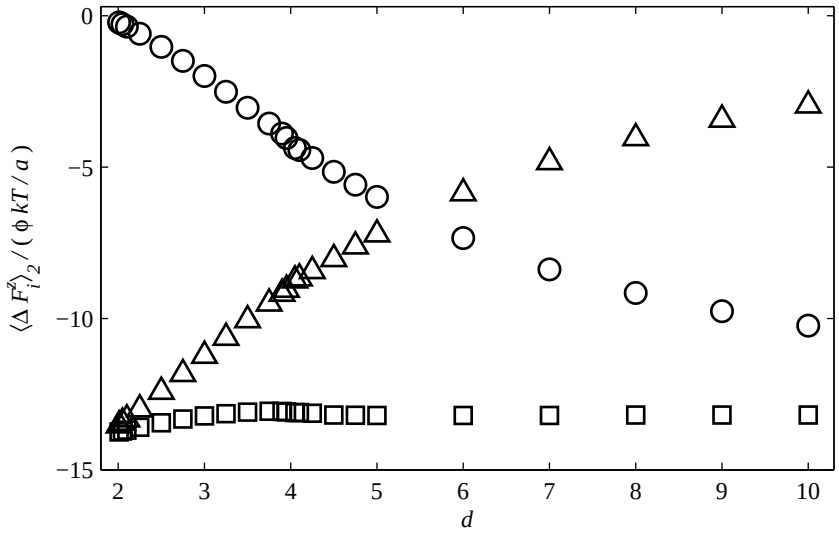


Figure 5.10: Entropic forces, $\langle \Delta F_i^z \rangle_2 / (\phi kT/a)$, versus $d$ for $Pe = 5$: legend is the same as in figure 5.8.

loidal particles: a prime example is the attractive depletion force between a pair of particles immersed in a dilute suspension of (smaller) particles at equilibrium. Like the forces calculated in the present work, depletion forces are entropic in nature, scaling with the thermal energy, $kT$. Furthermore, near equilibrium ($Pe \ll 1$) and for small separations ($d < 4$) the entropic forces on the trailing and leading probes point upstream and downstream, respectively, which can be interpreted as the dispersion exerting a net attractive force between the probes — somewhat akin to depletion attraction. However, there is an important difference: in our study the forces are generated as a consequence of the translating probes driving the microstructure of the dispersion out of equilibrium, whereas the equilibrium depletion forces do not rely on imposed motion of the particles; i.e., they are a purely thermodynamic (excluded-volume) effect. Moreover, in our case the dominant contribution to the (total) force on each probe is from its Stokes drag; the entropic force represent a small [$O(\phi)$] correction.

Recently, Dzubiella et al. (2003) have attempted to generalize the concept of depletion

forces to nonequilibrium, by computing the entropic forces on two stationary probes in a stream of smaller bath particles. When the bath particles flow along the line of centers of the probes, for moderate stream velocities they find [see their figure 3($b$)] that the magnitude of the force on the trailing probe is less than that on the leading probe, in agreement with our results for $Pe > 1$ (see figure 5.10). However, unlike us, they do not report a change in direction of the entropic force on the trailing probe with increasing $Pe$ for $d < 4$ (see figure 5.9). Although Dzubiella et al. (2003) investigated more general (non-axisymmetric) probe configurations, their analytical methods (as discussed in § 5.1) are restricted to widely separated particles and small stream velocities. We, on the other hand, have computed the nonequilibrium microstructure and entropic forces for all (axisymmetric) separations and probe velocities.

In this study, we neglected hydrodynamic interactions between particles. Although, as mentioned in § 5.1, there exist experimental systems for which this is a reasonable assumption, one should pause and consider their effect. For example, in the absence of hydrodynamic interactions at large $Pe$ the entropic force on the trailing probe vanishes, while the entropic force on the leading probe approaches the single probe limit (see figure 5.7). However, with hydrodynamic interactions this may not be so. For, as discussed by Khair and Brady (2006), in the limit of infinite $Pe$ the microstructure around a single moving probe attains spherical symmetry, i.e., the upstream boundary layer wraps over the entire (excluded-volume) surface of the probe, and the wake disappears. Physically, this occurs as bath particles from upstream 'stick' to the probe (due to hydrodynamic lubrication forces) as they are advected around it. Consequently, the force on the probe has equal contributions from the pushing of bath particles upstream of it and pulling of particles downstream of it. (Note, at infinite $Pe$ the force exerted by the dispersion on the probe is hydrodynamic, not

entropic, in origin.) Now, imagine two probes in the presence of hydrodynamic interactions at large $Pe$. The leading probe no longer creates a wake for the trailing probe to move through; likewise, the trailing probe does not create a wake of its own. We expect this qualitative change in the microstructure at large $Pe$ due to hydrodynamic interactions to be reflected in the computed forces. However, the inclusion of hydrodynamic interactions is beyond the scope of analytical theory, and one must resort to computer simulations, such as Stokesian Dynamics.

The theoretical framework developed in § 5.2 may be used to study other interesting problems. A natural extension is to consider two probes moving perpendicular to their line of centers, for which the microstructural deformation is no longer axisymmetric about their separation, $\boldsymbol{d}$. Consequently, we expect the entropic forces on the (top and bottom) probes to have components parallel and perpendicular to $\boldsymbol{d}$. For large $d = |\boldsymbol{d}|$ the parallel components for each probe vanish, while the perpendicular components are, by symmetry, identical and equal to that for a single moving probe. For smaller $d$ (close to, but greater than 4) a bath particle is just able to squeeze between the probes. The perpendicular components for each probe remain identical, but are now not equal to that for a single probe. In contrast, the parallel components should be in opposite directions: the parallel forces on the top and bottom probes point upward and downward, respectively, which may be viewed as the dispersion exerting a net repulsive force between the probes. Indeed, this behavior was seen by Dzubiella et al. (2003) [see their figure 3($a$)]. Furthermore, as mentioned in § 5.1, our theory can be easily extended to study the small bath particle limit of Dzubiella et al. (2003), which is somewhat more representative of experimental studies on depletion forces. Lastly, the Smoluchowski equation (5.3) applies when there is relative motion between the probes. Hence, for example, it can be used to study the motion of a

probe at fixed velocity approaching a stationary wall (which is, of course, just a probe of infinite radius): a simple problem, which could provide a starting point for investigating the patterning of surfaces using driven colloidal particles.

On a complementary note to the present study, one could fix the external forces on the probes and calculate their average velocities. Although qualitatively similar, there are important (and subtle) differences between the fixed-force and fixed-velocity cases; indeed, the formulation of the three-body Smoluchowski equation for the fixed-force problem is more involved. Nevertheless, one can arrive at an equation for the conditional pair-distribution function analogous to (5.6), in the limit where the bath particles are much more mobile (i.e., they have a far higher diffusivity) than the probes, which, in turn, requires the bath particles to be much smaller than the probes. As a first study, it would be wise to consider two (large) probes forced along their line of centers, $\boldsymbol{d}$, for which their average velocities will be directed along $\boldsymbol{d}$, also. For $Pe > 1$ (here, $Pe$ is defined as the dimensionless external force on the probes) and $d > 4$ the trailing probe would move through the wake created by the leading probe, which is practically devoid of bath particles. Furthermore, the trailing probe generates its own wake; hence, as per the fixed-velocity problem, it travels through a tunnel of suspending fluid. In contrast, the leading probe is retarded by the need to push bath particles out of its path. As such, one expects, in general, that the trailing probe moves faster than the leading probe, and it may eventually 'catch-up' and contact the leading probe. Continuing this process, one may add a second trailing probe (this is, unfortunately, beyond the realm of analytical theory; one must employ computer simulations), which will catch-up to the first trailing and leading probes. In this way, by adding yet more probes, one may form a 'train' of probes moving through the dispersion, which could provide a route for pattern formation in colloidal dispersions, and perhaps other complex materials. We

shall, however, leave this fascinating world of multi-particle interactions for future studies.

## 5.6 Bibliography

V. J. Anderson and H. N. W. Lekkerkerker. Insights into phase transition kinetics from colloid science. *Nature*, 416:811–815, 2002.

S. Asakura and F. Oosawa. On interaction between two bodies immersed in a solution of macromolecules. *J. Chem. Phys.*, 22:1255–1256, 1958.

J. Chakrabarti, J. Dzubiella, and Löwen. Reentrance effect in the lane formation of driven colloids. *Phys. Rev. E*, 70:012401, 2004.

J. C. Crocker, J. A. Matteo, A. D. Dinsmore, and A. G. Yodh. Entropic attraction and repulsion in binary colloids probed with a line optical tweezer. *Phys. Rev. Lett.*, 82: 4352–4355, 1999.

J. Dzubiella, G. P. Hoffman, and H. Löwen. Lane formation in colloidal mixtures driven by an external field. *Phys. Rev. E*, 65:021402, 2002.

J. Dzubiella, H. Löwen, and C. N. Likos. Depletion forces in nonequilibrium. *Phys. Rev. Lett.*, 91:248301, 2003.

L. Heldon, R. Roth, G. H. Koenderink, P. Leiderer, and C. Bechinger. Direct measurement of entropic forces induced by rigid rods. *Phys. Rev. Lett.*, 90:048301, 2003.

P. Jenkins and M. Snowden. Depletion flocculation in colloidal dispersions. *Adv. Colloid Interface Sci.*, 68:57–96, 1996.

P. D. Kaplan, J. L. Rouke, A. G. Yodh, and D. G. Pine. Entropically driven surface phase separation in binary colloidal mixtures. *Phys. Rev. Lett.*, 72:582–585, 1994.

A. S. Khair and J. F. Brady. Single particle motion in colloidal dispersions: A simple model for active and nonlinear microrheology. *J. Fluid Mech.*, 557:73–117, 2006.

P. Moon and D. M. Spencer. *Field theory handbook: including coordinate systems, differential equations, and their solutions*. Springer, 1961.

P. M. Morse and H. Feshbach. *Methods of theoretical physics. Part II.* McGraw-Hill, 1953.

T. M. Squires and J. F. Brady. A simple paradigm for active and nonlinear microrheology. *Phys. Fluids*, 17:073101, 2005.

R. Tehver, A. Maritan, J. Koplik, and J. R. Banavar. Depletion forces in hard-sphere colloids. *Phys. Rev. E*, 59:R1339, 1999.

R. Verma, J. C. Crocker, T. C. Lubensky, and A. G. Yodh. Entropic colloidal interactions in concentrated DNA solutions. *Phys. Rev. Lett.*, 81:4004–4007, 1998.

A. G. Yodh, L. Keng-Hui, J. C. Crocker, A. D. Dinsmore, R. Verma, and P. D. Kaplan. Entropically driven self-assembly and interaction in suspension. *Phil. Trans. R. Soc. A.*, 359:921–937, 2001.

# Chapter 6

# Conclusions

## 6.1 Conclusions & future directions

Over the past decade, microrheology has emerged as a technique to interrogate and manipulate complex fluids and biological materials at the microstructural scale. While advances in experimental microrheology methods continue unabated, theoretical developments, in general, struggle to keep pace. To address this imbalance, we have studied a prototypical model for active (nonlinear) microrheology: an externally driven 'probe' particle immersed in a hard-sphere dispersion of colloidal 'bath' particles. The hard-sphere colloidal dispersion is, perhaps, the 'simplest' of complex fluids; nevertheless, as shown in the previous chapters, its microrheological properties are nontrivial and require careful analysis.

In chapter 2 we investigated a probe traveling at fixed external force. The motion of the probe drives the microstructure of the dispersion out of equilibrium; counteracting this is the Brownian diffusion of the probe and bath particles. The degree of microstructural distortion is set by the dimensionless external force on the probe, or Péclet number, $Pe$. With the nonequilibrium microstructure in hand, we calculate the average translational velocity of the probe, and from the average velocity one can infer a 'microviscosity' of the dispersion via Stokes drag law. In particular, we demonstrated that at large $Pe$ particles experiencing short-ranged hydrodynamic lubrication interactions give a microviscosity that increases, or 'force-thickens'. This is reminiscent of the 'shear-thickening' at large $Pe$ (with $Pe$ the non-dimensional shear rate) observed in macrorheology (Bergenholtz et al. 2002). Indeed, after appropriate scaling, we were able to make a quantitative comparison (see figure 2.18). Shear-thickening complex fluids have recently been employed in the design of military armor (Lee et al. 2003); the onset and degree of thickening of the micro- (and macro-) viscosity are key design parameters. How do they vary with probe-bath size ratio

and probe pulling mode (fixed force versus fixed velocity)? Is the 'correct' size ratio for microrheology experiments that which gives a (scaled) onset and degree equal to that for the macroviscosity? For dilute systems these questions may be answered by extending the theoretical framework developed in chapter 2, while for concentrated dispersions (where one has to accurately account for the long-ranged, many-body hydrodynamic interactions between particles) the Stokesian Dynamics paradigm (Brady and Bossis 1988) is applicable.

In chapter 3 we considered a probe subjected to a small amplitude ($Pe \ll 1$) oscillatory force. In this case, the microviscosity has components in-phase (liquid-like) and out-of phase (solid-like) with the external forcing — a signature response of viscoelastic fluids. By computing the microviscosity as a function of oscillation frequency $\omega$ of the probe we were able to delineate the (linear) 'microviscoelastic' response of the dispersion. Again, after appropriate scaling, the micro results are in agreement with the equivalent macro measurements (see figures 3.2 and 3.3).

Nanometer scale interparticle forces play a crucial role in the stability, phase behavior, and rheology of colloidal dispersions (Wagner and Bender 2004). For instance, shear-thickening can be eliminated by suitable 'tuning' of these forces (Bergenholtz et al. 2002). In microrheology, the equivalent effect is the inhibition of force-thickening; however, only the hard-sphere 'excluded-annulus' model has been utilized to study this (see chapter 2). Thus, we need to apply the theory developed in chapter 2 to more realistic (e.g., Van der Waals, DLVO) interparticle forces. The inverse problem is also interesting; namely, can microrheology be used to infer nano-scale interparticle interactions? In macrorheology the answer is yes: for example, high-frequency measurements of the elastic modulus have been employed to determine the surface charge of electrostatically stabilized dispersions (Horn et al., 2000). Furthermore, the elastic modulus has been used to quantify the roughness,

or surface-slip, at particle surfaces (Fritz et al., 2002). In chapter 3 we showed that the elastic modulus diverges like $\omega^{1/2}$ as $\omega \to \infty$ for particles interacting via excluded-annulus interparticle forces. On the other hand, in the absence of hard-sphere interparticle forces the effect of hydrodynamic interactions yields a finite elastic modulus as $\omega \to \infty$. The formalism of chapter 3 may easily be extended to study the effect of more specific, or realistic, interparticle forces on the high-frequency behavior of the elastic modulus.

In chapter 4 we investigated an issue that has hitherto been untouched by the (micro-) rheological community: namely, what role does the shape of the probe play. For microrheology, this is a rare occurrence of theoretical analysis preceding experimental measurement. Specifically, we considered the probe to be a body of revolution with major and minor semi-axes $a$ and $b$, respectively, translating at constant velocity through a dispersion of spherical bath particles (of radii $b$). The probe's shape is such that when it's major(minor) axis is the axis of revolution the excluded-volume, or contact, surface between it and a bath particle is a prolate(oblate) spheroid. For a probe moving along its symmetry axis, the microviscosity was computed as a function of the aspect ratio of the probe, $\hat{a} = a/b$, thereby delineating the role of the probe's shape. For a prolate probe, regardless of the value of $\hat{a}$, the microviscosity monotonically decreases, or 'velocity-thins', from a Newtonian plateau at small $Pe$ (here, $Pe$ is the non-dimensional velocity of the probe) until a second Newtonian plateau is reached as $Pe \to \infty$. For an oblate probe, the microviscosity again transitions between two Newtonian plateaus: for $\hat{a} < 3.52$ (to two decimal places) the microviscosity at small $Pe$ is greater than at large $Pe$ (velocity-thinning); however, for $\hat{a} > 3.52$ the microviscosity at small $Pe$ is *less* than at large $Pe$, which suggests it 'velocity-thickens' as $Pe$ is increased. This anomalous velocity-thickening — due entirely to the probe shape — highlights the care needed when conducting microrheology experiments with non-spherical probes.

One of the main limitations of microrheology with a single spherical probe is that one can determine only a (scalar) microviscosity of a material. In contrast, macrorheology can, in principle, obtain the full stress tensor including normal stress differences and an isotropic osmotic pressure (Bergenholtz et al. 2002). Could a non-spherical probe give more than just a microviscosity? In chapter 4 we presented a preliminary analysis of this question, by considering a prolate probe that translates at an angle $\beta$ to its symmetry axis. In general, one must apply an external torque to the probe to prevent it from rotating. In the linear-response ($Pe \ll 1$) regime the dispersion does not exert a torque of the probe; consequently, the external torque is zero. However, far from equilibrium ($Pe \gg 1$) the dispersion does exert a torque on the probe that, in the absence of an external torque, would orient the probe in a broadside ($\beta = \pi/2$) configuration. From Leal's (Leal 1975) investigation on the translation of rod-like particles in a second-order fluid, a stable broadside configuration suggests that the quantity $4N_1 + N_2 < 0$ ($N_1$ and $N_2$ are the first and second normal stress differences, respectively) at large $Pe$. Within the 'radial-balance' approximation used to compute the microstructure at large $Pe$, this is consistent with the macrorheological findings of Brady and Morris (1997). However, as discussed in chapter 4, one must solve the 'full' microstructural problem at large $Pe$ before any definitive conclusions can be drawn. Moreover, as shown by Zarraga et al. (2000) and mentioned in § 4.7, it is not clear that the second-order fluid is a 'correct' model for colloidal dispersions at large $Pe$; hence, it may not be appropriate to infer normal stress differences from our model by comparison to Leal's (Leal 1975) results.

The discussion above does, nevertheless, highlight an important point: the non-viscometric flow generated by a prolate probe implies that one can determine only the combination $4N_1 + N_2$, and not $N_1$ and $N_2$ in isolation. In contrast, macrorheology utilizes viscometric

flows (simple shear, plane strain etc.), from which can yield separate measurements of $N_1$ and $N_2$. Thus, the challenge for microrheologists is to develop techniques that are capable of ascertaining normal stress differences independently.

In a broader context, microrheology is faced with several important challenges. For example, passive microrheology has been applied recently to characterizing the heterogeneous environment within living cells (Daniels et al. 2006). In fact, the *in vivo* application of microrheology to living cells has been given its own name: 'Bio-microrheology' (Weihs et al. 2006). In modeling this problem one must account for the interaction of the diffusing probe with the cell walls. More generally, how do the boundaries of a sample affect its microrheologically-measured properties? Could, for example, the change in microviscosity with probe position be used to construct a 'rheological map' of a cell? Simple low-Reynolds-number hydrodynamics tells us the force (and hence microviscosity) required to bring a particle close to a rigid wall diverges in the limit of contact. Can microrheology pick up on this? How does the elasticity and deformation of the cell wall come into play?

An interface between two materials (a cell membrane, for instance) is another type of boundary that presents challenges and opportunities for (micro-)rheologists. Very recently, the first passive interfacial microrheology studies have been reported (Anguelouch et al. 2006; Oetama and Walz 2006; Prasad et al. 2006). We are faced with many issues when an active probe is placed near or at an interface: What exactly is being measured? An interfacial (surface) microviscosity? Some combination of the microviscosities of the materials either side of the interface? What shape and size should the probe be? How far does the probe have to be inside one material so that it does not 'see' the interface? Does the motion of the probe deform the interface? The theoretical techniques developed in this thesis can serve as a sound starting point to tackle these interesting problems.

At the theoretical and computational levels, we need to extend our current models of microrheology to accurately describe more intricately microstructured materials, such as fibrous networks and gels. For example, yield-stress like behavior has been observed in active microrheology experiments of colloidal dispersions near the glass transition (Habdas et al. 2004); the existing (dilute) theories simply can't capture this.

In chapter 5 we considered the motion of two 'probe' particles traveling at constant, equal velocities through a hard-sphere dispersion, in an attempt to study entropic depletion forces out of equilibrium. The physical picture is simple: the moving probes disturb the tranquility of the dispersion; in response, the dispersion exerts a reactive entropic force on each probe, which depends on the non-dimensional velocity of the probes (i.e., the Péclet number, $Pe$) and their separation. When moving slowly ($Pe \ll 1$) we recover the (equilibrium) depletion attraction between probes. For rapid motion ($Pe \gg 1$) the leading probe does all the work in pushing bath particles out of its path, while the trailing probe gets a 'free ride'. Hence, the entropic force on the trailing probe vanishes, whereas the force on the leading probe approaches a limiting value equal to that for a single probe moving at large $Pe$. Conversely, if the probes moved with equal applied forces the trailing probe would, on average, move faster than the leading probe and eventually catch-up to it. By adding more (trailing) probes one may form a 'train' of particles moving through the dispersion, which constitutes a mechanism for pattern formation in complex fluids.

The discussion above points up many interesting questions: What happens if the probes move with different speeds? How do non-equilibrium depletion forces depend on the probe-bath size ratio? And how are they affected by interparticle forces (beyond hard-sphere repulsion) between the probes? What if the probes do not move along their line of centers? How many particles can one add to a colloidal 'train' before it buckles? Is the train stable

to small amplitude perturbations? These problems need to be addressed via analytical theory (by extending the formalism developed in chapter 5), computer simulations, and experiments. A possible experimental setup is to hold two (or more) colloidal particles at a fixed separation using optical traps and flow a complex fluid past them (via a translating stage). The entropic (depletion) force exerted on each probe is simply the negative of the force required to trap it (less the hydrodynamic drag).

Finally, we note that entropic attraction can be induced between not only colloidal particles but also particles and walls. Specifically, by geometric patterning of a surface one can create an 'entropic force field' useful in the self-assembly of colloids in a desired fashion (Dinsmore et al. 1996). Existing studies have been restricted to equilibrium systems; however, one can imagine that in a microfluidic device, for example, colloidal particles may be actively transported (driven) past a templated surface, and one needs to take account of this nonequilibrium forcing. The formalism of chapter 5 is readily applicable to study the motion of a colloid probe in the proximity of a rigid wall. The goal would be to determine the forces on the driven colloid and the wall as a function of the surface patterning, separation, and colloid motion (i.e., parallel or perpendicular to the wall).

## 6.2 Bibliography

A. Anguelouch, R. L. Leheny, and D. H. Reich. Application of ferromagnetic nanowires to interfacial microrheology. *Appl. Phys. Lett.*, 89:111914, 2006.

J. Bergenholtz, J. F. Brady, and M. Vicic. The non-Newtonian rheology of dilute colloidal suspensions. *J. Fluid Mech.*, 456:239–275, 2002.

J. F. Brady and G. Bossis. Stokesian dynamics. *Annu. Rev. Fluid. Mech.*, 20:111–157, 1988.

J. F. Brady and J. F. Morris. Microstructure of strongly sheared suspensions and its impact on rheology and diffusion. *J. Fluid Mech.*, 348:103–139, 1997.

B. R. Daniels, B. C. Masi, and D. Wirtz. Probing single-cell micromechanics in vivo: the micorheology of *C. elegans* developing embryos. *Biophys. J.*, 90:4712–4719, 2006.

A. D. Dinsmore, A. G. Yodh, and D. J. Pine. Entropic control of particle motion using passive surface microstructures. *Nature*, 383:239–242, 1996.

G. Fritz, B. J. Maranzano, N. J. Wagner, and N. Willenbacher. High frequency rheology of hard sphere colloidal dispersions measured with a torsional resonator. *J. Non-Newtonian Fluid Mech.*, 102:149–156, 2002.

P. Habdas, D. Schaar, A. C. Levitt, and E. R. Weeks. Forced motion of a probe particle near the colloidal glass transition. *Europhys. Lett.*, 79:477–483, 2004.

F. M. Horn, W. Richtering, J. Bergenholtz, N. Willenbacher, and N. J. Wagner. Hydrodynamic and colloidal interactions in concentrated charge-stabilized polymer dispersions. *J. Coll. Int. Sci.*, 225:166–178, 2000.

L. G. Leal. The slow motion of a slender rod-like particle in a second-order fluid. *J. Fluid Mech.*, 69:305–337, 1975.

Y. S. Lee, E. D. Wetzel, and N. J. Wagner. The ballistic impact characterists of Kevlar woven fabrics impregnated with a colloidal shear thickening fluid. *J. Mater. Sci.*, 38: 2825–2833, 2003.

R. J. Oetama and R. Y. Walz. Investigation of short-time particle dynamcs near an interface in the presence of nonadsorbed macro-ions. *Langmuir*, 22:8318–8325, 2006.

V. Prasad, S. A. Koehler, and E. R. Weeks. Two-particle microrheology of quasi-2d systems. *Phys. Rev. Lett.*, 97:176001, 2006.

N. J. Wagner and J. W. Bender. The role of nanoscale forces in colloid dispersion rheology. *MRS Bulletin*, 29:100–106, 2004.

D. Weihs, T. G. Mason, and M. A. Teitell. Bio-microrheology: A frontier in microrheology. *Biophys. J.*, 91:4296–4305, 2006.

I. E. Zarraga, D. A. Hill, and D. T. Leighton. The characterization of the total stress of concentrated suspensions of noncolloidal spheres in Newtonian fluids. *J. Rheol.*, 44: 185–220, 2000.